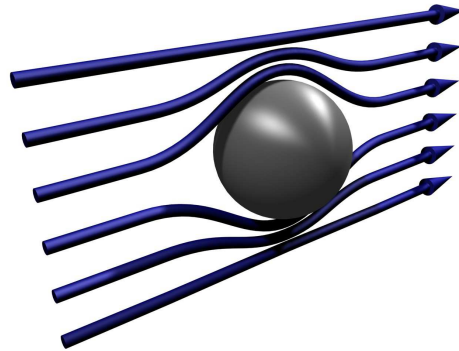


Mesoscopic Shelving Readout of Superconducting Qubits in Circuit Quantum Electrodynamics



Diploma Thesis

by Barbara Gabriele Ursula Englert

October 2008

Supervised by

Prof. Dr. Rudolf Gross and Prof. Dr. Enrique Solano

This work has emerged from a collaboration of

Chair for Experimental Physics (E23)

Walther-Meißner-Institut, Bayerische Akademie der Wissenschaften
Physics Department, Technische Universität München

Chair for Theoretical Solid State Physics

Physics Department, Ludwig-Maximilians-Universität München

Departamento de Química Física

Universidad del País Vasco UPV-EHU, Bilbao (Spain)



Abstract

Superconducting Josephson junction devices are one of the most promising candidates for the realization of a quantum computer. With these solid-state macroscopic quantum systems it is possible to reach the strong coupling regime in circuit quantum electrodynamics, where a superconducting qubit is coupled to the electromagnetic field of a microwave resonator. While these systems allow for accurate quantum operations, a major challenge is the efficient fault-tolerant quantum computation.

In this thesis, we present a method for measuring the quantum state of a superconducting qubit inside a microwave cavity based on a Mesoscopic Shelving Readout. The proposed protocol associates one qubit state with the generation of a mesoscopic coherent field, while the other qubit state remains associated with a vacuum field. By measuring the outgoing cavity field with conventional devices, an efficient detection of the qubit state can be achieved. The method uses a cyclic transition in a three-level qubit configuration to build the large cavity field which enables a high-fidelity measurement in the spirit of the successful electron shelving readout for trapped ions. We expect that the proposed technique can be adapted to different superconducting qubit designs and contribute to improve further the qubit readout fidelity. For the development of this Mesoscopic Shelving Readout, we also review the properties of superconducting qubits including their theoretical description in a self-contained manner and examine the coupling of these “artificial atoms” to a one-dimensional transmission line resonator in circuit quantum electrodynamics.

Contents

Abstract	iii
List of Figures	ix
List of Abbreviations	xi
Introduction	1
1 Qubits and their Physical Implementation	3
1.1 DiVincenzo's Requirements for a Scalable Quantum Computer	3
1.1.1 Scalability	4
1.1.2 Initialization	5
1.1.3 Stability	5
1.1.4 Control	6
1.1.5 Measurement	6
1.2 Qubit Dynamics	7
1.2.1 Two-level State	7
1.2.2 Qubit Decoherence	9
1.3 Coupling to an External Field	10
1.3.1 Rabi Oscillations	11
1.3.2 AC Stark Shift	12
1.4 Types of Qubits	13
1.4.1 Trapped Ions and Cavity QED	13
1.4.2 Other Architectures	14
2 Superconducting Qubits and Circuit Quantum Electrodynamics	15
2.1 Charge Qubits	17
2.1.1 Cooper Pair Box in the Charge Regime	17
2.1.2 Transmon Qubit	20
2.2 Flux Qubits	23
2.2.1 RF SQUID Qubit	24
2.2.2 Persistent Current Qubit	27
2.3 Phase Qubits	29
2.4 Circuit Quantum Electrodynamics with Superconducting Qubits	33
2.4.1 Capacitive coupling to the CPB Qubit	33
2.4.2 Circuit QED with the Transmon in the Dispersive Regime	36
2.4.3 Inductive Coupling to Flux Qubits	37

2.4.4	Circuit QED with Phase Qubits	38
3	State-of-the-Art in Superconducting Qubit Readout	41
3.1	Readout of Charge Qubits with a Single Electron Transistor	42
3.1.1	State Detection	42
3.1.2	Fidelity of the Readout	44
3.2	Dispersive Measurement Using Circuit QED	46
3.3	Readout with the Josephson Bifurcation Amplifier	50
3.3.1	Coupling of the Qubit to the Readout SQUID	50
3.3.2	State Detection	52
3.4	Tunnelling-Readout of Phase Qubits	54
4	Mesoscopic Shelving Readout	57
4.1	Electron Shelving in Trapped Ions	57
4.2	Evaluation of Shelving Ideas for SC qubits	59
4.3	The Idea of the Mesoscopic Shelving Readout	60
4.4	Analytical Model of the Mesoscopic Shelving Readout	62
4.4.1	Unitary Dynamics of the Driven Superconducting Qubit	62
4.4.2	Dissipative Model	65
4.5	State Detection	71
4.5.1	Cavity Field	71
4.5.2	Numerical Simulations in the Intermediate Regime	73
4.6	Characterization of the Mesoscopic Shelving Readout	76
4.6.1	Signal-to-Noise Ratio	76
4.6.2	Single-Shot Readout Fidelity	77
4.6.3	Quantum Non-Demolition Character	78
5	Conclusion and Outlook	79
	Appendices	81
A	Details on Quantum Mechanics	81
A.1	Time Evolution in Quantum Mechanics	81
A.1.1	Schrödinger Picture	81
A.1.2	Heisenberg Picture	82
A.1.3	Interaction Picture	82
A.2	Unitary Transformations	83
A.3	Stochastic Master Equation	84
A.4	Jaynes–Cummings Interaction	86
A.4.1	Dipole Interaction	86
A.4.2	Rotating Wave Approximation	87
A.5	Effective Hamiltonian Approach	87
B	Theory of Superconductivity and Josephson Junctions	89
B.1	London Theory	89
B.1.1	London Equations	90
B.1.2	Fluxoid Quantization	91
B.2	Josephson Effect	92

B.2.1	Josephson Equations	93
B.2.2	Josephson Coupling Energy	94
B.2.3	Josephson Inductance	95
B.2.4	DC and AC Josephson Effect	95
B.3	Whole Junction Dynamics	95
B.3.1	RCSJ Model	96
B.3.2	Hamiltonian of the Current-Biased Junction	97
B.3.3	Hamiltonian of the Voltage-Biased Junction	98
B.4	Superconducting Quantum Interference Devices	100
B.4.1	DC SQUID	100
B.4.2	RF SQUID	101
C	Detailed Calculations on SC Qubits	103
C.1	Charge Qubit Hamiltonian in the Charge Basis	103
C.2	Nonlinear Oscillator	104
C.3	Minima of the PCQ Potential	105
C.4	Quantization of the 1D Transmission Line Resonator	107
C.4.1	Capacitive Coupling	109
C.4.2	Inductive Coupling	109
C.5	Dispersive Regime of the Generalized JC Model	110
C.6	Time-Dependent “Constant” Term	111
D	Additional Information on the Mesoscopic Shelving Readout	113
D.1	Coherent States	113
D.2	Characteristic Functions and Quasi-Probability Distributions	114
D.3	Detailed Calculations on the MSR	116
D.3.1	Master Equation in Terms of ρ_{iF}	116
D.3.2	Transformation into Characteristic Functions	116
D.3.3	Fourier Transform	118
E	Measurement Techniques	121
E.1	Quadratures	121
E.2	Homodyne and Heterodyne Detection	122
E.3	Linear Amplifier	123
E.3.1	Floor Noise	124
E.3.2	Theoretical Description	124
	Bibliography	127
	Acknowledgements	135

List of Figures

1.1	Diagram of the DiVincenzo Requirements	3
1.2	Bloch Sphere Representation of a Qubit	5
1.3	Energy Spectrum of Qubit Dynamics	8
1.4	Energy Spectrum of a Qubit Coupled to an External Field	12
2.1	Comparison of SC qubit Implementations	16
2.2	Scanning Electron Microscopy of SC qubits	16
2.3	Circuit Diagram and Energy Landscape of the CPB Qubit	18
2.4	Transmon Qubit	21
2.5	Anharmonicity of the CPB as a Function of E_J/E_c	22
2.6	Circuit Diagram and Energy Landscape of the RF SQUID Qubit	24
2.7	Truncation of the Flux Qubit Hamiltonian and Energy Levels	26
2.8	Three-junction Persistent Current Qubit	28
2.9	Potential Energy Landscape of the PCQ	28
2.10	Circuit Diagram and Energy Landscape of the Phase Qubit	30
2.11	Potential Energy Landscape of the Flux-Biased Phase Qubit	32
2.12	Schematic Layout of the One-Dimensional Transmission Line Resonator	34
2.13	Experimental Realization of Circuit QED with a CPB	35
2.14	Schematic Layout of Circuit QED Implementation with Flux Qubits	38
2.15	Schematic Layout of Circuit QED Implementation with Phase Qubits	39
3.1	Experimental Setup and Pulse Sequence of the SET Readout	43
3.2	Measurement Scheme and Pulse Sequence of the Dispersive Readout	47
3.3	AC Stark Shift and Phase Shift in the Dispersive Limit	49
3.4	Bistability of the Driven Nonlinear Oscillator	52
3.5	Pulse Sequence and Switching Probability of the Bifurcation Amplifier Readout	53
3.6	Phase Qubit Operation and Measurement	54
3.7	Tunnelling Probabilities in the Phase Qubit Readout	56
4.1	Sketch of the Electron Shelving Readout in Trapped Ions	58
4.2	Sketch of the Mesoscopic Shelving Readout	60
4.3	Mean Photon Number in the Cavity	72
4.4	Numerical Simulations of the Mean Cavity Photon Number	75
4.5	Mean Transmitted Photon Rate for the Excited State	76
B.1	Sketch of a Josephson Junction	93
B.2	RCSJ Model	96

B.3	Circuit Diagram of the Voltage-Biased Single Electron Box	98
B.4	Circuit Diagram of the DC SQUID	101
B.5	Circuit Diagram of the RF SQUID	102
C.1	Energy Landscape of the Nonlinear Resonator	105
E.1	Sketch of a Homodyne Detection Scheme	122

List of Abbreviations

ac	A lternating C urrent
CPB	C ooper P air B ox
dc	D irect C urrent
JC	J aynes C ummings
JJ	J osephson J unction
MSR	M esosopic S helving R eadout
PCQ	P ersistent C urrent Q ubit
QED	Q uantum E lectro D ynamics
QND	Q uantum N on- D emolition
rf	R adio F requency
rms	R oot- M ean- S quare
RWA	R otating W ave A pproximation
SNR	S ignal-to- N oise R atio
SC	S uperconducting
SQUID	S uperconducting Q uantum I nterference D evice
TLR	T ransmission L ine R esonator

Introduction

Since the pioneering works of Feynman [1] and Deutsch [2] in the 1980s, an interdisciplinary community of scientists has been exploring the idea of quantum information processing. A quantum computer employs quantum-mechanical phenomena, such as state superposition and entanglement, that lead to a kind of parallel processing during computational operations. Due to this novel type of information processing, quantum algorithms can run exponentially faster than their classical counterparts.

Practical implementation of quantum computation requires the replacement of classical bits, that carry the information in an ordinary computer, by quantum bits (qubits). These qubits can be composed of any quantum system with two distinct quantum-mechanical states ($|0\rangle$ and $|1\rangle$) that can be placed into quantum superpositions. A computation then proceeds by combining manipulations of the superpositions in single qubits and controlled interactions of multiple qubits.

Many different implementations of quantum computers are being pursued today. Most of the proposals are based on qubits that are constructed from the microscopic degree of freedom, such as the spin of electrons or nuclei or transitions of single atoms or ions. Due to their naturally well isolation from the environment, these microscopic implementations decohere very slowly but are also hard to couple and to control without introducing decoherence.

We discuss a different experimental approach based on superconducting (SC) electrical circuits that behave as “artificial atoms”. Here, qubits are constructed from collective electro-dynamical modes of macroscopic SC electrical elements. These superconducting qubits (SC qubits) [3; 4; 5; 6] are very promising candidates for the realization of quantum information processors as they can be designed and fabricated using standard techniques from conventional electronics thus allowing for large-scale integration. Another advantage of this approach is that SC circuits have intrinsically large electromagnetic cross-sections, which implies they may easily be coupled together in complex topologies via simple linear electrical elements like capacitors, inductors, and transmission lines.

In the past decade, several different types (“flavours”) of SQubits have been engineered, quantum-mechanical Rabi oscillations have been observed [7], and two qubits have been coupled and entangled [8]. The current state-of-the-art allows for superposition states that live several microseconds, long enough for hundreds of operations on a single qubit. With improvements in the design of SC qubits, as well as in the materials and methods used for fabricating circuits, the lifetime of the stored quantum information may be further increased and the precision of qubit control enhanced.

Another advantage of SC qubits is that they can be coupled to the electromagnetic field of a microwave resonator in circuit quantum electrodynamics (QED). Circuit QED is a novel subject of interest in the field of solid-state quantum computation. It appears from the association of quantum-optical cavity QED with macroscopic quantum mechanics. This approach

offers the prospect of reaching an upper limit for the strong coupling of a quantum-mechanical two-level system to a single mode of the electromagnetic field.

The main focus of this work is the readout of SC qubits and the search of high fidelity. An open issue in SC qubits is the efficient determination of the qubit state. For quantum computation and quantum error correction, an accurate state measurement with a fidelity above 99% is essential [9]. Though several promising candidates for such a high-fidelity readout have been proposed [10; 11; 12; 13; 14], until now it was not possible to achieve the required fidelity.

In this work, a novel measurement technique for SC qubits that we term the Mesoscopic Shelving Readout is theoretically modelled. This technique uses ideas from the electron shelving readout of trapped ions and combines them with features from circuit QED. This may result in an accurate measurement of the quantum-mechanical state of an SC qubit.

Outline

The thesis is organized as follows. In the first chapter, we introduce DiVincenzo's criteria for a scalable quantum computer. We give a general overview of the dynamics of a qubit including decoherence mechanisms. Then, we show how the coupling of a qubit to a single mode of the electromagnetic field can be described with the Jaynes–Cummings model; we discuss the resonant and strongly detuned case with this model. Lastly, we present the implementation of qubits in different experimental architectures, where we especially discuss trapped ions and cavity QED.

In the second chapter, we focus on SC qubits. We show how to implement qubits using the charge, flux, or phase degree of freedom of a Josephson junction (JJ). We discuss the theoretical model for each of these qubits including certain attributes and features. Then, we introduce the concept of circuit QED with SC qubits. Here, we obtain the coupling strength of a charge, flux, or phase qubit coupled to a transmission line resonator.

In the third chapter, we present the state-of-the-art in the readout of SC qubits. We consider four readout techniques, the charge qubit readout with a single electron transistor (SET) [10], the dispersive readout using circuit QED [11], the Josephson bifurcation amplifier readout [12; 13], and the tunnelling-readout of phase qubits [14]. We examine each of these measurement schemes on its readout properties such as the readout fidelity and the measurement time.

In the fourth chapter, we firstly discuss the electron shelving readout of trapped ions. We then introduce our concept for the readout for SC qubits which is inspired from the electron shelving: the Mesoscopic Shelving Readout (MSR). We present the full analytical and numerical model of this readout technique including the dissipative dynamics. Lastly, we discuss the signal-to-noise ratio, the fidelity, and the quantum non-demolition character of the MSR. We show that it is possible to achieve a readout fidelity that approaches unity ($> 99\%$) in a fast qubit readout. To our knowledge, our proposal is the first that aims at such a high fidelity for the measurement of the state of an SC qubit.

Chapter 1

Qubits and their Physical Implementation

In theory, quantum computers have an amazing computing power that cannot be beaten by any classical computer [9]. However, the question appears how to implement quantum computation in realistic architectures. For this implementation, criteria are needed to identify useful ideas. For this purpose, in this chapter we firstly examine the “hows” of quantum computation, that is, we discuss the *DiVincenzo requirements* [15] for a scalable quantum computer. Secondly, we study qubit dynamics which includes the dynamics of a pure two-level system, the decoherence of a qubit, and the *Jaynes–Cummings* (JC) coupling to an electromagnetic field. At last, we have a look at the realization of qubits in different experimentally achievable architectures as in atomic, optical, electronic, and spin systems.

1.1 DiVincenzo’s Requirements for a Scalable Quantum Computer

For the implementation of quantum computation, five criteria have to be fulfilled: the *DiVincenzo requirements* [15]. These criteria deal with the conditions that are needed for qubits and

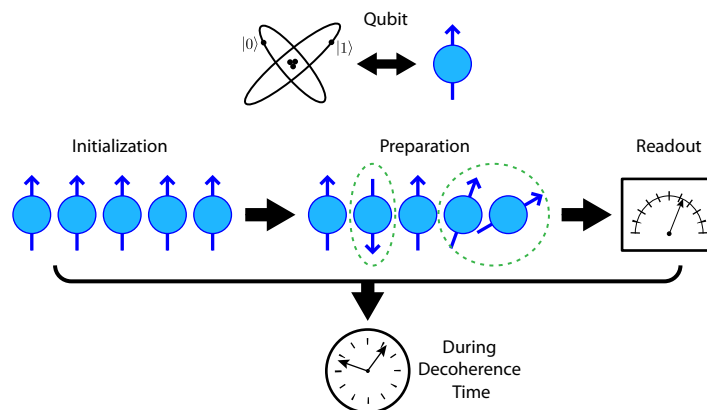


Figure 1.1: Diagram of the DiVincenzo requirements. For quantum computation, a scalable qubit that can be coupled to other qubits, initialized, controlled, and read out is needed.

the experimental setup, as the measurement and the control of the qubit. The DiVincenzo requirements are (see also Fig. 1.1)

1. Well-defined register of n scalable qubits with 2^n states accessible—*Scalability*,
2. Preparation of the qubit in a pure state, such as $|000\dots\rangle$, possible—*Initialization*,
3. Coherence times much longer than the gate operation time—*Stability*,
4. Universal set of gates for state manipulation—*Control*,
5. Single quantum measurement of the qubit—*Measurement*.

In the following sections, we take a closer look on these five criteria.

1.1.1 Scalability

To implement quantum computation, a physical system containing a collection of qubits is needed. A qubit is a quantum-mechanical two-level system like the two spin states of a spin-1/2-particle. A common way to describe the state of a qubit is to write it in terms of the eigenvectors $|0\rangle$ and $|1\rangle$ of the Pauli matrix σ^z ¹,

$$|0\rangle = \begin{pmatrix} 1 \\ 0 \end{pmatrix}, \quad |1\rangle = \begin{pmatrix} 0 \\ 1 \end{pmatrix}. \quad (1.1)$$

Many quantum phenomena are accepted for the implementation of qubits such as the electron spin (up/down), the polarization of a photon (horizontal/vertical), the spin of the atomic nucleus, the current in a superconducting (SC) loop (clockwise/anticlockwise), or the presence/absence of a particle, see also Sec. 1.4.

The general state of a single qubit (=one-qubit state) is a superposition of the two eigenstates $|0\rangle$ and $|1\rangle$,

$$|\Psi(t)\rangle_1 = \alpha(t)|1\rangle + \beta(t)|0\rangle, \quad (1.2)$$

where $\alpha(t)$ and $\beta(t)$ are time-dependent complex numbers obeying the normalization condition, $|\alpha(t)|^2 + |\beta(t)|^2 = 1$; the probability to find the qubit in state $|1\rangle$ ($|0\rangle$) then is $p_1(t) = |\alpha(t)|^2$ ($p_0(t) = |\beta(t)|^2$). The state of a single qubit fills up a two-dimensional complex vector space.

Writing α and β in terms of their argument and phases,

$$\alpha = e^{i\gamma} e^{i\varphi} \sin \frac{\eta}{2}, \quad \beta = e^{i\gamma} \cos \frac{\eta}{2}, \quad (1.3)$$

the state of the qubit can be described as a rotation of the state $|0\rangle$,

$$|\Psi\rangle = \begin{pmatrix} 1 & 0 \\ 0 & e^{i\varphi} \end{pmatrix} \begin{pmatrix} \cos \frac{\eta}{2} & -\sin \frac{\eta}{2} \\ \sin \frac{\eta}{2} & \cos \frac{\eta}{2} \end{pmatrix} \begin{pmatrix} 1 \\ 0 \end{pmatrix} = \cos \frac{\eta}{2} |0\rangle + e^{i\varphi} \sin \frac{\eta}{2} |1\rangle, \quad (1.4)$$

where the factor $e^{i\gamma}$ in Eq. (1.3) was ignored due to no observable physical effects [9]. The real values η and φ provide the phase information of the qubit state and define a point on

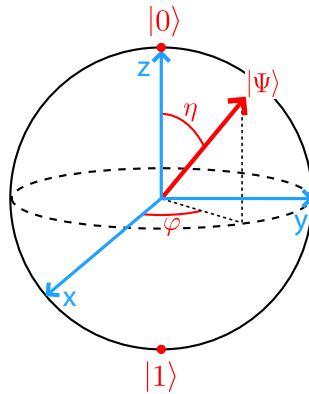


Figure 1.2: Bloch sphere representation of a qubit. The vector $|\Psi\rangle$ represents the state of the qubit in this three-dimensional sphere that represents the two-dimensional complex vector space. The state of the qubit is defined by the angles η and φ .

a three-dimensional unit sphere, the so-called *Bloch sphere*, see Fig. 1.2. The Bloch sphere provides a useful means of visualizing the state of a single qubit.

For quantum computation, coupling of at least two qubits is required. The state of an n -qubit register can be written as a time-dependent superposition of 2^n many-particle configurations,

$$|\Psi(t)\rangle_n = \alpha_1(t) |0\dots 00\rangle + \alpha_2(t) |0\dots 01\rangle + \alpha_3(t) |0\dots 10\rangle + \dots + \alpha_n(t) |1\dots 11\rangle, \quad (1.5)$$

where, again, the complex numbers $\alpha_i(t)$ ($i = 1, \dots, n$) obey the normalization condition, $\sum_{i=1}^n |\alpha_i(t)|^2 = 1$. In general, the state of n qubits is described by a 2^n -dimensional complex vector. Vice versa, if the state of n physical two-level systems has a dimension $< 2^n$, it cannot be used as an n -qubit state. The n -qubit state in general represents an entangled many-body state and thus cannot be written as a product of one-qubit states.

1.1.2 Initialization

It is generally necessary to initialize registers to a known value before performing computation. In addition, a continuous, fresh supply of qubits in a low-entropy state is required for quantum error correction (for more information on quantum error correction see e.g. [9]).

There are two major ways to initialize the state of the qubit: the system can be cooled down naturally to its ground state or it can be rotated into the desired state by a measurement or a gate operation.

1.1.3 Stability

The dynamics of a qubit in contact with its environment is characterized by coherence times, see also Sec. 1.2. For quantum computation, the “relevant” coherence times should be long

¹The Pauli spin matrices are: $\sigma^x = \begin{pmatrix} 0 & 1 \\ 1 & 0 \end{pmatrix} = |0\rangle\langle 1| + |1\rangle\langle 0|$, $\sigma^y = \begin{pmatrix} 0 & -i \\ i & 0 \end{pmatrix} = -i(|0\rangle\langle 1| - |1\rangle\langle 0|)$, and $\sigma^z = \begin{pmatrix} 1 & 0 \\ 0 & -1 \end{pmatrix} = |0\rangle\langle 0| - |1\rangle\langle 1|$, as can be found in any standard textbook of quantum mechanics; see e.g. [16].

enough for carrying out quantum gates. A quantum particle can have many coherence times corresponding to different degrees of freedom. Many of these coherence times can be irrelevant for the use of the particle as a qubit. The choice of the qubits basis states $|0\rangle$ and $|1\rangle$ determines the relevant coherence times.

The magnitude of the coherence time scale that is acceptable for fault-tolerant quantum computation (to maintain coherence “forever”) is $10^4 - 10^5$ times the “clock time”² of the quantum computer. In this case error correction can be successful [15].

1.1.4 Control

In quantum computation one has to allow the n -qubit state to evolve in a coherent way through unitary transformations acting on the qubits. These *quantum gates* are described by Hamiltonians \mathcal{H}_g ³ which generate the transformations as $U_g = e^{-i\mathcal{H}_g t/\hbar}$. The only constraint for \mathcal{H}_g is that the generated transformation has to be *unitary*, $U_g^\dagger U_g = 1$; any unitary matrix specifies a valid quantum gate [9].

Single qubit gates are generated by two-dimensional matrices that rotate the qubit state in the Bloch sphere. For multi-qubit gates a universal set of gates is required. A set of universal quantum gates is any set of gates to which any operation possible on a quantum computer can be reduced, that is, any other unitary operation can be expressed as a finite sequence of gates from the set. Equivalently, a set of universal quantum gates is a set of generators for the group of unitary matrices. Any unitary transformation acting on the state space of n qubits can be composed from single-spin operations and the controlled-NOT gate that is used to create entangled states. For more information on quantum gates see [9].

1.1.5 Measurement

One important requirement for quantum computation is the efficient readout of the qubit states. Successful fault-tolerant operations require certain minimum thresholds for the fidelity of state measurement. Moreover, qubit readout is important, not only for the determination of the final output state, but also for error correction which is essential for quantum computation. For efficient error correction in realistic implementations, errors below $10^{-3} = 0.1\%$ and thus a fidelity above 99.9% are required [9; 17].

The ultimate objective of a qubit readout device is to distinguish the *eigenstates* of the qubit in a single-shot *quantum non-demolition* (QND) measurement [4]. A QND measurement does not destroy the state of the qubit; after the measurement, the qubit remains in the measured eigenstate. This means, the measurement Hamiltonian, i.e. the interaction Hamiltonian of the qubit and the measurement device, commutes with the qubit Hamiltonian. The QND character of the measurement is not strictly required; nevertheless, it is a useful tool for preparation of the qubit state (see Sec. 1.1.2).

The density matrix corresponding to the single-qubit state (1.2) is given by

$$\rho = |\alpha|^2 |1\rangle \langle 1| + |\beta|^2 |0\rangle \langle 0| + \alpha\beta^* |1\rangle \langle 0| + \alpha^*\beta |0\rangle \langle 1|. \quad (1.6)$$

An ideal measurement of the qubit state should give the output “1” with probability $p_{\text{ideal}} = |\alpha|^2$ and “0” with probability $1 - p_{\text{ideal}} = |\beta|^2$ independent of $\alpha\beta^*$ ($\alpha^*\beta$) or other parameters of the system.

²The “clock time” is the time needed for the execution of an individual quantum gate.

³For any operator \hat{O} we only write \hat{O} if the difference between O and \hat{O} is not evident.

At this point it has to be noted that one cannot read out the *state* of a qubit in a single measurement since this is prohibited by quantum mechanics. One can only determine the *eigenstate* of the qubit. This means, the measurement projects the quantum-mechanical qubit state onto a classical state. It takes repeated measurements on a large number of replicas of the quantum state to determine the exact qubit state. This is known as *quantum tomography* [4; 18]. This means, the ideal measurement is conform to a spin projection of the qubit state on its eigenstates; the phase of the qubit is lost.

The difficulty of the readout problem is to extract information from the qubit without introducing noise at the same time. Furthermore, readout of a specific qubit must not destroy the state of other qubits in the system. The measurement connects the qubit with the open system of the detector, which collapses the combined system of qubit and measurement device to one of its common eigenstates. The measurement is accompanied by an inevitable perturbation of the qubit; this perturbation is given by the commutator of the interaction Hamiltonian (that describes the interaction of the qubit and the measurement device) and the qubit Hamiltonian. In the ideal QND case where this commutator is zero and the perturbation is minimal, the magnitude of the perturbation is given by the Heisenberg uncertainty relation. We will return to qubit measurement in chapter 3.

1.2 Qubit Dynamics

In quantum computation, one changes the qubit states, that was initialized in a first step, by applying dc- or rf-pulses to the qubit via control gates. To study the dynamics of the qubit under certain control operations, we firstly describe the dynamics of the general two-level state in this section, including the time evolution of the qubit state and the transformation of the spin in the energy eigenbasis. As a second step, we have a look on decoherence dynamics.

1.2.1 Two-level State

A qubit is described by two parameters: its level splitting ε_q and the coupling Δ_q between the levels⁴. Hence, the single-qubit Hamiltonian expressed in the $\{|0\rangle, |1\rangle\}$ eigenbasis of the qubit (cp. Eq. (1.1)) has the general form

$$\mathcal{H}_q = \frac{\varepsilon_q}{2} \bar{\sigma}^z + \frac{\Delta_q}{2} \bar{\sigma}^x, \quad (1.7)$$

with $\bar{\sigma}^z = |0\rangle\langle 0| - |1\rangle\langle 1|$ and $\bar{\sigma}^x = |0\rangle\langle 1| + |1\rangle\langle 0|$ being the Pauli matrices in the spin basis⁵. In this basis, we can write the state as $|\Psi\rangle = \alpha \begin{pmatrix} 0 \\ 1 \end{pmatrix} + \beta \begin{pmatrix} 1 \\ 0 \end{pmatrix}$ (in this thesis, α and β in general denote the complex constants which determine the probability to find the qubit in a specific eigenstate, independent of the basis). The matrix representation of the Hamiltonian in the spin basis thus is

$$\mathcal{H}_q = \frac{1}{2} \begin{pmatrix} \varepsilon_q & \Delta_q \\ \Delta_q & -\varepsilon_q \end{pmatrix} \quad (1.8)$$

⁴It has to be noted that for most of the qubit implementations, only the level splitting ε_q is required in the qubit Hamiltonian; however, we consider the most general form with a coupling Δ_q that appears in SC qubits.

⁵In this thesis we denote the Pauli matrices in the spin basis $\{|0\rangle, |1\rangle\}$ of the qubit with $\bar{\sigma}^i$ and that in the energy eigenbasis $\{|g\rangle, |e\rangle\}$ with σ^i ($i = x, y, z$).

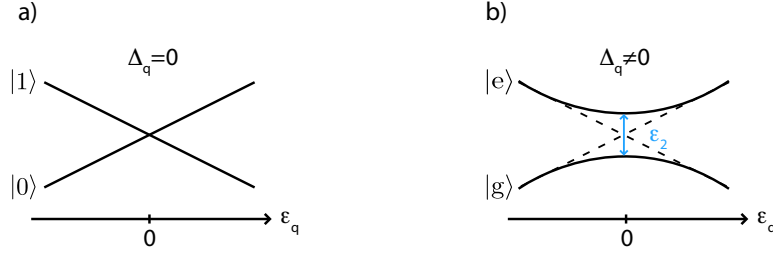


Figure 1.3: Energy spectrum of a two-level system (=qubit) with transition frequency ε_q in the case of **(a)** no coupling ($\Delta_q = 0$) between the qubit states $|0\rangle$ and $|1\rangle$ and **(b)** a coupling $\Delta_q \neq 0$ between the two states. For $\varepsilon_q = 0$, the degeneracy of the levels is lifted by the coupling Δ_q ; this leads to an anti-crossing between the two qubit states. The qubit then is in its dressed states $|g\rangle$ and $|e\rangle$ (see also text).

The eigenvalues of this matrix are

$$E_{e,g} = \pm \frac{\hbar}{2} \omega_q = \pm \frac{1}{2} \sqrt{\varepsilon_q^2 + \Delta_q^2}, \quad (1.9)$$

with corresponding eigenvectors

$$|e\rangle = \cos \vartheta_q |0\rangle + \sin \vartheta_q |1\rangle \quad (1.10a)$$

$$|g\rangle = -\sin \vartheta_q |0\rangle + \cos \vartheta_q |1\rangle. \quad (1.10b)$$

which are always dressed states except for $\Delta_q = 0$, see also Fig. 1.3. ϑ_q is given by $\tan \vartheta_q = \frac{-1 \pm \sqrt{1 + (\varepsilon_q/\Delta_q)^2}}{\varepsilon_q/\Delta_q}$. Using $\tan(2x) = \frac{2 \tan x}{1 - \tan^2 x}$ we obtain

$$\tan 2\vartheta_q = \frac{\Delta_q}{\varepsilon_q}. \quad (1.11)$$

which is defined for all values of Δ_q and ε_q except for $\varepsilon_q = 0$, the so-called *degeneracy point*, where $\vartheta = \pi/4$.

The Hamiltonian of the qubit in its energy eigenbasis reads

$$\mathcal{H}_q = \hbar \frac{\omega_q}{2} \sigma^z, \quad (1.12)$$

with $\sigma^z = |e\rangle\langle e| - |g\rangle\langle g|$; the qubit state in this basis is

$$|\Psi\rangle = \alpha |g\rangle + \beta |e\rangle. \quad (1.13)$$

Here, α and β are, again, complex numbers. If ε_q and Δ_q , and therewith the Hamiltonian, are time-independent, the evolved state⁶ of the qubit after a time t is (cp. App. A.2, Eqs. (A.20) and (A.21))

$$|\Psi(t)\rangle = \alpha |e\rangle e^{\frac{i}{2}\omega_q t} + \beta |g\rangle e^{-\frac{i}{2}\omega_q t}. \quad (1.14)$$

Thus, we can easily determine the time evolution of the qubit state in the energy eigenbasis.

⁶A detailed discussion of the time evolution in the different quantum-mechanical pictures, including unitary transformations, is given in App. A.1.

The transformation of the spin basis in the energy eigenbasis is given by

$$\bar{\sigma}^z = \cos 2\vartheta_q \sigma^z - \sin 2\vartheta_q \sigma^x, \quad (1.15a)$$

$$\bar{\sigma}^x = \sin 2\vartheta_q \sigma^z + \cos 2\vartheta_q \sigma^x. \quad (1.15b)$$

$\sin 2\vartheta_q$ and $\cos 2\vartheta_q$ have to be chosen such that the condition

$$\mathcal{H}_q^{0,1} = \mathcal{H}_q^{\text{g,e}}, \quad \Leftrightarrow \quad \frac{\varepsilon_q}{2} \bar{\sigma}^z + \frac{\Delta_q}{2} \bar{\sigma}^x = \frac{\hbar}{2} \omega_q \sigma^z \quad (1.16)$$

is fulfilled. This is given for

$$\cos 2\vartheta_q = \frac{\varepsilon_q}{\sqrt{\varepsilon_q^2 + \Delta_q^2}}, \quad \text{and} \quad \sin 2\vartheta_q = \frac{\Delta_q}{\sqrt{\varepsilon_q^2 + \Delta_q^2}}. \quad (1.17)$$

At the degeneracy point, $\varepsilon_q = 0$ and therefore $\sin \vartheta_q = \cos \vartheta_q = \frac{1}{\sqrt{2}}$ (for $\Delta_q > 0$); the qubit then is in its maximally dressed states, the $\bar{\sigma}^x$ eigenstates.

1.2.2 Qubit Decoherence

In this section, we give a short definition of quantum decoherence, that is, we examine the mechanism by which quantum systems interact with their environments; a detailed description of decoherence can be found in e.g. [19]. Decoherence dynamics can influence the stability of the qubit and thus the computational process strongly. Therefore, it is useful to know the decoherence dynamics of the system as good as possible. Without decoherence, the system is described by the density operator $\rho = |\Psi(t)\rangle\langle\Psi(t)|$, that follows the *master equation*⁷ (see also App. A.3)

$$\dot{\rho}(t) = -\frac{i}{\hbar} [\mathcal{H}, \rho]. \quad (1.18)$$

Here, \mathcal{H} and Ψ are the Hamiltonian and the qubit state in either the Schrödinger or the interaction picture (see App. A.1). Note that for a time-independent Hamiltonian, $\mathcal{H}_{\text{int}} = 0$ and hence $\dot{\rho} = 0$.

We now take into account the effect of the environment. In the most simple picture, the decoherence of a two-level system is described by two processes that are associated with two characteristic times scales with their corresponding decoherence rates:

- (i) The *longitudinal* or *energy relaxation* rate $\gamma = T_1^{-1}$ (T_1 being the decay time of the system) which describes $|e\rangle \leftrightarrow |g\rangle$ transitions that are induced by high-frequency fluctuations of the environment. Mostly, the energy relaxation results in the spontaneous emission of light; however, in solid-state systems other excitations such as phonons may also be important.
- (ii) The *transversal* or *pure dephasing*⁸ rate $\gamma_\phi = T_2^{-1}$ (T_2 being the pure dephasing time) which refers to the loss of phase coherence by low-frequency noise.

⁷The master equation corresponds to the Heisenberg equation (Eq. (A.7)) for the density operator. The density operator is also called density matrix.

⁸Since the relaxation of the system also has a contribution to the dephasing rate, the dephasing process itself is usually referred to as “pure”.

The Hamiltonian of the qubit in the energy eigenbasis $\{|g\rangle, |e\rangle\}$ and in the Schrödinger picture is $\mathcal{H} = \frac{\hbar}{2}\omega_q\sigma^z$. The spontaneous emission of the qubit is described by the stochastic master equation in the Schrödinger picture⁹ (see App. A.3)

$$\dot{\rho}(t) = -\frac{i}{\hbar}[\mathcal{H}, \rho] - \frac{\gamma}{2}\mathcal{L}[\sigma^-]\rho(t), \quad (1.19)$$

with the Liouvillian superoperator $\mathcal{L}[\sigma^-]\rho(t) = \sigma^+\sigma^-\rho(t) - 2\sigma^-\rho(t)\sigma^+ + \rho(t)\sigma^+\sigma^-$ and the decay rate γ . Therewith, the probability $p_e = \langle e|\rho|e\rangle \equiv \langle \sigma^+\sigma^- \rangle$ to find the qubit in the excited state (corresponding to $|\beta|^2$ in the previous section) satisfies the equation

$$\dot{p}_e(t) = -\gamma p_e(t) \quad \Rightarrow \quad p_e(t) = p_e(0)e^{-\gamma t}. \quad (1.20)$$

This means, the excited state decays exponentially in time, which describes spontaneous emission. The dipole polarization of the qubit is $\langle e|\rho|g\rangle \equiv \langle \sigma^- \rangle$ and obeys

$$\frac{d\langle \sigma^- \rangle}{dt} = -\left(i\omega_q + \frac{\gamma}{2}\right)\langle \sigma^- \rangle, \quad \Rightarrow \quad \langle \sigma^- (t) \rangle = \langle \sigma^- (0) \rangle e^{-(\gamma/2 + i\omega_q)t}. \quad (1.21)$$

The dipole oscillates at the transition frequency and decays, as it radiates.

Dephasing of the system can be described by coupling the σ^x component of the qubit to a reservoir, see App. A.3. The corresponding master equation in the interaction picture including spontaneous emission is [20]

$$\dot{\rho} = -\frac{\gamma}{2}\mathcal{L}[\sigma^-]\rho - \frac{\gamma_\phi}{4}[\sigma^z, [\sigma^z, \rho]], \quad (1.22)$$

with the dephasing rate γ_ϕ . The system is now described by the *Bloch equations*

$$\frac{d\langle \sigma^x \rangle}{dt} = -\left(\frac{\gamma}{2} + \gamma_\phi\right)\langle \sigma^x \rangle, \quad \Rightarrow \quad \langle \sigma^x (t) \rangle = \langle \sigma^x (0) \rangle e^{-(\frac{\gamma}{2} + \gamma_\phi)t}, \quad (1.23a)$$

$$\frac{d\langle \sigma^y \rangle}{dt} = -\left(\frac{\gamma}{2} + \gamma_\phi\right)\langle \sigma^y \rangle, \quad \Rightarrow \quad \langle \sigma^y (t) \rangle = \langle \sigma^y (0) \rangle e^{-(\frac{\gamma}{2} + \gamma_\phi)t}, \quad (1.23b)$$

$$\frac{d\langle \sigma^z \rangle}{dt} = -\gamma(\langle \sigma^z \rangle + 1) \quad \Rightarrow \quad \langle \sigma^z (t) \rangle = (\langle \sigma^z (0) \rangle + 1)e^{-\gamma t} - 1. \quad (1.23c)$$

The dephasing yields a decay in the x - and y -direction and thus of the qubit polarization; however, it does not affect the decay in z -direction.

1.3 Coupling to an External Field

A particularly interesting case appears when the qubit is coupled to a single mode of the electromagnetic field of a resonator. With this coupling, one can induce *Rabi oscillations* between the qubit states in the nearly-resonant regime (Sec. 1.3.1). In addition, one can very easily perform quantum gates with this coupling. In the strongly detuned regime, the coupling between the resonator and the qubit yields a qubit-state dependent shift of the resonator frequency (Sec. 1.3.2).

⁹Since the dynamics is more intuitive in the Schrödinger picture, we firstly use this picture.

The coupling between the resonator and the qubit is described by the *Jaynes–Cummings model* (JC) [21]. In this model, the interaction between the two systems is a dipole interaction. In the rotating wave approximation (RWA), the JC Hamiltonian reads

$$\mathcal{H} = \hbar\omega_r a^\dagger a + \hbar\frac{\omega_q}{2}\sigma^z + \hbar g \left(\sigma^+ a + \sigma^- a^\dagger \right), \quad (1.24)$$

with ω_r being the resonator frequency, ω_q the transition frequency of the qubit, g the coupling between the qubit and the resonator, a^\dagger (a) the bosonic creation (annihilation) operator of the resonator field, $\sigma^+ = |e\rangle\langle g|$ ($\sigma^- = |g\rangle\langle e|$) the qubit raising (lowering) operator, and $\sigma^z = |e\rangle\langle e| - |g\rangle\langle g|$; the *detuning* between the qubit and the resonator is $\Delta = \omega_q - \omega_r$. A detailed derivation of the JC Hamiltonian, including explanations on the RWA, is given in App A.4. We speak of *strong coupling* if the coupling g between the qubit and the electromagnetic field is much larger than the decay rates, $|g| \gg \{\gamma, \kappa\}$, with $\kappa = \omega_r/Q$ being the *cavity decay rate* (Q is the quality factor, also called Q-factor) and γ the decay rate of the two-level system. In the strong coupling limit, the splitting of the resonator states induced by the coupling to the qubit exceeds the linewidth given by the decay processes and thus the states can be resolved in a spectroscopy experiment [22].

1.3.1 Rabi Oscillations

In the nearly-resonant regime ($\Delta \approx 0$) one can induce *Rabi oscillations* between the qubit and the resonator, see also [4]. For the solution of the JC interaction in the nearly-resonant case the Hamiltonian has to be diagonalized only in the subspace $\{|e, n\rangle, |g, n+1\rangle\}$ of the Hilbert space [23],

$$\mathcal{H}^{(n)} = \begin{pmatrix} \langle e; n | \mathcal{H}_{\text{JC}} | e; n \rangle & \langle e; n | \mathcal{H}_{\text{JC}} | g; n+1 \rangle \\ \langle g; n+1 | \mathcal{H}_{\text{JC}} | e; n \rangle & \langle g; n+1 | \mathcal{H}_{\text{JC}} | g; n+1 \rangle \end{pmatrix}, \quad (1.25)$$

with $|n\rangle$ being the Fock state of the resonator (n is the number of photons). The Schrödinger equation in this subspace then reads

$$\hbar \begin{pmatrix} \omega_r n + \frac{\omega_q}{2} - E/\hbar & g\sqrt{n+1} \\ g\sqrt{n+1} & (\omega_r + 1) - \frac{\omega_q}{2} - E/\hbar \end{pmatrix} \begin{pmatrix} |e, n\rangle \\ |g, n+1\rangle \end{pmatrix} = 0. \quad (1.26)$$

The eigenvalues are given by

$$E_{\pm} = \hbar\omega_r \left(n + \frac{1}{2} \right) \pm \frac{\hbar}{2} \sqrt{\Delta^2 + 4g^2(n+1)} \quad (1.27)$$

with corresponding eigenvectors

$$|+, n\rangle = \cos \vartheta_n |e, n\rangle + \sin \vartheta_n |g, n+1\rangle, \quad (1.28a)$$

$$|-, n\rangle = -\sin \vartheta_n |e, n\rangle + \cos \vartheta_n |g, n+1\rangle, \quad (1.28b)$$

and the ground state $|g, 0\rangle$. ϑ_n is given by (cp. Sec. 1.2.1)

$$\tan 2\vartheta_n = \frac{2g\sqrt{n+1}}{\Delta}. \quad (1.29)$$

Fig. 1.4(a) shows the energy spectrum of these dressed states for $\Delta = 0$. The degeneracy of the states $|g, n+1\rangle$ and $|e, n\rangle$ is lifted by $2g\sqrt{n+1}$ due to the coupling to the resonator.

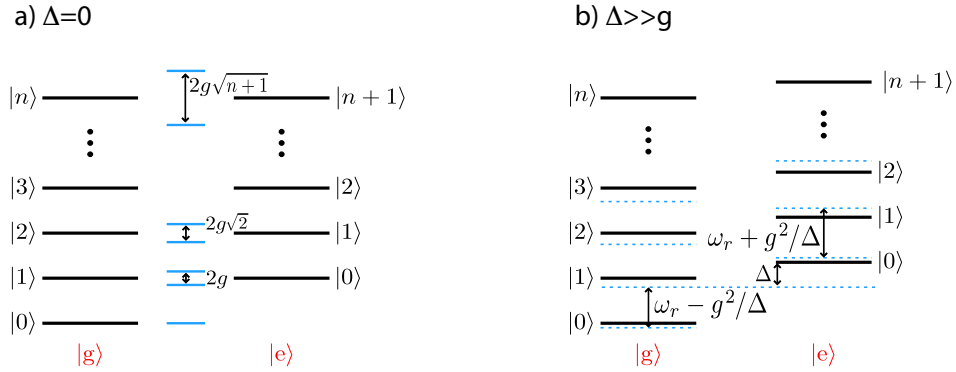


Figure 1.4: (a) Energy spectrum of the uncoupled (black) and the dressed (blue) qubit–resonator states in the case of zero detuning ($\Delta = 0$). The degeneracy of the pair states with $n + 1$ quanta is lifted by $2g\sqrt{n + 1}$ due to the interaction between the qubit and the resonator. (b) Energy spectrum in the dispersive regime (blue dashed lines). The second order coupling between the qubit and the resonator yields a shift in the resonator frequency that depends on the state of the qubit. See also [20; 22].

For a single excitation ($n = 0$), the dressed states of the qubit–resonator system are maximally entangled,

$$|\pm\rangle = \frac{1}{\sqrt{2}} (|g,0\rangle \pm |e,1\rangle). \quad (1.30)$$

In this case, the excitation is half qubit and half photon. If we assume the qubit to be initially in its excited state, $|\Psi_0\rangle = (|+\rangle - |-\rangle)/\sqrt{2}$, the evolved state in the case of zero detuning after a time t is

$$|\Psi_{\text{int}}(t)\rangle = \cos gt |e,0\rangle + \sin gt |g,1\rangle. \quad (1.31)$$

The probability P_x to find the qubit in state $|x\rangle$ ($x = (g,1), (e,0)$) after a time t therewith is

$$P_g = \sin^2 gt, \quad P_e = \cos^2 gt. \quad (1.32)$$

An initial state with an excited qubit ($|e,0\rangle$) therefore flops into a photon ($|g,1\rangle$) and back again at the vacuum Rabi frequency $g/2\pi$. For the solution of the system with n photons see e.g. [23].

Note that the derivation of the dynamics only works in the nearly-resonant regime since the Hamiltonian in the interaction picture then is time-independent. In the intermediate or dispersive regime, the Hamiltonian in the interaction picture is time-dependent. Therefore, the time-evolution operator can no longer be obtained easily (cp. App. A.1).

1.3.2 AC Stark Shift

Now, we consider the non-resonant, dispersive regime, with $|\Delta| \approx \sqrt{n + 1}g$. In this regime, no virtual excitations can be exchanged between the qubit and the resonator on the time scale $\Delta t < h/\Delta E$, but due to second order corrections, a shift in the transition frequencies of the qubit and the resonator is observed, see Fig. 1.4(b). This is the so-called *ac Stark shift*.

To calculate the dynamics in the dispersive regime, we use the method of the effective Hamiltonian, which is derived in App. A.5. We search for a transformation $U = e^{-S}$ that

eliminates the interaction part of the Hamiltonian to first order. A convenient choice is [22; 24]

$$S = \frac{g}{\Delta} \left(\sigma^+ a - \sigma^- a^\dagger \right). \quad (1.33)$$

Performing the transformation (A.42) up to the order g^2/Δ , the effective Hamiltonian of the dispersive qubit–resonator coupling thus reads

$$\mathcal{H}_{\text{qr}}^{\text{eff}} \approx \frac{\hbar}{2} \left(\omega_q + \frac{g^2}{\Delta} \right) \sigma^z + \hbar \left(\omega_r + \frac{g^2}{\Delta} \sigma^z \right) a^\dagger a. \quad (1.34)$$

One can see from this expression that the qubit transition frequency is ac Stark shifted by $(g^2/\Delta)n$; the ac Stark shift depends on the photon number. Vice versa, the resonator frequency is shifted by $\delta\omega_r = \pm g^2/\Delta$, whereas this shift depends on the state of the qubit. The constant shift g^2/Δ of the qubit transition frequency is the so-called Lamb shift.

The off-resonant coupling between the qubit and the cavity also yields a phase shift of the cavity [25; 26; 27],

$$\phi = \arctan \left(\frac{2g^2}{\kappa|\Delta|} \right) \sigma^z, \quad (1.35)$$

with κ being the decay rate of the resonator ($1/\kappa$ is the photon life time). The phase shift also depends on the qubit state; it has different signs for the two states $|g\rangle$ and $|e\rangle$.

1.4 Types of Qubits

In this last section of the chapter we present the implementations of qubits in different architectures. Since we use several methods from *trapped ions* in this thesis, the main focus lies on this qubit realization. SC qubits are introduced in detail in the next chapter. It has to be noted that most of the introduced systems are many-level systems. Therefore, it has to be possible to truncate the infinite-dimensional Hilbert space of such a system to two levels—the qubit levels. This can be done if the system provides a certain *anharmonicity* in its levels. A sufficiently large anharmonicity is needed to prevent qubit operations from exciting other transitions in the system.

1.4.1 Trapped Ions and Cavity QED

The first implementation of quantum gates in a physical system was proposed by Ignacio Cirac and Peter Zoller [28]. They suggested to use cold (alkaline earth) ions that are confined in a linear Paul trap [29]—*trapped ions*. Qubits can be encoded either by using narrow-optical (“forbidden”) transitions, radio-frequency transitions between Zeeman-split states or the internal hyperfine states of the ion [30]. Several other atoms can be added to achieve scalability. The other states of the qubit do not disturb the computation process; on the contrary, they are needed for the implementation of quantum gates and qubit readout [28]. Initialization of the qubit is done with optical pumping. The decay times of the qubit states in trapped ions, especially those for hyperfine qubits, are very long compared to the gate operation times.

Each ion can be manipulated individually with a focused laser beam, i.e. single-qubit operations are possible. The ion motion provides an additional degree of freedom which can be used to carry and convey information; the ions tend to move as a single body [30]. Cirac

and Zoller showed that linkage between the electronic states of the ion and the motion of the ensemble is possible and therefore the controlled-NOT gate can be achieved. The final readout of the ions is done with the very successful *electron shelving technique* (see Sec. 4.1). With this readout technique, a spectacular high fidelity readout above 99.99% is possible [17].

In these systems, one is able to control the qubit with a single mode of the electromagnetic field coupled to the qubit (which is theoretically described by the JC interaction, see Sec. 1.3); this is called *cavity quantum electrodynamics* (cavity QED). Strong coupling of the laser to the qubit can be achieved if the dipole momentum of the qubit is large. Therefore, Rydberg atoms are especially suitable for cavity QED.

Quantum computation with trapped ions is a highly advanced field. The control of the qubits is very good, the readout is the best possible, and the decoherence is small. Furthermore, a few years ago, the Innsbruck group was able to entangle eight qubits [31].

1.4.2 Other Architectures

There are several other proposals to implement quantum computation in different physical systems. The most intuitive idea is to use the spin of an electron or a nucleus as a qubit [32]. Control and readout of these devices is done with electron spin or nuclear magnetic resonance techniques. These qubits that are constructed from microscopic degrees of freedom are naturally very well isolated from their environment, and hence decohere very slowly. Due to this isolation from the environment, the main challenge of these implementations is enhancing the inter-qubit coupling and the qubit control to the level required for fast gate operations without introducing decoherence.

One can also use the polarization directions of a single photon as the two levels of a qubit. This design is especially suitable for quantum cryptography and quantum communication as the photons are moving with the speed of light [33].

Besides the atomic, spin, and optical devices there is also the field of electronic devices. For example one can use the excitonic levels of a quantum dot as a qubit. In these systems, strong coupling to an electromagnetic field was already achieved [34].

Finally, there is a variety of interesting proposals which use the quantized states of Josephson junctions involving either the charge, flux or phase degree of freedom; we discuss these SC qubits in detail in the following chapter.

Chapter 2

Superconducting Qubits and Circuit Quantum Electrodynamics

An interesting subject in the field of solid state quantum computation is that of *superconducting qubits* (SC qubits) where one uses the quantized states of *Josephson junctions* (JJs) to implement qubits in SC circuits. Due to their macroscopic size, SC qubits can be fabricated with standard lithography methods [6]. Thus, in contrast to microscopic systems like ion traps or nuclear spins, SC qubits are suitable for large-scale integration. It is also possible to achieve strong coupling of an SC qubit to a single mode of the electromagnetic field in the novel field of circuit QED with SC qubits. Moreover, the transition frequency of an SC qubit and the coupling strength can be varied with external fields. Nevertheless, due to their larger size, SC qubits are not well isolated from the environment resulting in short coherence times. A comparison of SC qubits with other architectures is shown in Fig. 2.1.

All SC qubits use the dynamics of a single JJ or several JJs connected in a loop such that they build a *superconducting quantum interference device* (SQUID). These junctions act as nonlinear resonators thus providing a sufficiently large anharmonicity in the energy dispersion. This gives the possibility to truncate the infinite-dimensional Hilbert space of the whole many-level system to a two-dimensional Hilbert space and thus to use the system as a qubit.

A JJ consists of two superconductors connected via a tunnelling barrier; it can be described by its *critical current* I_c (that depends on the SC material and the size of the junction) and the *gauge invariant phase difference* φ across the junction. The phase difference, φ , and the charge of the Cooper pairs, Q , represented by the number of Cooper pairs N , are canonically conjugated variables, yielding the commutator $[\hat{N}, \varphi] = -i$. Thus, \hat{N} can be associated with the momentum operator and φ with the position operator, which gives the operator replacement $\hat{N} = -i\partial/\partial\varphi$. This choice results in the Hamiltonian of a nonlinear oscillator, built by the *Josephson capacitance* C_J and the nonlinear *Josephson inductance* $L_J = \frac{L_{J,0}}{\cos\varphi}$, with $L_{J,0} = \Phi_0/2\pi I_c$. Here, $\Phi_0 = h/2e$ is the SC flux quantum.

Therefore, JJs are characterized by two characteristic energies—the *Cooper pair charging energy*¹ $E_c = \frac{(2e)^2}{2C_J}$, which is the energy required for storing a Cooper pair with charge $2e$ on the junction capacitance, and the *Josephson energy* $E_J = \frac{\Phi_0}{2\pi} I_c$, that is required for storing the flux quantity Φ_0 in the Josephson inductance and is a measure of the coupling strength

¹Note that in several works the charging energy E_c denotes the single electron charging energy; in this case, E_c would change to $4E_c$ in the entire calculations.

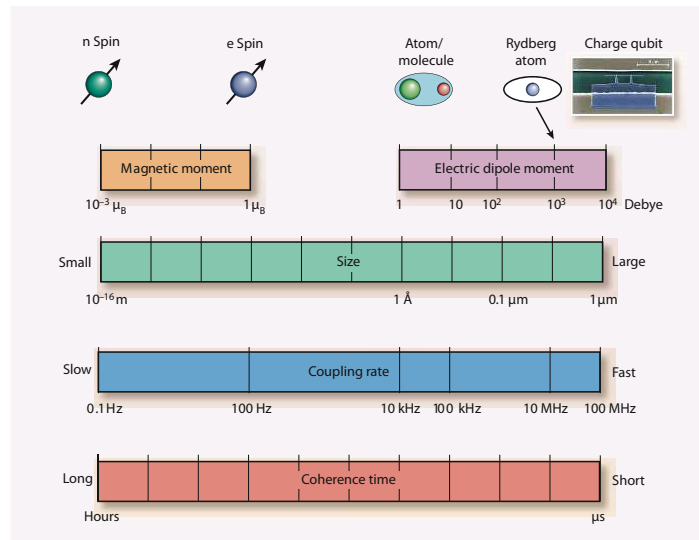


Figure 2.1: Comparison of SC qubits with other qubit implementations. The quantum systems can be compared according to their electric or magnetic dipole moments (or the magnitude of the emitter strength, top bars), the required transverse size of a cavity to reach maximal coupling (second bar), their coupling rates (third bar) to a technologically feasible ($1 \mu\text{m}$) cavity, and the expected lifetimes of coherent superpositions (bottom bar). Which quantum system is optimal depends on many details, including the ease of trapping or fabricating in a cavity, and on the many factors in the qubit environment that can affect the coherence times. Besides an SC qubits, many other quantum systems have microwave transitions that could be coupled to photons in a transmission line. Nevertheless, the maximal coupling strength is achieved with SC qubits due to their large size. Taken from [35].

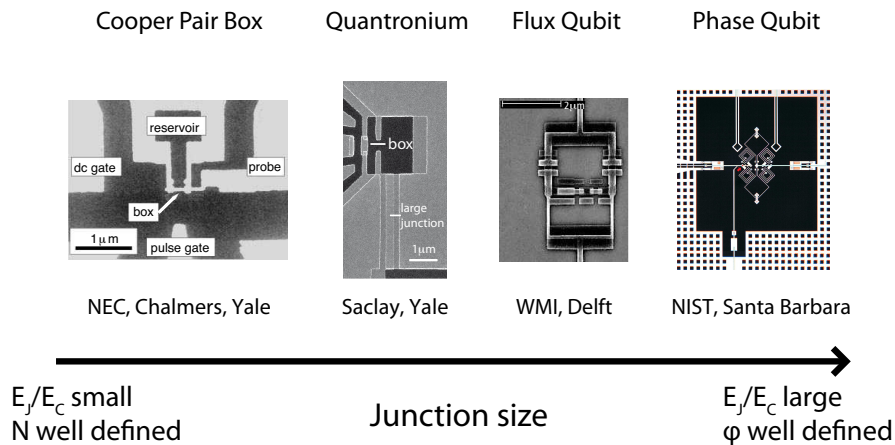


Figure 2.2: Scanning electron microscopy of the different SC qubit flavours including groups that are recently working with them. The ratio E_J/E_C increases with increasing junction sizes. In the different regimes either the phase or the Cooper pair number N are well defined and thus good quantum numbers. Taken from [7; 36; 37; 38].

across the junction. E_J represents a potential barrier that confines the particle representing the phase of the JJ with the corresponding potential $U = -E_J \cos \varphi$; E_c is associated with the quantum-mechanical kinetic energy $T = E_c \hat{N}^2$, yielding energy quantization. Rigorously speaking, particle confinement is impossible due to *macroscopic quantum tunnelling* through the potential barrier; however, the probability of tunnelling is small and the tunnelling may be neglected if the particle energy E is small compared to the Josephson energy, $E \ll E_J$ [4]. The transition frequency of the qubit strongly depends on E_c and E_J ; it lies in the microwave regime.

SC qubits can be divided into three species where each of them uses a different degree of freedom for qubit implementation—charge, flux, or phase—and operates in a different regime of E_J/E_c , see Fig. 2.2. The size of E_J/E_c can be varied by fabricating larger or smaller junctions, leading to larger or smaller C_J and therewith, respectively, to smaller or larger E_c^2 . Each of these possibilities to implement a qubit in SC circuits has its advantages and disadvantages which we discuss in detail in the following sections.

In this chapter we firstly illustrate the different types of SC qubits including their theoretical description and specific features³. Secondly, we present the implementation of quantum optics on a chip—circuit QED. Since a detailed discussion of superconductivity and the physics of JJs, including the derivation of the Hamiltonians, is given in App. B, we focus on the physics of SC qubits and do not go into detail on several aspects of superconductivity.

2.1 Charge Qubits

In this section we discuss SC qubits where the relevant degree of freedom in the dynamics is the charge on a SC island that is called *Cooper pair box* (CPB). These charge qubits are operated with an external gate voltage V_g ; one- and two-qubit gates can be performed with voltages and magnetic fields. Charge qubits can be coupled via capacitors, by shunting them in parallel with an additional inductance [3], or by connecting them via a JJ [39]. The latter proposal gives the possibility to turn the coupling between the qubits on and off.

The original proposal for the charge qubit—the *CPB qubit*—works in the charge regime, where $E_J/E_c \ll 1$ (Sec. 2.1.1). In this limit, the charge is well defined and the phase fluctuates strongly. A small Josephson coupling implies a good isolation of the island of the CPB, with a specific number of Cooper pairs trapped on the island [4]. The qubit then is built by a superposition of the two lowest charging states. This qubit is highly sensitive to fluctuations of V_g leading to short coherence times T_1 and T_2 . A new design, the *transmon* (Sec. 2.1.2), is operated at $E_J/E_c \gg 1$, giving the possibility to improve the coherence times. Even though both designs use a CPB, we only call the original proposal CPB qubit due to historical reasons.

2.1.1 Cooper Pair Box in the Charge Regime

The simplest architecture that is used to implement a qubit in SC circuits is the CPB qubit, which is the CPB operated in the charge regime. The CPB was first described by Büttiker [40] and experimentally realized by the Saclay group [41; 42]. The first realization of a charge qubit, including qubit dynamics in the time domain, was done by Nakamura et al. (NEC

² E_c can also be made small by shunting the device in parallel with a large capacitance.

³We do not go into detail on coupling of SC qubits; for more information on SC qubit coupling see e.g. [3; 4].

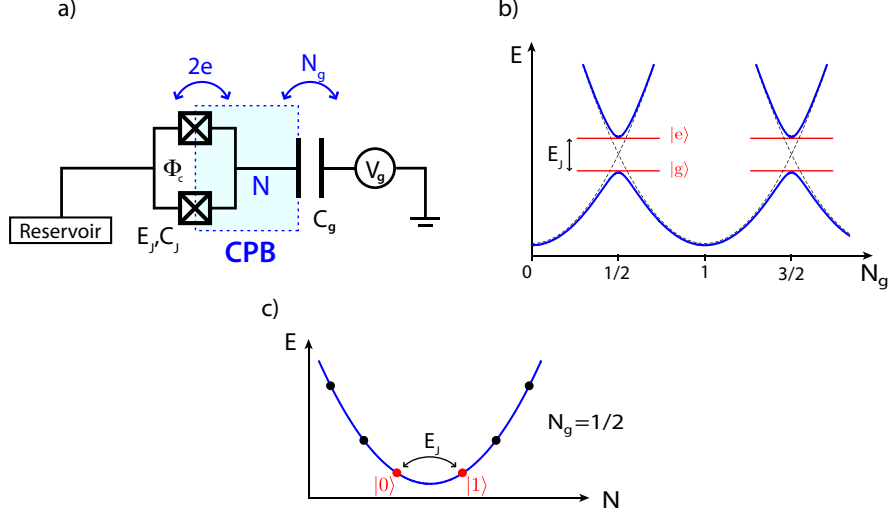


Figure 2.3: (a) Circuit diagram of the CPB qubit. The CPB is coupled to a reservoir via a dc SQUID (Josephson energy E_J , capacitance C_J) that consists of two identical JJs that are shunted in parallel; an external flux Φ_c threads the dc SQUID. Additionally, the CPB is operated with a gate voltage V_g . (b) Energy landscape of the CPB (blue) for $E_J/E_c \ll 1$ as a function of N_g . The Josephson coupling yields an anti-crossing of the charging parabolas (dashed lines). At $N_g = \frac{1}{2}$ (degeneracy point) the degeneracy of the charge states is lifted by E_J due to the Josephson coupling. (c) Electrostatic energy of the CPB at $N_g = \frac{1}{2}$; the two degenerated ground states are coupled via the Josephson coupling E_J (see also text).

group) [7; 43; 44; 45] by manipulating the CPB with external fields resulting in Rabi oscillations.

A circuit diagram of the CPB is shown in Fig. 2.3(a). A mesoscopic SC island—the CPB—is connected to a large SC reservoir through a dc SQUID that is built by two identical JJs shunted in parallel; additionally, the dc SQUID is threaded by an external flux Φ_c . The use of two junctions gives the possibility to control the Josephson energy of the JJ with Φ_c [46]. If we assume the loop inductance of the dc SQUID to be negligible⁴, it acts as a single JJ with tunable, flux-dependent Josephson energy (see App. B.4.1). $E_J = 2E_J^{\text{SJ}} \cos\left(\pi \frac{\Phi_c}{\Phi_0}\right)$ and Josephson capacitance $C_J = 2C_J^{\text{SJ}}$, with E_J^{SJ} and C_J^{SJ} being the properties of a single junction. The CPB is operated with a gate voltage V_g , coupled to the CPB via the gate capacitance C_g . This allows to control the charging energy of the island.

The Hamiltonian of the voltage-biased CPB is given by

$$\mathcal{H}_{\text{CPB}} = E_c \left(\hat{N} - N_g \right)^2 - E_J \cos \varphi, \quad (2.1)$$

where $\varphi = (\varphi_1 - \varphi_2)/2$ denotes the gauge-invariant phase difference over the SQUID loop ($\varphi_{1,2}$ being the phases of the single JJs), \hat{N} the Cooper pair number operator, E_J the Josephson energy, $E_c = (2e)^2/C_\Sigma$ the Cooper pair charging energy ($C_\Sigma = C_J + C_g$ being the total box capacitance), and $N_g = \frac{C_g V_g}{2e}$ the dimensionless gate charge. A detailed derivation of the Hamiltonian (2.1) is given in App. B.3.3 and B.4.1.

⁴This assumption is fulfilled for charge qubits since the loop size is very small. For $L = 0$, we can also neglect the induced flux and thus the magnetic energy of the loop. This is not fulfilled for the rf SQUID qubit that is described in Sec. 2.2.1.

We now assume that the CPB is in the charge regime, with $E_J/E_c \ll 1$ ($E_J/E_c \sim 0.1-1$). Hence, the only relevant degree of freedom is the number of Cooper pairs N on the island; in this case, N is a good quantum number. The charge regime is achieved when the SC energy gap is larger than both the charging energy E_J and the temperature⁵. Under these conditions only Cooper pairs tunnel and the system is described by the Hamiltonian:

$$\mathcal{H} = \sum_N \left(E_c (N - N_g)^2 |N\rangle\langle N| - \frac{E_J}{2} (|N+1\rangle\langle N| + \text{H.c.}) \right). \quad (2.2)$$

The derivation of this Hamiltonian starting from Eq. (2.1) is given in App. C.1. Fig. 2.3(b) shows the energy landscape of the CPB qubit for $E_J/E_c \ll 1$; the Josephson coupling leads to an anti-crossing of the charging parabolas (corresponding to the charging part of the Hamiltonian, $E_c(N - N_g)^2$). At $N_g = 1/2 \bmod 1$, where the two lowest charging states are degenerate, the splitting between the levels is only given by the Josephson energy E_J . Due to the large anharmonicity of the CPB states in the charge regime, the two lowest states thus can be used as a qubit.

To show that we can build a qubit between the two lowest states $|0\rangle$ and $|1\rangle$ ⁶ we firstly assume that we work near the *degeneracy point*, where $N_g = 1/2$. Therefore, we only have to take into account terms with $N = 0$ and $N = 1$ in the charging energy (since other terms have much higher energy) and only terms with $N = 0$ in the Josephson energy. To demonstrate the latter one, we utilize the Hamiltonian (2.2) in the interaction picture that is related to the Schrödinger picture via the unitary transformation $U = \exp \left[-\frac{i}{\hbar} \sum_N E_c (N - N_g)^2 |N\rangle\langle N| t \right]$ ⁷:

$$\mathcal{H}_{\text{int}} = - \sum_N \frac{E_J}{2} \left(e^{\frac{i}{\hbar} E_c [2(N_g - N) - 1]t} |N\rangle\langle N+1| + e^{-\frac{i}{\hbar} E_c [2(N_g - N) - 1]t} |N+1\rangle\langle N| \right). \quad (2.3)$$

All the terms in Eq. (2.3) except of $|0\rangle\langle 1|$ and $|1\rangle\langle 0|$ are fast rotating terms when we work near the degeneracy point, $N_g = 1/2$, and in the charge regime, $E_J/E_c \ll 1$, and therefore can be neglected in an RWA (see App. A.4.2 for more information on the RWA). Back in the Schrödinger picture, and after an energy shift $-N_g^2 - (1 - 2N_g)/2$, the Hamiltonian of the CPB qubit then reads

$$\mathcal{H}_{\text{CPB}} \approx -\frac{E_c}{2}(1 - 2N_g)\bar{\sigma}^z - \frac{E_J}{2}\bar{\sigma}^x, \quad (2.4)$$

with $\bar{\sigma}^z = |0\rangle\langle 0| - |1\rangle\langle 1|$ and $\bar{\sigma}^x = |0\rangle\langle 1| + |1\rangle\langle 0|$. This means, the CPB can be mapped to a pseudospin-1/2-particle with magnetic fields $E_c(1 - 2N_g)$ and E_J in z - and x -direction, respectively.

Diagonalization of the qubit Hamiltonian yields the eigenstates (cp. Sec. 1.2.1)

$$|e\rangle = \cos \vartheta_{\text{cq}} |0\rangle + \sin \vartheta_{\text{cq}} |1\rangle \quad (2.5a)$$

$$|g\rangle = -\sin \vartheta_{\text{cq}} |0\rangle + \cos \vartheta_{\text{cq}} |1\rangle. \quad (2.5b)$$

with corresponding eigenvalues

$$E_{\pm} = \pm \frac{\hbar}{2} \omega_{\text{cq}} = \pm \frac{1}{2} \sqrt{E_J^2 + [E_c(1 - 2N_g)]^2}, \quad (2.6)$$

⁵In this case, quasi-particle tunnelling is suppressed, see App. B.

⁶In general, we can build a charge qubit between the states $|N_q\rangle$ and $|N_q + 1\rangle$ in the environment of the degeneracy point $N_{gq} = N_q + \frac{1}{2}$. We concentrate on $N_q = 0$ without loss of generality.

⁷See App. A.1.3 and App. A.2 for more information on the interaction picture and unitary transformations.

and $\tan 2\vartheta_{\text{cq}} = E_J/[E_c(1 - 2N_g)]$. At the degeneracy point, $\sin \vartheta_{\text{cq}} = -\cos \vartheta_{\text{cq}} = -1/\sqrt{2}$. Working in this eigenbasis, the Hamiltonian of the CPB takes the form

$$\mathcal{H}_{\text{CQ}} = \frac{\hbar}{2}\omega_{\text{cq}}\sigma^z, \quad (2.7)$$

with $\sigma^z = |e\rangle\langle e| - |g\rangle\langle g|$ being the σ^z -operator in the energy eigenbasis $\{|g\rangle, |e\rangle\}$ of the qubit. At the degeneracy point, $N_g = 1/2$, the diagonal part of the qubit Hamiltonian vanishes and the levels are separated only by the Josephson energy E_J . At this point, the qubit states can no longer be distinguished into $|0\rangle$ and $|1\rangle$. For the dressed states at the degeneracy point, $|g/e\rangle = (|1\rangle \mp |0\rangle)/\sqrt{2}$, the average charge on the island is zero, while it changes to $\mp 2e$ far from the degeneracy point, where the qubit eigenstates approach pure charge states [4].

2.1.2 Transmon Qubit

The *transmon* is a charge qubit that is operated in an intermediate regime where $E_J/E_c \sim 10^2$ (*transmon regime*); it was first proposed and experimentally realized by the Yale group [25; 47]. This design leads to improved coherence times (T_1 and T_2) and therewith to a larger stability of the system. A precursor of the transmon qubit is the *quantronium* that is used by the Saclay group [36; 48; 49; 50]; it is also operated in an intermediate regime, but with smaller Josephson energy ($E_J/E_c \sim 1$)⁸.

The crucial features of the CPB qubit are its anharmonicity and the charge dispersion of the energy levels. The anharmonicity is needed to prevent excitations of the other transitions in the system; the larger the anharmonicity, the better the many-level system is suitable as a qubit. The charge dispersion describes the qubit sensitivity to charge noise; the smaller the charge dispersion, the less the qubit frequency changes in response to gate fluctuations. In general, the sensitivity of the qubit to first-order charge fluctuations is directly related to the differential charge dispersion $\partial E_{kl}/\partial N_{kl}$ ⁹, with $E_{kl} = E_l - E_k$ being the transition energy between the levels $|k\rangle$ and $|l\rangle$. In the CPB qubit, the sensitivity to charge noise is reduced by biasing the system to the charge degeneracy point ($N_g = 1/2$) since the charge dispersion has no slope there. However, the fluctuations even affect operations at this first-order insensitive sweet spot since they can drive the CPB away from this optimal working point. The magnitudes of charge dispersion and anharmonicity are both determined by the ratio E_J/E_c . Increasing this ratio decreases the charge dispersion and therefore the sensitivity of the system to first-order charge fluctuations; however, it also decreases the energy level anharmonicity of the qubit [25].

The transmon now exploits the fact that the charge dispersion decreases exponentially in E_J/E_c while the anharmonicity only decreases algebraically with a slow power law [48]. As shown in Fig. 2.4(a), the design of the transmon is similar to that of the CPB qubit (Sec. 2.1.1). Again, an SC island is coupled to a gate voltage V_g via the gate capacitance C_g and to a reservoir via a dc SQUID with Josephson energy E_J and Josephson capacitance C_J . However, the dc SQUID is now shunted by a large capacitance C_B that reduces the sensitivity to fluctuations of the gate voltage by reducing E_c ¹⁰. One could also use a large junction to

⁸Even though we are calling the quantronium “precursor”, it has different features as the transmon in several details. However, the theoretical steps yielding the quantronium and the transmon are very much alike.

⁹The sensitivity to second-order noise is consequently described by the curvature $\partial^2 E_{kl}/\partial N_{kl}^2$.

¹⁰It has to be noted that the quantronium is also shunted with an additional capacitance to reduce phase fluctuations.

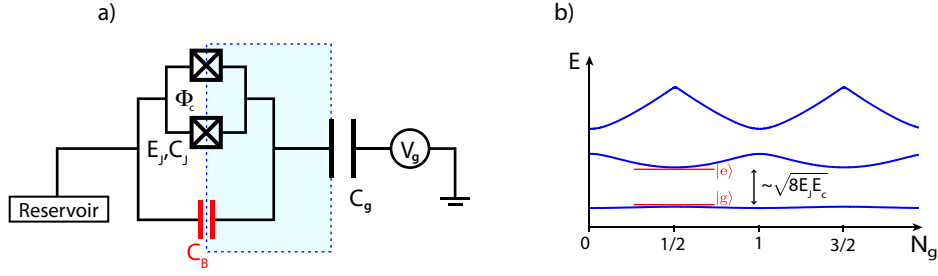


Figure 2.4: (a) Circuit diagram of the transmon qubit. Again, the CPB is coupled to an SC reservoir via a dc SQUID (see also Fig. 2.3(a)) and operated with a gate voltage V_g . But now, an additional capacitance C_B is shunted in parallel to the dc SQUID to suppress charge fluctuations. (b) Energy landscape of the CPB in the transmon regime where $E_J/E_c \gg 1$. In this case, the anharmonicity of the states decreases. Again, the two lowest states build the qubit.

reduce the charging energy; however, a large junction would lead to quasi-particle processes disturbing the qubit operations.

The Hamiltonian of the transmon is the same as for the CPB qubit (2.1), but now with $\tilde{C}_\Sigma = C_g + C_J + C_B$,

$$\mathcal{H}_{\text{CPB}} = E_c(\hat{N} - N_g)^2 - E_J \cos \varphi. \quad (2.8)$$

Again, $E_c = (2e)^2/2\tilde{C}_\Sigma$ is the charging energy, $\hat{N} = -i\partial/\partial\varphi$ the Cooper pair number operator, E_J the flux-dependent Josephson energy, and φ the phase difference of the SQUID.

Fig. 2.4(b) shows the energy landscape of the transmon; due to the large capacitance C_B , the charging energy E_c is now reduced. Therewith, the parabolas corresponding to the charging part of the Hamiltonian are broadened which decreases the anharmonicity; the levels split due to the Josephson coupling (see also Sec. 2.1.1). In this system, the qubit states $|e\rangle$ and $|g\rangle$ cannot be related to charge states; this was the same for the CPB qubit but only at the degeneracy point. With increasing E_J/E_c , the transmon eigenstates spread over an increasing number of charge states.

According to [25], N_g can be eliminated by a gauge transformation $\Psi(\varphi) = e^{iN_g\varphi} f(\varphi)$ since the strong Josephson coupling restricts φ to small values around zero which motivates the neglect of periodic boundary conditions. $\Psi(\varphi)$ is the wavefunction that obeys the stationary Schrödinger equation $\mathcal{H}_{\text{CPB}}\Psi(\varphi) = E\Psi(\varphi)$.

By expanding $\cos \varphi$ until φ^4 and neglecting constant terms, we obtain the Hamiltonian of a nonlinear oscillator,

$$\mathcal{H} \approx -E_c \frac{\partial^2}{\partial \theta^2} + \frac{1}{2} E_J \theta^2 - \frac{E_J}{24} \theta^4 = \hbar\omega_p \left(d^\dagger d + \frac{1}{2} \right) - \frac{E_c}{12} \left(d + d^\dagger \right)^4, \quad (2.9)$$

with $\omega_p = \sqrt{2E_c E_J}/\hbar \equiv 1/\sqrt{L_{J,0} C_J}$ being the *Josephson plasma frequency* and

$$d^\dagger = \sqrt{\frac{E_c}{\hbar\omega_p}} \left(\frac{\hbar\omega_p}{2E_c} \varphi - \frac{\partial}{\partial \varphi} \right), \quad d = \sqrt{\frac{E_c}{\hbar\omega_p}} \left(\frac{\hbar\omega_p}{2E_c} \varphi + \frac{\partial}{\partial \varphi} \right), \quad (2.10)$$

denoting the regular bosonic creation and annihilation operators for the harmonic oscillator approximating the transmon, respectively.

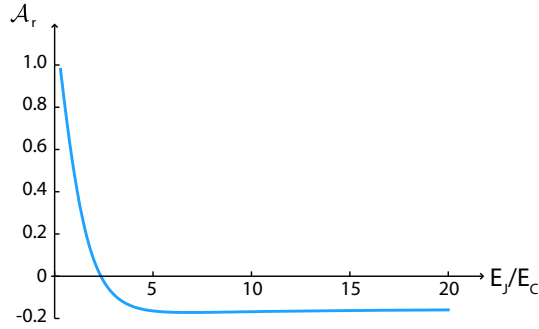


Figure 2.5: Reduced anharmonicity \mathcal{A}_r of the CPB as a function of E_J/E_c . The anharmonicity decreases fast for small E_J/E_c ; for values above $E_J/E_c \sim 4$, the decrease is no longer exponentially.

Since we work in the transmon regime ($E_c \ll E_J$), we can apply a first-order perturbation theory on the oscillator Hamiltonian (2.9), which is done in App. C.2. We obtain the energy levels ($k = \langle d^\dagger d \rangle$ being the occupation number),

$$E_k = \hbar\omega_p k - \frac{E_c}{48} (6k^2 + 6k + 3), \quad (2.11)$$

where we have neglected the zero-point energy of the oscillator. Due to the nonlinearity of the JJ that leads to the $(d + d^\dagger)^4$ -term in Eq. (2.9) (corresponding to φ^4), an anharmonic correction to the harmonic energy level dispersion of the oscillator occurs.

According to [25], we define the absolute and relative anharmonicity by

$$\mathcal{A} \equiv E_{12} - E_{01}, \quad \mathcal{A}_r \equiv \mathcal{A}/E_{01}. \quad (2.12)$$

The level spacing between the levels $|k\rangle$ and $|k+1\rangle$ is

$$E_{k,k+1} = E_{k+1} - E_k = \hbar\omega_p - E_c \frac{k+1}{4} \rightarrow \hbar\omega_p - E_c \frac{k}{4}, \quad (2.13)$$

where, in the last step, we have neglected the constant term $-E_c$. Therewith, the absolute and relative anharmonicity of the transmon in the nonlinear oscillator approximation are

$$\mathcal{A} = -\frac{E_c}{4}, \quad \mathcal{A}_r = -\sqrt{\frac{E_c}{2E_J}}. \quad (2.14)$$

Thus, for a non-vanishing charging energy E_c , the required anharmonicity is available. Fig. 2.5 shows the reduced anharmonicity of the CPB as a function of E_J/E_c . For $E_J/E_c \gtrsim 4$, the anharmonicity decreases slowly with a power law. Though, the anharmonicity of the transmon is still smaller than for the CPB qubit. With the relations (2.14), the optimal E_J/E_c range can be estimated [25].

The transmon Hamiltonian can also be solved exactly in the phase basis using *Mathieu functions* [6; 48]. With this functions it can be shown [25] that the differential charge dispersion is

$$\frac{\partial E_{01}}{\partial N_g} = \pi \varepsilon_1 \sin(2\pi N_g), \quad (2.15)$$

where $\varepsilon_1 \propto \exp\left[-\sqrt{2E_J/E_c}\right]$ is a fast decreasing function for $E_J/E_c \gg 1$.

It is important to note that due to the reduced anharmonicity of the transmon, virtual transitions through excited transmon states must be taken into account. Only after this we can restrict the transmon Hilbert space to the ground state and first excited state. The effective Hamiltonian of the transmon thus can only be obtained when the transmon is coupled to an electromagnetic field, which we discuss in Sec. 2.4.1.

The overlap of the transmon eigenstates with pure charge states is larger than that of the CPB qubit. For increasing E_J/E_c the transmon eigenstates spread over an increasing number of charge states. However, the transmon states can still be related to charge states since the charge fluctuations only grow slowly as E_J/E_c increases. To demonstrate this, we calculate the charge fluctuations in the oscillator approximation, where the transmon number operator is $\hat{N} = -i(E_J/2E_c)^{1/4}(d - d^\dagger)/\sqrt{2}$,

$$\sqrt{\langle \hat{N}^2 \rangle - \langle \hat{N} \rangle^2} = \left(\frac{E_J}{2E_c} \right)^{1/4} \left(k + \frac{1}{2} \right). \quad (2.16)$$

The fluctuations grow with $(E_J/2E_c)^{1/4}$. As an example, for $E_J/E_c = 100$, the number of Cooper pairs only fluctuates by approximately 1 or 2 in the ground and first excited state; thus, the charge fluctuations are only in the order of unity [25].

In conclusion, the transmon is an improved design of the CPB. It provides the anharmonicity required for quantum computation and is less sensitive to charge fluctuations of the gate charge. Thus, the transmon, in contrast to the CPB qubit, can also be operated away from the charge degeneracy point, yielding an improved controllability. It is also possible to obtain higher couplings in circuit QED (see Sec. 2.4) with the transmon. Therefore, the transmon is the best choice for quantum computation with SC qubits that use the charge degree of freedom.

2.2 Flux Qubits

In the previous section we have described the dynamics of SC qubits that use the charge degree of freedom. For this purpose, we were working in the charge regime ($E_J/E_c \ll 1$) where the charge is well defined and the phase fluctuates strongly. In this and the next section we review the quantum properties of SC qubits in the opposite regime, that is, the phase regime ($E_J/E_c \gg 1$) where the phase is well defined and the charge fluctuates. These systems were first proposed by Caldeira and Leggett [51] as test objects to study various quantum-mechanical effects, including macroscopic quantum tunnelling of the phase (or flux) as well as resonance tunnelling [3].

SC flux qubits use the flux degree of freedom of JJs, where circulating currents build the qubit states, for qubit operations. They are operated in the flux regime, where $E_J/E_c \sim 10^2$. Flux qubits exploit quantum tunnelling in a double-well potential to achieve an interaction between the two qubit states that are built by clockwise and anticlockwise currents circulating in a SC loop. They are controlled with external fluxes and can be coupled via a direct inductive coupling or, as the charge qubit, with an *LC* circuit. We firstly discuss the original design for the flux qubit in Sec. 2.2.1. It is a single JJ in an SC loop that builds an rf SQUID. Due to high sensitivity of this design to fluctuations of the magnetic environment, nowadays a three-junction qubit, the *persistent current qubit* (PCQ), is used as a flux qubit (see Sec. 2.2.2).

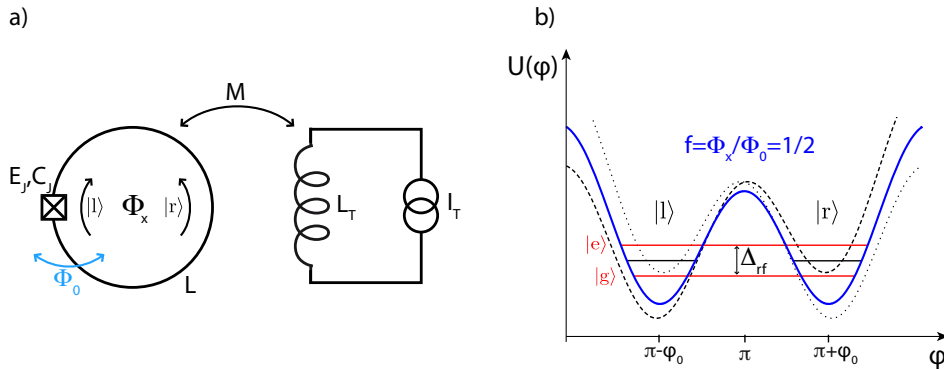


Figure 2.6: (a) Circuit diagram of the rf SQUID qubit. An rf SQUID, that consists of one JJ (Josephson energy E_J and capacitance C_J) in an SC loop with inductance L , is coupled to the inductance L_T of a tank circuit via a mutual inductance M . With this tank circuit, the rf SQUID is biased with an ac current $I_T(t)$ that leads to a flux Φ_x threading the loop. The induced flux in the loop is an integer multiple of the flux quantum Φ_0 ; the corresponding current circulates clockwise (left, $|l\rangle$) or anticlockwise (right, $|r\rangle$). (b) Potential energy landscape of the rf SQUID qubit for the cases $f \neq \frac{1}{2}$ (dotted for $f > \frac{1}{2}$, dashed for $f < \frac{1}{2}$) and $f = \frac{1}{2}$ (blue). The degeneracy of the flux states $|l\rangle$ and $|r\rangle$ is lifted by Δ_{rf} due to the Josephson coupling (see also text).

2.2.1 RF SQUID Qubit

The primary implementation of a flux qubit is the flux-biased rf SQUID. With this system it was possible to observe resonant tunnelling of macroscopic quantum levels [52]. The first superposition of states was shown by Friedman et al. [53].

Fig. 2.6(a) shows the circuit diagram of the rf SQUID qubit. A single JJ is placed inside a large SC loop with a large inductance L . The system is coupled to a tank circuit via a mutual inductance M ; an ac current in this tank circuit results in a flux Φ_x threading the loop. The biasing induces a flux in the loop that is an integer multiple of the flux quantum $\Phi_0 = h/2e$. The corresponding current circulates clockwise (left, $|l\rangle$) or anticlockwise (right, $|r\rangle$). As for the CPB qubit, instead of one JJ one could also use two junctions shunted in parallel which gives the possibility to control the Josephson coupling with an additional flux.

In Sec. 2.1 we have neglected the geometrical inductance L of the dc SQUID loop. Though, for SC circuits this inductance is important if $\Lambda = L_{J,0}/L < 1$, where $L_{J,0} = \frac{\Phi_0^2}{4\pi^2 E_J}$ is the Josephson inductance. If $\Lambda \ll 1$, the quantum variables can be related to the flux in the loops and their time derivatives. The rf SQUID qubit now is fabricated such that the loop inductance is large and the magnetic energy can no longer be neglected. Taking into account this magnetic energy, the Hamiltonian of the flux-biased rf SQUID reads

$$\mathcal{H}_{\text{RF}} = E_c \hat{N}^2 + \underbrace{\frac{E_L}{2} (\varphi - \varphi_x)^2 - E_J \cos \varphi}_{=U(\varphi)}. \quad (2.17)$$

Here, φ and φ_x are fluxes in units of $\Phi_0/2\pi$ ($\varphi = \frac{2\pi}{\Phi_0} \Phi$, $\varphi_x = \frac{2\pi}{\Phi_0} \Phi_x$), $\hat{N} = -i\partial/\partial\varphi$, again, is the Cooper pair number operator, $E_c = \frac{(2e)^2}{2C_J}$ is the charging energy of one Cooper pair, E_J the Josephson energy, and $E_L = \frac{\Phi_0^2}{4\pi^2 L}$ the magnetic energy of the persistent current circulating in

the loop. A detailed derivation of the rf SQUID Hamiltonian is given in App. B.4.2. Usually, the external flux is given in terms of the *magnetic frustration* $f = \frac{\Phi_x}{\Phi_0} = \frac{\varphi_x}{2\pi}$.

The potential of the rf SQUID qubit Hamiltonian (2.17) for different values of φ_x is shown in Fig. 2.6(b). At $f = \frac{1}{2}$ —the flux degeneracy point¹¹—we obtain a double-well potential with two degenerate phase states $|l\rangle$ and $|r\rangle$ corresponding to a clockwise and anticlockwise circulating current, respectively. For $E_J/E_L \gtrsim 1$, the potential $U(\varphi)$ has three minima at $\varphi = \pi$ and $\pi \pm \varphi_0$; φ_0 can be obtained by numerically solving $\varphi_0 - \varphi_x = -E_J/E_c \sin \varphi_0$. The two phase states are coupled via macroscopic quantum tunnelling resulting in the maximally entangled states

$$|e\rangle = \frac{1}{\sqrt{2}} (|l\rangle + |r\rangle), \quad |g\rangle = \frac{1}{\sqrt{2}} (|l\rangle - |r\rangle), \quad (2.18)$$

with an energy splitting Δ_{rf} corresponding to the tunnelling amplitude. If we move away with the external flux from the value $f = 1/2$, the double-well potential is tilted to the left or the right, lowering the $|l\rangle$ and $|r\rangle$ state, respectively (cp. Fig. 2.6(b)) [54].

By increasing the ratio E_J/E_L , one can increase the distance of the minima¹² and the height of the barrier between the wells. We choose the magnetic and the Josephson energy in the same order of magnitude, $\Lambda = L_{J,0}/L \lesssim 1$, (yielding a large self-inductance) since firstly the tunnelling is suppressed strongly if the tunnel barrier is too high and secondly the required anharmonicity would not be achievable.

For the derivation of the qubit Hamiltonian we mainly follow [5]. The potential in Eq. (2.17) can be approximated in the case that the tunnelling barrier is much smaller than the Josephson energy. We firstly introduce the new, shifted variables

$$\tilde{\varphi} = \varphi - \pi, \quad \text{and} \quad \tilde{\varphi}_x = \varphi_x - \pi. \quad (2.19)$$

The cosine-part of the potential then changes as $-\cos \varphi \rightarrow \cos \tilde{\varphi}$. Expanding the cosine and neglecting constant terms we get

$$U(\varphi) \approx E_L \left(-\frac{\lambda}{2} \tilde{\varphi}^2 - \tilde{\varphi}_x \tilde{\varphi} + \frac{1-\lambda}{24} \tilde{\varphi}^4 \right), \quad (2.20)$$

with $\lambda = E_J/E_L - 1 \equiv \beta_{L,\text{rf}} - 1 \ll 1$ determining the height of the tunnel barrier. In this approximation, the positions of the minima at $\tilde{\varphi}_x = 0$ are $\pm \tilde{\varphi}_0 = \pm \sqrt{6\lambda/(1+\lambda)}$. Therewith, the barrier height is approximated by

$$\Delta U_{\text{rf}} = U(0) - U(\pm \tilde{\varphi}_0) \approx -\frac{3}{2} E_L \frac{\lambda^2}{1+\lambda} = -\frac{3}{2} \left(E_J - 2E_L + \frac{E_L^2}{E_J} \right); \quad (2.21)$$

it directly depends on E_J with corrections in E_L .

To derive the qubit Hamiltonian we have to project the whole Hilbert space onto a subspace of the two qubit levels. Therefore, we firstly approximate the double-well potential with two harmonic potentials $U_{l/r} = U(\mp \varphi_0) + \frac{1}{2} U''(\varphi_0) (\varphi \pm \varphi_0)^2$ (see Fig. 2.7(a)) with corresponding Hamiltonians \mathcal{H}_l and \mathcal{H}_r and ground states $|l\rangle$ and $|r\rangle$, respectively. The level spacing between the different energy levels in the two wells is equal since the potentials are that of a harmonic oscillator. The ground states of the two harmonic oscillators have the same energy; if one considers the two oscillators as one system, the two states are degenerate.

¹¹As for the CPB, the degeneracy point $f = 1/2$ has to be seen as $f = 1/2 \bmod 1$.

¹²The maximal distance, which is obtained for $E_J/E_L \gg 1$, is $\Delta\varphi_0 = 2\varphi_0 = 2\pi$.

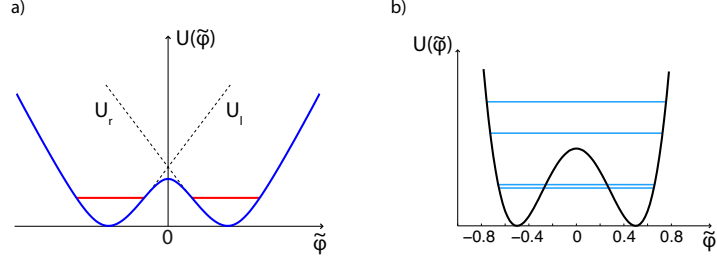


Figure 2.7: (a) Truncation of the flux qubit Hamiltonian at $f = \frac{1}{2}$; dashed lines indicate potentials of the left and right wells. Taken from [5]. (b) Energy levels of the flux qubit Hamiltonian. The two lower states build the qubit. As can be seen, the distance to the upper levels to the two qubit levels is large enough to use the rf SQUID as a qubit. Taken from [55].

This degeneracy is lifted due to state-dependent macroscopic quantum tunnelling between the two wells.

We now assume the bias flux to be near the degeneracy point, $\varphi_x \approx \pi$; accordingly, the states are nearly degenerate, $E_l \approx E_r$. Due to the tunnelling between the potential wells, the true ground state eigenfunction $|\Psi\rangle$ is a superposition of these two states

$$\mathcal{H}|\Psi\rangle = E|\Psi\rangle, \quad \text{with} \quad |\Psi\rangle = \alpha|l\rangle + \beta|r\rangle. \quad (2.22)$$

The qubit Hamiltonian is given by the matrix elements of the full Hamiltonian (2.17) taking into account only the two levels $|l\rangle$ and $|r\rangle$.

$$\mathcal{H}_{ll} = E_l + \langle l|U - U_l|l\rangle, \quad (2.23a)$$

$$\mathcal{H}_{rr} = E_r + \langle r|U - U_r|r\rangle, \quad (2.23b)$$

$$\mathcal{H}_{rl} = E_l \langle r|l\rangle + \langle r|U - U_l|l\rangle = \mathcal{H}_{lr}^*. \quad (2.23c)$$

The second terms in the diagonal matrix elements (2.23a) and (2.23b) are proportional to φ^4 , corresponding to a nonlinear oscillator with a quartic nonlinearity (see App. C.2). The level spacing is now no longer equal thus resulting in the required anharmonicity. Note that this approximation is only valid for $E_J/E_c \gg 1$ (see also the calculation for the transmon in Sec. 2.1.2). For the ground states $|l\rangle$ and $|r\rangle$, the energy corrections can be neglected since both states are equally shifted. Choosing the wavefunction real, $\mathcal{H}_{rl} = \mathcal{H}_{lr}$, and introducing $\Delta_{\text{rf}}/2 = \mathcal{H}_{rl}$ and $\varepsilon_{\text{rf}} = E_r - E_l$ we obtain the Hamiltonian of the rf SQUID qubit,

$$\mathcal{H}_{\text{RF}} \approx \frac{\varepsilon_{\text{rf}}}{2} \bar{\sigma}^z + \frac{\Delta_{\text{rf}}}{2} \bar{\sigma}^x, \quad (2.24)$$

with $\bar{\sigma}^z = |r\rangle\langle r| - |l\rangle\langle l|$ and $\bar{\sigma}^x = |l\rangle\langle r| + |r\rangle\langle l|$ being the Pauli matrices in the $\{|l\rangle, |r\rangle\}$ basis, and $\varepsilon_{\text{rf}} = 2I_{\text{rf}}\Phi_0(f - 1/2)$. The maximum circulating current I_{rf} and the level splitting Δ_{rf} depend on E_L , E_J , and E_c ; they have to be determined numerically. ε_{rf} can be tuned by the applied flux φ_x and is zero for $\Phi_x = \Phi_0/2 \bmod 1$ ($f = 1/2$). At the flux degeneracy point, $f = 1/2$, only the tunnelling probability Δ_{rf} determines the level spacing of the flux qubit states. The wavefunctions then correspond to the maximally entangled flux states (2.18). Far away from the degeneracy point, the qubit states are almost pure flux states, analogue to the charge states of the CPB qubit.

The Hamiltonian (2.24) can be diagonalized according to Sec. 1.2.1 which yields the qubit transition frequency

$$\hbar\omega_{\text{rf}} = \sqrt{\epsilon_{\text{rf}}^2 + \Delta_{\text{rf}}^2}. \quad (2.25)$$

The states of the qubit are built by currents with equal amplitude and opposite sign circulating clockwise ($|l\rangle$) or anticlockwise ($|r\rangle$) in the loop. In the energy eigenbasis $\{|g\rangle, |e\rangle\}$, the two eigenstates of the qubit have the expectation value [37]

$$\langle I_{\text{circ}} \rangle_{e,g} = \langle I_{\text{pcq}} \sigma^z \rangle_{e,g} = \langle I_{\text{rf}} (\cos 2\vartheta_{\text{rf}} \bar{\sigma}^z - \sin 2\vartheta_{\text{rf}} \bar{\sigma}^x) \rangle_{l,r} = \pm \frac{\epsilon_{\text{rf}}}{\sqrt{\epsilon_{\text{rf}}^2 + \Delta_{\text{rf}}^2}} I_{\text{pcq}}, \quad (2.26)$$

for the excited and ground state, respectively, whereas ϑ_{rf} is given by $\tan 2\vartheta_{\text{rf}} = \Delta_{\text{rf}}/\epsilon_{\text{rf}}$ (see also Sec. 1.2.1).

Fig. 2.7(b) shows a numerical calculation that has been done with the program Matlab [55]. The two qubit states are well separated from the other states of the rf SQUID. Thus, the approximations made above are valid for this system.

2.2.2 Persistent Current Qubit

The *persistent current qubit* (PCQ)¹³ is a flux qubit consisting of three JJs. It has been proposed and experimentally realized by the Delft group [56; 57]. A full theoretical description was done by Orlando et al. [58]. The design solves the problem of dephasing of the flux qubit by the environment.

The rf SQUID qubit requires a large inductance of the SQUID loop ($\Lambda = L_{J,0}/L \ll 1$) since the magnetic energy of the loop has to be comparable to the Josephson energy to form the required double-well potential. However, the main problem of the rf SQUID qubit is this large inductance; it makes the qubit vulnerable to dephasing by magnetic fluctuations of the environment [4]. To overcome these difficulties, it was suggested to replace the large loop inductance by the Josephson inductance of an additional tunnel junction. Thus, one can use circuits with $\Lambda \gg 1$ that are no longer sensitive to magnetic fluctuations.

Fig. 2.8 shows the circuit diagram of the PCQ; the architecture in principle is the same as for the rf SQUID qubit (see Fig. 2.6(a)), but now the SC loop contains three JJs connected in series. The two side junctions are identical, with Josephson energy E_J , whereas the third junction has a smaller area and therewith a Josephson energy αE_J , with $\alpha < 1$. An external flux Φ_x threads the loop. For the rf SQUID, this external flux produces a current, circulating in the SQUID loop; due to the large size of the loop this results in a magnetic energy. For the PCQ, the loop is small and thus we can neglect the magnetic energy of the circulating current, that is, we neglect the loop inductance. Therefore, the potential energy of the PCQ is the just the sum of the Josephson coupling energies of each junction,

$$U(\varphi_1, \varphi_2) = -E_J [\cos \varphi_1 + \cos \varphi_2 + \alpha \cos \varphi_3], \quad (2.27)$$

with $\varphi_{1,2,3}$ being the gauge-invariant phase differences of the junctions.

For a negligible loop inductance, fluxoid quantization around the loop containing the junctions requires

$$-2\pi f = \varphi_1 - \varphi_2 + \varphi_3, \quad (2.28)$$

¹³The name persistent current qubit has its origin in the two persistent currents of opposite direction that build the two qubit states.

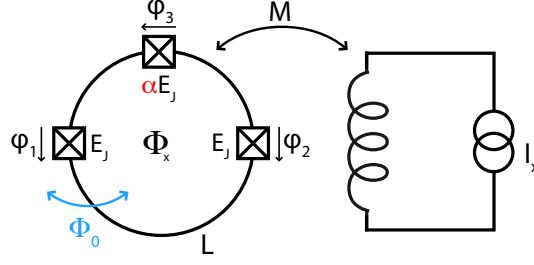


Figure 2.8: Circuit diagram of the PCQ. The loop now contains three JJs connected in series, whereas the two side junctions are identical (Josephson energy E_J), while the central, third junction has a smaller area (αE_J , $\alpha < 1$). Again, an external flux Φ_x is applied via a tank circuit. The arrows define the direction of the currents.

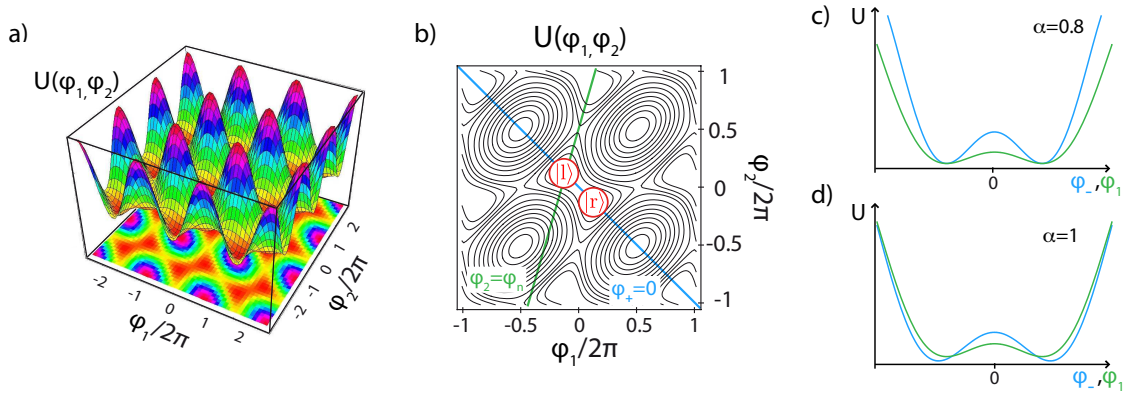


Figure 2.9: Potential energy landscape of the PCQ for $f = \frac{1}{2}$ and $\alpha = 0.8$. In (a) the potential is plotted three-dimensional (taken from [59]). An egg-box-like structure is evident. In (b) the potential is plotted in a contour line plot. The nested nearly circular shapes mark the maxima in the potential, and the figure-eight-shaped contours enclose two minima. The blue line marks the connection between the minima in one unit cell, where $\varphi_+ = 0$. The green line marks the connection between the minima in neighbouring unit cells, where $\varphi_2 \propto \varphi_1$ (see also text). (c) and (d) show the potential energy landscape along the blue and green line in (b) at $\alpha = 0.8$ and $\alpha = 1$, respectively. As for the rf SQUID, a double-well potential is formed.

with $f = \Phi_x/\Phi_0$ being the magnetic frustration. The potential then reads

$$U(\varphi_1, \varphi_2) = -E_J [\cos \varphi_1 + \cos \varphi_2 + \alpha \cos (2\pi f + \varphi_1 - \varphi_2)] \quad (2.29)$$

Figs. 2.9(a) and (b) show this potential for $f = 1/2$. For $1/2 < \alpha < 1$, a double-well potential is formed within each $2\pi \times 2\pi$ cell in the phase plane. The optimal value $\alpha \approx 0.7 - 0.8$ results in a separation of these cells by high potential barriers while tunnelling between the two minima within one cell is still possible [3]. The two minima thus contain the degenerated states $|l\rangle$ and $|r\rangle$ that build the qubit. The qubit states $|g\rangle$ and $|e\rangle$ are superpositions of these states and, again, correspond to clockwise and anticlockwise currents circulating in the loop.

We now set the external flux to half integer flux quantum, $f = 1/2$. Introducing the new variables $\varphi_{\pm} = (\varphi_1 \pm \varphi_2)/2$, the potential then reads

$$U(\varphi_+, \varphi_-) = -E_J [2 \cos \varphi_+ \cos \varphi_- - \alpha \cos 2\varphi_-]. \quad (2.30)$$

For $\alpha \leq 1/2$, U has one minimum at $(\varphi_+, \varphi_-) = (0, 0) \pmod{2\pi}$ (corresponding to $(\varphi_1, \varphi_2) = (0, 0)$); the calculation of the critical points is given in App. C.3). For $\alpha > 1/2$, this minimum splits into two minima at $(\varphi_+, \varphi_-) = (0, \pm \varphi^*)$ (corresponding to $(\varphi_1, \varphi_2) = (\varphi^*, -\varphi^*), (-\varphi^*, \varphi^*)$) with $\varphi^* = \arccos \frac{1}{2\alpha}$. The minima form a two-dimensional pattern repeated in a two-dimensional square lattice [58] enclosed by the maxima at $(\varphi_+, \varphi_-) = (\pm\pi, 0), (0, \pm\pi)$ (corresponding to $(\varphi_1, \varphi_2) = (\pm\pi, \pm\pi)$).

Figs. 2.9(c) and (d) show the potential energy along the directions between two minima in the same (blue) and neighbouring (green) unit cells (e.g. $(-\varphi^*, \varphi^*)$ and $(\varphi^*, 2\pi - \varphi^*)$); this corresponds to setting $\varphi_+ = 0$ or $\varphi_2 = (\pi/\varphi^* - 1)\varphi_1 + \pi \equiv \varphi_n$. For both values, a double-well potential is formed; the maxima correspond to the saddlepoints $(\varphi_1, \varphi_2) = (0, 0)$ and $(0, \pi/2)$ for $\varphi_+ = 0$ and $\varphi_2 = \varphi_n$, respectively (cp. App. C.3). For $\alpha = 0.8$ the energy barrier between the two minima in one unit cell ($\varphi_+ = 0$) is much lower than the energy barrier between the two minima in neighbouring unit cells ($\varphi_2 = \varphi_n$). For $\alpha = 1$ the two barriers are nearly the same. Since we want to build a qubit between minima in one unit cell, α is optimal for $\alpha \sim 0.7 - 0.8$. The potential landscape can be manipulated by changing α . Therefore, as for the CPB (Sec. 2.1.1), one could replace the central junction (αE_J) by two JJs shunted in parallel such that α can be controlled with external magnetic fields.

We choose α such that the energy barrier between two minima in one unit cell is lower than that of two neighbouring cells (blue line in Fig. 2.9(c)). A double-well potential with the minima $(\varphi_+, \varphi_-) = (0, \pm \varphi^*)$ is formed. Setting $\varphi_+ = 0$ we can expand the potential (2.30) in φ_- ,

$$U(\varphi_+ = 0, \varphi_-) \approx E_J \left[(1 - 2\alpha)\varphi_-^2 - \left(\frac{1}{12} - \frac{2}{3}\alpha \right) \varphi_-^4 \right]. \quad (2.31)$$

This potential has the same form as the approximated potential for the rf SQUID qubit (Eq. (2.20)). Correspondingly, the arguments that were given for the rf SQUID hold for the PCQ.

Therefore, the PCQ, as the rf SQUID qubit, is formed by two qubit states that correspond to a clockwise and anticlockwise current circulating in the loop. The Hamiltonian of the PCQ can be written according to [13],

$$\mathcal{H}_{\text{PCQ}} \approx \frac{\varepsilon_{\text{pcq}}}{2} \bar{\sigma}^z + \frac{\Delta_{\text{pcq}}}{2} \bar{\sigma}^x, \quad (2.32)$$

with $\bar{\sigma}^z = |1\rangle\langle 1| - |r\rangle\langle r|$ and $\bar{\sigma}^x = |1\rangle\langle r| + |r\rangle\langle 1|$ again being the Pauli matrices in the $\{|1\rangle, |r\rangle\}$ basis, and $\varepsilon_{\text{pcq}} = 2I_{\text{pcq}}\Phi_0(f - 1/2)$. The minimum energy level splitting Δ_{pcq} and the maximum persistent current I_{pcq} have to be determined numerically and depend on E_J , E_c , and α . The expectation value of the current circulating in the qubit loop can be calculated according to Eq. (2.26). Since the PCQ is no longer sensitive to magnetic fluctuations of the environment, it is the best choice for quantum computation using the flux degree of freedom.

2.3 Phase Qubits

An architecture that is operated in the pure “superconducting” limit, where $E_J/E_c \gg 1$ ($E_J/E_c \sim 10^4 - 10^6$), is the phase qubit. First works with this system were done in the 1980s; macroscopic quantum tunnelling and resonance tunnelling have been observed in several experiments, e.g. [60; 61; 62].

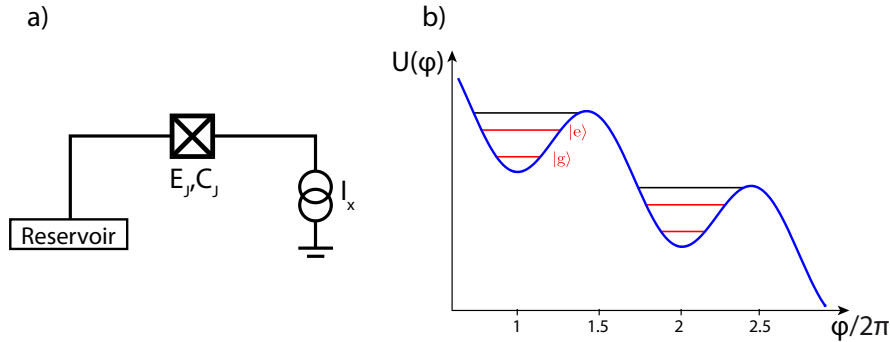


Figure 2.10: (a) Circuit diagram of the phase qubit; a single JJ, with Josephson coupling energy E_J and Josephson capacitance C_J , is driven with an external dc current I_x . (c) Potential energy diagram of the phase qubit. The current bias creates a tilt of the cosine-potential of the JJ (“tilted washboard potential”). The phase states $|g\rangle$ and $|e\rangle$ build the qubit.

The phase qubit uses the macroscopic phase of a JJ to implement a qubit, whereas a large nonlinearity is obtained by biasing the junction with a dc current very close to the critical current. The qubit states are built by the states of a nonlinear oscillator approximating the phase qubit. Superposition of these states and Rabi oscillations have been measured by the Martinis group [63]; recently, high-fidelity operations with a gate fidelity of 98% were performed [64]. It was also possible to couple and entangle two phase qubits [8]. Phase qubits can be coupled capacitively and controlled with microwave pulses.

A circuit diagram of the phase qubit is shown in Fig. 2.10(a); it is a JJ with Josephson energy E_J and Josephson capacitance C_J that is biased with a dc current I_x . Instead of one junction, as for the CPB (Sec. 2.1.1), one could, again, use two junctions shunted in parallel which allows to control the Josephson coupling to the SC reservoir with an external flux.

The Hamiltonian of the current-biased junction is given by

$$\mathcal{H}_{\text{PQ}} = E_c \hat{N}^2 - \underbrace{E_J \cos \varphi - \frac{\Phi_0}{2\pi} I_x \varphi}_{U(\varphi)}, \quad (2.33)$$

with, again, $\hat{N} = -i \frac{\partial}{\partial \varphi}$ being the Cooper pair number operator, E_J the Josephson energy, $E_c = \frac{(2e)^2}{2C_J}$ the charging energy of one Cooper pair, and I_x the externally applied flux. A detailed derivation of this Hamiltonian is given in App. B.3.2.

Fig. 2.10(b) shows the tilted cosine potential $U(\varphi)$ —the so-called *tilted washboard potential*—corresponding to the phase qubit Hamiltonian (2.33). For $I_x \lesssim I_c$ the external current yields a tilt of the cosine potential resulting in several wells where each well can be approximated with a cubic potential. This tilt increases with increasing I_x . In the classical regime, the particle representing the phase would either rest at the bottom of one of the wells or oscillate within the well. Due to the periodic motion, the average voltage ($\dot{\varphi}$) across the junction and therewith the average number of Cooper pairs N is zero. In the quantum regime the particle can no longer be confined due to macroscopic quantum tunnelling. However, for $E \ll E_J$, with E being the particle energy, the probability of tunnelling is small and thus can be neglected. As we show later in this section, this is fulfilled in the phase regime, where $E_J/E_c \gg 1$.

The minima and maxima of $U(\varphi)$ are located at $\varphi_0 = \arcsin\left(\frac{\Phi_0}{2\pi} \frac{I_x}{E_J}\right)$. Since $\arcsin x$ is

defined only for values $|x| \leq 1$, minima and maxima occur only for $I_x \leq \frac{2\pi}{\Phi_0} E_J \equiv I_c$. Whereas charge and flux qubits have to be biased near a suitable working point to allow good coherence times, the only restriction for the phase qubit is that it has to be biased at $I_x \lesssim I_c$ to obtain the tilted washboard potential, since for $I_x \ll I_c$, we would just have a cosine shape and for $I_x > I_c$ no minima would occur. Thus, we obtain the energy barrier of the potential, that is, the difference between the minimum and the maximum,

$$\Delta U_{\text{pq}} = U(\varphi_0^{\text{max}}) - U(\varphi_0^{\text{min}}) = \frac{\Phi_0}{2\pi} [I_x (2\varphi_0 - \pi) + 2I_c \cos \varphi_0]. \quad (2.34)$$

We now make a Taylor expansion of the potential $U(\varphi)$ about the minimum φ_0 , where $\cos \varphi_0 = \sqrt{1 - (I_x/I_c)^2}$. Therewith, one well of the tilted washboard potential can be approximated by the cubic form

$$U(\varphi) \approx \frac{\Phi_0}{2\pi} \left(\frac{1}{2} I_c \sqrt{1 - (I_x/I_c)^2} (\varphi - \varphi_0)^2 - \frac{1}{6} I_x (\varphi - \varphi_0)^3 \right), \quad (2.35)$$

where we have neglected the constant term $U(\varphi_0)$. In this approximation, the height of the potential barrier (2.34) is given by [61; 62; 65]

$$\Delta U_{\text{pq}} \approx \frac{2\sqrt{2}\Phi_0}{3\pi} I_c (1 - I_x/I_c)^{(3/2)}. \quad (2.36)$$

The quadratic term in Eq. (2.35) forms the potential of an harmonic oscillator leading to quantized energy levels with the oscillation frequency

$$\omega_p(I_x) = \frac{\sqrt{2E_c E_J}}{\hbar} \left(1 - (I_x/I_c)^2 \right)^{1/4}, \quad (2.37)$$

which is the current-dependent plasma frequency. Thus, in first order, the level spacing is homogeneous; the lowest energy levels $E_k = \hbar\omega_p(I_x)(k+1/2)$ (k being the occupation number of the oscillator) are determined by the plasma frequency. The levels are close to the bottom of one potential well if $E_J/E_c \gg 1$ and if the bias current is not too close to the critical value, $I_x < I_c$; thus, no tunnelling out of the wells occurs. Note that, as $I_x \rightarrow I_c$, ΔU_{pq} decreases rapidly to zero while $\omega_p(I_x)$ decreases much slower. Consequently, the number of states in the well decreases as I_x approaches I_c .

However, because of the cubic term in the potential, the energy levels are shifted, whereas the shift depends on the energy of the level itself. Therefore, the spacing between adjacent levels decreases with increasing energy in the well, see also App. C.2. Here, an increase of the bias current I_x decreases the spacings of the energy levels. This results in the required anharmonicity.

The two lowest transitions have the frequencies ($\omega_{mn} = \omega_m - \omega_n$) [65]

$$\omega_{10} \simeq \omega_p(I_x) \left(1 - \frac{5}{36} \frac{\hbar\omega_p(I_x)}{\Delta U_{\text{pq}}} \right), \quad (2.38a)$$

$$\omega_{21} \simeq \omega_p(I_x) \left(1 - \frac{10}{36} \frac{\hbar\omega_p(I_x)}{\Delta U_{\text{pq}}} \right), \quad (2.38b)$$

These two frequencies must be different to obtain a two-level system as a controllable qubit. The ratio $\Delta U_{\text{pq}}/\hbar\omega_p(I_x)$ parameterizes the anharmonicity of the cubic potential with regard

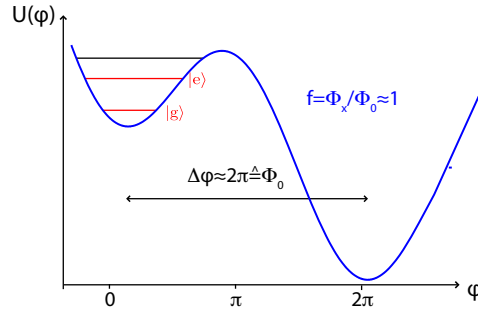


Figure 2.11: Potential energy diagram of the flux-biased phase qubit. Due to the flux bias at $f \approx 1$, the quartic potential of the rf SQUID (cp. Fig. 2.6(b)) is tilted to the right. The left well of the resulting potential can be approximated by a cubic potential. Since E_J is very large, the distance of the two minima is approximately $\Delta\varphi = 2\pi\Delta\Phi/\Phi_0 \approx 2\pi$.

to the qubit states, and gives an estimate of the number of states in the well. The reduced anharmonicity is $\mathcal{A}_r \approx -0.1$.

The state of the qubit can be controlled with the dc bias current I_x and a time-varying bias current $\Delta I(t)$, where $\Delta I(t)$ are the variations of the difference $I_c - I_x$. Making the transition $I_x \rightarrow I_x + \Delta I(t)$, the qubit Hamiltonian then is given by [6]

$$\mathcal{H}_{\text{PQ}} = \frac{\hbar}{2}\omega_{10}\bar{\sigma}^z + \frac{\hbar}{2\omega_{10}C_J}\Delta I(t)(\bar{\sigma}^x + \chi\bar{\sigma}^z), \quad (2.39)$$

with $\chi = \sqrt{\hbar\omega_{10}/3\Delta U_{\text{pq}}} \simeq 1/4$ for typical parameters, $\bar{\sigma}^z = |1\rangle\langle 1| - |0\rangle\langle 0|$, and $\bar{\sigma}^x = |0\rangle\langle 1| + |1\rangle\langle 0|$. In contrast to the flux and charge qubits, the phase qubit does not have a sweet spot, that is, a bias point where the $|0\rangle \leftrightarrow |1\rangle$ transition frequency has a local minimum. The Hamiltonian (2.39) cannot be cast into the typical form (1.7) and thus a $\bar{\sigma}^x$ rotation also produces a $\bar{\sigma}^z$ rotation. However, a sinusoidal current signal $\Delta I(t) \sim \sin \omega_{10}t$ can still produce $\bar{\sigma}^x$ rotations, whereas a low-frequency (quasi-dc) signal produces $\bar{\sigma}^z$ operations. Hence, the phase qubit state can be fully manipulated with dc and microwave pulses that are applied directly to the circuit.

The essential feature of the phase qubit is the cubic potential. This cubic potential can also be achieved with a flux-biased phase qubit. The direct application of a current to the phase qubit results in large noise disturbing the qubit coherence. Therefore, a current applied via a tank circuit is more suitable for qubit operations. The design of the flux-biased phase qubit is that of the rf SQUID qubit which was described in Sec. 2.2.1. In contrast to the rf SQUID qubit, the Josephson energy for the flux-biased phase qubit is now much larger than the magnetic energy. Moreover, the qubit is not biased near the degeneracy point, but far away from it, $f = \Phi_x/\Phi_0 \approx 1$. Note that the applied flux corresponds to a current in the qubit loop; thus, we will speak of applied currents in the following chapters. As shown in Fig. 2.11, the resulting potential is strongly tilted to the right. The left well of this potential can again be approximated by a cubic potential. Macroscopic quantum tunnelling to the right well changes the flux through the loop by $\sim \Phi_0$. The flux-biased phase qubit is an improved phase qubit design since the inductance L of the SC loop minimizes quasi-particle generation [66]. Therefore, nowadays, the flux-biased phase qubit is used instead of the current-biased phase qubit because of improved coherence and additional features for qubit readout that we discuss in Sec. 3.4.

2.4 Circuit Quantum Electrodynamics with Superconducting Qubits

In the previous sections we have shown that SC circuits act as artificial atoms whose many-level Hilbert space can be truncated to two qubit levels. In this section we now focus on the implementation of *circuit quantum electrodynamics* (circuit QED) with these systems. Circuit QED is the analogue to cavity QED in solid-state quantum computation. The emergence of circuit QED in the past few years has opened up new horizons for these solid-state based devices and has led to a confluence of the research in the fields of quantum optics, cavity QED, and mesoscopic superconductivity. This “quantum optics on a chip” gives the possibility to e.g. study fundamental quantum mechanics with macroscopic devices, to control solid state systems with quantized fields, and to use the coupled cavity for readout purposes. In contrast to quantum-optical cavity QED, circuit QED offers the tunability of the qubit transition frequency.

The idea of the implementation of circuit QED in SC circuits is to use a transmission line resonator and to couple it to an SC qubit. The first proposals by Schwab and collaborators [67; 68] study the effect of a CPB capacitively coupled to the resonator. During the last years, several circuit QED experiments have been accomplished with different types of SC qubits, as for example the generation of Fock states with charge or phase qubits [69; 70] or the analysis of the dynamics of a two-photon driven flux qubit [71]. In this section, we demonstrate the implementation of circuit QED with the different SC qubit flavours and calculate the coupling strengths of the qubits to a resonator.

2.4.1 Capacitive coupling to the CPB Qubit

We firstly consider the realization of circuit QED with SC charge qubits proposed by Blais et al. [22]. As shown in Fig. 2.12, the CPB is fabricated at the centre of a transmission line resonator (TLR) that consists of a full-wave section ($l = \lambda \approx 1$ cm) of an SC coplanar waveguide. The CPB and the TLR are coupled via the capacity C_g . The quasi-one-dimensional coplanar waveguide is built by a narrow-centre conductor (the TLR) and two nearby lateral ground planes that allow measurements of the amplitude and phase of the resonator transmission, and the introduction of dc and rf pulses to manipulate the qubit states. This on-chip “cavity” can be fabricated with existing lithographic techniques, e.g. by patterning a thin SC film deposited on a silicon chip [72].

The zero-point energy of this design is distributed over a very small effective volume which is an important advantage for the choice of a one-dimensional TLR. As shown in App. C.4, this leads to significant rms voltages between the centre conductor and the adjacent ground plane at the antinodal positions and thus to a strong coupling between the qubit and the resonator. In contrast to lumped LC circuits or current-biased large JJs, the qubit can be placed within the cavity formed by the transmission line to strongly suppress the spontaneous emission [22]. Furthermore, quality factors with $Q \sim 10^6$ can be achieved in TLRs and therewith the internal losses are very low.

For a finite length l , the transmission line behaves as a harmonic oscillator with resonance frequency $\omega_r = 1/\sqrt{L_r C_r}$ (L_r and C_r being the capacitance and inductance of the TLR, respectively). It is described by the Hamiltonian

$$\mathcal{H}_{\text{TLR}} = \hbar\omega_r a^\dagger a. \quad (2.40)$$

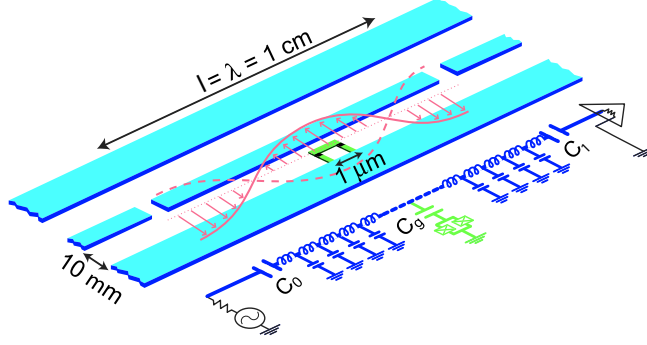


Figure 2.12: Schematic layout and equivalent lumped circuit representation of the proposed implementation of cavity QED using SC circuits. The 1D TLR (inductance L_r , capacitance C_r) consists of a full-wave section of a SC coplanar waveguide. A CPB is placed between the SC lines and is capacitively coupled to the centre trace at a maximum of the voltage standing wave via C_g , yielding a strong electric dipole interaction between the qubit and the cavity. Input and output signals of the box are coupled to the resonator via capacitive gaps (C_0 and C_1) in the centre line. Taken from [22].

Here, a and a^\dagger are the bosonic annihilation and creation operators of one resonator mode, respectively. We have neglected the zero-point energy $\hbar\omega_r/2$ of the resonator.

For a CPB fabricated inside a resonator, the dimensionless gate charge has an additional ac component N_g^{ac} . As shown in App. C.4, if the qubit is placed at the centre of the TLR, this quantum part is given by

$$N_g^{\text{ac}} = N_{\text{rms}}^{(2)} (a + a^\dagger), \quad \text{with} \quad N_{\text{rms}}^{(2)} = \frac{C_g}{2e} \sqrt{\frac{\hbar\omega_r}{2C_r}}. \quad (2.41)$$

$N_{\text{rms}}^{(2)}$ is the dimensionless rms charge between the centre conductor and the ground plane. The full quantization of the TLR including the calculation of the rms values is given in App. C.4.

To calculate the interaction of the CPB with the resonator, we have to add the quantum part N_g^{ac} to the dc component N_g [22] which corresponds to making the transition $N_g \rightarrow \delta N_g = N_g + N_g^{\text{ac}}$ in the CPB Hamiltonian (2.1). The total Hamiltonian of the whole qubit-resonator system then reads

$$\mathcal{H}_{\text{CQR}} = \hbar\omega_r a^\dagger a + E_c (\hat{N} - N_g)^2 - E_J \cos \varphi - 2E_c N_{\text{rms}}^{(2)} (\hat{N} - N_g) (a + a^\dagger). \quad (2.42)$$

We did not include the $(\delta N_g)^2$ -term since it is an artefact from the derivation of the charge Hamiltonian (see App. B.3.3).

We firstly consider the CPB qubit, that is, the CPB in the charge regime, cp. Sec. 2.1.1. In this regime, N is a good quantum number and the Hamiltonian can be expressed in terms of the number of Cooper pairs on the island, see Eq. (2.2). If the resonator frequency is much smaller than the transition frequencies to higher CPB levels, we again only have to take into account terms with $N = 0$ and $N = 1$ which yields

$$\mathcal{H}_{\text{CR}} = \hbar\omega_r a^\dagger a - \frac{E_c}{2} (1 - 2N_g) \bar{\sigma}^z - \frac{E_J}{2} \bar{\sigma}^x - E_c N_{\text{rms}}^{(2)} (a^\dagger + a) [1 - 2N_g - \bar{\sigma}^z]. \quad (2.43)$$

In the energy eigenbasis $\{|g\rangle, |e\rangle\}$ (see also Eqs. (2.5) and (2.7)) the system takes the form

$$\mathcal{H}_{\text{CR}} = \hbar\omega_r a^\dagger a + \frac{\hbar}{2} \omega_{\text{cq}} \sigma^z - E_c N_{\text{rms}}^{(2)} (a + a^\dagger) \left[1 - 2N_g - \cos 2\vartheta_{\text{cq}} \sigma^z + \sin 2\vartheta_{\text{cq}} \sigma^x \right], \quad (2.44)$$

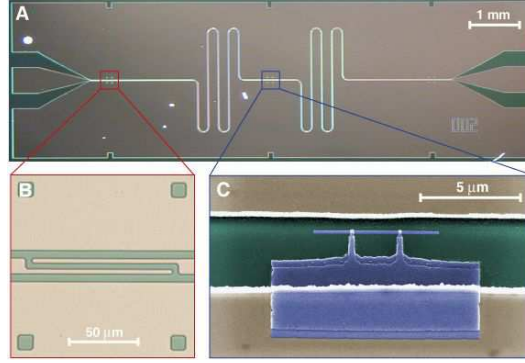


Figure 2.13: Scanning electron microscopy of the experimental realization of circuit QED with a CPB. **(a)** The SC niobium coplanar waveguide resonator is fabricated on an oxidized silicon chip using optical lithography. It is coupled by a capacitor at each end of the resonator (see **(b)**). **(b)** The capacitive coupling to the input and output lines and hence the coupled quality factor Q is controlled by adjusting the length and separation of the finger capacitors formed in the centre conductor. **(c)** False colour electron micrograph of a Cooper pair box (blue) fabricated onto the silicon substrate (green) into the gap between the centre conductor (top) and the ground plane (bottom) of a resonator (beige) using electron beam lithography and double angle evaporation of aluminium. The JJs are formed at the overlap between the long thin island parallel to the centre conductor and the fingers extending from the much larger reservoir coupled to the ground plane. Taken from [72].

with $\sigma^z = |e\rangle\langle e| - |g\rangle\langle g|$ and $\sigma^x = |e\rangle\langle g| + |g\rangle\langle e|$. At the degeneracy point, where $N_g = 1/2$ and therewith $\vartheta_{\text{cq}} = -\pi/4$, Eq. (2.44) immediately reduces to the JC Hamiltonian. To show that we obtain a JC interaction also for $N_g \neq \frac{1}{2}$, we utilize the Hamiltonian (2.44) in the interaction picture via the transformation $U = \exp[-i(\omega_r a^\dagger a + \frac{\omega_{\text{cq}}}{2} \sigma^z) t]$,

$$\begin{aligned} \mathcal{H}_{\text{CR}}^{\text{int}} = & -E_c N_{\text{rms}}^{(2)} \sin 2\vartheta_{\text{cq}} \left(\sigma^+ a e^{i(\omega_{\text{cq}} - \omega_r)t} + \sigma^- a^\dagger e^{-i(\omega_{\text{cq}} - \omega_r)t} \right) \\ & - E_c N_{\text{rms}}^{(2)} \left[\sin 2\vartheta_{\text{cq}} \left(\sigma^+ a^\dagger e^{i(\omega_{\text{cq}} + \omega_r)t} + \sigma^- a e^{-i(\omega_{\text{cq}} + \omega_r)t} \right) \right. \\ & \left. + (a e^{-i\omega_r t} + a^\dagger e^{i\omega_r t}) (1 - 2N_g - \cos 2\vartheta_{\text{cq}} \sigma^z) \right] \end{aligned} \quad \left. \vphantom{\mathcal{H}_{\text{CR}}^{\text{int}}} \right\} \begin{array}{l} \text{fast rotating} \\ \text{terms.} \end{array} \quad (2.45)$$

We can neglect the fast rotating terms in a RWA and therewith obtain the interaction Hamiltonian of the CPB qubit and the resonator,

$$\mathcal{H}_{\text{JC,C}} = \hbar\omega_r a^\dagger a + \frac{\hbar}{2} \omega_{\text{cq}} \sigma^z - \hbar g_{\text{cq}} (a^\dagger \sigma^- + a \sigma^+), \quad (2.46)$$

with $\hbar g_{\text{cq}} = E_c N_{\text{rms}}^{(2)} \sin 2\vartheta_{\text{cq}} = \frac{C_g}{C_\Sigma} e \sqrt{\frac{\hbar\omega_r}{2C_r}} \sin 2\vartheta_{\text{cq}}$, $\hbar\omega_{\text{cq}} = \sqrt{E_J^2 + [E_c(1 - 2N_g)]^2}$, $\sigma^+ = |e\rangle\langle g|$, and $\sigma^- = |g\rangle\langle e|$. At the charge degeneracy point, $\sin 2\vartheta_{\text{cq}} = -1$; the Hamiltonian (2.46) then takes the well-known form of the JC interaction with the coupling g_{cq} . Since $\sin 2\vartheta$ can be tuned via N_g , the coupling between the qubit and the resonator can be varied from zero to g_{cq} . The coupling g_{cq} is in the order of 100 MHz in this architecture. This means, we can achieve a tunable JC interaction with strong coupling in circuit QED with the CPB qubit; this gives the possibility to apply methods from quantum optics on this qubit. The experimental realization of circuit QED with a CPB is shown in Fig. 2.13.

2.4.2 Circuit QED with the Transmon in the Dispersive Regime

Hitherto, we have only considered the CPB in the charge regime. However, circuit QED is also possible for the transmon qubit that has been described in Sec. 2.1.2. In fact, the name “transmon qubit” has its origin in “transmission-line shunted plasma oscillation qubit”. After eliminating N_g with a gauge transformation, we obtain the Hamiltonian (2.42) rewritten in the basis of the uncoupled transmon states $|k\rangle$ [25]

$$\mathcal{H}_{\text{TR}} = \hbar\omega_r a^\dagger a + \hbar \sum_k \omega_k |k\rangle\langle k| + \hbar \sum_{k,l} g_{kl} |l\rangle\langle k| (a + a^\dagger) \quad (2.47)$$

with the coupling energies

$$\hbar g_{kl} = \hbar g_{lk} = 2E_c N_{\text{rms}}^{(2)} |\langle k | \hat{N} | l \rangle|, \quad (2.48)$$

where we have only considered the absolute value of the matrix element since the phase of the (complex valued) matrix element can be removed via a unitary transformation, see also App. A.4.1¹⁴; note that for the transmon $E_c = (2e)^2/2\tilde{C}_\Sigma$ with $\tilde{C}_\Sigma = C_J + C_g + C_B$. For $E_J/E_c \gg 1$, the transmon is well approximated by a nonlinear oscillator with the oscillation frequency $\omega_p = \sqrt{2E_J E_c}$ and the creation and annihilation operator $d^\dagger = \sum_k \sqrt{k+1} |k+1\rangle\langle k|$ and $d = \sum_k \sqrt{k} |k\rangle\langle k+1|$, respectively (cp. Eq. 2.10), where $|k\rangle$ now denotes an oscillator eigenstate (k being the occupation number). Since $\hat{N} = -i(E_J/(2E_c))^{(1/4)}(d - d^\dagger)/\sqrt{2}$ in this approximation, the general expression (2.47) can be simplified, so that only the coupling between neighbouring states $|k\rangle$ and $|k+1\rangle$ has to be taken into account,

$$|\langle k+1 | \hat{N} | k \rangle| = \sqrt{\frac{k+1}{2}} \left(\frac{E_J}{2E_c} \right)^{(1/4)} = |\langle k | \hat{N} | k+1 \rangle|. \quad (2.49)$$

The coupling $|\langle k+i | \hat{N} | k \rangle|$ between non-neighbouring states ($|i| > 1$) decreases with increasing j and increasing E_J/E_c .

Finally, after employing the RWA, we arrive at the effective generalized JC Hamiltonian of the transmon qubit

$$\mathcal{H}_{\text{JC,T}} = \hbar \sum_k \omega_k |k\rangle\langle k| + \hbar\omega_r a^\dagger a + \hbar \sum_k g_{k,k+1} \left[|k\rangle\langle k+1| a^\dagger + |k+1\rangle\langle k| a \right]. \quad (2.50)$$

This generalized version of the JC Hamiltonian does not allow for an exact analytical solution. Due to nearest-neighbour coupling of many transmon levels, the solution of the general case requires numerical methods. However, the dispersive limit of (2.50) allows for analytical solutions.

In the dispersive limit, the detunings $\Delta_{k,k+1} = \omega_{k+1} - \omega_k - \omega_r$ are large compared to the couplings, $|\Delta_{k,k+1}| \gg \sqrt{n+1}g_{k,k+1}$. In this case, we can eliminate the interaction between the resonator and the qubit to lowest order with a canonical transformation, see App. C.5 Eq. (C.49). Taking into account only states with $k = 0,1$ in Eq. (C.49) we get

$$\begin{aligned} \mathcal{H}_{\text{JC,T}}^{\text{eff}} = & \hbar\omega_0 |0\rangle\langle 0| + \hbar\omega_1 |1\rangle\langle 1| + \hbar\omega_r a^\dagger a \\ & + \hbar\chi_{0,1} |1\rangle\langle 1| - \hbar\chi_{0,1} a^\dagger a |0\rangle\langle 0| + \hbar(\chi_{0,1} - \chi_{1,2}) a^\dagger a |1\rangle\langle 1|, \end{aligned} \quad (2.51)$$

¹⁴This argument also can be applied to possible minus-signs.

with $\chi_{k,k+1} = g_{k,k+1}^2/\Delta_{k,k+1}$. Henceforward, we denote the states $|0\rangle$ and $|1\rangle$ with $|g\rangle$ and $|e\rangle$, respectively, for consistency in the notation. After neglecting constant terms and renormalizing the qubit and resonator frequency, we obtain the effective JC Hamiltonian of the transmon in the dispersive limit

$$\mathcal{H}_{\text{JC,T}}^{\text{eff}} = \frac{\hbar}{2} \left(\omega_t - \frac{g_t^2}{\Delta_t} \right) \sigma^z + \left(\hbar\omega_r' + \hbar\frac{g_t^2}{\Delta_t} \sigma^z \right) a^\dagger a, \quad (2.52)$$

with $\omega_t = \omega_e - \omega_g \approx \omega_p = \sqrt{2E_J E_c}$, $g_t \equiv g_{g,e} = \frac{C_g}{C_\Sigma} e \sqrt{\frac{\hbar\omega_r}{2C_r}} \cdot \left(\frac{2E_J}{E_c} \right)^{1/4}$, $\Delta_t = \omega_t - \omega_r$, and the Lamb-shifted resonator frequency $\omega_r' = \omega_r - \chi_{e,2}/2$.

As already mentioned, the coupling g_t increases with increasing E_J/E_c . Thus, the achievable coupling is larger than for the CPB qubit. This result is quite remarkable. While the sensitivity of the transmon spectrum to the dc component N_g decreases exponentially, the ac response to the oscillating cavity field N_g^{ac} increases in a power-law fashion [25].

2.4.3 Inductive Coupling to Flux Qubits

Circuit QED with flux qubits can be achieved with an inductive coupling of the qubit to a TLR. After the first experimental implementation [73], several impressive experiments have been performed with this design, e.g. [37; 71; 74]. An intuitive theoretical description of the system is given in [75]; we mainly follow this work to derive the coupling strength.

Figs. 2.14(a) and (b) show a schematic layout of the implementation of circuit QED with flux qubits. As the charge qubit, the flux qubit is placed at the centre of a TLR, but now it couples to the resonator via a mutual inductance M .

For the calculation of the JC Hamiltonian, as for the charge qubit, an additional quantum part has to be added to the bias of the qubit, but now this quantum part is the external ac flux,

$$\Phi_x^{\text{ac}} = \Phi_{\text{rms}}^{(2)} (a + a^\dagger), \quad \text{with} \quad \Phi_{\text{rms}}^{(2)} = M \sqrt{\hbar\omega_r} 2L_r. \quad (2.53)$$

A detailed calculation of the inductive coupling of the TLR, including an approximation for the mutual inductance, is given in App. C.4.

Replacing f by $f + \Phi_x^{\text{ac}}/\Phi_0$ in the flux qubit Hamiltonian (Eq. (2.24) or (2.32)) we obtain the Hamiltonian of the coupled system,

$$\mathcal{H}_{\text{FR}} = \hbar\omega_r a^\dagger a + \frac{\varepsilon_{\text{fq}}}{2} \bar{\sigma}^z + \frac{\Delta_{\text{fq}}}{2} \bar{\sigma}^x + I_{\text{fq}} \Phi_{\text{rms}}^{(2)} \sigma^z (a + a^\dagger) \quad (2.54)$$

with $\varepsilon_{\text{fq}} = 2I_{\text{fq}}\Phi_0(f - 1/2)$ (fq represents the rf SQUID and the persistent current qubit, with fq = rf or pcq; cp. Sec. 2.2), $\bar{\sigma}^z = |r\rangle\langle r| - |l\rangle\langle l|$, and $\bar{\sigma}^x = |l\rangle\langle r| + |r\rangle\langle l|$.

Again, we evaluate the Hamiltonian in the energy eigenbasis $\{|g\rangle, |e\rangle\}$ of the qubit; the Hamiltonian then reads

$$\mathcal{H}_{\text{FR}} = \hbar\omega_{\text{fq}} \sigma^z + \hbar\omega_r a^\dagger a + I_{\text{fq}} \Phi_{\text{rms}}^{(2)} (a + a^\dagger) (\cos 2\vartheta_{\text{fq}} \sigma^z - \sin 2\vartheta_{\text{fq}} \sigma^x) \quad (2.55)$$

with $\sigma^z = |e\rangle\langle e| - |g\rangle\langle g|$, $\sigma^x = |e\rangle\langle e| - |g\rangle\langle g|$,

$$\omega_{\text{fq}} = \sqrt{[2I_{\text{fq}}(\Phi_x - \Phi_0/2)]^2 + \Delta_{\text{fq}}^2}, \quad \text{and} \quad \tan 2\vartheta_{\text{fq}} = \frac{\Delta_{\text{fq}}}{\varepsilon_{\text{fq}}}. \quad (2.56)$$

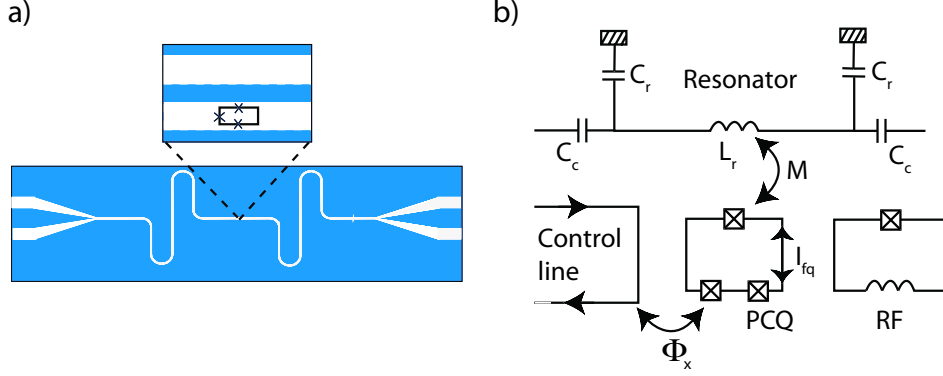


Figure 2.14: (a) Sketch of typical coplanar waveguide resonator of length $l = \lambda \approx 1$ cm (cp. Fig. 2.12). Also shown is how the qubit can be placed in between the centre conductor and the ground plane of the waveguide. (b) Circuit diagram of a flux qubit (PCQ or rf SQUID) coupled to a coplanar TLR via the mutual inductance M . The TLR (capacitance C_r , inductance L_r) is weakly coupled to external transmission lines via coupling capacitors C_c . The qubit is biased with the magnetic flux Φ_x . A persistent current I_{fq} circulates in the loop. Both taken from [75].

As for the charge qubit, we apply an RWA to eliminate fast rotating terms (cp. Eq. (2.45)). Therewith, the final JC Hamiltonian of the interaction between the resonator and the flux qubit is

$$\mathcal{H}_{\text{JC,F}} = \hbar\omega_{fq}\sigma^z + \hbar\omega_r a^\dagger a - \hbar g_{fq} (a^\dagger \sigma^- + a \sigma^+). \quad (2.57)$$

The coupling $\hbar g_{fq} = M \sqrt{\frac{\hbar\omega_r}{2L_r}} \sin 2\vartheta_{fq}$ is now maximal at the flux degeneracy point, where $f = 1/2$.

2.4.4 Circuit QED with Phase Qubits

Circuit QED with SC phase qubits is a very advanced field. It was possible to couple two phase qubits to a TLR and to control the quantized field of the cavity [47; 76; 77]. Fig. 2.15 shows the experimental implementation of circuit QED with phase qubits used in [76]. Two flux-biased phase qubits are coupled to the input ports, and therewith to the $\lambda/2$ -mode, of a TLR. The state of the qubits can be determined via dc SQUIDS coupled inductively to the qubits (see Sec. 3.4).

In first order, the phase qubit can be described by a harmonic oscillator with the oscillation frequency $\omega_p(I_x) = \sqrt{2E_J E_c} (1 - (I_x/I_c)^2)^{1/4}$. The annihilation and creation operators are the same as for the transmon (2.10), but now with the current-dependent plasma frequency $\omega_p(I_x)$ and $E_J/E_c \sim 10^4 - 10^6$. Therefore, the coupling of the TLR to the phase qubit can be calculated the same way as for the transmon, but now only the two qubit states $|g\rangle$ and $|e\rangle$ have to be taken into account since higher transitions would yield to quantum tunnelling out of the potential well. The TLR couples to the phase qubit with charging energy $E_c = (2e)^2/2C_J$ and Josephson energy E_J via a gate capacitance C_g . As for the transmon, we express this coupling in terms of the dimensionless gate charge $N_g^{ac} = N_{\text{rims}}^{(1)}(a + a^\dagger)$ ($N_{\text{rims}}^{(1)} = N_{\text{rims}}^{(2)}/\sqrt{2}$ since the qubit now couples to the lowest eigenmode of the resonator, see also App. C.4); the

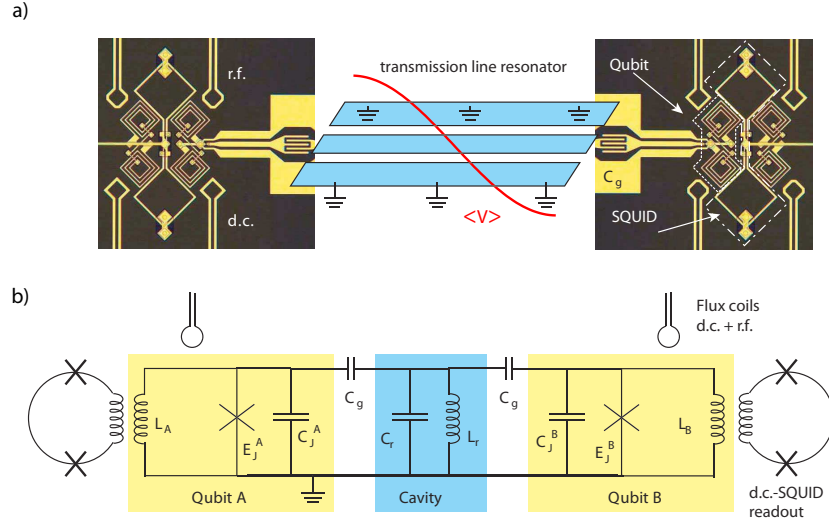


Figure 2.15: (a) Illustration of a quantum memory element with two Josephson phase qubits connected via coupling capacitors C_g to either end of a resonant cavity. The red line depicts the voltage amplitude of the lowest $\lambda/2$ -mode. (b) Equivalent circuit of the element near the $\lambda/2$ -resonance. The cavity, with an effective capacitance C_r and inductance L_r , is capacitively coupled (C_g) to the qubits ($C_J^{A/B}$, $E_J^{A/B}$). The qubits are flux-biased via flux coils; readout is done with a dc SQUID inductively ($L_{A/B}$) coupled to the qubits. Both taken from [76].

coupling strength of the TLR to the phase qubit then is [78]

$$\hbar g_{\text{pq}} = 2E_c N_{\text{rms}}^{(1)} \langle g | \hat{N} | e \rangle \approx \frac{1}{2} \sqrt{\frac{\hbar \omega_p(I_x)}{E_c}} \frac{C_g}{C_J} \sqrt{\frac{\hbar \omega_r}{C_r}}. \quad (2.58)$$

Since $E_J/E_c \gg 1$, this coupling is very large; therefore, strong coupling can also be achieved with SC phase qubits capacitively coupled to a TLR.

Summary

In this chapter we have presented the implementation of qubits in SC circuits. We have shown that the first four DiVincenzo requirements are fulfilled in these systems. SC qubits can be built and coupled to each other by using different degrees of freedom (scalability). They can be initialized by letting them decay to the ground state in the beginning. Stability of SC qubits is achieved by biasing them at a suitable working point or choosing improved designs. Coupling SC qubits to resonators in circuit QED furthermore suppresses the spontaneous emission. Lastly, SC qubits can be controlled with external dc and rf fields and with a single mode of an electromagnetic field in circuit QED. However, we have not considered the measurement of SC qubits until now. We discuss the readout of SC qubits in detail in the following chapters.

Chapter 3

State-of-the-Art in Superconducting Qubit Readout

While SC qubits have the advantages of scalability of the physical parameters and easily achievable strong coupling in circuit QED, they also suffer from serious deficits compared to other proposals (especially in comparison with trapped ions, their quantum-optical counterparts). As already mentioned, the coherence times of SC qubits are very short due to their mesoscopic size. Accessorily, the lack of highly efficient readout techniques is a major problem in these systems. Focusing on the last point, though all the proposed readout schemes for SC qubits have in principle no fundamental limit to fidelity, they mostly suffer from technical problems such as noise and parameter constraints.

A measurement technique can be characterized by its readout fidelity, the QND character of the measurement and its back-action on the qubit, and the measurement time¹. The readout fidelity of the measurement is defined as [6]

$$F = 1 - (P_g(e) + P_e(g)) = P_e(e) + P_g(g) - 1, \quad (3.1)$$

where $P_y(x)$ is the probability of measuring the (classical) output y when the qubit was projected on the eigenstate $|x\rangle$ by the measurement ($x, y = g, e$). According to the definition of $P_y(x)$, $P_g(g) + P_e(g) = 1$ and $P_g(e) + P_e(e) = 1$. Ideally, $P_g(g) = P_e(e) = 1$ and thus $F = 100\%$. We again note at this point that the qubit is in a superposition of the ground and excited state after the state preparation, $|\Psi_0\rangle = \alpha|g\rangle + \beta|e\rangle$. Due to the laws of quantum mechanics, a single measurement can only yield the eigenstate of the qubit, i.e. the state on which the qubit was projected by the measurement. To determine the complex-valued numbers α and β , that correspond to the probability of a projection on state $|g\rangle$ and $|e\rangle$, respectively, several measurements have to be accomplished.

For the measurement, the qubit has to be coupled to the measurement device via a Hamiltonian $\mathcal{H}_{\text{meas}}$. For an ideal QND measurement, the commutator of the measurement and the qubit Hamiltonian is zero. The QND property is only needed if the qubit must be left in the measured eigenstate after the qubit readout. However, a QND measurement can be used for state preparation and additional measurements that improve the readout fidelity. If the QND character is not ideal, the measurement has a back-action on the qubit. This means, the detection might change the qubit eigenstate or have an influence on the coherence times.

¹There are several other attributes that can be used to characterize a readout; however, we focus on the most important ones.

For fast quantum computation and error correction, the measurement must not take too long. A short measurement is also required since otherwise the qubit would decay before it is measured. Furthermore, the back-action of the measurement on the qubit is less for a short measurement time.

In this chapter we review the state-of-the-art in SC qubit readout. We focus on the most promising techniques which are the readout of charge qubits with a single electron transistor (SET), the dispersive measurement of charge qubits with an oscillator, the flux qubit readout with a Josephson bifurcation amplifier, and the tunnelling-readout of phase qubits. All these proposals have their advantages and disadvantages which we also examine.

3.1 Readout of Charge Qubits with a Single Electron Transistor

A readout method that uses the charge degree of freedom to measure the state of the CPB qubit was proposed by Astafiev et al. [10]. The charge on the CPB island is measured via quasi-particle tunnelling to a SET island. The use of a charge trap between the SET and the CPB allows separation in time of the state control and the state readout and enables further processing of the data in a classical way. This single-shot measurement is a simple and easily applicable readout scheme that results in a calculated readout fidelity of 87% for the state $|1\rangle$ and 93% for $|0\rangle$ (where the states correspond to the charging states $|N\rangle$). Astafiev et al. do not use a resonator coupled to the qubit to achieve a JC interaction, forgoing the advantages of circuit QED. Furthermore, the CPB qubit is not biased at the charge degeneracy point; therefore, the stability of the qubit is rather low compared to other proposals. This readout method can only be used for the CPB qubit since it detects the charge on an SC island.

3.1.1 State Detection

Figs. 3.1(a) and (b) show the experimental setup for the state detection. The CPB qubit is capacitively coupled to a charge trap via C_{bt} that is, in turn, capacitively coupled to a single-electron transistor (SET) via C_{st} . The CPB, trap, and SET island are each biased with a gate voltage $V_{g,k}$ via a gate capacitance $C_{g,k}$, with $k = b, t, s$, respectively. The islands are each connected to the ground via C_k (whereas $C_b \equiv C_\Sigma = C_J + C_{g,b}$). Due to the trap, the qubit becomes electrostatically decoupled from the SET and a separation in time of the state manipulation and readout processes is possible.

Fig. 3.1(c) shows the pulse operation. Firstly, a control pulse is applied for a time t_c to prepare the qubit state. During this qubit manipulation, the trap is kept unbiased to prohibit charge relaxation to the trap. After a delay time t_d , a readout pulse, that lasts a time t_r , is applied to the trap to measure the state of the qubit. If there exists an extra Cooper pair on the SC island when the readout pulse starts, it can escape to the trap through quasi-particle tunnelling, and one can detect if the trap has additional electrons. Thus, one can determine if the qubit is in state $|1\rangle$ (trap charged) or state $|0\rangle$ (trap uncharged).

A detailed discussion of the CPB qubit Hamiltonian has been done in Sec. 2.1.1. We deal with quasi-particle tunnelling in this section, thus, the change of the notation in the qubit Hamiltonian from N , denoting the number of Cooper pairs, to N_b^e , denoting the number of excess electrons on the box, is self-evident. Therefore, the electrostatic energy of the island k

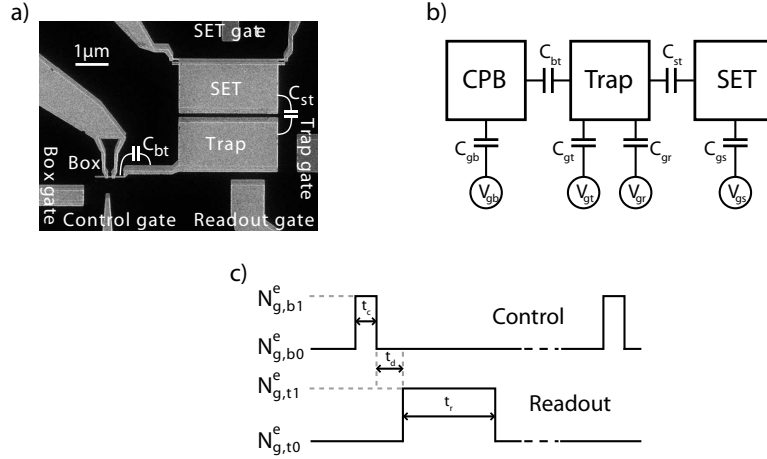


Figure 3.1: Experimental setup for the charge readout where (a) shows the scanning electron micrograph (taken from [10]) and (b) a sketch of the device. A CPB is coupled to a charge trap via a capacitance $C_{b,t}$. The trap, in turn, is coupled to a measurement SET via $C_{s,t}$. The potentials of the islands are controlled via capacitively ($C_{g,b}$, $C_{g,t}$, and $C_{g,s}$) coupled voltage gates ($V_{g,b}$, $V_{g,t}$, and $V_{g,s}$, respectively). Readout is done with the readout gate ($C_{g,r}$, $V_{g,r}$). (c) Schematical representation of the pulse operation. After the control pulse t_c , a delay time t_d is awaited. Lastly, a readout pulse t_r is applied to measure the state of the qubit. See also text and [10].

($k = b,t$) is

$$U_k(N_k^e, N_{g,k}^e) = E_c^k (N_k^e - N_{g,k}^e)^2. \quad (3.2)$$

Here, $E_c^k = e^2/2C_k$ ($C_b \equiv C_\Sigma$) is the single-electron charging energy of the island k , N_k^e the number of additional electrons on the island, and $N_{g,k}^e = C_{g,k}V_{g,k}/e$ the dimensionless gate charge, but now for one electron ($V_{g,k}$ being the gate/pulse voltage of island k). The Hamiltonians of the CPB qubit and the trap then read

$$\mathcal{H}_{\text{CPB}} = \Delta E \bar{\sigma}^z - \frac{E_J}{2} \bar{\sigma}^x, \quad (3.3)$$

$$\mathcal{H}_{\text{T}} = U_t(N_t^e, N_{g,t}^e) |N_t^e\rangle \langle N_t^e|. \quad (3.4)$$

The energy difference $\Delta E = \frac{1}{2} [U_b(0, N_{g,b}^e) - U_b(2, N_{g,b}^e)] = 2E_c^b (1 - N_{g,b}^e)$ between the states $|0\rangle$ and $|1\rangle$ is the same as in Eq. (2.4).

For the preparation of the state, one firstly lets the qubit relax to the ground state, which is nearly the pure charge state $|0\rangle$. During this process, the gate charge of the qubit is fixed to $N_{g,b0}^e \neq 1$. For the duration of the control time t_c , the qubit eigenbasis is now instantly changed by applying a rectangular control pulse, which brings the system to $N_{g,b1}^e$. We choose the gate voltage at the charge degeneracy point $N_{g,b1}^e = 1$. Therefore, the qubit will be rotated only by the $\bar{\sigma}^x$ -term of the Hamiltonian (3.3). After the state preparation, the qubit is in the dressed state

$$|\psi\rangle_c = \cos\left(\frac{\omega_J t_c}{2}\right) |0\rangle + \sin\left(\frac{\omega_J t_c}{2}\right) |1\rangle, \quad (3.5)$$

where $\omega_J = E_J/\hbar$. Hence, after the pulse, the probability of finding the qubit in state $|1\rangle$ is $|\sin(\frac{\omega_J t_c}{2})|^2$. The gate charge now is switched back to the initial value $N_{g,b0}^e$.

After the state preparation (and a delay time t_d), the trap gate voltage is changed from $N_{g,t0}^e$ to $N_{g,t1}^e$. The SET current is adjusted to an operation point where either one or two trapped quasi particles yield a negative switch of the SET current [10].

To achieve quasi-particle tunnelling from the CPB to the trap, the process $(N_b^e, N_t^e) \rightarrow (N_b^e - 1, N_t^e + 1)$ has to be energetically feasible ((N_b^e, N_t^e) represents the box-trap quasi particle configuration). Neglecting the Josephson coupling to the reservoir in (3.3), we obtain the inequality

$$U_b(N_b^e, N_{g,b0}^e) + U_t(N_t^e, N_{g,t1}^e) > U_b(N_b^e - 1, N_{g,b0}^e) + U_t(N_t^e + 1, N_{g,t1}^e) + 2\Delta_{sc}, \quad (3.6a)$$

$$\iff \Delta N_{g,t}^e > \tilde{N}_{g,t}^e + N_t^e + \eta_c(2 - N_b^e), \quad (3.6b)$$

where $\Delta N_{g,t}^e \equiv N_{g,t1}^e - N_{g,t0}^e$ is the amplitude of the readout pulse (cp. Fig. 3.1(c)), $\eta_c = C_t/C_b$, $\tilde{N}_g^t = 1/2 - \eta_c(3/2 - N_{g,b0}^e) + 2\Delta_{sc}C_t/e - N_{g,t0}^e$, and $2\Delta_{sc}$ is the energy gap of the SC material.

For three different quasi-particle tunnellings, three threshold amplitudes for the pulse amplitude $\Delta N_{g,t}^e$ can be defined:

$$\text{Region (I):} \quad (2,0) \rightarrow (1,1), \quad \Delta N_{g,t}^e > N_{gA}^e, \quad N_{gA}^e \equiv \tilde{N}_{g,t}^e. \quad (3.7a)$$

$$\text{Region (II):} \quad (2,0) \rightarrow (1,1) \rightarrow (0,2), \quad \Delta N_{g,t}^e > N_{gB}^e, \quad N_{gB}^e \equiv \tilde{N}_{g,t}^e + (1 + \eta_c). \quad (3.7b)$$

$$\text{Region (III):} \quad (0,0) \rightarrow (-1,1), \quad \Delta N_{g,t}^e > N_{gC}^e, \quad N_{gC}^e \equiv \tilde{N}_{g,t}^e + (2 + \eta_c). \quad (3.7c)$$

Within region (I) one quasi particle tunnels from the box to the trap. In region (III) tunnelling becomes possible even for state $|0\rangle$. In region (II) where $N_{gB}^e < \Delta N_{g,t}^e < N_{gC}^e$, two quasi particles may escape to the trap. Hence, the highest probability of measuring the trapped quasi particle occurs in this region. Thus, the pulse amplitude should be adjusted within region (II). $N_{g,i}^e$ ($i = A, B, C$) has to be developed from the experiment [10].

After the measurement, the trap relaxes to its ground state in a tunnelling process of the extra charge to the reservoir via the box.

3.1.2 Fidelity of the Readout

To compare the readout design with other proposals, we want to know the efficiency of the measurement, defined as the probability of measuring state $|0\rangle$ or $|1\rangle$ of the SC qubit correctly. For the calculation of the readout fidelity, we assume that once the charge is trapped, it is detected with 100% probability. We now examine the relaxation dynamics of the system. Since the relaxation of the qubit is very small at the charge degeneracy point, we neglect the decay of the qubit during the control time t_c . Thus, we expect the qubit to be perfectly in state $|\psi\rangle_c$, introduced in Eq. (3.5). Three main relaxation processes, described by the relaxation rates γ_{t1} , γ_{t0} , and γ remain. The relaxation rate γ_{t1} describes relaxation of state $|1\rangle$ to the trap during the measurement pulse t_r . The corresponding quasi-particle tunnelling process is $(2,0) \rightarrow (0,2)$. The relaxation dynamics of state $|0\rangle$ to the trap is describes by the weak relaxation rate γ_{t0} , according to the ‘‘dark switches’’ $(0,0) \rightarrow (-2,2)$. γ ($\gamma \ll \gamma_{t1}$) is the relaxation rate of the qubit to the reservoir (the decay rate) during the delay time t_d between the control and readout pulse ($(2,0) \rightarrow (0,0)$).

The total number of shots is n_{total} . We denote the number of events in which the qubit is in the excited state $|1\rangle$ with n^* , the number of ground states $|0\rangle$ with n , and the number of

events in which the trap is found to be charged with m . Expressed in terms of the box-trap quasi particle configuration (N_b^e, N_t^e) , n^* corresponds to the $(2,0)$ configuration, n to $(0,0)$, and m to $(0,2)$. Initially, that means, right after the control pulse, the number of excited states is $n^*(0) \equiv n_0^*$, and thus, the number of ground states $n(0) = n_{\text{total}} - n_0^*$. No charges are trapped in the beginning and hence $m(0) = 0$.

We want to determine the change in time of m within the time interval $[t, t + dt]$. n^* can relax to the trap with the rate γ_{t1} or to state $|0\rangle$ with γ . The number of ground states n is changed by the relaxation of state $|1\rangle$ and by relaxation to the trap with the rate γ_{t0} . Therefore, we obtain a set of differential equations²,

$$dn^*(t) = -(\gamma_{t1} + \gamma) n^*(t) dt, \quad n^*(0) = n_0^*, \quad (3.8a)$$

$$dn(t) = (-\gamma_{t0} n(t) + \gamma n^*(t)) dt, \quad n(0) = n_{\text{total}} - n_0^*, \quad (3.8b)$$

$$dm(t) = (\gamma_{t1} n^*(t) + \gamma_{t0} n(t)) dt, \quad m(0) = 0. \quad (3.8c)$$

These equations are solved by

$$m(t) = \left(n_{\text{total}} - n_0^* \frac{\gamma_{t1} - \gamma_{t0}}{\gamma_{t1} + \gamma - \gamma_{t0}} \right) [1 - e^{-\gamma_{t0} t}] + n_0^* \frac{\gamma_{t1}(\gamma_{t1} - \gamma_{t0})}{(\gamma_{t1} + \gamma)(\gamma_{t1} + \gamma - \gamma_{t0})} [1 - e^{-(\gamma_{t1} + \gamma)t}]. \quad (3.9)$$

Since $\gamma \ll \gamma_{t1}$ and thus $\gamma_{t1}/(\gamma_{t1} + \gamma) \approx 1$, $m(t)$ is approximated by

$$m(t) \approx n_{\text{total}} [1 - e^{-\gamma_{t0} t}] + n_0^* \frac{\gamma_{t1} - \gamma_{t0}}{\gamma_{t1} + \gamma - \gamma_{t0}} [e^{-\gamma_{t0} t} - e^{-(\gamma_{t1} + \gamma)t}]. \quad (3.10)$$

If the readout pulse length $t = t_r$ satisfies the conditions $\gamma_{t0} \ll t_r^{-1} \ll (\gamma_{t1} + \gamma)$, Eq. (3.10) is approximated by

$$m(t_r) \approx n_{\text{total}} \gamma_{t0} t_r + n_0^* \frac{\gamma_{t1}}{\gamma_{t1} + \gamma} [1 - \gamma_{t0} t_r]. \quad (3.11)$$

With this result we can estimate an efficiency of the single-shot readout. $P_y(x)$ is defined as the probability to detect state $|y\rangle$ ($y = 0, 1$, corresponding to a charged or uncharged trap) when the qubit was projected on state $|x\rangle$ ($x = 0, 1$). Writing the total number of detected events after the readout time, $m(t_r)$, in Eq. (3.10) in terms of $P_y(x)$, we obtain

$$m(t_r) = n_0^* P_1(1) + (n_{\text{total}} - n_0^*) P_1(0). \quad (3.12)$$

Therewith, the efficiencies of the readout are

$$P_1(1) = \frac{\gamma_{t1} + \gamma \gamma_{t0} t_r}{\gamma_{t1} + \gamma}, \quad P_1(0) = \gamma_{t0} t_r. \quad (3.13)$$

Since $P_y(x)$, $P_0(0) + P_1(0) = 1$ and $P_0(1) + P_1(1) = 1$, we then can calculate the probabilities of detecting the correct state.

The values γ_{t1} , γ , γ_{t0} , and t_r have to be determined by the experiment; they are [10]

$$\gamma_{t1} = (37 \text{ ns})^{-1}, \quad \gamma_{t0} = (4.2 \text{ } \mu\text{s})^{-1}, \quad \gamma = (220 \text{ ns})^{-1}, \quad t_r = 300 \text{ ns}. \quad (3.14)$$

²It has to be noted that the equation for $m(t)$ in the original work [10] differs from our equation. However, the solution of the set of differential equations presented in the work of Astafiev et al. is not in agreement with the given equation. Moreover, the units in the equation for $m(t)$ are wrong in [10]. Thus, we assume a mistake at this part of the paper and present an alternative equation.

The energy relaxation time $T_1 = 1/\gamma$ of the qubit is relatively low compared to other experiments (see e.g. [11; 22; 72]). This is due to the fact that during the delay and readout time, the qubit is not biased to charge degeneracy. Adequate decay rates can only be achieved at charge degeneracy. A slight detuning to a point $N_{g,b}^e \neq 1$ results in a huge decrease in the decay time. Moreover, the readout time t_r is rather long compared to other experiments (see e.g. the experiments described in the rest of this chapter).

We obtain the probabilities of detecting state $|1\rangle$ or $|0\rangle$ correctly

$$P_1(1) = 0.87, \quad P_0(0) = 0.93. \quad (3.15)$$

These efficiencies might be improved a little by optimizing the relaxation rates and fabrication procedure. Note that the fidelities were obtained with many assumptions, such as the perfect detection of the electrons with the SET. Consequently, very likely, the real fidelities are less than these values.

The charge qubit readout with an SET has a relatively high readout efficiency. However, this efficiency cannot be improved a lot since many decay effects disturb the readout scheme. Furthermore, the measurement destroys the state of the qubit and is very slow since the readout time is $t_r = 300$ ns, where the delay time has not been taken into account.

3.2 Dispersive Measurement Using Circuit QED

In this section, we examine the readout suggestion of the Yale group [11; 22; 72]. This proposal uses a circuit QED setup to induce Rabi oscillations and to measure the qubit. The measurement is done with a QND homodyne measurement. It measures the phase and frequency shift of a resonator coupled to the qubit; this shift depends on the qubit state.

A visibility, defined as the maximum qubit population difference observed in a Rabi oscillation experiment, of more than 95% is obtained. This experiment is the first to obtain a visibility that approaches unity. Therefore, a very accurate qubit control is achieved. The readout proposal yields a very low single-shot readout fidelity of only 70 – 80% [79]. Nevertheless, this proposal is a QND measurement since the interaction between the resonator and the ac measurement field does not affect the qubit state. Thus, the fidelity can be increased by measuring several times. Since the qubit is coupled to a resonator and operated at the degeneracy point, the coherence times can be enormously enhanced compared to the previous proposal ($T_1 \approx 7 \mu\text{s}$).

The measurement scheme uses two fields and a resonator to control and read out the qubit state. Hence, several higher-order interactions, that are hard to control, between the fields, the resonator and the qubit may occur.

A sketch of the driven cavity is shown in Fig. 3.2(a). In this experiment, an SC qubit, with ground and excited state $|g\rangle$ and $|e\rangle$ and transition frequency ω_q , is coupled to a single mode of the electromagnetic field of a TLR with resonance frequency ω_r . The proposals of the Yale group use the CPB qubit and the transmon in the experiment. However, since all types of SC qubits can be coupled to a resonator in circuit QED (Sec. 2.4), this readout scheme can also be applied to flux and phase qubits.

The quantum state of the SC qubit is coherently controlled with a microwave pulse of frequency $\omega_s \approx \omega_q$. The microwave pulse and the qubit are strongly detuned from the resonator with detunings $\Delta_{sr} = \omega_s - \omega_r$ and $\Delta_{qr} = \omega_q - \omega_r$, respectively (later in this section we will set $\Delta_{sr} = \Delta_{qr} \equiv \Delta$). However, due to higher-order corrections, this microwave pulse

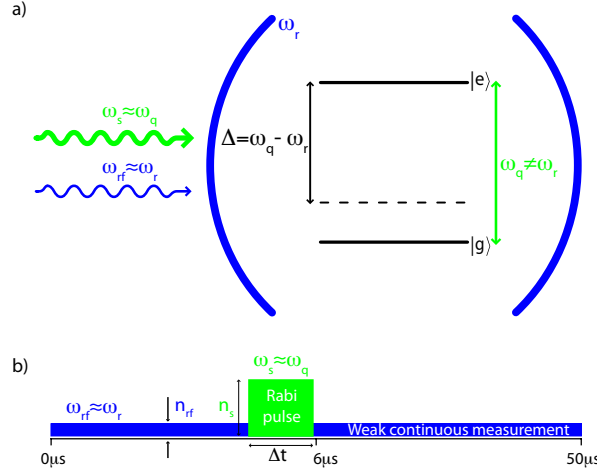


Figure 3.2: (a) Sketch of the measurement scheme. The qubit (transition frequency ω_q), is placed inside a cavity (transition frequency ω_r), that is far detuned from the cavity (detuning $|\Delta_{qr}| = |\omega_q - \omega_r| > g$, with g being the coupling between the qubit and a single photon of the cavity; Δ_{qr} will be set to Δ later in this section). The cavity is driven axially with two microwave fields with frequencies $\omega_s \approx \omega_q$ and $\omega_{rf} \approx \omega_r$ that populate the cavity with n_s and $n_{rf} \ll n_s$ drive photons, respectively, due to higher order corrections in the Hamiltonian. (b) Measurement sequence of Rabi oscillations, with Rabi pulse length Δt , pulse frequency ω_s (amplitude $\propto \sqrt{n_s}$), and continuous measurement at frequency ω_{rf} (amplitude $\propto \sqrt{n_{rf}}$).

populates the cavity with n_s drive photons that rotate the qubit and generate Rabi oscillations (see below). Readout is done with a second, weak microwave pulse, $\omega_{rf} \approx \omega_r$.

Fig. 3.2(b) shows the pulse sequence of the measurement. The weak measurement pulse ω_{rf} is applied during the whole time. The control pulse ω_s is applied for a time Δt to induce Rabi oscillations in the qubit. Once the qubit is rotated, the phase and frequency shift of the measurement pulse is detected in a homodyne measurement. The qubit state can be determined from these shifts.

We now consider the case of the driven system. Two coherent microwave pulses, with frequencies ω_s and ω_{rf} , are applied axially to the cavity that is coupled off-resonantly to the qubit. The Hamiltonian of the complete systems thus reads

$$\begin{aligned} \mathcal{H}_{\text{driven}} = & \frac{\hbar}{2} \omega_q \sigma^z + \hbar \omega_r a^\dagger a + \hbar g (\sigma^+ a + \sigma^- a^\dagger) \\ & + \hbar \Omega_s (e^{i\omega_s t} a + e^{-i\omega_s t} a^\dagger) + \hbar \Omega_{rf} (e^{i\omega_{rf} t} a + e^{-i\omega_{rf} t} a^\dagger), \end{aligned} \quad (3.16)$$

with g being the (quantum-mechanical) coupling of the qubit to the cavity and Ω_i ($i = s, rf$) the coupling strength between driving field ω_i and the cavity ($\Omega_i = |\mu_i| g_i$, where $|\mu_i|$ denotes the field amplitude and g_i the quantum mechanical coupling).

Again, we want to calculate the effective Hamiltonian, wherefore we firstly go into a reference frame rotating with the driving field ω_s via the transformation $U = \exp[-i\omega_s(a^\dagger a + \sigma^z/2)t]$ (cp. App. A.1.3). The Hamiltonian then reads

$$\begin{aligned} \mathcal{H}_{\text{d,rot}} = & \frac{\hbar}{2} (\omega_q - \omega_s) - \hbar \Delta_{sr} a^\dagger a + \hbar g (\sigma^+ a + \sigma^- a^\dagger) + \hbar \Omega_s (a + a^\dagger) \\ & + \hbar \Omega_{rf} (e^{i(\omega_{rf} - \omega_s)t} a + e^{-i(\omega_{rf} - \omega_s)t} a^\dagger). \end{aligned} \quad (3.17)$$

We firstly want to eliminate the off-resonant coupling between the driving field ω_s and the cavity. Therefor, we apply the unitary transformation $U_1 = \exp\left[-\frac{\Omega_s}{\Delta_{sr}}(a^\dagger - a)\right]$ with $|\Delta_{sr}| \gg \Omega_s$. Following the steps in App. C.5, this yields

$$\begin{aligned} \mathcal{H}_{\text{d,rot}}^{\text{eff},1} &= \frac{\hbar}{2}(\omega_q - \omega_s) - \hbar\Delta_{sr}a^\dagger a + \hbar g(\sigma^+ a + \sigma^- a^\dagger) + \hbar\frac{g\Omega_s}{\Delta_{sr}}(\sigma^+ + \sigma^-) \\ &+ \hbar\Omega_{\text{rf}}\left(e^{i(\omega_{\text{rf}} - \omega_s)t} a + e^{i(\omega_{\text{rf}} - \omega_s)t} a^\dagger\right) + \hbar\frac{g\Omega_{\text{rf}}}{\Delta_{sr}}\left(e^{i(\omega_{\text{rf}} - \omega_s)t} + e^{-i(\omega_{\text{rf}} - \omega_s)t}\right), \end{aligned} \quad (3.18)$$

where constant shifts have been neglected. The time-dependent, "constant" terms with $e^{\pm i(\omega_{\text{rf}} - \omega_s)t}$ can be neglected since they just generate a global phase (see App. C.6).

Still, the coupling between the qubit and the resonator has to be eliminated. For this purpose, we apply the unitary transformation $U_2 = \exp\left[-\frac{g}{\Delta_{qr}}(\sigma^+ a - \sigma^- a^\dagger)\right]$. Therefore, we obtain the final effective Hamiltonian in the rotating frame,

$$\begin{aligned} \mathcal{H}_{\text{d,rot}}^{\text{eff}} &= \frac{\hbar}{2}\left(\omega_q - \omega_s + \frac{g^2}{\Delta_{qr}}\sigma^z\right) - \hbar\left(\Delta_{sr} - \frac{g^2}{\Delta_{qr}}\sigma^z\right)a^\dagger a \\ &+ \hbar\Omega_{\text{rf}}\left(e^{i(\omega_{\text{rf}} - \omega_s)t} a + e^{-i(\omega_{\text{rf}} - \omega_s)t} a^\dagger\right) + \hbar\frac{g\Omega_s}{\Delta_{sr}}(\sigma^+ + \sigma^-). \end{aligned} \quad (3.19)$$

The coupling Ω_{rf} is very weak; thus, we did not take into account the second order couplings between ω_{rf} and the qubit. Since $\omega_q \approx \omega_s$ we set $\Delta_{qr} = \Delta_{sr} \equiv \Delta$ henceforward. Back in the non-rotating frame the Hamiltonian reads

$$\begin{aligned} \mathcal{H}_{\text{driven}}^{\text{eff}} &= \frac{\hbar}{2}\left(\omega_q + \frac{g^2}{\Delta}\right)\sigma^z + \hbar\left(\omega_r + \frac{g^2}{\Delta}\right)a^\dagger a + \hbar g(\sigma^+ a + \sigma^- a^\dagger) \\ &+ \hbar\Omega_{\text{rf}}\left(e^{i\omega_{\text{rf}}t} a + e^{-i\omega_{\text{rf}}t} a^\dagger\right) + \hbar\frac{g\Omega_s}{\Delta}(e^{-i\omega_s t}\sigma^+ + e^{i\omega_s t}\sigma^-). \end{aligned} \quad (3.20)$$

The last term, $\hbar\frac{g\Omega_s}{\Delta}(e^{-i\omega_s t}\sigma^+ + e^{i\omega_s t}\sigma^-)$, of Eq. (3.19) rotates the qubit and hence induces Rabi oscillations whereas different values of ω_s generate different rotations. The transition frequency of the qubit is ac Stark and Lamb shifted by $\frac{g^2}{\Delta}(n + 1/2)$. Therefore, the resonator frequency depends on the state of the qubit. Fig. 3.3(a) shows this entanglement of the qubit and the resonator. In the dispersive limit, two transmission curves are visible, corresponding to the ground and excited state of the qubit.

The off-resonant coupling between the qubit and the resonator also yields a phase shift of the field that leaks out the resonator [11; 22; 27]

$$\Delta\phi = \arctan\left(\frac{2g^2}{\kappa|\Delta|}\right)\sigma^z, \quad (3.21)$$

with κ being the decay rate of the resonator ($1/\kappa$ is the photon life time). The phase shift also depends on the qubit state; it has different signs for the two states $|g\rangle$ and $|e\rangle$. Fig. 3.3(b) shows this state-dependent phase shift. The smaller the detuning, the clearer the phase difference between the ground and excited state can be determined. Thus, the qubit state can be distinguished from the phase shift of the resonator.

The coupling between the cavity and the measurement pulse, $\mathcal{H}_{\text{rf}} = \hbar\Omega_{\text{rf}}(e^{i\omega_{\text{rf}}t} a + e^{-i\omega_{\text{rf}}t} a^\dagger)$, populates the cavity with n_{rf} measurement photons. This measurement field adopts the phase

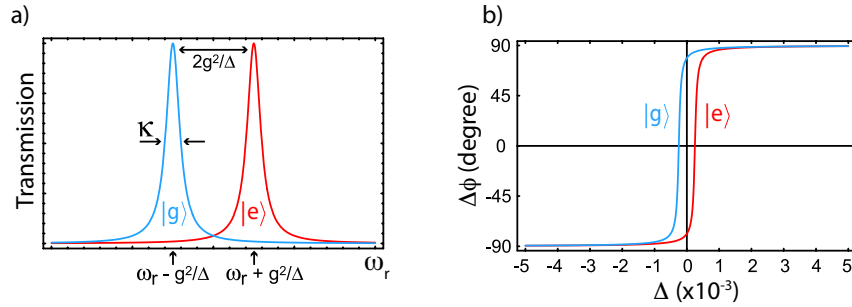


Figure 3.3: (a) Transmission spectrum of the resonator in the dispersive limit. The transmission spectrum (linewidth κ) is “pulled” by an amount $\pm g^2/\Delta$, depending on the state of the qubit (red for $|e\rangle$, blue for $|g\rangle$). Additional peaks near ω_q corresponding to qubit flips are suppressed by g/Δ . (b) Phase shift of the resonator field for the two states of the qubit as a function of Δ . Readout of the qubit is realized at, or close to, zero detuning where the dependence of the phase shift on the qubit state is largest. Coherent manipulations of the qubit are realized close to the qubit frequency. Taken from [22].

and the state of the resonator field. Therefore, we can measure the phase shift ϕ and the frequency shift $g^2\Delta$ of the resonator field by measuring the phase shift and the frequency shift of the rf field in a homodyne measurement (see App. E.2). With this, the state of the qubit can be reproduced.

In the measurement of the small rf signal, an amplifier is used. This amplifier adds noise in addition to amplifying the signal and can obscure the original signal. The signal-to-noise ratio (SNR) of the measurement is then given by the ratio of the number of photons $n_{\text{sig}} = n\kappa\Delta t/2$, accumulated over the integration period τ , divided by the detector noise $n_{\text{amp}} = k_B T_N/\hbar\omega_r \approx 100$ (T_N being the noise temperature of the amplifier).

$$\text{SNR} = \frac{n\kappa\tau}{2n_{\text{amp}}} \quad (3.22)$$

The integration time is limited by the qubit’s decay time $T_1 = 1/\gamma$ and the number of photons by the critical amplitude of the resonator $n_{\text{crit}} \approx 100$. The SNR can be very large if the qubit lifetime is longer than a few cavity decay times [22].

In the experiment [11], the SNR in an integration time of 100 ns is approximately 25. To determine the readout fidelity, each trace of the data has to be analyzed individually to assess the most likely prepared qubit state [27]. The single-shot readout fidelity for the qubit state integrated over the relaxation time ($T_1 \approx 7 \mu\text{s}$) then is approximately 30%. This fidelity can be improved by either using an amplifier with lower noise temperature or a larger signal power. In the current experiments, a fidelity of 70 – 80% [79] was achieved.

Nevertheless, this measurement is a QND measurement, since the interaction Hamiltonian of the cavity and the measurement field \mathcal{H}_{rf} does commute with the qubit Hamiltonian. Only the very small second-order effect of the coupling between the qubit and the measurement field might disturb the QND character of the measurement.

In conclusion, the dispersive readout scheme is a rather slow measurement (~ 100 ns) since many measurements have to be carried out for a high fidelity. The SNR is limited in practice due to nonlinear effects that occur at a stronger driving field [80]. Due to the QND character of the measurement, the qubit remains in the measured state and can be used for further processing.

3.3 Readout with the Josephson Bifurcation Amplifier

Another QND-like measurement uses the *Josephson bifurcation amplifier* to read out the qubit state. It was firstly proposed and experimentally realized in a quantum circuit by Siddiqi et al. [12; 81]. This readout method is based on an rf-driven JJ that acts as a nonlinear resonator coupled to the qubit via a quadratic type of interaction. As a result of this nonlinear coupling, the resonance frequency of the oscillator becomes qubit-state dependent. The state of the qubit can thus be inferred from a measurement of the properties of the oscillator. Under certain driving conditions, the resonator state also depends on the qubit state; therewith, the qubit state is amplified and can be determined with a fidelity up to 95%. However, due to the interaction with the oscillator, a decrease of the qubit coherence time and a change of the qubit bias is observed [82]; consequently, the QND character of the measurement is not ideal.

Nowadays, this method is used to determine the state of a flux qubit, see e.g. [37; 82; 83; 84; 85]. A dc SQUID, which is a nonlinear oscillator, is coupled to the qubit via a mutual inductance M and driven with an ac microwave signal. The driving picks up the phase of the oscillator that depends on the resonance frequency ω_{res} and the state of the oscillator and thus on the qubit state.

3.3.1 Coupling of the Qubit to the Readout SQUID

We concentrate on the PCQ, that is described in Sec. 2.2.2, since only this qubit is used in the experiment³. The uncoupled PCQ Hamiltonian is given by

$$\mathcal{H}_{\text{PCQ}} = \frac{\varepsilon_{\text{pcq}}}{2} \bar{\sigma}^z + \frac{\Delta_{\text{pcq}}}{2} \bar{\sigma}^x. \quad (3.23)$$

with $\bar{\sigma}^z = |1\rangle\langle 1| - |r\rangle\langle r|$. The qubit states are built by currents circulating in the loop. This current depends on the qubit state; in the $\{|1\rangle, |r\rangle\}$ basis its expectation value is $I_{\text{circ,q}} = I_{\text{pcq}} \bar{\sigma}^z$ (cp. Sec. 2.2). Rabi oscillations of the qubit can be induced with a flux pulse $\delta\Phi_{ac}$.

The qubit is now coupled to a current-biased dc SQUID via a mutual inductance M . In the experiment, an ac microwave signal $I_d(t)$ with amplitude I_{d0} and frequency ω_s close to the resonance frequency ω_{res} , is used to drive the dc SQUID. The Hamiltonian of the uncoupled current-biased readout SQUID reads

$$\mathcal{H}_{\text{RS,u}} = E_{c,\text{rs}} \hat{N}^2 - E_{J,\text{rs}} \cos \varphi - \frac{\Phi_0}{2\pi} I_d(t) \varphi, \quad (3.24)$$

with $E_{c,\text{rs}} = (2e)^2/2C_{J,\text{rs}}$ being the charging energy of the readout SQUID, $E_{J,\text{rs}} = E_{J,\text{rs}}^0 \cos(\pi f_{x,\text{rs}})$ the flux-dependent Josephson energy (with $f_{x,\text{rs}} = \Phi_{x,\text{rs}}/\Phi_0$ and $E_{J,\text{rs}}^0 = 2E_{J,\text{rs}}^{\text{SJ}}$, $E_J^{\text{rs,SJ}}$ being the Josephson energy of the single junction), \hat{N} the Cooper pair number operator, and φ the phase of the readout SQUID.

Due to the inductive coupling of the two systems, the average flux induced in the SQUID loop by the qubit is $MI_{\text{pcq}} \bar{\sigma}^z$. The external flux through the SQUID loop then changes as

$$f_{x,\text{rs}} \rightarrow f_{sq} = f_{x,\text{rs}} + f_{x,q}, \quad (3.25)$$

with $f_{x,q} = MI_{\text{pcq}} \bar{\sigma}^z / \Phi_0$. If we assume that the flux generated by the qubit is small, we do not have to take into account the magnetic energy and can use a linear approximation for

³Of course, the measurement would also work for the rf SQUID qubit.

this flux. The Josephson coupling energy now reads

$$\begin{aligned}
-E_{J,\text{rs}}^0 \cos(\pi f_{sq}) \cos \varphi &= -E_{J,\text{rs}}^0 \cos \varphi [\cos(\pi f_{x,rs}) \cos(\pi f_{x,q}) - \sin(\pi f_{x,rs}) \sin(\pi f_{x,q})] \\
&\approx -E_{J,\text{rs}}^0 \cos \varphi \cos(\pi f_{x,rs}) + E_{J,\text{rs}}^0 \cos \varphi \pi f_{x,q} \sin(\pi f_{x,rs}) \\
&= -E_{J,\text{rs}} \cos \varphi + \underbrace{MI_{\text{pcq}} I_{\text{circ,rs}} \bar{\sigma}^z}_{=\mathcal{H}_{\text{QS}}} \cos \varphi,
\end{aligned} \tag{3.26}$$

where \mathcal{H}_{QS} is the Hamiltonian that describes the coupling of the qubit to the readout SQUID. $I_{\text{circ,rs}} = \Phi_0/\pi \cdot E_{J,\text{rs}}^0 \sin(\pi f_{x,rs})$ is the maximum value of the circulating current in the SQUID loop (cp. App. B.4.1). Introducing the state- and flux-dependent Josephson energy $\mathcal{E}_{J,\bar{\sigma}^z} = E_{J,\text{rs}} - MI_{\text{circ,rs}} I_{\text{pcq}} \bar{\sigma}^z$, the complete Hamiltonian of the readout SQUID reads

$$\mathcal{H}_{\text{RS}} = \mathcal{H}_{\text{RS,u}} + \mathcal{H}_{\text{QS}} = E_{c,\text{rs}} \hat{N}^2 - \mathcal{E}_{J,\bar{\sigma}^z} \cos \varphi - \frac{\Phi_0}{2\pi} I_d(t) \varphi \tag{3.27}$$

Expanding the cosine up to φ^4 and assuming that we are in the flux regime, where $E_{J,\text{rs}}/E_{c,\text{rs}} \gg 1$, we can approximate this Hamiltonian by

$$\mathcal{H}_{\text{RS}} \approx \hbar\omega_{\text{res}} d^\dagger d - \frac{E_{c,\text{rs}}}{48} (d^\dagger + d)^4 - \sqrt{\frac{E_{c,\text{rs}}}{\hbar\omega_{\text{res}}}} \frac{\Phi_0}{2\pi} I_d(t) (d^\dagger + d), \tag{3.28}$$

with the bosonic creation and annihilation operators

$$d^\dagger = \sqrt{\frac{E_{c,\text{rs}}}{\hbar\omega_{\text{res}}}} \left(\frac{\hbar\omega_{\text{res}}}{2E_{c,\text{rs}}} \varphi - \frac{\partial}{\partial \varphi} \right), \quad \text{and} \quad d = \sqrt{\frac{E_{c,\text{rs}}}{\hbar\omega_{\text{res}}}} \left(\frac{\hbar\omega_{\text{res}}}{2E_{c,\text{rs}}} \varphi + \frac{\partial}{\partial \varphi} \right), \tag{3.29a}$$

respectively, and

$$\hbar\omega_{\text{res}} = \sqrt{2\mathcal{E}_{J,\bar{\sigma}^z} E_{c,\text{rs}}}. \tag{3.29b}$$

This is the same approximation that we have already used for the transmon in Sec. 2.1.2. It describes a nonlinear driven oscillator with the resonance frequency ω_{res} ; due to the coupling to the qubit, the resonance frequency now depends on the state of the qubit. The interaction Hamiltonian can be described in terms of the creation and annihilation operators d^\dagger and d ; in first order, we get

$$\mathcal{H}_{\text{QS}} \approx -\frac{1}{2} \underbrace{\sqrt{\frac{E_{c,\text{rs}}}{2\mathcal{E}_{J,\bar{\sigma}^z}}} MI_{\text{pcq}} I_{\text{circ,rs}}}_{\equiv \hbar g_{\text{QS}}} \bar{\sigma}^z (d^\dagger + d)^2, \tag{3.30}$$

with $\hbar g_{\text{QS}}$ being the coupling energy. This quadratic-type of interaction is the reason for the qubit-state-dependent resonance frequency of the oscillator.

To determine the QND character of the measurement, the commutator of the measurement Hamiltonian and the qubit Hamiltonian has to be determined; it reads

$$[\mathcal{H}_{\text{QS}}, \mathcal{H}_{\text{PCQ}}] = \frac{\Delta_{\text{pcq}}}{i} \hbar g_{\text{QS}} \bar{\sigma}^y (d^\dagger + d)^2. \tag{3.31}$$

This commutator depends on $\bar{\sigma}^y = -i(|l\rangle\langle r| - |r\rangle\langle l|)$, the tunnelling probability Δ_{pcq} , and the coupling g_{QS} . If we assume the product $\Delta_{\text{pcq}} g_{\text{QS}}$ to be small, the commutator is nearly zero; this means, the measurement is QND-like.

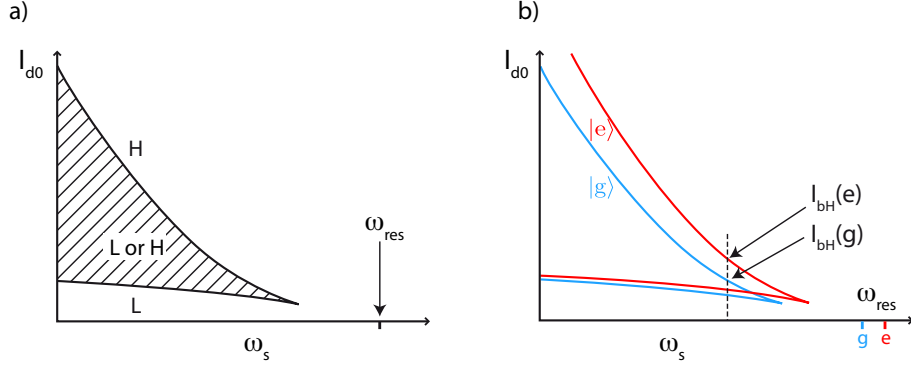


Figure 3.4: (a) Stability diagram of the driven oscillator as a function of the driving frequency ω_s . In the hatched region, two oscillation states are possible. Below the hatched region, only the state L with low oscillation amplitude is present. Above, only the state H , with high amplitude, is possible. ω_{res} is the resonance frequency of the undriven system. (b) Limits of the bistability region for the cases of a qubit in state $|g\rangle$ (blue) or $|e\rangle$ (red). Due to the state-dependency of the nonlinear oscillator, the stability diagrams (and also the resonance frequencies) of the two states differ. At a certain frequency (indicated by a dashed line), the bifurcation thresholds $I_{bH}(g)$ and $I_{bH}(e)$ differ significantly. Both taken from [37].

3.3.2 State Detection

To a good level of approximation, the circuit can be described by the classical *Duffing oscillator model* [86]. In this model, for $\omega_s > \omega_{\text{res}} \left[1 - \frac{\sqrt{3}}{2Q}\right]$, the oscillator state results in one unique forced oscillation state. For $\omega_s < \omega_{\text{res}} \left[1 - \frac{\sqrt{3}}{2Q}\right]$, three solutions are possible, depending on the driving amplitude I_{d0} :

$$\begin{aligned}
 I_{d0} < I_{bL} &: && \text{one oscillation state:} && L \\
 I_{bL} < I_{d0} < I_{bH} &: && \text{two oscillations states:} && L \text{ or } H \\
 I_{bH} < I_{d0} &: && \text{one oscillation state:} && H.
 \end{aligned} \tag{3.32}$$

I_{bL} and I_{bH} are the values of the driving current where *bifurcation* occurs, dependent on ω_s and the parameters of the resonant circuit; the oscillator then either resides in the lower (L) or the higher (H) state. In our circuit, damping of the oscillator arises from quasi-particle tunnelling and thus the quality factor of the oscillator is $Q = R\sqrt{C_{J,\text{rs}}/L_{J0,\text{rs}}}$ ($C_{J,\text{rs}}$ being the Josephson capacitance, $L_{J0,\text{rs}}$ the Josephson inductance of the readout SQUID, and R the resistance that describes the normal current, see also App. B.3.1).

Fig. 3.4(a) shows the stability diagram of the driven oscillator as a function of the driving frequency. For different values of the driving frequency and amplitude, the oscillation state results in L or H or both. If one starts with $I_{d0} < I_{bL}$ and slowly increases the driving amplitude, the oscillator resides in state L until I_{d0} reaches I_{bH} where the oscillator switches to state H . Thermal fluctuations will cause the transition $L \rightarrow H$ to occur randomly at $I_{bL} < I_{d0} < I_{bH}$. Vice versa, a decrease of the driving amplitude starting at $I_{d0} > I_{bH}$ resides in H until I_{d0} reaches I_{bL} .

This *bistable* regime, where the oscillator shows hysteretic behaviour, can be used to determine the state of the qubit. The bifurcation current I_{bH} strongly depends on the resonance

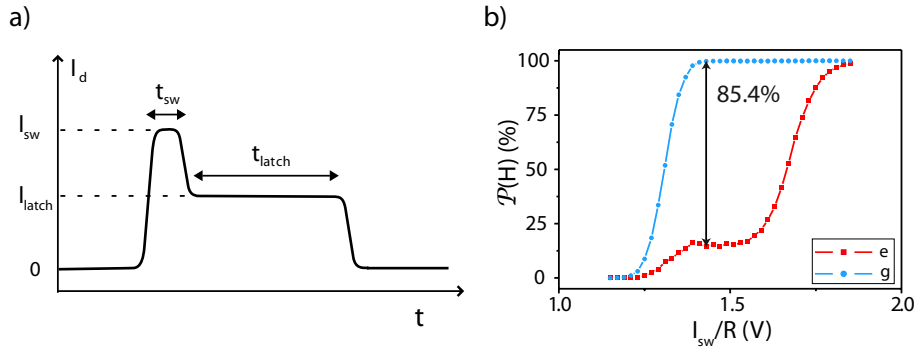


Figure 3.5: (a) Pulse sequence of the oscillator driving amplitude for a typical readout pulse (taken from [84]) (see also text). (b) Switching probability ($\mathcal{P}(H)$) curves for the qubit in state $|g\rangle$ (blue) and $|e\rangle$ (red) as a function of the switching current I_{sq} (see also text). Both taken from [37].

frequency ω_{res} of the oscillator⁴. Fig. 3.4(b) shows the stability diagram of the oscillator for the ground ($|g\rangle$) and excited ($|e\rangle$) state of the qubit. As can be seen, $I_{bH}(g)$ and $I_{bH}(e)$ differ significantly at a certain driving frequency. The oscillator is set to this fixed frequency; the rate of the transition $L \rightarrow H$ then strongly depends on the qubit state.

One can also use the *monostable* regime of the oscillator to measure the qubit state. This regime does not exploit the $L \rightarrow H$ transition. One measures the phase and the voltage of the driven oscillator that also depend on $\bar{\sigma}^z$. This just corresponds to a flux measurement with a dc SQUID, see e.g. [54].

We now focus on the bistable regime since the novel ideas are used in this measurement technique. Fig. 3.5(a) shows the pulse sequence of the driving amplitude. It has to be noted that in [37], a voltage instead of a current is used to control the probing power; however, the principle is the same since voltage and current are related by the resistance R of the measurement device via Ohm's law. The oscillator is driven with an ac pulse of fixed frequency $\omega_s < \omega_{\text{res}} [1 - \sqrt{3}/(2Q)]$. Firstly, the amplitude I_{d0} is set to a value I_{sw} , with $I_{bL} < I_{\text{sw}} \lesssim I_{bH}$, such that the oscillator switches to the H state with a high probability if the qubit was projected on $|g\rangle$ by the measurement, while it stays in the L state if the qubit was projected on $|e\rangle$. The information of the qubit state is thus transferred on the oscillator state. In the ideal case, the oscillator is in state H if the qubit was in $|g\rangle$ and in L if the qubit was in $|e\rangle$. The second part of the pulse (latching) has a reduced amplitude I_{latch} such that both transitions $L \rightarrow H$ and $H \rightarrow L$ have negligibly small probabilities. The pulse duration t_{latch} is set long enough to allow amplifier noise suppression; therefore, discrimination of the states H and L against electrical noise is possible. In the measurement, the oscillator states can then be distinguished via their amplitudes (low for L and high for H).

To determine the readout contrast of the measurement, the state of the qubit is firstly prepared in the ground state with large probability by waiting for a time much longer than the qubit relaxation time. Ideally, the oscillator is then in the higher state H . The probability $\mathcal{P}(H)$ that the oscillator is switched into state H is then measured for different values of I_{sw} by repeating the measurement sequence many times. The qubit is then rotated in the excited state with a π -pulse and $\mathcal{P}(H)$ is measured again. Ideally, $\mathcal{P}(H) = 1$ for $|g\rangle$ and $\mathcal{P}(H) = 0$ for $|e\rangle$. Fig. 3.5(b) shows the switching probability curves when the qubit is prepared in

⁴The lower bifurcation current I_{bL} also depends on ω_{res} , but not that strongly as I_{bH} .

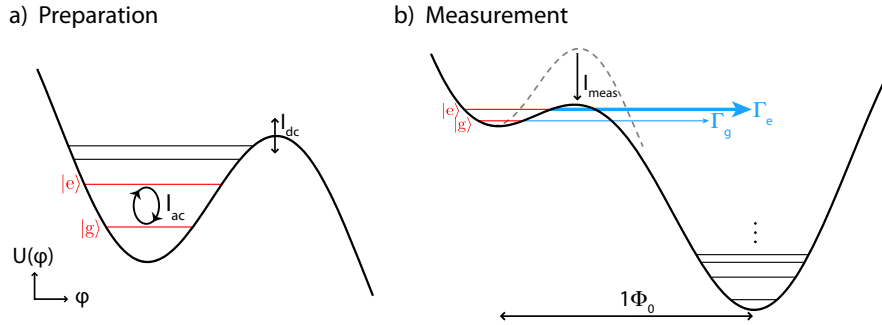


Figure 3.6: Potential energy of the phase qubit during (a) state preparation and (b) state measurement. The state is prepared with ac microwave pulses I_{ac} (x - and y - rotations) and dc pulses I_{dc} (z -rotation). During the readout, the potential barrier is reduced with a dc measurement pulse I_{meas} , allowing only the state $|e\rangle$ to tunnel out of the well with a high tunnelling rate (see also text).

the ground or excited state. The maximum separation between the two curves, that is the readout contrast, is 85.4%. Thus, if we assume that the state $|e\rangle$ is prepared optimally, the oscillator state switches with an efficiency of 85.4%.

The readout fidelity can be calculated by following the general arguments introduced in [85]. The fidelity is determined by the decay of the oscillator and the qubit during the switching and latching time. During the first part of the latching time, no relevant decay mechanisms occur since during this time the oscillator state is prepared. Therefore, the latching time t_{latch} mainly determines the readout fidelity. It has to be much shorter than the qubit and the oscillator coherence times to gain a high-fidelity readout. A detailed analysis of the decay of the system in the end results in an intrinsic readout fidelity, that is the fidelity of the experiment where non-ideal state preparation was already taken into account, of 95% [85].

The readout with the Josephson bifurcation amplifier results in a high readout fidelity. However, the QND character of this measurement scheme is not ideal; therefore, additional measurements have a lower fidelity and the back-action on the qubit is not negligible. The measurement time (~ 50 ns [37]) is not very long, but still needs to be improved.

3.4 Tunnelling-Readout of Phase Qubits

The last measurement scheme we consider is the readout of flux-biased phase qubits using state tunnelling⁵ that was developed by the Martinis group [14]. In this measurement, the flux in the qubit loop that depends on the qubit state is measured with a dc SQUID. This readout scheme is very fast ($\sim 2-4$ ns) and results in a fidelity above 90% [64; 87] ($\sim 93\%$ for $|e\rangle$ and $\sim 96\%$ for $|g\rangle$). With this advanced measurement technique it was also possible to measure gate fidelities of $\sim 98\%$ [64] and to perform a state measurement of coupled phase qubits [88]. Nevertheless, this measurement destroys the state of the qubit (quantum demolition measurement) and therefore cannot be used for qubit initialization or additional measurements.

⁵In principle, one could also use a regular current-biased phase qubit; however, the qubit has to be coupled to a dc SQUID via a mutual inductance for measurement purposes. Therewith, the flux-biased phase qubit is the best choice for this readout.

Fig. 3.6 shows the potential energy of the phase qubit during qubit preparation and measurement. As already derived for the rf SQUID (cp. Sec. 2.2.1), the height of the potential barrier ΔU_{fp} of the flux-biased phase qubit depends on the magnetic energy of the loop, $E_L = \Phi_0^2/(4\pi^2 L)$, the Josephson energy of the junction, E_J , and the external flux bias $\varphi_x = 2\pi\Phi_x/\Phi_0$,

$$\Delta U_{\text{fp}} \approx \frac{1}{2} (E_L + E_J) \varphi_0^2 - E_L \varphi_x \varphi_0 - \frac{E_J}{24} \varphi_0^4 \sim \varphi_x, \quad (3.33)$$

whereas φ_0 is the position of the potential minimum (the maximum is located at $\varphi \approx \pi$ for $\varphi_x \approx 2\pi$); we have neglected constant terms in this approximation. The flux bias corresponds to dc and ac currents circulating in the loop since $\Phi_x = L \cdot I_x$. Consequently, we will talk about external currents in the following.

In the experiment, at first an external dc current is adjusted such that the height of the potential barrier is high enough to suppress tunnelling of the qubit states out of the potential well. The potential then can be approximated by a cubic potential and thus with a nonlinear oscillator model; the two lowest oscillator states build the qubit, whereas the well altogether contains 3 – 5 oscillator states. The qubit state then is prepared by applying ac microwave pulses I_{ac} to induce x - and y -rotations and quasi-dc (low-frequency) pulses I_{dc} that induce z -rotations, cp. Fig. 3.6(a).

After the state preparation, the qubit is in a superposition of the ground and excited state. To measure the qubit state, a dc readout pulse with a width of ~ 5 ns that adiabatically reduces the well depth is applied. The pulse is chosen such that the state $|e\rangle$ lies very near the top of the well when the current pulse is at its maximal value I_{meas} , see also Fig. 3.6(b). The excited state $|e\rangle$ now tunnels to the right side of the well with the tunnelling rate Γ_e that is at least 2 orders of magnitude larger than the tunnelling rate Γ_g of $|g\rangle$. Calculations show that the ratio of these two tunnelling rates for a shallow well is $\Gamma_e/\Gamma_g \approx 10^2$ whereas this rate decreases with increasing bias current [89].

The actual measurement time is shorter than the full width of the measurement pulse because the tunnelling rate Γ_e is exponentially sensitive to the total bias current. Therefore, the qubit will be far more likely to tunnel near the peak of the readout current which results in an estimated effective measurement duration of 2–4 ns. This is a very short time, more than an order of magnitude shorter than previous measurement techniques of the phase qubit, where the qubit state $|e\rangle$ was driven to a higher level which then tunneled to the right well [66]; the time is also lots of shorter than the measurement times of the readout schemes introduced in the previous sections. The probabilities of tunnelling during the time τ (switching to the right well), $P_{s,e}$ and $P_{s,g}$ for levels $|e\rangle$ and $|g\rangle$, respectively, are given by ($k = e, g$)

$$P_{s,k} = 1 - \exp \left[- \int_0^\tau \Gamma_k(t) dt \right], \quad (3.34)$$

where the fact that Γ_k can be time-dependent has been taken into account. $\Gamma_k(t)$ can be obtained with a WKB approximation and depends on the value of the current pulse. The maximum measurement fidelity after the readout pulse is defined as the difference of the tunnelling probability when the qubit was projected on state $|e\rangle$ versus state $|g\rangle$.

In the following we mainly follow the arguments and methods derived in [89]. Fig 3.7 shows the tunnelling probabilities as a function of the pulse length τ and the maximum readout current I_{meas} , obtained with a WKB-approximation. I_{meas} is normalized by the

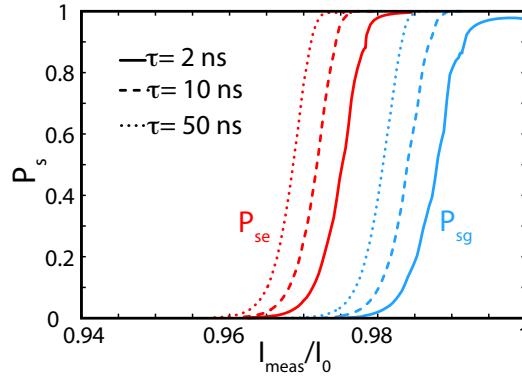


Figure 3.7: The probabilities $P_{s,e}$ (red lines, left hand side) and $P_{s,g}$ (blue lines, right hand side) of tunnelling to the right well during the measurement pulse starting from the states $|e\rangle$ or $|g\rangle$, respectively. The probabilities are plotted as a function of the readout time τ and the maximum readout current I_{meas} normalized by the critical value I_0 at which the barrier between the two wells disappears, starting at the initial current $I_i = 0.94I_0$. The pulse duration is $\tau = 2$ ns (solid lines) 10 ns (dashed lines), or 50 ns (dotted lines). Taken from [89].

critical current I_0 at which the barrier between the two wells disappears. The current starts at the initial value $I_i \approx 0.94I_0$, where approximately 5 states are in the left well. The curves remain at practically 0% probability for small measurement currents and saturate at 100% for a large enough I_{meas} (“S-curve” shape)⁶. The current shift between the curves for $P_{s,g}$ and $P_{s,e}$ for all times is sufficiently large to reliably distinguish between $|g\rangle$ and $|e\rangle$. However, the measurement error, defined as $(P_{s,g} + P_{s,e})/2$, is finite for any I_{meas} ; it is in the order of 1% at the optimal point. The minimal measurement error decreases with increase of the pulse duration τ and can be further reduced by changing the qubit parameters. Even though the separation of the two S-curves decreases with increase of τ , they become sharper, leading to better discrimination between the states $|e\rangle$ and $|g\rangle$. It has to be noted that the WKB-approximation does not take into account the discreteness of the levels in the right well. A full numerical simulation of the system would result in oscillations of the switching probabilities.

If one state has tunneled to the right well, the flux in the qubit loop is changed by $\sim \Phi_0$. This flux change now can easily be read out with a pulsed critical-current measurement in a SQUID detector that is inductively coupled to the qubit loop⁷.

In first experiments, only a fidelity of 63% has been achieved. This fidelity has been increased above 90% by separating the capacitive element from the JJ, that is, shunting a small JJ in parallel with a large capacitance to achieve a small charging energy instead of using a large JJ [87] (cp. Sec. 2.1.2). Due to this capacitance, the back-action of the measurement device on the qubit is reduced significantly.

In conclusion, the tunnelling-readout of phase qubits results in a high readout fidelity and is very fast. However, the readout destroys the state of the qubit and therefore, the state is lost for additional measurements and computational processes and cannot be prepared with this technique. Moreover, the tunnelling readout can only be used for phase qubits.

⁶The switching probability $P_{s,g}$ for $\tau = 1$ ns does not fully approach 100% since the pulse duration is too short.

⁷This corresponds to the measurement in the monostable regime in Sec. 3.3.

Chapter 4

Mesoscopic Shelving Readout

In the previous chapter we have discussed the state-of-the-art in SC qubit readout and we have shown that fast measurements of SC qubits with relatively high fidelities are possible. Nevertheless, even the highest achieved fidelity of $\sim 95\%$ is not sufficient for the requirements of quantum computation. As already mentioned in Sec. 1.1.5, a fidelity above 99% is necessary for efficient quantum computation, that is, quantum error correction and determination of the computational output. It is difficult to improve the fidelities of the existing readout techniques to this value. Therefore, novel ideas for the readout of SC qubits is required that breaks the limit of 99% fidelity.

For this, we have a look at qubit readout in other physical fields and see if we can adopt some of these ideas to SC qubits. A prominent technique is the very successful electron shelving readout in trapped ions. We show that it is possible to apply ideas from the electron shelving on SC qubits. By combining these with novel ideas, we get a new readout technique that we term the *Mesoscopic Shelving Readout* (MSR) [90]. We show that with this readout technique it might be possible to achieve a fidelity above 99% in a very short readout time.

In this chapter, we firstly describe the concept of the electron shelving readout in trapped ions. Then, we compare available features in trapped ion with those in SC qubits. This then leads us to the concept of the MSR. After introducing the basic principle of the MSR, we present the analytical model including the decay of the cavity. We also show numerical simulations for the full dissipative dynamics including qubit decay and off-resonant couplings. Lastly, we discuss the SNR, the fidelity, and the QND character of the measurement.

4.1 Electron Shelving in Trapped Ions

In contrast to SC qubits, experiments in trapped ions have exceeded the threshold of 99% years ago. Recent experiments report a fidelity of 99.99% [17]. In this section, we introduce this successful electron shelving readout of trapped ions. This technique was suggested by H. Dehmelt in the 1960s [91; 92; 93]; in 1989, the Nobel Prize in Physics was awarded to H. Dehmelt due to his contributions for the development of atomic precision spectroscopy.

In trapped ions, the qubit is represented by a selected pair of internal atomic states that are e.g. Zeeman-splitted or hyperfine states. The transition frequency of the two qubit states lies in the optical regime, in contrast to SC qubits where the transition frequency lies in the microwave regime. Though the Hilbert space of the atom can be truncated to this pair of states, atoms are many-level systems and thus, several other energy levels lie near the two

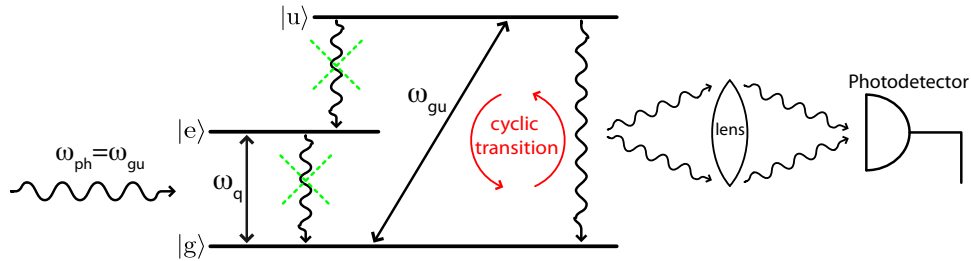


Figure 4.1: Sketch of the electron shelving readout. The qubit is encoded in the states $|g\rangle$ and $|e\rangle$; a third level $|u\rangle$ is used for state detection. A detection signal is collected on the $|g\rangle \leftrightarrow |u\rangle$ transition if the qubit is projected on the state $|g\rangle$. If the qubit is projected on the state $|e\rangle$, no fluorescence is observed. Many measurement shots can be accomplished due to the cyclic feature of the measurement (see also text).

qubit levels. The shelving readout now exploits the existence of these levels. Fig. 4.1 shows the principle idea of the shelving readout. After the state preparation with a laser pulse, the qubit is in a superposition of the ground and the excited state, $|\Psi_0\rangle = \alpha|g\rangle + \beta|e\rangle$. For efficient quantum computation, the coherence time of the qubit has to be as long as possible and thus the transition $|g\rangle \leftrightarrow |e\rangle$ is reduced (indicated by green dashed lines). We now take into account a third level $|u\rangle$ that is chosen such that the transition $|e\rangle \leftrightarrow |u\rangle$ is forbidden and the transition $|g\rangle \leftrightarrow |u\rangle$ is allowed.

For the state measurement, a photon that is resonant to the transition $|u\rangle \leftrightarrow |g\rangle$ is sent on the qubit, $\omega_{\text{ph}} = \omega_{\text{gu}}$. If the ion collapses to the eigenstate $|g\rangle$, the state is excited to $|u\rangle$ by the photon. $|u\rangle$ then decays back to $|g\rangle$ in a short time by sending out a photon with the same frequency as the incoming photon. This fluorescence signal can be detected with a single photodetector. If the ion collapses to the eigenstate $|e\rangle$, no fluorescence signal is observed—the state is shelved. Thus, in the experiment, one photon is detected for $|g\rangle$ and zero photons for $|e\rangle$.

Until now, we have only considered the ideal case where the single photodetector always clicks if one photon is sent out from the qubit. In real life, the photodetector has a certain efficiency η_d ; high-quality photodetectors have $\eta_d \approx 80\%$, but $\eta_d = 20\%$ is also possible. This means that only 20% of the photons produce a “click” in the detector. Though, the fluorescence process can be repeated many times until the qubit decays so that even the worst photodetector can detect a photon; this is the cyclic transition depicted in Fig. 4.1. At this point we note that the values of the photodetector efficiencies are only valid in the optical regime where photons have a sufficiently high energy. As already mentioned, the transition frequency of trapped ion qubits lies in the optical regime; we return to this subject later in this chapter.

To calculate the number of cycles that are required for an efficient state detection, we follow the method introduced in [94]. We assume that the detector has no “dark counts” meaning that it does not click if no photons are sent in from the qubit. Therefore, the probability of detecting state $|e\rangle$ when the qubit is in state $|e\rangle$ is $P_e(e) = 1$ (the probabilities $P_y(x)$ and the corresponding readout fidelity have been introduced in the introductory part of chapter 3). The efficiency of the detector is then given by the number of detected photons divided by the number of total photons, $\eta_d = n_d/N$. The probability that one photon is not detected by the detector then is $(1 - n_d/N)$. Accordingly, the probability that after N cycles

no photons are detected is

$$P_N(0) = \left(1 - \frac{n_d}{N}\right)^N \simeq e^{-n_d} = e^{-\eta_d N}. \quad (4.1)$$

The probability that at least one photon is detected, corresponding to detecting state $|g\rangle$ if the qubit was projected on $|g\rangle$, then is

$$P_g(g) = 1 - e^{-\eta_d N}. \quad (4.2)$$

Even for the worst efficiency of $\eta_d = 20\%$, after $N = 50$ cycles we get $P_g(g) \approx 99.995\%$ and thus a fidelity of

$$F = P_e(e) + P_g(g) - 1 = 99.995\%. \quad (4.3)$$

As already mentioned, this huge fidelity was also achieved in the experiment [17].

4.2 Evaluation of Shelving Ideas for SC qubits

The electron shelving readout results in a huge fidelity readout. Consequently, it would be convenient to achieve a shelving-like readout in SC qubits. For this purpose, we compare features of trapped ions with those of SC qubits and analyze if a shelving readout is possible in SC circuits.

Firstly, the shelving readout uses three levels to shelve the ground state on the upper state. Since we have many levels accessible in SC qubits, this third shelving level is easy to achieve.

Secondly, selection rules are required to assure that the upper state only decays to the ground state and not to the excited state. Like atoms, SC qubits have selection rules; however, they are more rudimental than the distinctive selection rules in atoms. At the degeneracy point, i.e. at the point where the energy dispersion has no slope, dipole transitions are only possible between two neighbouring qubit states [95]. Therefore, we have rudimental selection rules for the charge and the flux qubit at the degeneracy point. Since phase qubits have no degeneracy point, selection rules are not available in these systems.

Nevertheless, it is possible to engineer additional selection rules by placing the qubit inside a cavity. The spontaneous emission rate of a qubit (in general, a two-level state) is changed when it is coupled resonantly to a cavity; this is known as the *Purcell effect* [96]. The Purcell effect arises from the fact that the cavity has a reduced mode volume compared to the free space and thus prefers excitations that are resonant to these modes. We assume that no photons are inside the cavity in the beginning and that we are in the strong coupling regime. If the qubit is resonant with the cavity, the system is in an equally weighted superposition of a single photon state and the excited qubit state (see also Sec. 1.3.1). The decay rate of the qubit then is $(\gamma + \kappa)/2$, with γ being the decay rate of the excited state in absence of the cavity and $\kappa = \omega_r/Q$ the cavity decay rate (ω_r being the resonance frequency and Q the quality factor of the cavity) [22]. Consequently, the lifetime of the qubit is reduced to $T_{1,\kappa} = 2/(\gamma + \kappa)$. This means, the resonant transition in the presence of the cavity is “more allowed” than in the absence of the cavity. If the qubit is in the regime of large detuning, where $|\Delta| = |\omega_q - \omega_r| \gg g$, the decay rate reduces to $\gamma - (g/\Delta)^2 \kappa$. The lifetime of the qubit in the dispersive limit is increased which corresponds to forbidding the transition. In conclusion, selection rules are available in SC qubits and we can engineer additional ones that allow for a cyclic transition and an efficient state shelving.

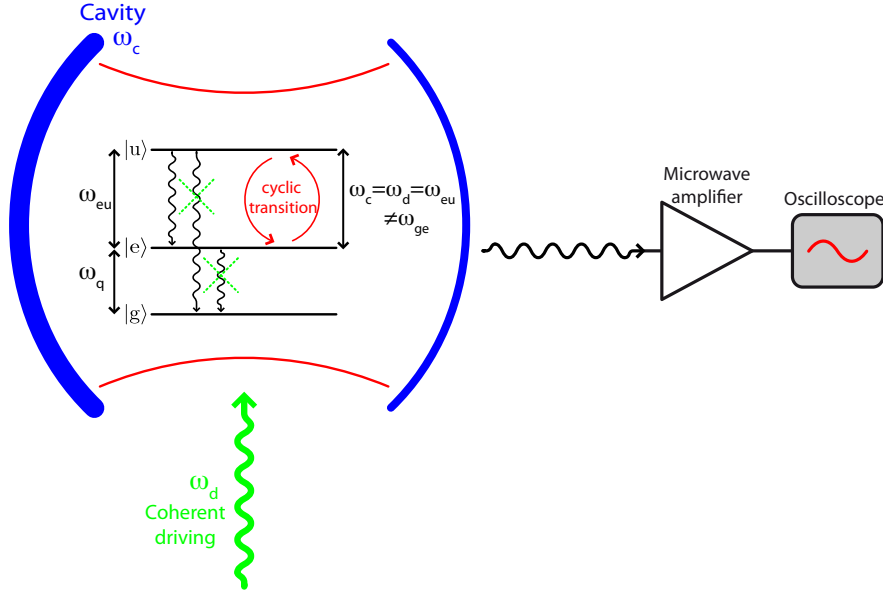


Figure 4.2: Sketch of the MSR. A three-level system, where the qubit is encoded in the first two levels, is placed inside a cavity with transition frequency ω_r . The cavity is coupled resonantly to the transition $|e\rangle \leftrightarrow |u\rangle$ with transition frequency ω_{eu} . In addition, this transition is driven with a coherent field ω_d . The transitions $|g\rangle \leftrightarrow |e\rangle$ and $|g\rangle \leftrightarrow |u\rangle$ are reduced (green dashed lines). If the qubit was projected on state $|e\rangle$, a mesoscopic field leaks out the cavity; the field then is amplified with a linear amplifier and measured with an oscilloscope. The ground state is associated with the vacuum field (see also text).

For the measurement of the fluorescence signal, a single photodetector is necessary. This is the main problem because the transition frequency of SC qubits lies in the microwave regime. Until now, single microwave photodetectors are not available in this regime. However, it is possible to detect coherent fields in the microwave regime efficiently by amplifying the field with a linear amplifier and measuring the amplified field with an oscilloscope. The linear amplifier has a certain floor noise of ~ 20 photons in the microwave regime ($\omega/2\pi \approx 10$ GHz) and at low temperatures (~ 10 K). Therefore, a field with a mean photon number above this floor noise is required (see App. E.3 for more information on the measurement with a linear amplifier and the floor noise). Therefore, we need a mesoscopic field instead of a single photon that is associated with one qubit state whereas the other state is associated with the vacuum. Since we already require a cavity for the selection rules, it would be convenient to also use this cavity for the creation of the field. In the following section, we therefore discuss how to build this required field.

4.3 The Idea of the Mesoscopic Shelving Readout

We now discuss the configuration of our readout proposal where a mesoscopic field is built inside a cavity if the qubit was projected on the excited state and a negligible field if the qubit was projected on the ground state. Since this readout is inspired from the electron shelving readout in trapped ion, we term it *Mesoscopic Shelving Readout* (MSR), although several new ideas are used in this technique.

Fig. 4.2 shows a sketch of the MSR. The qubit is built by the two states $|g\rangle$ and $|e\rangle$ with the transition frequency ω_q . We now take into account a third level $|u\rangle$. This level can be e.g. a superposition of the higher charge states (corresponding to $N = 2,3$) of the CPB qubit or the third level of the anharmonic oscillator potential of the phase qubit. The transition $|e\rangle \leftrightarrow |u\rangle$ with the transition frequency ω_{eu} is coupled resonantly with a strong coupling to an initially empty cavity mode (resonance frequency ω_r). Due to this coupling, the off-resonant transitions $|g\rangle \leftrightarrow |e\rangle$ and $|g\rangle \leftrightarrow |u\rangle$ are reduced by the Purcell effect; the resonant transition $|e\rangle \leftrightarrow |u\rangle$ is allowed. For flux and charge qubits, at the degeneracy point, the transition $|g\rangle \leftrightarrow |u\rangle$ is also forbidden by the selection rules in SC qubits.

The qubit state is prepared as for the dispersive readout that is described in Sec. 3.2. A field that is resonant to the qubit transition ω_q and thus off-resonant to the cavity drives the cavity axially. Due to second-order processes, this field can rotate the qubit. After the state preparation, the qubit will be in a superposition of the ground and the excited state,

$$|\Psi_0^q\rangle = \alpha |g\rangle + \beta |e\rangle. \quad (4.4)$$

The field that is used for the state preparation is now switched off and we can measure the qubit state.

Our measurement procedure can be described as follows. To start the measurement, a strong microwave driving field that is also resonant to the transition ω_{eu} is switched on; thus, we have $\omega_{eu} = \omega_r = \omega_d$. Since the driving field is also resonant to the cavity, it is important that the former is orthogonal with the cavity mode in order to minimize the crosstalk between them.

Let us assume that the qubit was projected on the excited state. The driving field then excites $|e\rangle$ to the upper state $|u\rangle$. This upper state interacts with the cavity via a JC interaction meaning that due to the strong coupling to the cavity, the state immediately decays back to $|e\rangle$ by sending a photon into the cavity (this corresponds to Rabi oscillations that fastly rotate the qubit to the ground state and the cavity excitation to one photon state). But now, the driving field, again, excites $|e\rangle$ to $|u\rangle$ and $|u\rangle$ sends out a second photon. This cyclic process is repeated until the driving field is switched off. The wavefunctions of the photons in the cavity superpose and so the driving has produced a coherent field in the cavity. Therefore, if the qubit was projected on $|e\rangle$, the cavity is populated with a large, mesoscopic field. Since the cavity has a certain loss, the field leaks out the cavity. Then, it is amplified with a linear amplifier and measured with an oscilloscope.

The qubit can also be projected on the ground state by the measurement. If this happens, the driving field does not excite the qubit and therewith, the cavity is left empty. Therefore, we expect no outgoing field for the ground state. However, the driving field scatters into the cavity via the qubit. This crosstalk between the driving and the cavity results in a population of the cavity even if the qubit was projected on the ground state. The produced field is negligibly small because the crosstalk is small.

In conclusion, we expect a large coherent field at the cavity output if the qubit was projected on the excited state and a small field if the qubit was projected on the ground state. Thus, the state of the qubit can be determined with a high efficiency.

4.4 Analytical Model of the Mesoscopic Shelving Readout

In this section we present the analytical model of the MSR. We firstly discuss the unitary dynamics of the system; then, we consider the dissipative model where the decay of the cavity is taken into account.

4.4.1 Unitary Dynamics of the Driven Superconducting Qubit

For the analytical model, we consider the two-level system, built by $|e\rangle$ and $|u\rangle$, which is coupled to the cavity and the driving field. The Hamiltonian that describes the system depicted in Fig. 4.2 reads

$$\begin{aligned} \mathcal{H}_{\text{MSR}} = & \hbar \frac{\omega_{\text{eu}}}{2} \sigma_{\text{eu}}^z + \hbar \omega_r a^\dagger a + \hbar \omega_d b^\dagger b + \hbar g_{\text{eu}} \left(\sigma_{\text{eu}}^+ a + \sigma_{\text{eu}}^- a^\dagger \right) \\ & + \hbar g_d \left(\sigma_{\text{eu}}^+ b + \sigma_{\text{eu}}^- b^\dagger \right) + \hbar g_{\text{ct}} \left(a^\dagger b + ab^\dagger \right). \end{aligned} \quad (4.5)$$

Here, b (b^\dagger) denotes the annihilation (creation) operator of the driving field with the transition frequency ω_d (this field will be treated classically later). a (a^\dagger) denotes the annihilation (creation) operator of the resonator field with the transition frequency ω_r . The operators $\sigma_{\text{eu}}^+ = |u\rangle\langle e|$, $\sigma_{\text{eu}}^- = |e\rangle\langle u|$, and $\sigma_{\text{eu}}^z = |u\rangle\langle u| - |e\rangle\langle e|$, describe the $|e\rangle \leftrightarrow |u\rangle$ transition with ω_{eu} being the transition frequency. We do not take into account the energy of the ground state due to the fact that the ground state is rotated neither by the driving field nor by the cavity (the qubit transition is off-resonant to both fields). The couplings that have to be taken into account are that of the resonator to the upper states of the SC qubit (coupling energy $\hbar g_{\text{eu}}$) and the driving field to the same qubit transition ($\hbar g_d$). Additionally, due to the presence of the qubit, a coupling of the driving field to the cavity field occurs. This *crossstalk* between the driving and the cavity is taken into account by the coupling $\hbar g_{\text{ct}}$. This term has to be deduced from the full network analysis of two cavities coupled to a qubit [97]. Since we assume the driving field to be orthogonal to the cavity, this term only arises from the presence of the qubit in the cavity; it is very small compared to g_{eu} , usually less than $10\% \cdot g_{\text{eu}}$.

We now choose the cavity and the driving field both resonant with the transition $|e\rangle \leftrightarrow |u\rangle$, $\omega_r = \omega_d = \omega_{\text{eu}}$, and assume the driving field to be a classical (=coherent) field with field amplitude $|\mu|$,

$$\begin{aligned} b & \rightarrow \mu e^{-i\omega_d t} = |\mu| e^{-i\omega_d t} e^{i\phi}, \\ b^\dagger & \rightarrow \mu^* e^{i\omega_d t} = |\mu| e^{i\omega_d t} e^{-i\phi}. \end{aligned} \quad (4.6)$$

The phase ϕ can be eliminated by applying the unitary transformation

$$U^\phi = \exp \left[i\phi \left(a^\dagger a + \frac{\sigma_{\text{eu}}^z}{2} \right) \right]. \quad (4.7)$$

Neglecting constant terms, the Hamiltonian now reads

$$\begin{aligned} \mathcal{H}'(t) = & \hbar \frac{\omega_{\text{eu}}}{2} \sigma_{\text{eu}}^z + \hbar \omega_r a^\dagger a + \hbar g_{\text{eu}} \left(\sigma_{\text{eu}}^+ a + \sigma_{\text{eu}}^- a^\dagger \right) \\ & + \hbar \Omega_d \left(e^{-i\omega_d t} \sigma_{\text{eu}}^+ + e^{i\omega_d t} \sigma_{\text{eu}}^- \right) + \hbar \Omega_{\text{ct}} \left(e^{-i\omega_d t} a^\dagger + e^{i\omega_d t} a \right), \end{aligned} \quad (4.8)$$

with the classical couplings $\Omega_d = g_d |\mu|$ and $\Omega_{\text{ct}} = g_{\text{ct}} |\mu|$.

We utilize the Hamiltonian in a reference frame rotating with the driving field frequency, via the transformation

$$U^d = \exp \left[-i\omega_d \left(a^\dagger a + \frac{\sigma_{\text{eu}}^z}{2} \right) t \right]. \quad (4.9)$$

In the rotating frame, we get

$$\mathcal{H}^d = \hbar\Omega_d \sigma_{\text{eu}}^x + \hbar g_{\text{eu}} \left(\sigma_{\text{eu}}^+ a + \sigma_{\text{eu}}^- a^\dagger \right) + \hbar\Omega_{\text{ct}} \left(a^\dagger + a \right), \quad (4.10)$$

with $\sigma_{\text{eu}}^x = \sigma_{\text{eu}}^+ + \sigma_{\text{eu}}^-$. Defining

$$\begin{aligned} \mathcal{H}^d &= \mathcal{H}_0 + \mathcal{H}^I, & \mathcal{H}_0 &= \hbar\Omega_d \sigma_{\text{eu}}^x, \\ \mathcal{H}^I &= \hbar g_{\text{eu}} \left(\sigma_{\text{eu}}^+ a + \sigma_{\text{eu}}^- a^\dagger \right) + \hbar\Omega_{\text{ct}} \left(a^\dagger + a \right), \end{aligned} \quad (4.11)$$

we derive the Hamiltonian in the interaction picture with the transformation $U^{\text{int}} = \exp \left[-\frac{i}{\hbar} \mathcal{H}_0 t \right]$

$$\begin{aligned} \mathcal{H}_{\text{int}} &= \hbar \frac{g_{\text{eu}}}{2} \left\{ (|+\rangle\langle +| - |-\rangle\langle -| - e^{2i\Omega_d t} |+\rangle\langle -| + e^{-2i\Omega_d t} |-\rangle\langle +|) a + \text{H.c.} \right\} \\ &\quad + \hbar\Omega_{\text{ct}} \left(a^\dagger + a \right), \end{aligned} \quad (4.12)$$

where the dressed states

$$|\pm\rangle = \frac{1}{\sqrt{2}} (|e\rangle \pm |g\rangle) \quad (4.13)$$

are the eigenstates of the σ^x -operator, with $\sigma_{\text{eu}}^x = |u\rangle\langle e| + |e\rangle\langle u| = |+\rangle\langle +| - |-\rangle\langle -|$. We now assume to be in the *strong driving regime*, where $\Omega_d \gg g_{\text{eu}}$. Under this condition, we can apply an RWA and eliminate the fast rotating terms $e^{\pm 2i\Omega_d t}$ in Eq. (4.12). The assumption of strong driving is essential for the existence of the analytical solutions of the model. Due to this approximation, the analytical calculation of the full time evolution, even in the dissipative model, is possible.

After neglecting the fast rotating terms, we obtain the final effective Hamiltonian of the driven two-level system in the interaction picture

$$\mathcal{H}_{\text{eff}} = \hbar \frac{g_{\text{eu}}}{2} (\sigma_{\text{eu}}^+ + \sigma_{\text{eu}}^-) (a + a^\dagger) + \hbar\Omega_{\text{ct}} (a^\dagger + a), \quad (4.14)$$

The first part of this Hamiltonian simultaneously realizes JC and anti-JC interactions in the RWA. It is interesting to note that even though we started with the JC interaction that rotates the qubit in Eq. (4.5), the qubit is no longer rotated by this effective Hamiltonian. The simultaneous JC and anti-JC interaction would, apart from the crosstalk-term Ω_{ct} , result in a coherent field state if the qubit was projected on the excited state by the measurement, and in a vacuum field state if it was projected on the ground state [98].

Initially, the qubit is in a superposition of the ground state $|g\rangle$ and the excited state $|e\rangle$, $|\Psi_0^q\rangle = \alpha |g\rangle + \beta |e\rangle$ (the upper state $|u\rangle$ is not populated in the beginning). The cavity does not contain any photons in the beginning and so the initial cavity field is $|\Psi_0^r\rangle = |0\rangle$. The initial state of the whole qubit-resonator system then reads

$$|\Psi_0\rangle = |\Psi_0^q\rangle \otimes |\Psi_0^r\rangle = (\alpha |g\rangle + \beta |e\rangle) \otimes |0\rangle = \alpha |g\rangle \otimes |0\rangle + \frac{\beta}{\sqrt{2}} (|+\rangle + |-\rangle) \otimes |0\rangle. \quad (4.15)$$

The evolved state after a time t can be determined with the time-evolution operator; since the effective Hamiltonian is time-independent in the rotating frame, the time evolution of the state then reads (cp. App. A.1)

$$|\Psi(t)\rangle = e^{-i\mathcal{H}_{\text{eff}}t/\hbar} |\Psi_0\rangle = \exp \left[-i \left(\frac{g_{\text{eu}}}{2} \sigma_{\text{eu}}^x + \Omega_{\text{ct}} \right) t a^\dagger - \text{H.c.} \right]. \quad (4.16)$$

As can be seen, the time evolution of the state is just given by the displacement operator

$$|\Psi(t)\rangle = \mathcal{D} \left[-i \left(\frac{g_{\text{eu}}}{2} \sigma_{\text{eu}}^x + \Omega_{\text{ct}} \right) t \right] |\Psi_0\rangle, \quad (4.17)$$

whereas the displacement operator creates a coherent state from the vacuum (see App. D.1 for more details on coherent states),

$$\mathcal{D}(\alpha) = e^{\alpha a^\dagger - \alpha^* a}, \quad |\alpha\rangle \equiv \mathcal{D}(\alpha) |0\rangle = e^{-\frac{|\alpha|^2}{2}} \sum_{n=0}^{\infty} \frac{\alpha^n}{\sqrt{n!}} |n\rangle. \quad (4.18)$$

Therefore, the evolved state reads

$$|\Psi(t)\rangle = \alpha |g\rangle |\bar{\nu}(t)\rangle + \frac{\beta}{\sqrt{2}} \left(|+\rangle |\bar{\eta}(t) + \bar{\nu}(t)\rangle + |-\rangle |-\bar{\eta}(t) + \bar{\nu}(t)\rangle \right). \quad (4.19)$$

Here, $|\pm\bar{\eta}(t)\rangle$ and $|\bar{\nu}(t)\rangle$ are coherent fields with field amplitudes

$$\bar{\eta}(t) = -i \frac{g_{\text{eu}}}{2} t \quad \text{and} \quad \bar{\nu}(t) = -i \Omega_{\text{ct}} t, \quad (4.20)$$

respectively.

This implies that a coherent field $|\pm\bar{\eta}(t) + \bar{\nu}(t)\rangle$ is created inside the cavity if the qubit was projected on the excited state $|e\rangle = (|+\rangle + |-\rangle)/\sqrt{2}$; the ground state $|g\rangle$ is associated only with the small crosstalk-field $|\bar{\nu}(t)\rangle$. So, we expect a large field for $|e\rangle$ and a small field for $|g\rangle$ inside the cavity. Even though we also expect a field for the ground state, this allows us to discriminate the two states of the qubit with a high efficiency because the crosstalk coupling Ω_{ct} is very small compared to the coupling of the qubit to the cavity, g_{eu} .

Let us finally calculate the mean number of photons inside the cavity for the two states $|g\rangle$ and $|e\rangle$. A coherent state $|\alpha\rangle$ is defined as an eigenstate of the annihilation operator a [99] with the eigenvalue α , $a|\alpha\rangle = \alpha|\alpha\rangle$. The mean photon number of a coherent state then is

$$N = \langle \hat{n} \rangle = \langle \alpha | a^\dagger a | \alpha \rangle = \alpha \alpha^* \langle \alpha | \alpha \rangle = |\alpha|^2. \quad (4.21)$$

Therefore, depending on the state on which the qubit was projected the mean photon number in the cavity will be

$$\bar{N}_e(t) = |\bar{\eta}(t)|^2 + |\bar{\nu}(t)|^2 = \left(\frac{g_{\text{eu}}^2}{4} + \Omega_{\text{ct}}^2 \right) t^2 \quad \text{for state } |e\rangle, \quad (4.22a)$$

$$\bar{N}_g(t) = |\bar{\nu}(t)|^2 = \Omega_{\text{ct}}^2 t^2 \quad \text{for state } |g\rangle. \quad (4.22b)$$

Thus, the photon number in the cavity grows with a quadratic power law. A more detailed discussion of the mean photon numbers is given in Sec 4.5.

4.4.2 Dissipative Model

Hitherto, we have only considered the unitary dynamics of the system, that is, we have only calculated the field inside the cavity without taking into account the decay of the cavity. However, we want to know the field that leaks out the cavity since this is the field that is measured. For this purpose, we include the dissipative coupling of the cavity to the environment. We assume to be in the limit of zero temperature, where the cavity cannot absorb a photon from the environment but only emit a photon into the environment. The system dynamics then can be described by the master equation for a damped harmonic oscillator (see App. A.3),

$$\dot{\rho}_{\text{QF}} = -\frac{i}{\hbar}[\mathcal{H}_{\text{eff}}, \rho_{\text{QF}}] - \frac{\kappa}{2}\mathcal{L}[a]\rho_{\text{QF}}, \quad (4.23)$$

with the cavity decay rate κ and the Liouvillian superoperator $\mathcal{L}[a]\rho_{\text{QF}}$

$$\mathcal{L}[a]\rho_{\text{QF}} = a^\dagger a \rho_{\text{QF}} - 2a \rho_{\text{QF}} a^\dagger + \rho_{\text{QF}} a^\dagger a. \quad (4.24)$$

Following the methods introduced in [100], we firstly introduce the decomposition of the density matrix in field and qubit parts,

$$\begin{aligned} \rho_{\text{QF}} = & |+\rangle\langle +| \otimes \rho_{1F}(t) + |-\rangle\langle -| \otimes \rho_{2F}(t) + |+\rangle\langle -| \otimes \rho_{3F}(t) \\ & + |-\rangle\langle +| \otimes \rho_{4F}(t) + |g\rangle\langle +| \otimes \rho_{5F}(t) + |g\rangle\langle -| \otimes \rho_{6F}(t) \\ & + |+\rangle\langle g| \otimes \rho_{7F}(t) + |-\rangle\langle g| \otimes \rho_{8F}(t) + |g\rangle\langle g| \otimes \rho_{9F}(t). \end{aligned} \quad (4.25)$$

where the field parts of the density matrix, $\rho_{iF}(t)$ ($i = 1, \dots, 9$), are defined as

$$\begin{aligned} \rho_{1F}(t) &= \langle +|\rho_{\text{QF}}(t)|+\rangle, & \rho_{2F}(t) &= \langle -|\rho_{\text{QF}}(t)|-\rangle, \\ \rho_{3F}(t) &= \langle +|\rho_{\text{QF}}(t)|-\rangle, & \rho_{4F}(t) &= \langle -|\rho_{\text{QF}}(t)|+\rangle, \\ \rho_{5F}(t) &= \langle g|\rho_{\text{QF}}(t)|+\rangle, & \rho_{6F}(t) &= \langle g|\rho_{\text{QF}}(t)|-\rangle, \\ \rho_{7F}(t) &= \langle +|\rho_{\text{QF}}(t)|g\rangle, & \rho_{8F}(t) &= \langle -|\rho_{\text{QF}}(t)|g\rangle, \\ \rho_{9F}(t) &= \langle g|\rho_{\text{QF}}(t)|g\rangle. \end{aligned} \quad (4.26)$$

With this decomposition, we can write the density operator in its matrix representation in the $\{|+\rangle, |-\rangle, |g\rangle\}$ basis, where $|+\rangle = (1, 0, 0)^T$, $|-\rangle = (0, 1, 0)^T$, and $|g\rangle = (0, 0, 1)^T$. The density operator in the matrix representation in this basis then reads

$$\rho_{\text{QF}} = \begin{pmatrix} \rho_{1F}(t) & \rho_{3F}(t) & \rho_{7F}(t) \\ \rho_{4F}(t) & \rho_{2F}(t) & \rho_{8F}(t) \\ \rho_{5F}(t) & \rho_{6F}(t) & \rho_{9F}(t) \end{pmatrix}. \quad (4.27)$$

This means, $\rho_{1F}(t)$, $\rho_{2F}(t)$, and $\rho_{9F}(t)$ are diagonal in the $\{|+\rangle, |-\rangle, |g\rangle\}$ basis, whereas the other field parts are off-diagonal and thus can be removed by tracing over the qubit variables (we will come back to this matrix representation in the next section).

Initially, the SC qubit is in the state $|\Psi_0\rangle \equiv |\Psi_0^q\rangle \otimes |\Psi_0^r\rangle = (\alpha|g\rangle + \beta|e\rangle) \otimes |0\rangle$, whereas $|\Psi_0^q\rangle = \alpha|g\rangle + \beta|e\rangle$ and $|\Psi_0^r\rangle = |0\rangle$ are the initial states of the qubit and the resonator, respectively, and $|e\rangle = (|+\rangle + |-\rangle)/\sqrt{2}$. This means that the initial qubit–field density operator is $\rho_{\text{QF}}(0) = |\Psi_0^q\rangle\langle\Psi_0^q| \otimes |0\rangle\langle 0|$. Thus, the initial field density operators $\rho_{iF}(0)$ are

$$\rho_{iF}(0) = |0\rangle\langle 0| \cdot \begin{cases} \frac{|\beta|^2}{2}, & i = 1, 2, 3, 4, \\ \frac{\beta^* \alpha}{\sqrt{2}}, & i = 5, 6, \\ \frac{\beta \alpha^*}{\sqrt{2}}, & i = 7, 8, \\ |\alpha|^2, & i = 9. \end{cases} \quad (4.28)$$

With the decomposition of the density operator (4.25), the master equation (4.23) can be rewritten to the following set of differential equations for the field operators $\rho_{iF}(t)$ (see App. D.3 for more details),

$$\begin{aligned}
\dot{\rho}_{1,2F} &= \mp i \frac{g_{\text{eu}}}{2} [a^\dagger + a, \rho_{1,2F}] - i\Omega_{\text{ct}} [a^\dagger + a, \rho_{1,2F}] + \mathcal{L}[a]\rho_{1,2F}, \\
\dot{\rho}_{3,4F} &= \mp i \frac{g_{\text{eu}}}{2} \{a^\dagger + a, \rho_{3,4F}\} - i\Omega_{\text{ct}} [a^\dagger + a, \rho_{3,4F}] + \mathcal{L}[a]\rho_{3,4F}, \\
\dot{\rho}_{5,6F} &= \pm i \frac{g_{\text{eu}}}{2} \rho_{5,6F}(a^\dagger + a) - i\Omega_{\text{ct}} [a^\dagger + a, \rho_{5,6F}] + \mathcal{L}[a]\rho_{5,6F}, \\
\dot{\rho}_{7,8F} &= \mp i \frac{g_{\text{eu}}}{2} (a^\dagger + a)\rho_{7,8F} - i\Omega_{\text{ct}} [a^\dagger + a, \rho_{7,8F}] + \mathcal{L}[a]\rho_{7,8F}, \\
\dot{\rho}_{9F} &= -i\Omega_{\text{ct}} [a^\dagger + a, \rho_{9F}] + \mathcal{L}[a]\rho_{9F},
\end{aligned} \tag{4.29}$$

where braces $\{\dots\}$ denote the anticommutator symbol.

We now map these equations onto a set of partial differential equations for the characteristic functions of the Wigner probability distribution (see App. D.2 for more information on the characteristic functions); they are the expectation value of the displacement operator,

$$\chi_i(\xi, t) = \text{Tr}_F [\rho_{iF}(t) \mathcal{D}(\xi)], \tag{4.30}$$

where $\mathcal{D}(\xi)$, again, denotes the displacement operator (ξ being a complex variable),

$$\mathcal{D}(\xi) = e^{\xi a^\dagger - \xi^* a}. \tag{4.31}$$

The functions $\chi_i(\xi, t)$ do not fulfill all conditions for quantum characteristic functions, however, they are continuous and square-integrable [100]. With this transformation, the partial differential equations for the density matrices (4.29) that depend on the creation and annihilation operator a and a^\dagger , respectively, change into a set of partial differential equations that depend on the complex variable ξ . Even though, an analytical expression of the expectation value of the field density operators can be found, the full solution for the operator equations (4.29) is not possible. This problem can be overcome by using characteristic functions.

As shown in App. D.3, the transformed partial differential equations read:

$$\begin{aligned}
\frac{\partial \chi_{1,2}}{\partial t} &= \left[\pm i \frac{g_{\text{eu}}}{2} \left(1 \pm \frac{2\Omega_{\text{ct}}}{g_{\text{eu}}} \right) (\xi + \xi^*) + \Lambda(\mathcal{L}[a]) \right] \chi_{1,2}, \\
\frac{\partial \chi_{3,4}}{\partial t} &= \left[i\Omega_{\text{ct}} (\xi + \xi^*) \mp i g_{\text{eu}} \left(\frac{\partial}{\partial \xi} - \frac{\partial}{\partial \xi^*} \right) + \Lambda(\mathcal{L}[a]) \right] \chi_{3,4}, \\
\frac{\partial \chi_{5,6}}{\partial t} &= \left[\pm i \frac{g_{\text{eu}}}{4} \left(1 \pm \frac{4\Omega_{\text{ct}}}{g_{\text{eu}}} \right) (\xi + \xi^*) \pm i \frac{g_{\text{eu}}}{2} \left(\frac{\partial}{\partial \xi} - \frac{\partial}{\partial \xi^*} \right) + \Lambda(\mathcal{L}[a]) \right] \chi_{5,6}, \\
\frac{\partial \chi_{7,8}}{\partial t} &= \left[\pm i \frac{g_{\text{eu}}}{4} \left(1 \pm \frac{4\Omega_{\text{ct}}}{g_{\text{eu}}} \right) (\xi + \xi^*) \mp i \frac{g_{\text{eu}}}{2} \left(\frac{\partial}{\partial \xi} - \frac{\partial}{\partial \xi^*} \right) + \Lambda(\mathcal{L}[a]) \right] \chi_{7,8}, \\
\frac{\partial \chi_9}{\partial t} &= \left[i\Omega_{\text{ct}} (\xi + \xi^*) + \Lambda(\mathcal{L}[a]) \right] \chi_9,
\end{aligned} \tag{4.32}$$

with $\Lambda(\mathcal{L}[a])\chi_i$ ($i = 1, \dots, 9$) being the transformed Liouvillian superoperator,

$$\Lambda(\mathcal{L}[a])\chi_i \equiv \text{Tr}_F [\mathcal{L}[a] \rho_{iF}(t) \mathcal{D}(\xi)] = -\frac{\kappa}{2} |\xi|^2 \chi_i - \frac{\kappa}{2} \left(\xi \frac{\partial}{\partial \xi} + \xi^* \frac{\partial}{\partial \xi^*} \right) \chi_i. \tag{4.33}$$

Rewriting the complex variable ξ in terms of its real and imaginary part, $\xi = x + iy$, we get $x = (\xi + \xi^*)/2$ and $y = (\xi - \xi^*)/2$. The derivatives with respect to ξ and ξ^* then can be written as

$$\frac{\partial}{\partial \xi} = \frac{1}{2} \left(\frac{\partial}{\partial x} - i \frac{\partial}{\partial y} \right), \quad \text{and} \quad \frac{\partial}{\partial \xi^*} = \frac{1}{2} \left(\frac{\partial}{\partial x} + i \frac{\partial}{\partial y} \right). \quad (4.34)$$

Eqs. (4.32) then become

$$\begin{aligned} \frac{\partial \chi_{1,2}}{\partial t} &= \left[\pm i g_{\text{eu}} \left(1 \pm \frac{2\Omega_{\text{ct}}}{g_{\text{eu}}} \right) x + \Lambda(\mathcal{L}[a]) \right] \chi_{1,2}, \\ \frac{\partial \chi_{3,4}}{\partial t} &= \left[2i\Omega_{\text{ct}} x \mp g_{\text{eu}} \frac{\partial}{\partial y} + \Lambda(\mathcal{L}[a]) \right] \chi_{3,4}, \\ \frac{\partial \chi_{5,6}}{\partial t} &= \left[\pm i \frac{g_{\text{eu}}}{2} \left(1 \pm \frac{4\Omega_{\text{ct}}}{g_{\text{eu}}} \right) x \pm \frac{g_{\text{eu}}}{2} \frac{\partial}{\partial y} + \Lambda(\mathcal{L}[a]) \right] \chi_{5,6}, \\ \frac{\partial \chi_{7,8}}{\partial t} &= \left[\pm i \frac{g_{\text{eu}}}{2} \left(1 \pm \frac{4\Omega_{\text{ct}}}{g_{\text{eu}}} \right) x \mp \frac{g_{\text{eu}}}{2} \frac{\partial}{\partial y} + \Lambda(\mathcal{L}[a]) \right] \chi_{7,8}, \\ \frac{\partial \chi_9}{\partial t} &= \left[i\Omega_{\text{ct}} x + \Lambda(\mathcal{L}[a]) \right] \chi_9, \end{aligned} \quad (4.35)$$

where $\Lambda(\mathcal{L}[a])\chi_i$ ($i = 1, \dots, 9$) has changed as

$$\Lambda(\mathcal{L}[a])\chi_i = -\frac{\kappa}{2} (x^2 + y^2) \chi_i - \frac{\kappa}{2} \left(x \frac{\partial}{\partial x} + y \frac{\partial}{\partial y} \right) \chi_i. \quad (4.36)$$

With a shift of the variable y ($\tilde{y} = y \pm 2g_{\text{eu}}/\kappa$ in the equations for $\chi_{3,4}$ and $\bar{y} = y \pm g_{\text{eu}}/\kappa$ in the equations for $\chi_{5,6}$ and $\chi_{7,8}$) we obtain

$$\begin{aligned} \frac{\partial \chi_{1,2}}{\partial t} + \frac{\kappa}{2} \left(x \frac{\partial}{\partial x} + y \frac{\partial}{\partial y} \right) \chi_{1,2} &= \left(x [C'_1(x) \pm C'_2(x)] + y D'_1(y) \right) \chi_{1,2}, \\ \frac{\partial \chi_{3,4}}{\partial t} + \frac{\kappa}{2} \left(x \frac{\partial}{\partial x} + \tilde{y} \frac{\partial}{\partial \tilde{y}} \right) \chi_{3,4} &= \left(x C'_1(x) + \tilde{y} [D'_1(\tilde{y}) \pm D'_2(\tilde{y})] \right) \chi_{3,4}, \\ \frac{\partial \chi_{5,6}}{\partial t} + \frac{\kappa}{2} \left(x \frac{\partial}{\partial x} + \bar{y} \frac{\partial}{\partial \bar{y}} \right) \chi_{5,6} &= \left(x [C'_1(x) \pm C'_3(x)] + \bar{y} [D'_1(\bar{y}) \mp D'_3(\bar{y})] \right) \chi_{5,6}, \\ \frac{\partial \chi_{7,8}}{\partial t} + \frac{\kappa}{2} \left(x \frac{\partial}{\partial x} + \bar{y} \frac{\partial}{\partial \bar{y}} \right) \chi_{7,8} &= \left(x [C'_1(x) \pm C'_3(x)] + \bar{y} [D'_1(\bar{y}) \pm D'_3(\bar{y})] \right) \chi_{7,8}, \\ \frac{\partial \chi_9}{\partial t} + \frac{\kappa}{2} \left(x \frac{\partial}{\partial x} + y \frac{\partial}{\partial y} \right) \chi_9 &= \left(x C'_1(x) + y D'_1(y) \right) \chi_9, \end{aligned} \quad (4.37)$$

where we have introduced the derivatives of the functions

$$\begin{aligned} C_1(x) &= -\frac{\kappa}{4} x^2 + 2i\Omega_{\text{ct}} x, & C_2(x) &= i g_{\text{eu}} x, & C_3(x) &= \frac{i}{2} g_{\text{eu}} x, \\ D_1(y) &= -\frac{\kappa}{4} y^2, & D_2(y) &= 2g_{\text{eu}} \left(y - \frac{g_{\text{eu}}}{\kappa} \ln(y) \right), & D_3(y) &= g_{\text{eu}} \left(y - \frac{g_{\text{eu}}}{2\kappa} \ln(y) \right). \end{aligned} \quad (4.38)$$

The partial differential equations in Eq. 4.37 generally read

$$\frac{\partial \chi_i}{\partial t} + \frac{\kappa}{2} \left(x \frac{\partial}{\partial x} + \check{y} \frac{\partial}{\partial \check{y}} \right) \chi_i = \left(x H'_i(x) + \check{y} G'_i(\check{y}) \right) \chi_i, \quad (4.39)$$

where $H_i(x)$ and $G_i(\check{y})$ denote the functions on the right-hand side of Eq. (4.37) and

$$\check{y} = \begin{cases} y, & i = 1,2,9, \\ \tilde{y}, & i = 3,4, \\ \bar{y}, & i = 5,6,7,8. \end{cases} \quad (4.40)$$

We solve Eq. (4.39) by using the *method of characteristics* as shown in [99]¹. In this method, the partial differential equation is reduced to a system of ordinary differential equations on a hypersurface that is given by the characteristic curves. The ordinary differential equations then can be integrated easily from an initial function. On the characteristic curves, we have

$$dt = \frac{2 dx}{\kappa x} = \frac{2 d\check{y}}{\kappa \check{y}}, \quad (4.41a)$$

$$\frac{dx}{x} = \frac{d\check{y}}{\check{y}}, \quad (4.41b)$$

$$\frac{2 d\check{y}}{\kappa \check{y}} = \frac{d\chi_i}{(xH'_i(x) + \check{y}G'_i(\check{y})) \chi_i}. \quad (4.41c)$$

Eq. (4.41a) and results in the following equations that hold on a characteristic curve,

$$K_1 = xe^{-\kappa t/2}, \quad K_2 = \check{y}e^{-\kappa t/2}. \quad (4.42)$$

From Eqs. (4.41b) and (4.41c), we obtain

$$\frac{d\chi_i}{\chi_i} = \frac{2}{\kappa} \cdot \frac{(xH'_i(x) + \check{y}G'_i(\check{y}))}{\check{y}} d\check{y} = \frac{2}{\kappa} (H'_i(x)dx + G'_i(\check{y})d\check{y}). \quad (4.43)$$

This equation can easily be solved by integration,

$$\chi_i = K_3 \exp\left(\frac{2}{\kappa} [H_i(x) + G_i(\check{y})]\right). \quad (4.44)$$

A general solution of the partial differential equation can be obtained by making the integration constant K_3 a function of K_1 and K_2 , $K_3 = F_i(K_1, K_2)$. This function follows from the initial functions at $t = 0$ that are associated with the initial density matrices in Eq. (4.28) and given by

$$\chi_{i,0}(x,y) \equiv \chi_i(x,y,0) = \zeta_i \exp\left(-\frac{x^2 + y^2}{2}\right), \quad \text{with} \quad \zeta_i = \begin{cases} \frac{|\beta|^2}{2}, & i = 1,2,3,4, \\ \frac{\beta^* \alpha}{\sqrt{2}}, & i = 5,6, \\ \frac{\beta \alpha^*}{\sqrt{2}}, & i = 7,8, \\ |\alpha|^2, & i = 9. \end{cases} \quad (4.45)$$

Since

$$\chi_{i,0}(x,y) = F_i(x,y) \exp\left(\frac{2}{\kappa} [H_i(x) + G_i(\check{y})]\right), \quad (4.46)$$

¹We will not go into detail on the mathematical theory of the characteristic curves since it would go beyond the scope of this thesis. Note that the characteristics have nothing to do with the characteristic functions of the Wigner probability function, χ_i .

we finally arrive at

$$K_3 = F_i(xe^{-\kappa t/2}, \check{y}e^{-\kappa t/2}) = \frac{\chi_{i,0}(xe^{-\kappa t/2}, \check{y}e^{-\kappa t/2})}{\exp\left(\frac{2}{\kappa} [H_i(xe^{-\kappa t/2}) + G_i(\check{y}e^{-\kappa t/2})]\right)}. \quad (4.47)$$

Using Eqs. (4.44) and (4.47), the time-dependent solutions of the characteristic functions then read

$$\begin{aligned} \chi_{1,2}(x,y,t) &= \frac{|\beta|^2}{2} \exp\left(-\frac{x^2+y^2}{2} \pm 2i\frac{g_{\text{eu}}}{\kappa} \left[1 \pm \frac{2\Omega_{\text{ct}}}{g_{\text{eu}}}\right] x \left[1 - e^{-\kappa t/2}\right]\right), \\ \chi_{3,4}(x,y,t) &= \frac{|\beta|^2}{2} f_1(t) \exp\left(-\frac{x^2+y^2}{2} \mp \frac{2ig_{\text{eu}}}{\kappa} \left[iy \mp \frac{2\Omega_{\text{ct}}}{g_{\text{eu}}}\right] x \left[1 - e^{-\kappa t/2}\right]\right), \\ \chi_{5,6}(x,y,t) &= \frac{\beta^*\alpha}{\sqrt{2}} f_2(t) \exp\left(-\frac{x^2+y^2}{2} \pm i\frac{g_{\text{eu}}}{\kappa} \left[\left(1 \pm \frac{4\Omega_{\text{ct}}}{g_{\text{eu}}}\right) x + iy\right] \left[1 - e^{-\kappa t/2}\right]\right), \\ \chi_{7,8}(x,y,t) &= \frac{\beta\alpha^*}{\sqrt{2}} f_2(t) \exp\left(-\frac{x^2+y^2}{2} \pm i\frac{g_{\text{eu}}}{\kappa} \left[\left(1 \pm \frac{4\Omega_{\text{ct}}}{g_{\text{eu}}}\right) x - iy\right] \left[1 - e^{-\kappa t/2}\right]\right), \\ \chi_9(x,y,t) &= |\alpha|^2 \exp\left(-\frac{x^2+y^2}{2} + \frac{4i\Omega_{\text{ct}}}{\kappa} x \left[1 - e^{-\kappa t/2}\right]\right), \end{aligned} \quad (4.48)$$

where we have introduced the fast-decreasing functions

$$\begin{aligned} f_1(t) &= \exp\left(-2\frac{g_{\text{eu}}^2}{\kappa} t + \frac{4g_{\text{eu}}^2}{\kappa^2} \left[1 - e^{-\kappa t/2}\right]\right), \\ f_2(t) &= \exp\left(-\frac{g_{\text{eu}}^2}{2\kappa} t + \frac{g_{\text{eu}}^2}{\kappa^2} \left[1 - e^{-\kappa t/2}\right]\right). \end{aligned} \quad (4.49)$$

Rewriting Eqs. (4.48) in terms of the complex variable $\xi = x + iy$ and the time-dependent functions

$$\begin{aligned} \eta(t) &= -i\frac{g_{\text{eu}}}{\kappa} \left[1 - e^{-\kappa t/2}\right], \\ \nu(t) &= -2i\frac{\Omega_{\text{ct}}}{\kappa} \left[1 - e^{-\kappa t/2}\right], \end{aligned} \quad (4.50)$$

results in the following form of the characteristic functions,

$$\begin{aligned} \chi_{1,2}(\xi,t) &= \frac{|\beta|^2}{2} \exp\left(-\frac{|\xi|^2}{2} + \xi \{\pm\eta^*(t) + \nu^*(t)\} - \xi^* \{\pm\eta(t) + \nu(t)\}\right), \\ \chi_{3,4}(\xi,t) &= \frac{|\beta|^2}{2} f_1(t) \exp\left(-\frac{|\xi|^2}{2} + \xi \{\mp\eta^*(t) + \nu^*(t)\} - \xi^* \{\pm\eta(t) + \nu(t)\}\right), \\ \chi_{5,6}(\xi,t) &= \frac{\beta^*\alpha}{\sqrt{2}} f_2(t) \exp\left(-\frac{|\xi|^2}{2} + \xi \{\pm\eta^*(t) + \nu^*(t)\} - \xi^* \nu(t)\right), \\ \chi_{7,8}(\xi,t) &= \frac{\beta\alpha^*}{\sqrt{2}} f_2(t) \exp\left(-\frac{|\xi|^2}{2} + \xi \nu^*(t) - \xi^* \{\pm\eta(t) + \nu(t)\}\right), \\ \chi_9(\xi,t) &= |\alpha|^2 \exp\left(-\frac{|\xi|^2}{2} + \xi \nu^*(t) - \xi^* \nu(t)\right). \end{aligned} \quad (4.51)$$

The corresponding density operators $\rho_{iF}(t)$ follow from the Fourier transform of the characteristic functions

$$W_i(\delta, \delta^*) = \frac{1}{\pi^2} \int d^2\xi \chi_i(\xi,t) \exp(\delta\xi^* - \delta^*\xi). \quad (4.52)$$

Here, δ is a complex variable and $\int d^2\chi = \int_{-\infty}^{\infty} dx \int_{-\infty}^{\infty} dy$ denotes a two-dimensional integral over the complex plane. These are two-dimensional Fourier transforms of the characteristic functions $\chi_i(\xi, t)$ that define the Wigner probability distributions $W_i(\delta, \delta^*)$. The relation of the Wigner function and the density operator is given by [99]

$$W_i(\delta, \delta^*) = \frac{2}{\pi^2} \int d^2\gamma \langle \delta + \gamma | \rho_{iF}(t) | \delta - \gamma \rangle \exp(\delta^* \gamma - \delta \gamma^*), \quad (4.53)$$

where γ and δ again denote complex variables (note that this γ has nothing to do with a decay rate). The calculation of the transformation is given in App D.3.3. The density operators then are

$$\begin{aligned} \rho_{1F}(t) &= \frac{|\beta|^2}{2} |\eta(t) + \nu(t)\rangle \langle \eta(t) + \nu(t)|, \\ \rho_{2F}(t) &= \frac{|\beta|^2}{2} |-\eta(t) + \nu(t)\rangle \langle -\eta(t) + \nu(t)|, \\ \rho_{3F}(t) &= \frac{|\beta|^2}{2} \frac{f_1(t)}{e^{-2|\eta(t)|^2}} |\eta(t) + \nu(t)\rangle \langle -\eta(t) + \nu(t)|, \\ \rho_{4F}(t) &= \frac{|\beta|^2}{2} \frac{f_1(t)}{e^{-2|\eta(t)|^2}} |-\eta(t) + \nu(t)\rangle \langle \eta(t) + \nu(t)|, \\ \rho_{5F}(t) &= \frac{\beta^* \alpha}{\sqrt{2}} \frac{f_2(t)}{e^{-|\eta(t)|^2/2}} |\nu(t)\rangle \langle \eta(t) + \nu(t)|, \\ \rho_{6F}(t) &= \frac{\beta^* \alpha}{\sqrt{2}} \frac{f_2(t)}{e^{-|\eta(t)|^2/2}} |\nu(t)\rangle \langle -\eta(t) + \nu(t)|, \\ \rho_{7F}(t) &= \frac{\beta \alpha^*}{\sqrt{2}} \frac{f_2(t)}{e^{-|\eta(t)|^2/2}} |\eta(t) + \nu(t)\rangle \langle \nu(t)|, \\ \rho_{8F}(t) &= \frac{\beta \alpha^*}{\sqrt{2}} \frac{f_2(t)}{e^{-|\eta(t)|^2/2}} |-\eta(t) + \nu(t)\rangle \langle \nu(t)|, \\ \rho_{9F}(t) &= |\alpha|^2 |\nu(t)\rangle \langle \nu(t)|. \end{aligned} \quad (4.54)$$

Therewith, the full density matrix of the qubit–resonator system that was introduced in Eq. (4.25) reads

$$\begin{aligned} \rho_{\text{QF}} &= \frac{|\beta|^2}{2} \left(|+\rangle \langle +| \otimes |\eta(t) + \nu(t)\rangle \langle \eta(t) + \nu(t)| \right. \\ &\quad \left. + |-\rangle \langle -| \otimes |-\eta(t) + \nu(t)\rangle \langle -\eta(t) + \nu(t)| \right) \\ &+ \frac{|\beta|^2}{2} \frac{f_1(t)}{e^{-|\eta(t)|^2}} \left(|+\rangle \langle -| \otimes |\eta(t) + \nu(t)\rangle \langle -\eta(t) + \nu(t)| \right. \\ &\quad \left. + |-\rangle \langle +| \otimes |-\eta(t) + \nu(t)\rangle \langle \eta(t) + \nu(t)| \right) \\ &+ \frac{\beta^* \alpha}{\sqrt{2}} \frac{f_2(t)}{e^{-|\eta(t)|^2/2}} \left(|g\rangle \langle +| \otimes |\nu(t)\rangle \langle \eta(t) + \nu(t)| \right. \\ &\quad \left. + |g\rangle \langle -| \otimes |\eta(t) + \nu(t)\rangle \langle \nu(t)| \right) \\ &+ \frac{\beta \alpha^*}{\sqrt{2}} \frac{f_2(t)}{e^{-|\eta(t)|^2/2}} \left(|+\rangle \langle g| \otimes |\eta(t) + \nu(t)\rangle \langle \nu(t)| \right. \\ &\quad \left. + |-\rangle \langle g| \otimes |-\eta(t) + \nu(t)\rangle \langle \nu(t)| \right) \\ &+ |\alpha|^2 |g\rangle \langle g| \otimes |\nu(t)\rangle \langle \nu(t)|. \end{aligned} \quad (4.55)$$

At the end of this section, we now discuss the two limiting cases for short ($\kappa t \ll 1$) and long ($\kappa t \gg 1$) timescales for a better understanding of the dynamics. In the next section, we then focus on the state measurement. In the limit of short times, the density matrix is just that of the unitary dynamics that were derived in the previous section. For $\kappa t \ll 1$, we can expand the $[1 - e^{-\kappa t/2}]$ -term in $\eta(t)$ and $\nu(t)$ until the first order in t , and that in $f_1(t)$ and $f_2(t)$ until the second order (since they contain the exponential function of this term), by using the Taylor expansion $1 - e^{-\kappa t/2} \approx \kappa t/2 - \kappa^2 t^2/8$. Therefore, for short times, the functions are approximated by

$$\begin{aligned}\eta(t) &\approx -i\frac{g_{\text{eu}}}{2}t = \bar{\eta}(t), & \nu(t) &\approx -i\Omega_{\text{ct}}t = \bar{\nu}(t), \\ f_1(t) &\approx e^{-2|\bar{\eta}(t)|^2}, & f_2(t) &\approx e^{-|\bar{\eta}(t)|^2/2},\end{aligned}\quad (4.56)$$

so that the state of the qubit–field system is well described by

$$|\Psi(t)\rangle = \alpha|g\rangle|\bar{\nu}(t)\rangle + \frac{\beta}{\sqrt{2}}\left(|+\rangle|\bar{\eta}(t) + \bar{\nu}(t)\rangle + |-\rangle|-\bar{\eta}(t) + \bar{\nu}(t)\rangle\right). \quad (4.57)$$

This means, in the limit of short times the unitary dynamics dominate and the field grows with the same power-law fashion as for the calculations where the cavity decay was not taken into account (cp. Sec. 4.4.1).

On the other hand, the steady state ($t \rightarrow \infty$) of the qubit–field system is the mixed state

$$\begin{aligned}\rho_{\text{QF}}^{\text{ss}} &= |\alpha|^2|g\rangle\langle g| \otimes |\nu^{\text{ss}}\rangle\langle \nu^{\text{ss}}| + \frac{|\beta|^2}{2}\left(|+\rangle\langle +| \otimes |\eta^{\text{ss}} + \nu^{\text{ss}}\rangle\langle \eta^{\text{ss}} + \nu^{\text{ss}}| \right. \\ &\quad \left. + |-\rangle\langle -| \otimes |-\eta^{\text{ss}} + \nu^{\text{ss}}\rangle\langle -\eta^{\text{ss}} + \nu^{\text{ss}}|\right),\end{aligned}\quad (4.58)$$

with

$$\eta^{\text{ss}} = -\frac{ig_{\text{eu}}}{\kappa}, \quad \text{and} \quad \nu^{\text{ss}} = -\frac{2i\Omega_{\text{ct}}}{\kappa}. \quad (4.59)$$

For long times, the field inside the cavity saturates at the steady state values η^{ss} and ν^{ss} . This has its origin in the fact that the cavity population by the driving field is in an equilibrium with the cavity loss after a time $t \approx 1/\kappa$.

4.5 State Detection

We now again focus on the measurement of the qubit state. In the MSR, the excited state is associated with a large cavity field and the ground state with a small field that originates from the crosstalk. In this section, we discuss this coherent field that is generated in the cavity by the driving and the corresponding outleaking field. We firstly focus on the analytical model; then, we present numerical simulations in the intermediate driving regime including all dissipative dynamics and off-resonant couplings of the system.

4.5.1 Cavity Field

We obtain the reduced density operator for the cavity field by tracing over the qubit variables $\{|+\rangle, |-\rangle, |g\rangle\}$

$$\begin{aligned}\rho_F(t) &= \text{Tr}_Q[\rho_{\text{QF}}(t)] = \rho_{1F}(t) + \rho_{2F}(t) + \rho_{9F}(t) = |\alpha|^2|\nu(t)\rangle\langle \nu(t)| \\ &\quad + \frac{|\beta|^2}{2}\left(|\eta(t) + \nu(t)\rangle\langle \eta(t) + \nu(t)| + |-\eta(t) + \nu(t)\rangle\langle -\eta(t) + \nu(t)|\right),\end{aligned}\quad (4.60)$$

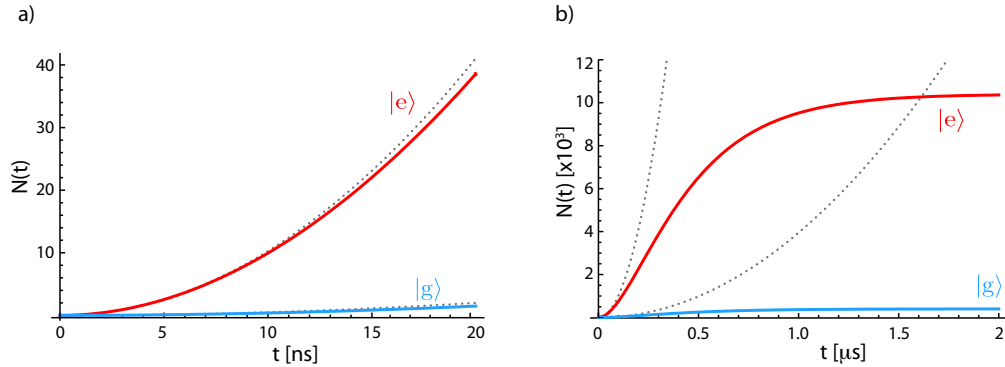


Figure 4.3: Mean photon number in the cavity for the ground state (blue) and the excited state (red) (for $g_{\text{eu}}/2\pi = 100$ MHz, $\kappa/2\pi = 1$ MHz and $\Omega_{\text{ct}}/2\pi = 10$ MHz). The grey dotted lines show the mean photon number of the unitary dynamics. (a) and (b) only differ in the timescale that is plotted.

which is always a mixed state. This partial trace can be made clear by considering the matrix representation of the density operator in Eq. (4.27) and taking the trace of this matrix, which just corresponds to summing up the diagonal elements.

The dynamics associated with the excited state is given by $\rho_{1F}(t)$ and $\rho_{2F}(t)$; the dynamics of the ground state is described by $\rho_{9F}(t)$. Again, we expect a large field $|\pm\eta(t) + \nu(t)\rangle$ for state $|e\rangle$ and the small crosstalk-field $|\nu(t)\rangle$ for state $|g\rangle$ ($\eta(t)$ and $\nu(t)$ have been introduced in Eq. (4.50)).

The mean photon number inside the cavity is now given by the trace over the field variables,

$$\langle \hat{n} \rangle = \text{Tr}_F \left[a^\dagger a \rho_F(t) \right]. \quad (4.61)$$

Thus, the mean photon number of the cavity field mapped on the excited state $|e\rangle$ or the ground state $|g\rangle$, $N_e(t)$ and $N_g(t)$, respectively, is

$$N_e(t) = |\eta(t)|^2 + |\nu(t)|^2 = \left(\frac{g_{\text{eu}}}{\kappa} + \frac{2\Omega_{\text{ct}}}{\kappa} \right)^2 \left[1 - e^{-\kappa t/2} \right]^2 \quad \text{for state } |e\rangle, \quad (4.62a)$$

$$N_g(t) = |\nu(t)|^2 = \frac{4\Omega_{\text{ct}}^2}{\kappa^2} \left[1 - e^{-\kappa t/2} \right]^2 \quad \text{for state } |g\rangle, \quad (4.62b)$$

Fig. 4.3 shows the time-dependent mean photon number for the two qubit states using the realistic parameters $g_{\text{eu}}/2\pi = 100$ MHz and $\kappa/2\pi = 1$ MHz and an overestimated crosstalk coupling of $\Omega_{\text{ct}}/2\pi = 10$ MHz (in the experiment, this coupling lies around 2 MHz [97]). Also shown are the photon numbers for the unitary dynamics, where the cavity does not decay (grey dotted lines). Firstly, we observe that for short times (Fig. 4.3(a)) the curves for the dissipative and the unitary dynamics are nearly the same whereas the curves of the dissipative dynamics converge to a constant value for larger times (Fig. 4.3(b)). This is exactly the behaviour that we have discussed in the end of the previous section. As can be seen clearly, $N_e(t)$, which is the mean number of photons in the cavity when the qubit was projected on the excited state, differs significantly from $N_g(t)$ even for the overestimated crosstalk coupling of 10 MHz. Thus, the number of photons for state $|e\rangle$ and $|g\rangle$ can be distinguished easily. $N_e(t)$ grows very fast in time and saturates in the steady state, which is reached after ~ 1 μs (Fig. 4.3(b)).

The number of photons in the steady state for $|e\rangle$ is $N_e^{\text{ss}} = \left(\frac{g_{\text{eu}}}{\kappa} + \frac{2\Omega_{\text{ct}}}{\kappa}\right)^2 \approx 10^4$ photons; this is a huge number of photons. The steady state field that is built inside the cavity for the ground state has $N_g^{\text{ss}} = \frac{4\Omega_{\text{ct}}^2}{\kappa^2} = 400$ photons inside the cavity. So, the field for the ground state is two order of magnitudes smaller than the field for the excited state. This means, we can neglect the crosstalk field from now on. Moreover, the negligence of the crosstalk field just corresponds to shifting the number of photons by $-\frac{4\Omega_{\text{ct}}^2}{\kappa^2} [1 - e^{-\kappa t/2}]^2 \equiv -N_g(t)$ since this crosstalk term appears in both the ground and excited state mean photon number.

Neglecting the crosstalk, the mean number of photons for the state $|e\rangle$ and $|g\rangle$ now are

$$N_e(t) = N_e^{\text{ss}} [1 - e^{-\kappa t/2}]^2 \quad \text{for state } |e\rangle, \quad \text{with } N_e^{\text{ss}} = \left(\frac{g_{\text{eu}}}{\kappa}\right)^2, \quad (4.63a)$$

$$N_g(t) = 0 \quad \text{for state } |g\rangle. \quad (4.63b)$$

Until now, we have only considered the photons inside the cavity; however, we cannot build the measurement devices in the cavity. Hence, we want to know the field that leaks out the cavity. The photons bounce against the resonator walls with the rate κ , so the mean transmitted photon rate for the excited state is

$$\dot{N}_{\text{out}}^{\text{ss}} = \kappa \cdot N_e(t) = \kappa \cdot N_e^{\text{ss}} [1 - e^{-\kappa t/2}]^2 = \frac{g_{\text{eu}}^2}{\kappa} [1 - e^{-\kappa t/2}]^2. \quad (4.64)$$

The steady state value of this leakage field is $\dot{N}_{\text{out}}^{\text{ss}} = g_{\text{eu}}^2/\kappa = 6 \cdot 10^4 \frac{\text{photons}}{\mu\text{s}}$. This is an amazingly huge photon rate in a time of only $1 \mu\text{s}$. Though, as we show in Sec. 4.6, we do not have to reach the steady state for a high-fidelity state measurement.

4.5.2 Numerical Simulations in the Intermediate Regime

An interesting question is, if our assumptions are also valid in a more realistic picture. So, is a large field also achievable in the intermediate driving regime? For the solutions with an intermediate driving strength, where $\Omega_d \approx g_{\text{eu}}$, that include the decay of the qubit and off-resonant couplings, numerical simulations are required. For the numerical simulations we choose the charge qubit in different regimes as a proof of principle. The Hamiltonian of the CPB coupled to the cavity and the driving field can be calculated according to Sec. 2.4 but now N_g^{ac} also contains the classical driving field with amplitude V and frequency ω_d ,

$$N_g^{\text{ac}} = N_{\text{rms}}^{(2)} (a^\dagger + a) + \frac{C_g V}{2e} \cos(\omega_d t), \quad (4.65)$$

with $N_{\text{rms}}^{(2)} = \frac{C_g}{2e} \sqrt{\frac{\hbar\omega_r}{2C_r}}$. The final Hamiltonian then also includes a term

$$(N_g^{\text{ac}})^2 = N_{\text{rms}}^{(2)} \frac{C_g V}{e} \cos(\omega_d t) (a^\dagger + a) + \left[N_{\text{rms}}^{(2)} (a^\dagger + a) \right]^2 + \left[\frac{C_g V}{2e} \cos(\omega_d t) \right]^2. \quad (4.66)$$

The last two terms can be neglected since they are an artifact from the calculation of the voltage-biased JJ (cp. App. B.3.3). The first term represents the crosstalk between the driving and the cavity; therewith, the classical crosstalk-coupling for the charge qubit is

$$\hbar\Omega_{\text{ct}} = N_{\text{rms}}^{(2)} \frac{C_g V}{e} = \frac{C_g^2 V}{2e^2} \sqrt{\frac{\hbar\omega_r}{2C_r}}. \quad (4.67)$$

Following the steps in Sec. 2.4, this results in the generalized JC Hamiltonian of the complete system,

$$\begin{aligned} \mathcal{H}_{\text{sys}} = & \hbar \sum_k \omega_k |k\rangle\langle k| + \hbar \omega_r a^\dagger a + \hbar \sum_k g_{k,k+1} |k\rangle\langle k+1| \left(a^\dagger + a \right) \\ & + \hbar \sum_k \Omega_{k,k+1} \cos(\omega_d t) |k\rangle\langle k+1| + \hbar \Omega_{\text{ct}} \left(e^{-i\omega_d t} a^\dagger + e^{i\omega_d t} a \right), \end{aligned} \quad (4.68)$$

where we have only taken into account the coupling between two neighbouring states. Note that the RWA has not been applied on this Hamiltonian. Thus, the numerical simulations also take into account fast rotating terms. The coupling energies are

$$\hbar g_{k,k+1} = \hbar g_{k+1,k} = 2E_c N_{\text{rms}}^{(2)} \left| \langle k | \hat{N} | k+1 \rangle \right|, \quad (4.69a)$$

$$\hbar \Omega_{k,k+1} = \hbar \Omega_{k+1,k} = E_c \frac{C_g V}{e} \left| \langle k | \hat{N} | k+1 \rangle \right|, \quad (4.69b)$$

corresponding to g_{eu} and Ω_d in the previous sections, respectively. The first two levels of the Hamiltonian (4.68) build the qubit states ($|0\rangle \equiv |g\rangle$ and $|1\rangle \equiv |e\rangle$), whereas the auxiliary level coincides with the third level ($|2\rangle \equiv |u\rangle$).

In the numerical simulations, we now take into account the (non-radiative) decay of the SC qubit. The evolution of the total density matrix of the system obeys the master equation

$$\dot{\rho} = -\frac{i}{\hbar} [\mathcal{H}_{\text{sys}}, \rho] - \frac{\kappa}{2} \mathcal{L}[a]\rho - \Gamma \rho. \quad (4.70)$$

The dissipator $\Gamma \rho$ written in the basis of the uncoupled qubit states reads

$$(\Gamma \rho)_{kl} = \frac{\gamma_k + \gamma_l}{2} \rho_{kl} - (1 - \delta_{kl}) \gamma_\phi \rho_{kl} - \delta_{kl} \sum_j \rho_{jj} \gamma_{j \rightarrow k}, \quad (4.71)$$

with $\gamma_k = \sum_{k \neq l} \gamma_{k \rightarrow l}$ being the total decay rate of the state $|k\rangle$ and γ_ϕ the total dephasing rate which we choose to be equal for all qubit levels.

In the simulations, we solve the master equation (4.70) numerically in a subspace of four qubit and n_{ph} photon states. We assume the decay rates of these four qubit levels to be

$$\begin{aligned} \gamma_0 &= \gamma_g = 0, \\ \gamma_1 &= \gamma_e = \gamma_{e \rightarrow g} \equiv \gamma, \\ \gamma_2 &= \gamma_u = \gamma_{u \rightarrow e} = 10\gamma, \\ \gamma_3 &= \gamma_{3 \rightarrow u} + \gamma_{3 \rightarrow e} + \gamma_{3 \rightarrow g} = 100\gamma, \end{aligned} \quad (4.72)$$

where the selection rules for the charge qubit at the degeneracy point have been taken into account by setting $\gamma_{u \rightarrow g} = 0$. The relaxation and dephasing rate of the qubit, $\gamma = T_1^{-1}$ and $\gamma_\phi = T_2^{-1}$, respectively, are obtained from the experiment [11; 25; 101] and depend on the ratio E_J/E_c .

Fig. 4.4 shows the numerical solutions of the master equation in a charge-phase regime ($E_J/E_c = 1$, 4.4(a)) and an intermediate transmon regime ($E_J/E_c = 8$, 4.4(b)). For the comparison of the different solutions, the figure shows the analytical solutions for the unitary dynamics $\bar{N}^e(t)$ (black dashed lines) and dissipative dynamics of the cavity $N^e(t)$ (blue dashed lines) with the corresponding numerical data in the intermediate regime (red bold lines and

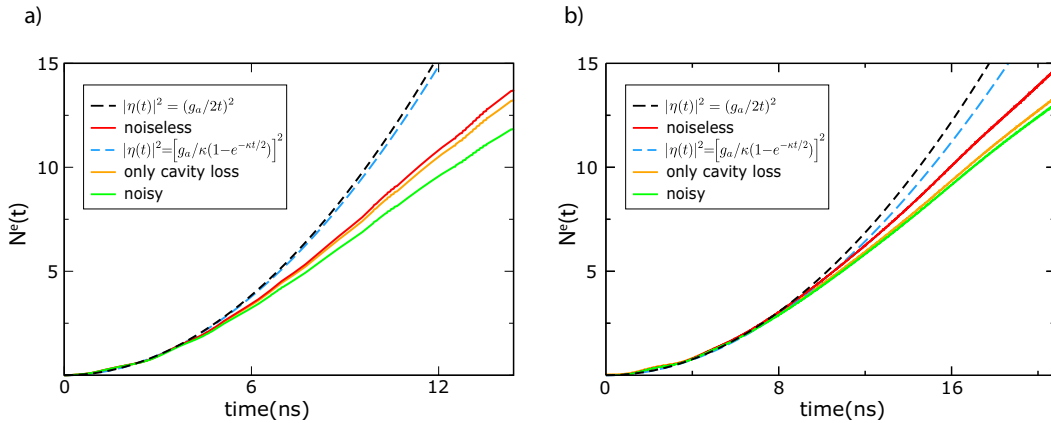


Figure 4.4: Numerical simulations of the mean cavity photon number for $|e\rangle$. Shown are the analytical solutions $\bar{N}^e(t)$ (black dashed line) and $N^e(t)$ (blue dashed line) with the corresponding numerical data (red bold line and orange bold line, respectively) and the full “noisy” dynamics (green line). Simulations have been done considering four levels of the CPB and n_{ph} photon number states. In both pictures, we use $g_{\text{eu}}/2\pi = 150$ MHz, $\kappa/2\pi = 1.6$ MHz, $\Omega_{\text{d}} = 5g_{\text{eu}}$, and $\Omega_{\text{ct}}/2\pi = 10$ MHz. **(a)** shows the simulations in the intermediate transmon regime, with $E_{\text{J}} = 8E_{\text{c}} = h \cdot 20$ GHz, $T_1 = 2 \mu\text{s}$, $T_2 = 1 \mu\text{s}$, and $n_{\text{ph}} = 22$, and **(b)** in the charge-phase regime, with $E_{\text{J}} = E_{\text{c}} = h \cdot 10$ GHz, $T_1 = 5 \mu\text{s}$, $T_2 = 500$ ns, and $n_{\text{ph}} = 25$ (see also text).

orange bold lines, respectively). The green lines show the full dynamics including the decay of the qubit. Due to the truncation of the Hilbert space to n_{ph} photon states, the curves show small oscillations which are more distinctive for the smaller photon state number of $n_{\text{ph}} = 22$ in (a) compared to $n_{\text{ph}} = 25$ in (b). Thus, we expect that this oscillations disappear when more photon states are taken into account.

In the figures, it is possible to notice a slower increase with respect to the analytical models of the mean cavity photon number even in the numerically noiseless case (red lines) due to the intermediate driving strength and the presence of more qubit levels and off-resonant couplings. The effect of the qubit decoherence (green curves) leads to a further reduction of the mean cavity photon number growth. However, even for this realistic model, if the qubit is projected on the excited state $|e\rangle$, significant photon numbers can be achieved within very short measurement times. Thus, we expect a large measurement fidelity even in the intermediate, noisy case.

Finally, we remark that we expect similar results for the flux qubit since it also couples strongly to the cavity field and has selection rules at the degeneracy point. For the phase qubit, the mean photon number might be further reduced due to the absence of selection rules. The MSR cannot be directly applied in a deep transmon regime ($E_{\text{J}}/E_{\text{c}} \gg 1$) due to the non-sufficient anharmonicity between the levels. In fact, in this case the measurement field will be almost resonant also with the qubit, thus inducing unwanted transitions. Nevertheless, modified measurement schemes exploiting a different auxiliary level or a two-photon measurement drive can in principle be engineered.

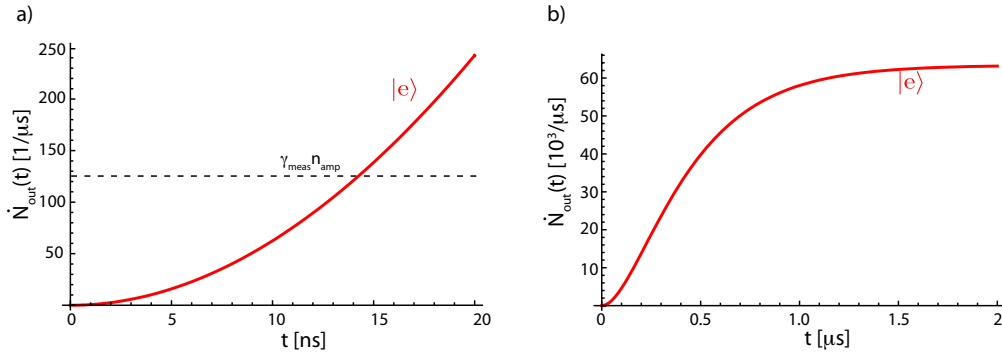


Figure 4.5: Mean transmitted photon rate for the excited state. In (a) the rate is illustrated for small times, (b) shows the steady state behaviour. The dashed line in (a) marks the photon rate that has to be exceeded for an efficient measurement (SNR > 1).

4.6 Characterization of the Mesoscopic Shelving Readout

For the characterization of the MSR, we want to know the measurement time that assures a good SNR, the fidelity of our readout technique, and the QND character.

4.6.1 Signal-to-Noise Ratio

For the measurement, the coherent field that leaks out the cavity (Eq. (4.64)) is increased with a linear amplifier and then measured with an oscilloscope.

As discussed in App. E.3, a linear amplifier has a certain floor noise that is given by the ratio of the thermal energy of the amplifier noise ($T_N = 10$ K) and the energy of the measured photons ($\omega_r/2\pi \approx 10$ GHz) [22],

$$n_{\text{amp}} = \frac{k_B T_N}{\hbar \omega_r} \approx 20. \quad (4.73)$$

We define the SNR after a time t as the outcoming cavity photon rate divided by the photon number of the amplifier and the measurement bandwidth γ_{meas} ,

$$\text{SNR}(t) = \frac{\kappa \cdot N_e(t)}{\gamma_{\text{meas}} \cdot n_{\text{amp}}}. \quad (4.74)$$

The device that sets the measurement bandwidth in the experiment is that with the narrowest bandwidth; thus, we have $\gamma_{\text{meas}} = \kappa$. The photon number of the outleaking field can be discriminated against the noise of the linear amplifier if $\text{SNR} > 1$.

To achieve this ratio, the measurement time τ has to be

$$\tau \geq -\frac{2}{\kappa} \ln \left(1 - \sqrt{\frac{\gamma_{\text{amp}} \cdot n_{\text{amp}}}{\kappa \cdot N_e^{\text{ss}}}} \right) = -\frac{2}{\kappa} \ln \left(1 - \sqrt{\frac{n_{\text{amp}}}{N_e^{\text{ss}}}} \right) \approx 15 \text{ ns}. \quad (4.75)$$

This time is very short, much shorter than the coherence time ($T_1 \approx 2$ μ s) of the qubit.

Fig. 4.5 shows the photon rate that leaks out the cavity for the excited state, again, for short (Fig. 4.5(a)) and long timescales (Fig. 4.5(b)). The dashed line marks the photon rate where the SNR exceeds 1. As can be seen, the outcoming field grows rapidly for short times thus giving the possibility of a very fast high-fidelity readout.

4.6.2 Single-Shot Readout Fidelity

Let us now have a look at the fidelity of the readout. According to [6] (see also Eq. (3.1)), the fidelity can be defined as

$$F = P_e(e) + P_g(g) - 1 = 1 - (P_g(e) + P_e(g)), \quad (4.76)$$

where $P_y(x)$ is the conditional probability to measure the state y when the qubit was projected on $|x\rangle$ by the measurement ($\{x,y\} = \{g,e\}$). Let τ be the measurement time which assures a sufficient SNR. For the qubit measurement, a coherent field state with a *mean* photon number $N_e(\tau)$ ($N_g(\tau)$) in a time $1/\kappa$ is measured. However, this does not mean that we also measure $N_e(\tau)$ ($N_g(\tau)$). As shown in App. D.1, a coherent field has a Poissonian distribution of the photon number. Thus, the probability of detecting n_d photons when the mean photon number is N is

$$P(n_d) = e^{-N} \frac{N^{n_d}}{n_d!}, \quad \text{with} \quad \sum_{n_d=0}^{\infty} P(n_d) = 1. \quad (4.77)$$

For example, for a mean photon number of $N \approx 20$, the probability of measuring N photons is only 8.9%; this probability decreases with increasing photon number. We define $n_{th}(\tau)$ as the threshold photon number which allows us to distinguish between the qubit states; it depends on the measurement time since the mean number of photons for the qubit states and therewith the threshold photon number grows in time. Then, the probability $P_e(e)$ is the sum of the coefficients of all Fock states in the coherent state that have photon numbers above the threshold, when the qubit was projected on $|e\rangle$,

$$P_e(e) = \sum_{n=n_{th}}^{\infty} e^{-N_e(\tau)} \frac{(N_e(\tau))^{n_{th}}}{n_{th}!} = 1 - \sum_{n=0}^{n_{th}} e^{-N_e(\tau)} \frac{(N_e(\tau))^n}{n!}. \quad (4.78)$$

where $N_e(t)$ is given by Eq. (4.62) (we take the crosstalk into account to show that we get a high fidelity even with this term). Consistently, for $P_g(g)$ we have to consider the photon numbers below the threshold value and the qubit in the ground state,

$$P_g(g) = \sum_{n=0}^{n_{th}} e^{-N_g(\tau)} \frac{(N_g(\tau))^n}{n!}. \quad (4.79)$$

Let us now assume that we measure for a time of $\tau = 25$ ns, where $N_e(\tau) \approx 60$ photons and $N_g(\tau) \approx 2$ photons. We set the threshold photon number of this measurement time to a totally overestimated value of $n_{th} = 40^2$. This means that any output with a photon number above $n_{th} = 40$ will be associated with the excited state and any output with lower photon number with the ground state. The sums in Eq. (4.78) and (4.79) can easily be calculated with e.g. Mathematica. The probabilities for these values then are

$$\begin{aligned} P_e(e) &= 99.5\%, \\ P_g(g) &= 100\%. \end{aligned} \quad \Rightarrow \quad F = 99.5\%. \quad (4.80)$$

This means, even for the unrealistically high value of $n_{th} = 40$ (and also an overestimated value for the crosstalk, $\Omega_{ct} = 10$ MHz) and a very short measurement time of $\tau = 25$ ns, the fidelity of the readout scheme approaches unity.

²The linear amplifier has a Gaussian photon number distribution; the probability that the noise of the linear amplifier is above 40 in one single shot is below 10^{-6} , see also App. E.3.

In conclusion, we have an SNR of the measurement device that exceeds 1 for a time of 15 ns. The fidelity of the readout scheme is above 99% for a measurement time of ~ 25 ns. For more realistic parameters of Ω_{ct} and N_{th} , the measurement time is even decreased. To our knowledge, this is the first readout technique for SC qubits that prognoses a fidelity that approaches unity in such a short measurement time and only for a single shot. Since the proposed measurement-scheme gives good knowledge of the qubit state in z -direction, it will lead to a full tomography of the wavefunction with a following rotation of the driving field in the x - and y -direction.

4.6.3 Quantum Non-Demolition Character

Finally, we analyze the QND character of the MSR. For this, we firstly calculate the commutator of the qubit Hamiltonian and the interaction Hamiltonian of the qubit with the readout device. If this commutator is zero, we have a QND measurement. The interaction Hamiltonian is given by (see also Eq. (4.5))

$$\mathcal{H}_{\text{meas}} = \hbar g_{\text{eu}} \left(\sigma_{\text{eu}}^+ a + \sigma_{\text{eu}}^- a^\dagger \right) + \hbar \Omega \left(\sigma_{\text{eu}}^+ + \sigma_{\text{eu}}^- \right). \quad (4.81)$$

The qubit Hamiltonian, as usual, reads

$$\mathcal{H}_q = \frac{\hbar}{2} \omega_q \sigma^z, \quad (4.82)$$

with $\sigma^z = |e\rangle\langle e| - |g\rangle\langle g|$. Therewith, the commutator is

$$[\mathcal{H}_q, \mathcal{H}_{\text{meas}}] = \frac{\hbar^2}{2} \omega_q \left[g_{\text{eu}} \left(\sigma_{\text{eu}}^- a^\dagger - \sigma_{\text{eu}}^+ a \right) + \Omega_d \left(\sigma_{\text{eu}}^- - \sigma_{\text{eu}}^+ \right) \right] \neq 0. \quad (4.83)$$

This means, strictly speaking, we do not have a QND measurement.

However, let us discuss the interaction Hamiltonian (4.81) in detail. The interaction Hamiltonian only acts on the excited state of the qubit. This means, if the qubit was projected on $|g\rangle$ by the measurement, it remains in $|g\rangle$. Thus, for the ground state, the MSR is a QND measurement and can be used for state preparation and additional state readout.

Now, what happens if the qubit was projected on the excited state? After the driving field is switched off, the system will either be in state $|e\rangle$ or $|u\rangle$. An additional measurement of the system will then again result in the measurement of a large coherent field. Since we associate the measurement of such a large field with the excited state, we again have the output $|e\rangle$. Thus, the system can be used for additional measurements. Nevertheless, if the system is in either state $|u\rangle$ or $|e\rangle$ after the measurement, the qubit state $|e\rangle$ is destroyed since we get Rabi oscillations between the cavity and the $|e\rangle \leftrightarrow |u\rangle$ transition, that is, the state switches between $|e\rangle$ and $|u\rangle$. Thus, the excited state is not available for additional quantum computational processes which means that for the excited state the MSR is not a QND measurement in the usual sense.

Therefore, we call the readout scheme a ‘‘QND-like measurement’’ since additional measurements are possible but the state of the qubit itself is destroyed and thus the measurement in general cannot be used for state preparation or additional computational processes.

Chapter 5

Conclusion and Outlook

The goal of this work was to develop a novel readout technique for superconducting (SC) qubits that breaks the limit of 99% fidelity. Current readout fidelities in SC qubits are not large enough for the requirements of quantum computation.

Therefore, we have theoretically introduced this new high-fidelity readout technique that profits from circuit quantum electrodynamics (QED) and is inspired from the electron shelving readout in trapped ions. We have shown how this Mesoscopic Shelving Readout (MSR) can be used to determine the state of an SC qubit by using a third qubit level such that the transition of the upper two states is coupled resonantly to a microwave cavity and driven (also resonantly) with a strong microwave driving field. The MSR can be used to readout phase, flux, and charge qubits, whereas the readout scheme is especially suitable for the two last ones since only in charge and flux qubits, selection rules are available at the degeneracy point.

We have presented the analytical model of the MSR, where we have used techniques from quantum optics to describe the system. The dissipative dynamics predicts a mesoscopic field outside the cavity for one qubit state and a small, negligible field for the other qubit state. Additional numerical simulations confirm that a large field is also achievable in the intermediate driving regime. As we have demonstrated, the readout may result in an amazingly high fidelity above 99% in a fast ($\tau \approx 25$ ns) single-shot QND-like qubit measurement. This represents a big step forward for the implementation of quantum computation in solid-state architectures.

All the technical requirements for the MSR are experimentally feasible. Therefore, future experiments can lead to an unprecedented high measurement fidelity of SC qubits. Thus, the next step is the experimental realization of this new readout technique. Further theoretical works will have to study how this readout technique can be used in standard and one-way quantum computation in different architectures, that is, for example how we can use the MSR for efficient quantum error correction.

Appendix A

Details on Quantum Mechanics

We use many tools of quantum mechanics in this thesis. Consequently, we recapitulate some of these in this part of the appendix.

A.1 Time Evolution in Quantum Mechanics

We firstly have a short review on the time evolution on quantum mechanical states and operators in the three mainly used pictures in quantum mechanics, the *Schrödinger*, the *Heisenberg* and the *interaction picture*; the latter one is also known as the *Dirac picture*.

A.1.1 Schrödinger Picture

In the Schrödinger picture, the state of the system evolves in time whereas the operators (corresponding to observables) are constant in time. The time evolution of the wavefunction $|\Psi_S(t)\rangle$ is given by the Schrödinger equation

$$\frac{\partial}{\partial t} |\Psi_S(t)\rangle = -\frac{i}{\hbar} \mathcal{H}_S(t) |\Psi_S(t)\rangle, \quad (\text{A.1})$$

where we use the notation $\mathcal{H}_{S(\text{H/int})}$ ($|\Psi_{S(\text{H/int})}\rangle$) for the Hamiltonian (wavefunction) in the Schrödinger (Heisenberg/interaction) picture, respectively. This equation is generally solved by

$$|\Psi_S(t, t_0)\rangle = U(t, t_0) |\Psi_S(t_0)\rangle, \quad \text{with } U(t_0, t_0) = \mathbf{1}, \quad (\text{A.2})$$

where $|\Psi_S(t_0)\rangle$ is the initial wavefunction and $U(t, t_0)$ is a unitary operator, the so-called *time-evolution operator* which also obeys the Schrödinger equation¹,

$$\frac{\partial}{\partial t} U(t, t_0) = -\frac{i}{\hbar} \mathcal{H}_S(t) U(t, t_0). \quad (\text{A.3})$$

From now on, we set $t_0 = 0$. The previous equation can be integrated (see e.g. [16]) which yields the time-evolution operator

$$U(t) = T e^{-\frac{i}{\hbar} \int_0^t \mathcal{H}_S(t') dt'}, \quad (\text{A.4})$$

¹Strictly speaking, this equation is an operator equation which is equivalent to the Schrödinger equation.

with T being the *time ordering operator*. If we assume that the $\mathcal{H}_S(t')$ at different times commute with each other, we do not have to take into account T .

For a time-independent (\equiv conservative) Hamiltonian, Eq. (A.4) then reduces to

$$U(t) = e^{-i\mathcal{H}_S t/\hbar}. \quad (\text{A.5})$$

A.1.2 Heisenberg Picture

In the Heisenberg picture, operators are time-dependent and the state vectors are time-independent. The states in the Heisenberg picture are given by $|\Psi_H\rangle = U^\dagger(t) |\Psi_S(t)\rangle = |\Psi_S(0)\rangle$; an operator (and also the Hamiltonian) O_S therefore changes as

$$O_H(t) = U^\dagger(t) O_S U(t). \quad (\text{A.6})$$

Inserting this expression in the Schrödinger equation (A.3) yields the equation that corresponds to the Schrödinger equation in the Heisenberg picture—the *Heisenberg equation*—for the operator O_H

$$i\hbar \frac{dO_H(t)}{dt} = [O_H(t), \mathcal{H}_H(t)] + i\hbar \frac{\partial O_H(t)}{\partial t}. \quad (\text{A.7})$$

Mostly, O_H is not explicitly time-dependent and therefore the last part in the Heisenberg equation disappears.

A.1.3 Interaction Picture

In the interaction picture both the wavefunction and the operators are time-dependent. This picture is mainly used if one part of the Hamiltonian is time-dependent and the other not. The Hamiltonian $\mathcal{H}_S(t)$ firstly is divided into two hermitian parts,

$$\mathcal{H}_S(t) = \mathcal{H}_S^0 + \mathcal{H}_S'(t), \quad (\text{A.8})$$

where \mathcal{H}_S^0 is the time-independent and $\mathcal{H}_S'(t)$ is the time-dependent part of the Hamiltonian. To solve the Schrödinger equation (A.3), the unitary operator $U(t)$ is also divided in a time-independent and a time-dependent part²,

$$U(t) = U_0(t) U'(t), \quad (\text{A.9})$$

$$\text{with } \dot{U}_0(t) = -\frac{i}{\hbar} \mathcal{H}_0 U_0(t) \quad \text{and} \quad \dot{U}'(t) = -\frac{i}{\hbar} \mathcal{H}_{\text{int}}(t) U'(t), \quad (\text{A.10})$$

which immediately gives us

$$U_0(t) = e^{-i\mathcal{H}_0 t/\hbar}. \quad (\text{A.11})$$

The state vector in the interaction picture is now given by

$$|\Psi_{\text{int}}(t)\rangle = U_0^\dagger(t) |\Psi_S(t)\rangle = U'(t) |\Psi_S(t_0)\rangle. \quad (\text{A.12})$$

The operators transform as

$$O_{\text{int}}(t) = U_0^\dagger(t) O_S U_0(t), \quad (\text{A.13})$$

²We only differentiate between U_0 and U' in this part of the thesis since we always write the explicit form of the transformations in the other parts.

whereas the Hamiltonian in the interaction picture itself is

$$\mathcal{H}_{\text{int}}(t) = i\hbar\dot{U}_0^\dagger(t)U_0(t) + U_0^\dagger(t)\mathcal{H}_S U_0(t) = U_0^\dagger(t)\mathcal{H}'_S U_0(t). \quad (\text{A.14})$$

The operators, again, evolve according to the Heisenberg equation (A.7), but now only the time-independent part of the Hamiltonian, \mathcal{H}_0 , appears in the commutator.

In most cases, the Hamiltonian in the interaction picture, $\mathcal{H}_{\text{int}}(t)$, is time-independent. In this case, one can easily derive the state evolution,

$$|\Psi_{\text{int}}(t)\rangle = e^{i\mathcal{H}_{\text{int}}t/\hbar}|\Psi_S(0)\rangle. \quad (\text{A.15})$$

The Heisenberg and the interaction picture are especially suitable in cases where the dynamics of a system that is coupled to an environment shall be analyzed (see Sec. 1.2.2). This dissipative dynamics cannot be described with the Schrödinger equation.

A.2 Unitary Transformations

Since in this thesis, and generally in quantum mechanics, we have to deal with many unitary transformations, we want to find a more easy way to calculate them. Therefore, in this section we rewrite the transformation (A.5) in terms of the eigenfunctions of the Hamiltonian. We assume the Hamiltonian to be time-independent; thus, the eigenfunctions $|\varepsilon_n\rangle$, with corresponding eigenvalues E_n , are conform with the time-independent Schrödinger equation,

$$\mathcal{H}|\varepsilon_n\rangle = E_n|\varepsilon_n\rangle. \quad (\text{A.16})$$

The eigenfunctions span the Hilbert space ($|\varepsilon_n\rangle\langle\varepsilon_n| = \mathbf{1}$) and are orthogonal ($\langle\varepsilon_k|\varepsilon_l\rangle = \delta_{kl}$ with δ_{kl} denoting the Kronecker-Delta). Therefore, the wavefunction $|\Psi\rangle$ can be expressed in terms of the eigenfunctions,

$$|\Psi\rangle = \sum_n |\varepsilon_n\rangle \underbrace{\langle\varepsilon_n|\Psi\rangle}_{=\alpha_n} = \sum_n \alpha_n |\varepsilon_n\rangle. \quad (\text{A.17})$$

The Hamiltonian can be written in matrix form, whereas all off-diagonal elements disappear since the Hamiltonian is diagonal in its eigenbasis,

$$\mathcal{H} = \sum_n E_n |\varepsilon_n\rangle\langle\varepsilon_n|, \quad (\text{A.18})$$

With this knowledge we can now rewrite the transformation U (which is the time-evolution operator),

$$\begin{aligned} U(t) &= e^{-i\mathcal{H}t/\hbar} = e^{-it/\hbar\sum_n E_n|\varepsilon_n\rangle\langle\varepsilon_n|} = \sum_{k=0}^{\infty} \frac{(-it/\hbar\sum_n E_n|\varepsilon_n\rangle\langle\varepsilon_n|)^k}{k!} \\ &= \mathbf{1} + \sum_n |\varepsilon_n\rangle\langle\varepsilon_n| \sum_{k=1}^{\infty} \frac{(-iE_n t/\hbar)^k}{k!} = \sum_n |\varepsilon_n\rangle\langle\varepsilon_n| e^{-iE_n t/\hbar}. \end{aligned} \quad (\text{A.19})$$

We now examine two examples which also are needed in the main part of this thesis.

a) $\mathcal{H} \propto \sigma^z$

We consider a two-level Hamiltonian of the form $\mathcal{H} = \hbar \frac{\omega}{2} \sigma^z$, with $\sigma^z = |e\rangle\langle e| - |g\rangle\langle g|$ and $\mathbf{1} = |g\rangle\langle g| + |e\rangle\langle e|$. The initial wavefunction is $|\Psi_0\rangle = \alpha |g\rangle + \beta |e\rangle$. The evolved state thus reads

$$\begin{aligned} |\Psi(t)\rangle &= e^{-i\mathcal{H}t/\hbar} |\Psi_0\rangle = e^{-\frac{i}{2}\omega t \sigma^z} |\Psi_0\rangle = e^{-\frac{i}{2}\omega t |e\rangle\langle e|} e^{\frac{i}{2}\omega t |g\rangle\langle g|} |\Psi_0\rangle \\ &= \left(\mathbf{1} + |g\rangle\langle g| \sum_{k=1}^{\infty} \frac{\left(\frac{i}{2}\omega t\right)^k}{k!} \right) \cdot \left(\mathbf{1} + |e\rangle\langle e| \sum_{k=1}^{\infty} \frac{\left(-\frac{i}{2}\omega t\right)^k}{k!} \right) |\Psi_0\rangle \\ &= \left(\mathbf{1} + |g\rangle\langle g| \sum_{k=1}^{\infty} \frac{\left(\frac{i}{2}\omega t\right)^k}{k!} + |e\rangle\langle e| \sum_{k=1}^{\infty} \frac{\left(-\frac{i}{2}\omega t\right)^k}{k!} \right) |\Psi_0\rangle \\ &= \left(|g\rangle\langle g| e^{\frac{i}{2}\omega t} + |e\rangle\langle e| e^{-\frac{i}{2}\omega t} \right) |\Psi_0\rangle, \end{aligned} \quad (\text{A.20})$$

Summarized we get

$$|\Psi(t)\rangle = \alpha e^{-\frac{i}{2}\omega t} |g\rangle + \beta e^{+\frac{i}{2}\omega t} |e\rangle \quad (\text{A.21})$$

b) $\mathcal{H} \propto a^\dagger a$

The Hamiltonian of a harmonic oscillator has the form $\mathcal{H} = \hbar\omega a^\dagger a = \hbar\omega \sum_n n |n\rangle\langle n|$, with n being the number of excitations. The initial state is $|\Psi_0\rangle = \sum_n \alpha_n |n\rangle$. The evolved state, according to Eq. (A.19), is

$$|\Psi(t)\rangle = e^{-i\omega t \sum_n n |n\rangle\langle n|} |\Psi_0\rangle = \left(\sum_n |n\rangle\langle n| e^{-i\omega n t} \right) |\Psi_0\rangle = \sum_n \alpha_n e^{-i\omega n t} |n\rangle. \quad (\text{A.22})$$

A.3 Stochastic Master Equation

For the analysis of the dissipative dynamics of a given quantum-mechanical system, a stochastic master equation that describes the coupling of the system to the environment is required. The state of a given system can be described by the master equation⁴. The master equation in the quantum mechanical picture k ($k = \text{S, H, int}$) reads

$$\rho(t) = |\Psi_k(t)\rangle\langle \Psi_k(t)|, \quad (\text{A.23a})$$

$$\dot{\rho}_{\text{S}} = -\frac{i}{\hbar} [\mathcal{H}_{\text{S}}, \rho_{\text{S}}], \quad \dot{\rho}_{\text{H}} = 0, \quad \dot{\rho}_{\text{int}} = -\frac{i}{\hbar} [\mathcal{H}_{\text{int}}, \rho_{\text{int}}], \quad (\text{A.23b})$$

where \mathcal{H}_k is the Hamiltonian and $|\Psi_k\rangle$ the qubit state of the system in picture k . In the following, we always write $\dot{\rho} = -i\frac{\dot{\mathcal{H}}}{\hbar}[\mathcal{H}, \rho]$ since it should now be clear how the master equation in certain picture looks like.

We now want to describe the loss dynamics of the system; for this purpose, we follow the derivations in [20; 19]. We start in the Schrödinger picture, where the system is described by the Hamiltonian \mathcal{H}_{S} . We now consider a reservoir described by the Hamiltonian \mathcal{H}_{R} and

³Normally, the Hamiltonian of an electromagnetic field has the form $\mathcal{H} = \hbar\omega \left(a^\dagger a + \frac{1}{2} \right)$ with $\frac{\hbar}{2}\omega$ being the zero-point energy of the field. Since this term only yields an energy shift, we neglect it in this thesis.

⁴This equation corresponds to the Heisenberg equation of motion (A.7) for the density operator.

an interaction between the system and the reservoir, $V(t)$. The total Hamiltonian of the two coupled systems then reads

$$\mathcal{H}^{\text{tot}} = \mathcal{H}_S + \mathcal{H}_R + V(t). \quad (\text{A.24})$$

If the Hamiltonians of the pure systems, \mathcal{H}_S and \mathcal{H}_R , do not depend on time, the total Hamiltonian in the interaction picture is just $V_{\text{int}}(t)$. The master equation of the total system thus reads

$$\dot{\rho}_{\text{tot}}(t) = -\frac{i}{\hbar}[V_{\text{int}}(t), \rho_{\text{tot}}(t)]. \quad (\text{A.25})$$

The reservoir variables can be traced out which yields the reduced density matrix

$$\rho(t) = \text{Tr}_R\{\rho_{\text{tot}}(t)\}. \quad (\text{A.26})$$

The master equation (A.25) can be integrated iterative which yields the reduced density matrix in a second order perturbation [20].

We now model the reservoir as a collection of bosonic field modes with frequency ω_k described by the creation and annihilation operators d_k^\dagger and d_k , respectively; d_k^\dagger and d_k obey the usual commutation relation for the mode operators of the bosonic field modes, $[d_i, d_k^\dagger] = \delta_{ik}$. The Hamiltonian of the system is given by $\mathcal{H}_S = \hbar\omega S^\dagger S$, where S^\dagger and S are the creation and annihilation or raising and lowering operators that describe the system, e.g. $S^\dagger = \sigma^+$ ($S = \sigma^-$) for a qubit or $S^\dagger = a^\dagger$ ($S = a$) for a harmonic oscillator. The interaction part is given by a JC interaction with the coupling constant g_k (see Sec. A.4). The total Hamiltonian thus reads

$$\mathcal{H}^{\text{tot}} = \hbar\omega_0 S^\dagger S + \hbar \sum_k \omega_k d_k^\dagger d_k + \hbar \sum_k \left(g_k d_k^\dagger S + g_k^* d_k S^\dagger \right), \quad (\text{A.27})$$

and

$$V_{\text{int}}(t) = \hbar \sum_k \left(g_k d_k^\dagger S e^{i(\omega_0 - \omega_k)t} + g_k^* d_k S^\dagger e^{-i(\omega_0 - \omega_k)t} \right). \quad (\text{A.28})$$

After a long and physically uninteresting calculation that can be found in the literature (see e.g. [20; 99]), one obtains the stochastic master equation in the *Markov approximation* in the thermal equilibrium:

$$\begin{aligned} \dot{\rho}(t) &= \frac{\Gamma}{2}(N+1) \left(2S\rho S^\dagger - S^\dagger S\rho - \rho S^\dagger S \right) + \frac{\Gamma}{2}N \left(2S^\dagger \rho S - S S^\dagger \rho - \rho S S^\dagger \right) \\ &= -\frac{\Gamma}{2}(N+1)\mathcal{L}[S^\dagger]\rho - \frac{\Gamma}{2}N\mathcal{L}[S]\rho, \end{aligned} \quad (\text{A.29})$$

with the number of thermal photons

$$N(\omega_0) = \left(e^{\hbar\omega_0/k_B T} - 1 \right)^{-1}, \quad (\text{A.30a})$$

and the *Liouvillian superoperator*

$$\mathcal{L}[S]\rho(t) = S^\dagger S\rho(t) - 2S\rho(t)S^\dagger + \rho(t)S^\dagger S. \quad (\text{A.30b})$$

Here, T denotes the temperature and k_B the Boltzmann factor; $\Gamma = \rho^2(\omega_0)g^2(\omega_0)$ is the damping rate. The first part of Eq. (A.29) describes the emission of a photon by the system,

the second part the absorption. In the case of zero temperature⁵ $N = 0$. The master equation in a certain picture thus reduces to

$$\dot{\rho}(t) = -\frac{i}{\hbar}[\mathcal{H}, \rho] - \frac{\Gamma}{2}\mathcal{L}[S]\rho(t), \quad (\text{A.31})$$

From this expression, we can easily obtain the master equation of a harmonic oscillator described by $a^\dagger \equiv S^\dagger$ and $a \equiv S$ and the decay rate $\kappa \equiv \Gamma$. Analogue, this gives the master equation of a qubit with $\sigma^+ \equiv S^\dagger$, $\sigma^- \equiv S$, and $\gamma \equiv \Gamma$.

The stochastic master equation (A.31) describes only the decay in the energy basis of the system. To describe the dephasing of a two-level system, one has to take into account a reservoir that couples to the σ^z and not the σ^x component of the system [19]:

$$V_{\text{dephase}} = \hbar\sigma^z \sum_k \left(g_k d_k^\dagger + g_k^* d_k \right). \quad (\text{A.32})$$

This Hamiltonian commutes with σ^z and thus does not contribute to the decay of the inversion.

A.4 Jaynes–Cummings Interaction

In this part of the appendix we give a more detailed discussion of the interaction between a two-level system (=qubit) and a single mode of the electromagnetic field, the so-called *Jaynes–Cummings* (JC) interaction [21]. For this treatment, we assume the quantization of the electromagnetic field to be known; for more information on this subject see e.g. [16] or [102].

A.4.1 Dipole Interaction Between an Electromagnetic Field and a Two-Level System

We consider a qubit with frequency ω_q that couples to a single mode of the electromagnetic field of e.g. a resonator (=cavity) with frequency ω_r that is described by the creation and annihilation operators a^\dagger and a , respectively. The Hamiltonian of the non-interacting part is given by

$$\mathcal{H}_0 = \hbar\omega_r a^\dagger a + \hbar\frac{\omega_q}{2}\sigma^z, \quad (\text{A.33})$$

a^\dagger and a act on the Fock state $|n\rangle$ (n being the photon number) as

$$a^\dagger |n\rangle = \sqrt{n+1} |n+1\rangle, \quad a |n\rangle = \sqrt{n} |n-1\rangle, \quad a^\dagger a |n\rangle = n |n\rangle. \quad (\text{A.34})$$

In the Hamiltonian we have, as in the rest of this thesis, neglected the zero-point energy $\frac{\hbar}{2}\omega_r$ of the field since it only leads to an energy shift.

The coupling of the resonator and the qubit can be described via a dipole coupling. The electromagnetic field in the dipole approximation in the Schrödinger picture is given by [102]

$$\mathcal{E} = \sqrt{\frac{\hbar\omega_r}{2\varepsilon_0 V}} \varepsilon \left(a + a^\dagger \right). \quad (\text{A.35})$$

⁵This condition is fulfilled at optical frequencies.

where ε_0 denotes the dielectric constant, V the volume of the resonator, and ε the polarization of the field. The dipole momentum of the qubit is described by the σ^x operator ($\sigma^x = |g\rangle\langle e| + |e\rangle\langle g| = \sigma^+ + \sigma^-$),

$$\mathbf{d} = \delta\sigma^- + \delta^*\sigma^+ = |\delta| \left(e^{i\phi}\sigma^- + e^{-i\phi}\sigma^+ \right) \rightarrow |\delta|\sigma^x, \quad (\text{A.36})$$

where, in the last step, we have removed the phase ϕ via the unitary transformation with $U = e^{-\frac{i}{2}\phi\sigma^z}$ (cp. Eq. (A.20)); δ is the (complex-valued) dipole strength of the qubit.

The complete Hamiltonian of the interaction between the qubit and the field in the Schrödinger picture thus reads

$$\mathcal{H}_{\text{QF}} = \mathcal{H}_0 + \mathbf{d} \cdot \boldsymbol{\varepsilon} = \mathcal{H}_0 + \underbrace{\sqrt{\frac{\hbar\omega_r}{2\varepsilon_0 V}} \varepsilon |\delta| \sigma^x}_{\equiv \hbar g} (a + a^\dagger). \quad (\text{A.37})$$

The interaction part of the Hamiltonian consists of two parts—the JC and the anti JC interaction,

$$\mathcal{H}_{\text{QF}} = \mathcal{H}_0 + \hbar g \left(\underbrace{a^\dagger\sigma^+ + a\sigma^-}_{\text{anti JC}} + \underbrace{a^\dagger\sigma^- + a\sigma^+}_{\text{JC}} \right). \quad (\text{A.38})$$

A.4.2 Rotating Wave Approximation

To obtain the JC Hamiltonian, we introduce the *rotating wave approximation* (RWA). In this approximation, one neglects very fast rotating terms since they do not affect the dynamics of the system; this corresponds to averaging in time.

We can evaluate the qubit–field Hamiltonian (A.38) in the interaction picture (Sec. A.1.3) by applying the transformation $U = e^{-i\mathcal{H}_0 t/\hbar}$,

$$\mathcal{H}_{\text{QF}}^{\text{int}} = \hbar g \left(a^\dagger\sigma^+ e^{i(\omega_r + \omega_q)t} + a\sigma^- e^{-i(\omega_r + \omega_q)t} + a\sigma^+ e^{i\Delta t} + a^\dagger\sigma^- e^{-i\Delta t} \right). \quad (\text{A.39})$$

Here, $\Delta = \omega_q - \omega_r$ is the *detuning* between the resonator and the qubit. Mostly, $|\Delta| \ll |\omega_q + \omega_r|$; this means that the anti JC parts of Eq. (A.39) ($a^\dagger\sigma^+$ and $a\sigma^-$) oscillate with a much higher frequency than the JC parts ($a^\dagger\sigma^-$ and $a\sigma^+$). Therefore, we neglect those rapidly oscillating terms in an RWA.

Back in the Schrödinger picture the JC Hamiltonian thus reads

$$\mathcal{H}_{\text{JC}} = \hbar\omega_r a^\dagger a + \hbar\frac{\omega_q}{2}\sigma^z + \hbar g \left(a^\dagger\sigma^- + a\sigma^+ \right). \quad (\text{A.40})$$

A.5 Effective Hamiltonian Approach

For the solution of the JC interaction in the dispersive regime, we require the method of effective Hamiltonians. We suppose a given Hamiltonian of the general form

$$\mathcal{H} = \mathcal{H}_0 + \mathcal{H}_1, \quad (\text{A.41})$$

where \mathcal{H}_0 denotes the non-interacting part of the Hamiltonian and \mathcal{H}_1 includes the interaction. We want to isolate higher order interactions of this Hamiltonian. For this, we use the

Schrieffer–Wolff transformation [103] to derive the effective Hamiltonian of the system. In this transformation, one performs a unitary transformation which eliminates \mathcal{H}_1 to first order

$$\mathcal{H}_{\text{eff}} = e^S \mathcal{H} e^{-S} = \mathcal{H}_0 + \mathcal{H}_1 + [S, \mathcal{H}_0] + [S, \mathcal{H}_1] + \sum_{n=2}^{\infty} \frac{1}{n!} [S, \mathcal{H}_0 + \mathcal{H}_1]_{(n)}, \quad (\text{A.42})$$

where we have expanded the transformation with the *Baker-Campbell-Hausdorff relation* (see e.g. [16]):

$$e^L M e^{-L} = \sum_{n=0}^{\infty} \frac{1}{n!} [L, M]_{(n)}, \quad (\text{A.43a})$$

with

$$\begin{aligned} [L, M]_{(0)} &= M, & [L, M]_{(1)} &= [L, M], \\ [L, M]_{(n)} &= [L, [L, M]_{(n-1)}]. \end{aligned} \quad (\text{A.43b})$$

\mathcal{H}_{eff} should have no terms which are first order in \mathcal{H}_1 . Thus, the requirement for S is

$$[S, \mathcal{H}_0] = -\mathcal{H}_1, \quad (\text{A.44})$$

This yields the effective Hamiltonian

$$\mathcal{H}_{\text{eff}} = \mathcal{H}_0 + \sum_{n=1}^{\infty} \frac{n}{(n+1)!} [S, \mathcal{H}_1]_{(n)} \approx \mathcal{H}_0 + [S, \mathcal{H}_1] + \frac{1}{2} [S, [S, \mathcal{H}_1]]. \quad (\text{A.45})$$

Note that not for all Hamiltonians a transformation that fulfills $[S, \mathcal{H}_0] = -\mathcal{H}_1$ can be found. In this case, Eq. (A.42) has to be used to calculate the effective Hamiltonian.

Appendix B

Theory of Superconductivity and Josephson Junctions

In this part of the appendix we recapitulate the theory of superconductivity. We explicitly present the *London theory* wherewith we explain the *Josephson effect* and the properties and applications of *Josephson junctions* (JJs). Then, we introduce the *resistively and capacitively shunted junction model* (RCSJ-model) which gives us the possibility to describe JJs quantum mechanically with a Hamiltonian. Lastly, we have a look at the main properties of *superconducting quantum interference devices* (SQUIDs) including their theoretical description.

Since there are several works describing the phenomena and theories of superconductivity, see e.g. [54; 104; 105; 106], we will just focus on the results that are important for this thesis. We will mainly follow the derivations and explanations of [54] to obtain the different equations and to describe the properties of superconductors.

B.1 London Theory

The London theory is a phenomenological theory for $T = 0$. It describes the main electromagnetic properties of a superconductor such as the ideal conductivity, the Meißner-Ochsenfeld effect [107] and the fluxoid quantization in multiply connected superconductors. Moreover, it motivates the theoretical description of the Josephson effects with the Josephson equations [108]. However, it does not describe the pairing of electrons to Cooper pairs, the existence of type II superconductors, and the temperature response of superconductors. This can be done with the *BCS* or the *Ginzburg-Landau theory*, see e.g. [105; 106].

Since we have to deal with Cooper pairs¹, the mass and the charge of the considered particles are different from those of electrons,

$$q \rightarrow Q = -\mathcal{K}e, \quad m \rightarrow M = \mathcal{K}m_e, \quad (\text{B.1})$$

where the factor $\mathcal{K} = 2$ takes into account the pairing of electrons to Cooper Pairs.

¹In superconductivity, two electrons are bound to Cooper pairs that are quasi-bosons. See e.g. [109] for more information on Cooper pairs.

B.1.1 London Equations

We start with the Schrödinger equation of a particle with mass M and charge Q in an electromagnetic field that is described by the vector potential $\mathbf{A}(\mathbf{r}, t)$ and the scalar potential $\phi(\mathbf{r}, t)^2$,

$$i\hbar \frac{\partial \Psi(\mathbf{r}, t)}{\partial t} = \frac{1}{2M} \left(\frac{\hbar}{i} \nabla - Q\mathbf{A}(\mathbf{r}, t) \right)^2 \Psi(\mathbf{r}, t) + Q\phi(\mathbf{r}, t) \Psi(\mathbf{r}, t). \quad (\text{B.2})$$

$\mathbf{A}(\mathbf{r}, t)$ and $\phi(\mathbf{r}, t)$ are related to the magnetic and electric field via $\mathbf{B}(\mathbf{r}, t) = \nabla \times \mathbf{A}(\mathbf{r}, t)$ and $\mathbf{E}(\mathbf{r}, t) = -\nabla\phi(\mathbf{r}, t) - \frac{\partial \mathbf{A}(\mathbf{r}, t)}{\partial t}$, respectively.

Superconductivity is a coherent quantum phenomenon of all Cooper pairs [109]; thus, the main assumption of the London theory is that the entire ensemble can be described by a *macroscopic quantum wavefunction*

$$\Psi(\mathbf{r}, t) = \sqrt{\rho(\mathbf{r}, t)} \cdot e^{i\theta(\mathbf{r}, t)}. \quad (\text{B.3})$$

This representation corresponds to the so-called *Madelung transformation*³ [110]. Here, θ denotes the *macroscopic phase* of the superconductor, and ρ is the local Cooper pair density (ρ_e being the local electron density),

$$\rho(\mathbf{r}, t) = \frac{1}{\mathcal{K}} \rho_e(\mathbf{r}, t) = |\Psi(\mathbf{r}, t)|^2. \quad (\text{B.4})$$

Additionally, the whole ensemble has to satisfy the normalization condition

$$\int dV |\Psi(\mathbf{r}, t)|^2 = N = \mathcal{K}N_e, \quad (\text{B.5})$$

with N being the number of Cooper pairs and N_e the number of electrons.

The Schrödinger equation for Ψ now changes into two equations for ρ and θ ; therefore, we obtain

$$\hbar \frac{\partial \theta}{\partial t} + \frac{1}{2} M \mathbf{v}^2 + Q\phi = U_{\text{qm}}, \quad (\text{B.6})$$

$$\frac{\partial \rho}{\partial t} + \nabla \cdot (\rho \mathbf{v}) = 0. \quad (\text{B.7})$$

Here, U_{qm} is the quantum mechanical Bohm potential [111], $U_{\text{qm}} = \frac{\hbar^2 \nabla^2 \sqrt{\rho}}{2m\sqrt{\rho}}$, and \mathbf{v} the particle velocity that corresponds to the probability current,

$$\mathbf{j}(\mathbf{r}, t) = \rho \mathbf{v}(\mathbf{r}, t) = \frac{\hbar \rho}{M} \nabla \gamma(\mathbf{r}, t). \quad (\text{B.8})$$

where we have introduced the *gauge-invariant phase gradient* $\nabla \gamma$,

$$\boxed{\nabla \gamma(\mathbf{r}, t) = \nabla \theta - \frac{Q}{\hbar} \mathbf{A}}, \quad (\text{B.9})$$

²For the sake of simplicity we will not write the dependency of the quantities on (\mathbf{r}, t) in each equation.

³Like every complex value, Ψ can be written in terms of its absolute value $\sqrt{\rho(\mathbf{r}, t)}$ and the argument $\theta(\mathbf{r}, t)$, which are both real values. This is the Madelung transformation.

according to the *gauge-invariant phase* γ ⁴. Eqs. (B.6) and (B.7) correspond to hydrodynamic equations of motion [110]. Eq. (B.7) is equivalent to a continuity equation for ρ and \mathbf{j} , and Eq. (B.6) is conform to the hydrodynamic equation for an irrotational flow in a conservative potential. In the semiclassical limit ($\hbar \rightarrow 0$), we can neglect U_{qm} ; Eq. (B.6) then corresponds to a Hamilton–Jacobi equation for the action function $\hbar\theta$ [111].

The probability current is related to a supercurrent density, $\mathbf{J}_s = Q\mathbf{j}$ ⁵ of the charged particle. Likewise, the probability density corresponds to a charge density $\rho_s = Q\rho = -e\rho_e$. \mathbf{J}_s and ρ_s also obey the continuity equation.

Therefore, we obtain the main equations of the London theory in the semiclassical limit:

$$-\hbar \frac{\partial \theta(\mathbf{r}, t)}{\partial t} = \frac{M}{2\rho_s^2(\mathbf{r}, t)} \mathbf{J}_s^2(\mathbf{r}, t) + Q\phi(\mathbf{r}, t), \quad (\text{B.10})$$

$$\mathbf{J}_s(\mathbf{r}, t) = \frac{\hbar}{Q\Lambda} \nabla \gamma(\mathbf{r}, t), \quad (\text{B.11})$$

with $\Lambda = \frac{M}{\rho_s Q^2} = \frac{m_e}{\rho_e e^2}$ being the *London coefficient*. These equations already are the London equations, but in an uncommon notation. The London equations in the more familiar form can be derived easily by considering the curl and the time derivative of the supercurrent (B.11) together with the Maxwell equations and the continuity equation (B.7). Introducing the *London penetration depth* $\lambda_L = \sqrt{\frac{\Lambda}{\mu_0}} = \sqrt{\frac{m_e}{\mu_0 \rho_e e^2}}$, this yields

$$\frac{\partial}{\partial t} (\Lambda \mathbf{J}_s) = \mathbf{E} + \frac{1}{e\rho_e} \nabla (\Lambda \mathbf{J}_s^2) \quad (\text{1st London equation}), \quad (\text{B.12})$$

$$\nabla^2 \mathbf{B} = \frac{1}{\lambda_L^2} \mathbf{B} \quad (\text{2nd London equation}). \quad (\text{B.13})$$

The first London equation can be linearized for $|\mathbf{E}| \gg |\mathbf{v}_s| \cdot |\mathbf{B}|$ [54], which corresponds to neglecting the second term on the right hand side (kinetic energy of the superelectrons); this linearized equation describes the ideal conductivity of the superconductor. The second equation describes the screening of an applied magnetic field by a thick superconductor, which is the Meißner–Ochsenfeld effect [107]. The field falls off exponentially in the superconductor with $e^{-\lambda_L x}$.

The first London equation also results from Lorentz’s law and the second London equation. This shows that not the ideal conductivity, but the perfect diamagnetism is the more fundamental property of the SC state. Note that the London equations—especially the London coefficient Λ and therewith the London penetration depth λ_L —do not depend on the factor \mathcal{K} . All results could have been achieved without the assumption of having Cooper pairs.

B.1.2 Fluxoid Quantization

One quantum-mechanical consequence of the macroscopic quantum nature of superconductors is the quantization of the flux in unites of the fluxoid quantity Φ_0 in multiply connected

⁴It can be shown that γ is invariant under the gauge transformations $\mathbf{A} \rightarrow \mathbf{A} + \nabla\chi$ and $\phi \rightarrow \phi - \frac{\partial\chi}{\partial t}$, with χ being an arbitrary scalar function.

⁵The supercurrent I_s then is $I_s = \int d\mathbf{S} \cdot \mathbf{J}_s$. For a homogeneous supercurrent density the supercurrent is just $I_s = \mathbf{S} \cdot \mathbf{J}_s$.

superconductors. The fluxoid quantization proves the hypothesis that electrons build Cooper pairs which are responsible for the SC state.

We start with the supercurrent density (Eq. (B.11)).

$$\mathbf{J}_s = \frac{\hbar}{Q\Lambda} \nabla\gamma, \quad (\text{B.14})$$

and integrate over a loop through the multiply connected superconductor,

$$-\frac{\hbar}{Q} \oint d\mathbf{r} \cdot \nabla\theta = \oint d\mathbf{r} \cdot (\mathbf{A} + \Lambda\mathbf{J}_s), \quad (\text{B.15})$$

$$-\frac{\hbar}{Q} \underbrace{\oint d\mathbf{r} \cdot \nabla\theta}_{2\pi n} = \underbrace{\int d\mathbf{S} \cdot (\mathbf{B} + \Lambda\nabla \times \mathbf{J}_s)}_{\text{fluxoid } \Phi'}, \quad (\text{B.15}')$$

$$n \frac{2\pi\hbar}{2e} = \Phi', \quad (\text{B.15}'')$$

where we have used the theorem of Stokes. This yields the fluxoid quantity

$$\boxed{\Phi_0 = \frac{h}{2e}}. \quad (\text{B.16})$$

Deep in the superconductor, flux and fluxoid are the same since the supercurrent density \mathbf{J}_s vanishes⁶; this is not the case for the outer shell. Note that in a simply connected superconductor the integral over $\nabla\theta$ vanishes and therefore no flux can be found in such a superconductor; in this case, Eq. (B.15') is just the integral form of the second London equation.

With the fluxoid quantity, the phase difference φ can be related to a magnetic flux, $\varphi = 2\pi \frac{\Phi}{\Phi_0}$.

B.2 Josephson Effect

A second consequence of the macroscopic inherent quantum nature of superconductors appears if two superconductors are weakly coupled via an electrical contact, e.g. a tunnelling barrier or a point contact, see Fig. B.1. We assume an SIS (superconductor-insulator-superconductor) contact, without loss of generality. In the normal conducting case, electrons can tunnel through the barrier. In the SC case, at $T = 0$, no quasi particles can be found at the Fermi level and we expect no normal current through the metal. If the applied voltage is big enough to break up Cooper pairs, which is the case for $eV \geq 2\Delta$, a normal current through the contact can be observed again; see also Sec. B.3.1.

In both cases, also Cooper pairs tunnel through the contact in a coherent process; the tunnelling probability for this process is the same as that for single electrons. This quantum interference of the two superconductors is called *Josephson effect* [108], and the junction therefore *Josephson junction* (JJ).

⁶In general, if the thickness of the SC material is much larger than λ_L , we can choose an integral contour deep inside the SC material where in very good approximation we have $\mathbf{J}_s = 0$.

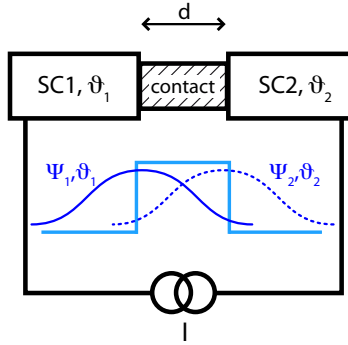


Figure B.1: Sketch of a Josephson junction. Two superconductors, SC1 and SC2 with phases θ_1 and θ_2 , respectively, build a Josephson junction (JJ) when they are coupled weakly via an electrical contact. This leads to the Josephson effect that is due to quantum interference of the two macroscopic wavefunctions of the superconductors.

B.2.1 Josephson Equations

The two superconductors are described by their probability densities ρ_1 and ρ_2 and their phases $\theta_1 \equiv \theta(-\frac{d}{2}, t)$ and $\theta_2 \equiv \theta(\frac{d}{2}, t)$. We assume the densities to be equal, $\rho_1 = \rho_2 \equiv \rho_s/Q$, and homogeneous; the second assumption is warranted for small junction areas⁷. For the derivation of the Josephson equations we follow the general method of L. D. Landau and E. M. Lifschitz [112]. Since the Josephson equations are derived from the London equations, these equations also only hold for $T = 0$.

We introduce the *gauge-invariant phase difference* φ with its definition

$$\varphi(\mathbf{r}, t) = \gamma_2(\mathbf{r}, t) - \gamma_1(\mathbf{r}, t) \equiv \int_1^2 d\mathbf{l} \cdot \nabla \gamma = \theta_2 - \theta_1 + \frac{2\pi}{\Phi_0} \int_1^2 d\mathbf{l} \cdot \mathbf{A}. \quad (\text{B.17})$$

The current density \mathbf{J}_s through the junction is a function of this phase difference, $\mathbf{J}_s = \mathbf{J}_s(\varphi)$. The gauge-invariant phases are well-defined modulo 2π . Thus, $\mathbf{J}_s(\varphi)$ has to be a periodic function in φ . Likewise, the current I_s also must be a periodic function,

$$I_s(\varphi) = \sum_n \left(I_{o,n} \sin n\varphi + I_{e,n} \cos n\varphi \right). \quad (\text{B.18})$$

Under a time reversal transformation both the current and the phase change sign; therefore, the cosine term cannot describe the current properly. Since we are considering weak coupling, the sum converges very fast and all expansion coefficients except of $I_{o,1} \equiv I_c$ vanish. Therefore, we obtain

$$\boxed{I_s = I_c \sin \varphi} \quad (\text{1}^{\text{st}} \text{ Josephson equation}), \quad (\text{B.19})$$

which is also called the *current–phase relation*.

The *Josephson critical current* I_c for $T = 0$ can be obtained from the BCS theory [106],

$$I_c = \frac{\pi \Delta}{2eR_n}, \quad (\text{B.20})$$

⁷We cannot always neglect the size of the junction. Especially for Josephson junctions in external fields, we would have to change this [54].

with S being the face of the JJ, Δ the energy gap, and R_n the resistance of the superconductor in the normal state. Here, as in the rest of this thesis, we assumed the energy gaps of the two superconductors to be equal.

The second Josephson equation, which describes the change in time of the phase difference φ , can be derived from Eq. (B.17). We examine the time derivative of the gauge-invariant phase difference which reads

$$\begin{aligned} \frac{\partial\varphi}{\partial t} = & -\frac{1}{\hbar} \left\{ \frac{M}{2\rho_s} (\mathbf{J}_s^2(\mathbf{r}_2, t) - \mathbf{J}_s^2(\mathbf{r}_1, t)) \right. \\ & \left. + Q(\phi(\mathbf{r}_2, t) - \phi(\mathbf{r}_1, t)) \right\} + \frac{2\pi}{\Phi_0} \frac{\partial}{\partial t} \int_1^2 \mathbf{dl} \cdot \mathbf{A}(\mathbf{r}, t), \end{aligned} \quad (\text{B.21})$$

where we have used Eq. (B.10) to obtain Eq. (B.21). The supercurrent density across the junction is continuous, and therefore $\mathbf{J}_s^2(\mathbf{r}_2, t) = \mathbf{J}_s^2(\mathbf{r}_1, t)$. Thus, we obtain

$$\frac{\partial\varphi}{\partial t} = \frac{2\pi}{\Phi_0} \int_1^2 \mathbf{dl} \cdot \left(\nabla\phi + \frac{\partial\mathbf{A}}{\partial t} \right) = \frac{2\pi}{\Phi_0} \int_1^2 \mathbf{dl} \cdot (-\mathbf{E}). \quad (\text{B.21}')$$

The line integral over the electric field is just the voltage V between the two Josephson junctions. Eq. (B.21') then immediately yields the *voltage–phase relation*

$$\boxed{\frac{\partial\varphi}{\partial t} = \frac{2\pi}{\Phi_0} V} \quad (\text{2}^{\text{nd}} \text{ Josephson equation}). \quad (\text{B.22})$$

The two Josephson equations, (B.19) and (B.22), can also be obtained from the microscopic BCS–theory [106], the phenomenological Ginzburg–Landau theory [105] or a quantum well ansatz that was proposed by Richard Feynman [54; 104].

B.2.2 Josephson Coupling Energy

The energy $E_{J,c}$ that is stored in the JJ can be calculated by integrating over the electrical power $P = I_s \cdot V$:

$$E_{J,c} = \int_0^t dt' I_s \cdot V = \frac{\Phi_0 I_c}{2\pi} \int_0^t dt' \sin\varphi(t') \frac{\partial\varphi(t')}{\partial t'}. \quad (\text{B.23})$$

With $\varphi(t') \equiv \tilde{\varphi}$ and the integral limits $\tilde{\varphi}(0) = 0$ and $\tilde{\varphi}(t) = \varphi$ we can write the integral as

$$E_{J,c} = \frac{\Phi_0 I_c}{2\pi} \int_0^\varphi d\tilde{\varphi} \sin\tilde{\varphi}, \quad (\text{B.24})$$

and therefore obtain the *Josephson coupling energy*

$$\boxed{E_{J,c} = E_J (1 - \cos\varphi)}, \quad \text{with } E_J = \frac{\Phi_0 I_c}{2\pi}. \quad (\text{B.25})$$

E_J is the *Josephson energy* of the JJ.

B.2.3 Josephson Inductance

Taking the time derivative of the first Josephson equation and using the second Josephson equation we obtain

$$\dot{I}_s = I_c \frac{\Phi_0}{2\pi} V \cos \varphi. \quad (\text{B.26})$$

If we remember that the induced voltage of an inductance is $V = L \cdot \dot{I}$, we can immediately see that the JJ behaves as a nonlinear inductance

$$\boxed{L_J = \frac{L_{J,0}}{\cos \varphi}}, \quad \text{with } L_{J,0} = \frac{\Phi_0}{2\pi I_c}. \quad (\text{B.27})$$

B.2.4 DC and AC Josephson Effect

The most obvious effects that follow from the Josephson equations (B.19) and (B.22) are the dc and the ac Josephson effect.

For a constant voltage V Eq. (B.22) can be integrated very easily and yields

$$\varphi(t) = \varphi_0 + \frac{2\pi}{\Phi_0} V \cdot t, \quad (\text{B.28})$$

with $\varphi_0 = \varphi(t=0)$ being a constant value. The supercurrent then reads

$$I_s = I_c \sin \left(\varphi_0 + \frac{2\pi}{\Phi_0} V \cdot t \right). \quad (\text{B.29})$$

Thus, for $V = 0$, a constant direct current $I_s = I_c \sin \varphi_0$ crosses the junction due to the difference in the phases of the superconductors. This is the *dc Josephson effect*.

For a constant voltage $V \neq 0$ the Josephson current is oscillating at the Josephson frequency

$$\frac{\omega}{V} = \frac{2\pi}{\Phi_0} \approx 500 \frac{\text{MHz}}{\mu\text{V}}. \quad (\text{B.30})$$

This is the *ac Josephson effect*. Therefore, the JJ can be considered as a voltage controlled oscillator that can be used to generate very high frequencies (≈ 500 GHz at 1 meV) [54].

There are several other effects that follow from the Josephson equations. For a detailed information see [54; 104].

B.3 Whole Junction Dynamics

The Josephson equations characterize the properties of the JJ very accurately at zero voltage and zero temperature. In this regime the whole dynamics is described by the Josephson equations (B.19) and (B.22). To derive the Lagrangian and the Hamiltonian of the junction, one has to take into account additional channels which is done with the *resistively and capacitively shunted junction model* (RCSJ model). In this section, we introduce this model and derive the Hamiltonian of the JJ.

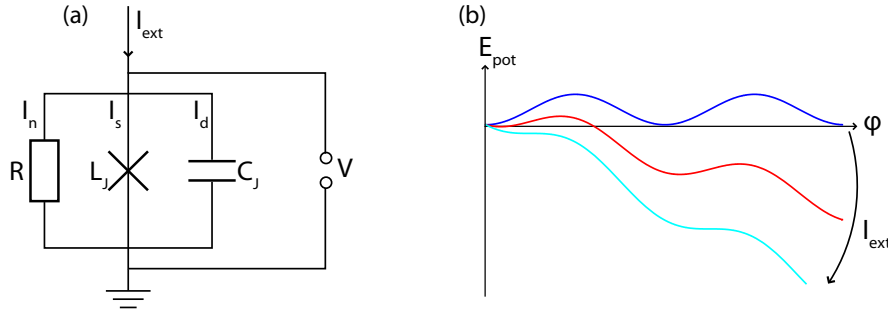


Figure B.2: (a) Equivalent circuit for a JJ in the voltage-state. A current I_{ext} is applied to the junction. This yields the Josephson current channel I_s , corresponding to the ideal JJ; the normal current channel I_n , with the resistance R ; and the displacement current channel I_d , with the Josephson capacitance C_J . The junction is probed via the voltage V . In this thesis, a simple cross in a circuit diagram indicates an ideal JJ and a boxed cross a real JJ. (b) Motion of the gauge-invariant phase difference of the JJ in the tilted washboard potential. Increasing the applied current I_{ext} results in a tilt of the potential. See also [54; 104].

B.3.1 RCSJ Model

In the voltage-state, where $|V| > 0$ due to a change in time of the gauge-invariant phase difference, additional current channels appear, the resistive and the capacitive channel, see Fig. B.2(a). Therefore, a JJ can be described by an equivalent circuit with both a resistance and a capacitance shunted in parallel to the JJ. This is the resistively and capacitively shunted junction model [113; 114] which describes the response curves to external fields and the dynamics of the JJ very well.

At both finite voltages $|V| \geq 2\Delta/e$ and finite temperatures $T > 0$ Cooper pairs are broken up into quasi particles. These quasi particles can tunnel through the junction which yields a *normal current* I_n . The normal current is described by the resistance R and the voltage V via

$$I_n = \frac{V}{R} = \frac{\Phi_0}{2\pi} \frac{\dot{\varphi}}{R}. \quad (\text{B.31})$$

where we have taken into account the second Josephson equation (B.22).

Accessorially, a JJ also has a finite capacitance C_J since it has a geometry like a parallel plate capacitor. At a time-dependent voltage, this then leads to a *displacement current* I_d that is given by

$$I_d = C_J \cdot \dot{V}(t) = C_J \frac{\Phi_0}{2\pi} \ddot{\varphi}(t). \quad (\text{B.32})$$

Due to Kirchhoff's laws the sum of the different current channels is equal to the bias current,

$$I_{\text{ext}} = I_s + I_n + I_d. \quad (\text{B.33})$$

Therefore, we can obtain a non-linear differential equation for the gauge-invariant phase difference φ :

$$I_{\text{ext}} = I_c \sin \varphi + \frac{\Phi_0}{2\pi} \frac{\dot{\varphi}}{R} + \frac{\Phi_0}{2\pi} C_J \ddot{\varphi}. \quad (\text{B.34})$$

This equation of motion is equivalent to that of the motion of a particle with mass $C_J \left(\frac{\Phi_0}{2\pi}\right)^2$ in a so-called *tilted washboard potential* with the potential energy $U = E_J(1 - \cos \varphi - \frac{I}{I_c} \varphi)$

and the damping $\frac{1}{R} \left(\frac{\Phi_0}{2\pi}\right)^2$, see Fig. B.2(b)⁸.

B.3.2 Hamiltonian of the Current-Biased Junction

We now want to treat both the gauge-invariant phase difference φ and the charge Q as quantum mechanical variables and describe the dynamics of a JJ with a Hamiltonian. We firstly have to determine the Lagrangian of the circuit in order to find the canonically conjugated variables.

To present the circuit dynamics in the Lagrangian form, and therewith in the Hamiltonian form, we assume the damping term $\frac{\Phi_0}{2\pi} \dot{\varphi}$ in the Kirchoff equation (B.34) to be zero. This assumption is fulfilled for low temperatures ($T \approx 0$) and small voltages ($|V| < 2\Delta/e$) as the normal current I_n is negligible in this regime.

We want to obtain the kinetic and potential energy appendant to Eq. (B.34). Again, the stored energy can be calculated by integrating over the electrical power P , see Sec. B.2.2; therewith, the energy of the current channel I_i ($i = e, s, d$) is

$$E_i = \frac{\Phi_0}{2\pi} \int_0^t dt' \dot{\varphi} \cdot I_i. \quad (\text{B.35})$$

The kinetic energy corresponds to the displacement current (B.32) and thus reads

$$T(\dot{\varphi}) = \frac{1}{2} \left(\frac{\Phi_0}{2\pi}\right)^2 C_J \dot{\varphi}^2 = \frac{Q^2}{2C_J}. \quad (\text{B.36})$$

It is common to describe this *charging energy* (or *electrostatic energy*) in terms of the number of Cooper pairs, N , and the charging energy of one Cooper pair, $E_c = \frac{(2e)^2}{2C_J}$,

$$T(\dot{\varphi}) = E_c N^2. \quad (\text{B.37})$$

The potential energy consists of the energy of the Josephson supercurrent and the magnetic energy of the bias current,

$$U(\varphi) = E_J (1 - \cos \varphi) - \frac{\Phi_0}{2\pi} I_{\text{ext}} \varphi, \quad (\text{B.38})$$

which gives us the classical Lagrangian of the junction,

$$\mathcal{L} = \frac{1}{2} \left(\frac{\Phi_0}{2\pi}\right)^2 C_J \dot{\varphi}^2 - E_J (1 - \cos \varphi) + \frac{\Phi_0}{2\pi} I_{\text{ext}} \varphi. \quad (\text{B.39})$$

In order to quantize the circuit equation (B.34), we follow the conventional way of canonical quantization. The canonically conjugate variable of φ is proportional to the number of Cooper pairs N ,

$$\frac{\partial \mathcal{L}}{\partial \dot{\varphi}} = \left(\frac{\Phi_0}{2\pi}\right)^2 C_J \dot{\varphi} = \hbar N. \quad (\text{B.40})$$

⁸Another analogue of the dynamics of the JJ is the physical pendulum [54; 104].

Thus, the charge corresponds to the momentum of the circuit and the phase to the position which gives us the quantum mechanical commutator relation of the variables $\hat{\varphi}$ and \hat{N} as the quantization condition,

$$[\hat{N}, \hat{\varphi}] = -i. \quad (\text{B.41})$$

Therefore, we can make the operator replacement

$$N \rightarrow \hat{N} = -i \frac{\partial}{\partial \varphi}. \quad (\text{B.42})$$

\hat{N} can be associated with the momentum operator and $\hat{\varphi}$ with the position operator; in this thesis we will write φ instead of $\hat{\varphi}$ since the difference between them should be clear. This then yields the Hamiltonian of the current-biased Josephson junction

$$\mathcal{H}_{\text{cJ}} = E_c \hat{N}^2 - E_J \cos \varphi - \frac{\Phi_0}{2\pi} I_{\text{ext}} \varphi, \quad (\text{B.43})$$

where we have neglected constant terms.

B.3.3 Hamiltonian of the Voltage-Biased Junction

To derive the Hamiltonian of a voltage-biased JJ, we firstly have to take a closer look at the so-called Single Electron Box (SEB), see Fig B.3. The derivation of the voltage-biased SEB can be found in [115]; we adopt the derivation of [116].

A metallic island, the SEB, is connected to a voltage source via a capacitance and a tunnel junction. It is possible to add or remove single electrons to or from the island with this device. The Gibbs free energy of the circuit reads

$$G(V_g, q_t, q_g) = \frac{q_t^2}{2C_t} + \frac{q_g^2}{2C_g} - \tilde{q}V_g, \quad (\text{B.44})$$

where the first two terms correspond to the charging energies of the two electrodes and the third term $\tilde{q}V_g$ represents the work done by the voltage source, \tilde{q} being the charge that passed the voltage generator. To rewrite G as a function only of the gate voltage V_g and the number

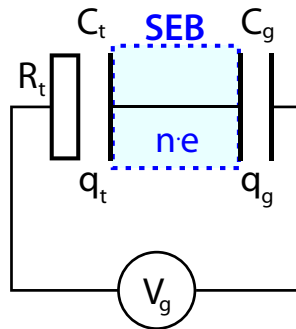


Figure B.3: Equivalent circuit of the Single Electron Box. A metallic island is connected to a voltage source V_g via the gate capacitance C_g and a tunnel junction with capacitance C_t and resistance R_t . With this device it is possible to put a well-defined number of excess electrons onto the island.

of excess electrons on the island n_e , we have a look at the equations of the circuit following from charge conservation,

$$V_g = \frac{q_t}{C_t} + \frac{q_g}{C_g}, \quad (\text{B.45a})$$

$$n_e e = -q_t + q_g. \quad (\text{B.45b})$$

We solve these equations with respect to q_t and q_g which gives

$$q_t(n, V_g) = \frac{C_t}{C_\Sigma} (C_g V_g - n_e e), \quad (\text{B.46a})$$

$$q_g(n, V_g) = \frac{C_g}{C_\Sigma} (C_t V_g + n_e e), \quad (\text{B.46b})$$

with $C_\Sigma = C_t + C_g$. We obtain the charge \tilde{q} via an analysis of the charge variation at the electrodes when the charge on the island changes from $n_e = 0$ to a certain value n_e ,

$$\tilde{q} = n_e e + \underbrace{q(n_e, V) - q(0, V)}_{\text{variation at the tunnel electrode}} = \underbrace{q_g(n_e, V) - q_g(0, V)}_{\text{variation at the gate electrode}} = \frac{C_g}{C_\Sigma} n_e e. \quad (\text{B.47})$$

Substituting Eqs. (B.46a), (B.46b), and (B.47) in Eq. (B.44) yields Gibb's free energy as a function of the applied voltage and the number of electrons on the island,

$$G = \frac{C_t C_g}{2C_\Sigma} V_g^2 + \frac{1}{2C_\Sigma} (n_e e)^2 - \frac{C_g}{C_\Sigma} n_e e V_g = \frac{1}{2C_\Sigma} (n_e e - C_g V_g)^2 + \underbrace{\frac{C_g C_t - C_g^2}{2C_\Sigma} V_g^2}_{=\text{const.}}. \quad (\text{B.48})$$

The constant terms can be neglected since they only lead to an energy shift. Therewith, the Gibbs free energy now reads

$$G(V, n) = \tilde{E}_c^{\text{se}} (n_e - n_{eg})^2, \quad (\text{B.49})$$

with $\tilde{E}_c^{\text{se}} = \frac{e^2}{2C_\Sigma}$ being the charging energy of a single electron in the voltage-biased SEB⁹ and $n_{eg} = \frac{C_g V_g}{e}$ the dimensionless gates charge.

In a JJ, the capacitance C_t corresponds to the Josephson capacitance C_J . For the case of Cooper pairs, the number of electrons n_e changes into the number of Cooper pairs N , the charging energy into $\tilde{E}_c = \frac{(2e)^2}{2C_\Sigma} (C_\Sigma = C_J + C_g)$, and the dimensionless gates charge n_{eg} into $N_g = \frac{C_g V_g}{2e}$. Thus, for the voltage-biased junction the charging energy term, Eq. (B.37), changes as

$$E_c \hat{N}^2 \rightarrow \tilde{E}_c (\hat{N} - N_g)^2, \quad (\text{B.50})$$

and the Hamiltonian of the voltage-biased junction thus reads

$$\boxed{\mathcal{H}_{\text{vJ}} = \tilde{E}_c (\hat{N} - N_g)^2 - E_J \cos \varphi} \quad (\text{B.51})$$

We indicate the voltage-biased charging energy of a Cooper pair \tilde{E}_c with a \sim only in cases where the notation is not explicit.

⁹The \sim indicates that we do have a voltage-biased SEB and therefore $E_c^{\text{se}} = \frac{e^2}{2C_t}$, being the charging energy of the unbiased system, changes into \tilde{E}_c^{se} .

B.4 Superconducting Quantum Interference Devices

In this section we describe *Superconducting Quantum Interference Devices* (SQUIDs) that are the elementary circuits to implement SC qubits. A SQUID combines two basic phenomena that are due to the macroscopic phase coherence in superconductors, the fluxoid quantization and the Josephson effect. It is composed of a SC loop that is intersected by one (rf SQUID, Sec. B.4.1) or two (dc SQUID, Sec. B.4.2) Josephson junctions¹⁰. In JJs, the maximal current strongly modulates with the applied field, see [54]. This sensitivity increases with increasing size of the junction. As a result, SQUIDs are the most sensitive detectors for external magnetic fields.

B.4.1 DC SQUID

The dc SQUID consists of two JJs that are connected in parallel on a SC loop, see Fig. B.4. As the name implies, the dc SQUID is operated by applying a direct current (dc) I_{dc} .

To derive the Hamiltonian of the dc SQUID, we start with Kirchhoff's laws. If we assume the JJs to be identical¹¹, and therefore $I_{c1} = I_{c2}$, we obtain the total current

$$I_s = I_{s1} + I_{s2} = I_c \sin \varphi_2 - I_c \sin \varphi_1 = 2I_c \sin(\phi_-) \cos(\phi_+), \quad (\text{B.52})$$

where we have, following the notation of [4], introduced the new variables

$$\phi_{\pm} = \frac{\varphi_2 \pm \varphi_1}{2}. \quad (\text{B.53})$$

Integration over the whole SC loop [54] yields

$$\phi_+ = \pi \frac{\Phi}{\Phi_0}. \quad (\text{B.54})$$

This constraint comes from flux quantization in multiply connected superconductors. The supercurrent through the dc SQUID then is

$$I_s^{\text{dc}} = 2I_c \cos\left(\pi \frac{\Phi}{\Phi_0}\right) \sin \phi_-. \quad (\text{B.55})$$

For small junctions or small applied currents, the inductance of the loop and therewith the flux generated in the loop by the circulating current can be neglected. In this case, Φ is just the external flux Φ_{ext} . If the induced flux cannot be neglected, the flux Φ is given by the sum of the external flux Φ_{ext} and the induced flux Φ_L due to the circulating screening current I_{circ} ,

$$\Phi = \Phi_{\text{ext}} + \Phi_L = \Phi_{\text{ext}} + LI_{\text{circ}}. \quad (\text{B.56})$$

We assume the two sides of the loop to be identical; therefore, the circulating current reads

$$I_{\text{circ}} = \frac{I_{s1} - I_{s2}}{2}. \quad (\text{B.57})$$

¹⁰There are several SQUIDs available. A detailed description of those devices is given in [54; 117].

¹¹The calculation for non-identical junctions does not differ much from ours; see e.g. [6; 48].

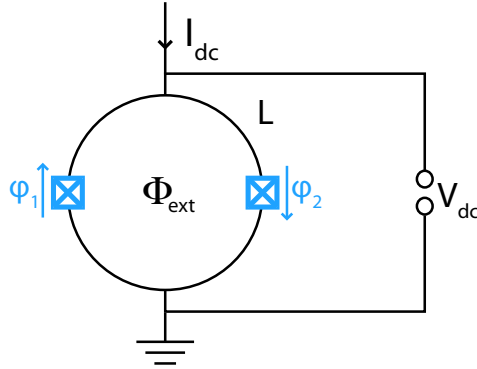


Figure B.4: Circuit diagram of the current-biased dc SQUID. It is formed by two identical JJs with phases φ_1 and φ_2 in a SC loop (inductance L). Arrows indicate the direction of the positive Josephson current. The dc SQUID is operated with an applied direct current I_{dc} . An external flux Φ_{ext} threads the loop. Readout of the dc SQUID is done with the voltage signal V_{dc} .

Therewith, the total flux Φ threading the loop is

$$\begin{aligned}\Phi &= \Phi_{\text{ext}} + \frac{1}{2}LI_c(\sin \varphi_1 - \sin \varphi_2) \\ &= \Phi_{\text{ext}} + LI_c \sin\left(\pi \frac{\Phi}{\Phi_0}\right) \cos(\phi_-).\end{aligned}\tag{B.58}$$

In general, Eq. (B.58) together with Eq. (B.55) have to be solved self-consistently for the flux Φ for different conditions of the loop inductance L and the external current I_{ext} . To analyze limiting cases of the external flux one introduces the *screening parameter* $\beta_{L,\text{dc}} = 2\frac{LI_c}{\Phi_0}$; it represents the ratio of the magnetic flux generated by the maximum possible circulating current $I_{\text{circ}} = I_c$ and $\Phi_0/2$; for further information see [54].

For $\beta_{L,\text{dc}} \ll 1$ the inductance of the loop is negligible and we easily obtain the Hamiltonian of the current-biased dc SQUID¹². Henceforth, we write $\varphi \equiv \phi_-$ for consistency in the notation. Finally, the dc SQUID Hamiltonian reads

$$\mathcal{H}_{\text{dc}} = E_c \hat{N}^2 - E_J(\Phi_x) \cos \varphi - \frac{\Phi_0}{2\pi} I_{\text{dc}} \varphi,\tag{B.59}$$

with $E_J(\Phi_{\text{ext}}) = 2E_J \cos\left(\pi \frac{\Phi_{\text{ext}}}{\Phi_0}\right)$ being the flux-dependent Josephson coupling energy. Thus, if we neglect the loop inductance, the dc SQUID acts like a single JJ with flux-tunable Josephson coupling.

B.4.2 RF SQUID

The rf SQUID is formed by a SC loop with inductance L containing only one JJ, see Fig B.5. In contrast to the dc SQUID (which is operated with a direct current) it is operated by applying a radio frequency (rf) current via an inductively coupled resonant tank circuit.

Again, flux quantization imposes a constraint for the total flux Φ in the loop [54],

$$\varphi = 2\pi \frac{\Phi}{\Phi_0}.\tag{B.60}$$

¹²The full Lagrangian of the dc SQUID, including also the induced flux can be found in [4].

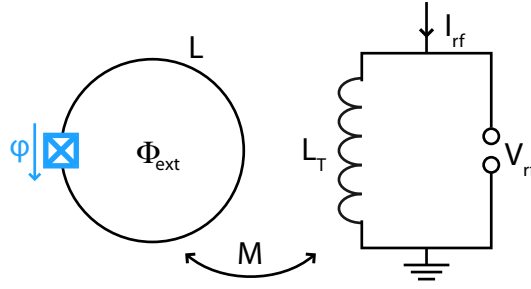


Figure B.5: Circuit diagram of the rf SQUID which is formed only by a single JJ with phase φ in a SC loop (inductance L). It is coupled to an oscillating tank circuit (inductance L_T) via a mutual inductance M . Again, an external flux Φ_{ext} threads the loop. V_{rf} is the readout signal.

The supercurrent in the loop is just that of a single JJ,

$$I_s^{\text{rf}} = I_c \sin \left(2\pi \frac{\Phi}{\Phi_0} \right). \quad (\text{B.61})$$

In the case of the rf SQUID the circulating current and the supercurrent are identical, $I_{\text{circ}} = I_s^{\text{rf}}$. Therewith, we can determine the total flux Φ in the loop,

$$\Phi = \Phi_{\text{ext}} + LI_{\text{circ}} = \Phi_{\text{ext}} + LI_c \sin \left(2\pi \frac{\Phi}{\Phi_0} \right). \quad (\text{B.62})$$

The screening parameter for the rf SQUID is $\beta_{L,\text{rf}} = 2\pi \frac{LI_c}{\Phi_0}$; note that $\beta_{L,\text{rf}} = \Lambda^{-1}$ with $\Lambda = L_{J,0}/L$. Again, for $\beta_{L,\text{rf}} \ll 1$ the total flux would just be the external flux. For $\beta_{L,\text{rf}} \gtrsim 1$, the magnetic energy of the loop $E_L = \Phi_0^2/4\pi^2 L$ is in the order of the Josephson coupling energy $E_L = \Phi_0 I_c/2\pi$ ($\beta_{L,\text{rf}} = E_J/E_L$). In this regime, the induced flux is just $\Phi_0 - \Phi_{\text{ext}} \bmod 1$ or $-\Phi_{\text{ext}}$ to reach an integer multiple of Φ_0 in the loop.

We do not neglect the induced flux since SC qubits that consist of rf SQUIDs are build with the intent to have a non-vanishing inductance L . The kinetic energy of the rf SQUID is, again, given by the charging energy $E_c \hat{N}^2$. The potential energy consists of two parts. The first part is the Josephson coupling energy having its seeds in the supercurrent. The second part is due to the magnetic energy of the flux in the loop¹³. It is generated by the circulating screening current I_{circ} ; thus, the magnetic energy is $\frac{1}{2} LI_{\text{circ}}^2 = (\Phi - \Phi_{\text{ext}})^2/2L$. Therefore, the total Hamiltonian of the rf SQUID reads

$$\mathcal{H}_{\text{rf}} = E_c \hat{N}^2 + \frac{(\Phi - \Phi_{\text{ext}})^2}{2L} - E_J \cos \left(2\pi \frac{\Phi}{\Phi_0} \right). \quad (\text{B.63})$$

The first term of the Hamiltonian, corresponding to the kinetic energy, can be neglected since the number of Cooper pairs is constant in absence of macroscopic quantum tunnelling.

¹³We have neglected the magnetic energy in the Hamiltonian of the dc SQUID since we have used $L \approx 0$. The magnetic energy would also appear in dc SQUIDs for large junction sizes.

Appendix C

Detailed Calculations on SC Qubits

In this part of the appendix, we give details on some calculations that would go beyond the scopes of the main part of the thesis.

C.1 Charge Qubit Hamiltonian in the Charge Basis

To derive the charge representation of the CPB Hamiltonian, we start in the *phase representation* $|\varphi\rangle$,

$$\mathcal{H} = E_c \left(\hat{N} - N_g \right)^2 - \frac{E_J}{2} \left(e^{i\hat{\varphi}} + e^{-i\hat{\varphi}} \right). \quad (\text{C.1})$$

N and $\hat{\varphi}$ are canonically conjugated variables, $[\hat{N}, \hat{\varphi}] = -i$ and therefore $\hat{N} = |\varphi\rangle - i \frac{\partial}{\partial \hat{\varphi}} \langle \varphi|$ (see App. B.3.3) and vice versa $\hat{\varphi} = |N\rangle + i \frac{\partial}{\partial N} \langle N|$. We want to express the Hamiltonian (C.1) in the *charge representation* $|N\rangle$. For this purpose, we firstly write the number operator as $\hat{N} = d^\dagger d = \sum_N N |N\rangle \langle N|$, where d^\dagger and d are bosonic creation and annihilation operators for Cooper pairs, respectively, that obey the commutation relations:

$$[d, d^\dagger] = 1, \quad [d^\dagger, d^\dagger] = [d, d] = 0. \quad (\text{C.2})$$

According to [99; 118], the creation and annihilation operators in terms of \hat{N} and $\hat{\varphi}$ are

$$\begin{aligned} d &= e^{i\hat{\varphi}} \hat{N}^{1/2}, \\ d^\dagger &= \left(e^{i\hat{\varphi}} \hat{N}^{1/2} \right)^\dagger = \hat{N}^{1/2} e^{-i\hat{\varphi}}, \end{aligned} \quad \text{with} \quad \hat{N}^{1/2} = \sum_N \sqrt{N} |N\rangle \langle N|. \quad (\text{C.3})$$

d and d^\dagger fulfill the commutation relations (C.2) and the condition $\hat{N} = d^\dagger d$:

$$d^\dagger d = \hat{N}^{1/2} e^{-i\hat{\varphi}} e^{i\hat{\varphi}} \hat{N}^{1/2} = \hat{N}, \quad (\text{C.4a})$$

$$dd^\dagger = e^{i\hat{\varphi}} \hat{N} e^{-i\hat{\varphi}} = e^{i\hat{\varphi}} \left(-i \frac{\partial}{\partial \hat{\varphi}} \right) e^{-i\hat{\varphi}} = 1 + \hat{N}, \quad (\text{C.4b})$$

$$\Rightarrow [d, d^\dagger] = dd^\dagger - d^\dagger d = 1, \quad [d, d] = [d^\dagger, d^\dagger] = 0. \quad (\text{C.4c})$$

Therewith, the Hamiltonian in the charge representation reads

$$\mathcal{H}_{\text{CQ}} = \sum_N \left(E_c (N - N_g)^2 |N\rangle \langle N| - \frac{E_J}{2} (|N+1\rangle \langle N| + |N\rangle \langle N+1|) \right). \quad (\text{C.5})$$

Note that this representation is only possible in the charge regime, where $E_J/E_c \ll 1$ since N is only a good quantum number in this regime.

C.2 Nonlinear Oscillator

Since we need the theory of nonlinear oscillators several times in this thesis, we recapitulate the basic theoretical description of such a system in this part of the appendix. We start with the Hamiltonian of a nonlinear oscillator

$$\mathcal{H} = \mathcal{H}_0 + \mathcal{H}_1, \quad (\text{C.6a})$$

with

$$\mathcal{H}_0 = \frac{p^2}{2m} + \frac{1}{2}m\omega^2 x^2, \quad (\text{C.6b})$$

$$\mathcal{H}_1 = C_4 x^4, \quad \text{or} \quad \mathcal{H}_1 = C_3 x^3. \quad (\text{C.6c})$$

Here, $p = \frac{\hbar}{i} \frac{\partial}{\partial x}$ is the momentum operator, m the mass of the particle¹, ω the oscillator frequency, and C_4 (C_3) is a constant associated with the nonlinearity x^4 (x^3). \mathcal{H}_0 describes the usual harmonic oscillator, \mathcal{H}_1 contains the nonlinearities that can for example be quartic, cubic, or both.

We now consider the quartic nonlinearity $\mathcal{H}_1 = C_4 x^4$. Following the usual steps for the solution of the harmonic oscillator (see e.g. [16]), we firstly introduce the bosonic creation and annihilation operators d^\dagger and d ,

$$d^\dagger = \frac{1}{\sqrt{2\hbar\omega m}} (\omega m x - ip), \quad d = \frac{1}{\sqrt{2\hbar\omega m}} (\omega m x + ip), \quad (\text{C.7a})$$

with the inversion

$$x = \sqrt{\frac{\hbar}{2\omega m}} (d + d^\dagger), \quad p = -i\sqrt{\frac{\hbar\omega m}{2}} (d - d^\dagger). \quad (\text{C.7b})$$

\mathcal{H}_0 and \mathcal{H}_1 in terms of d and d^\dagger thus read

$$\mathcal{H}_0 = \hbar\omega \left(d^\dagger d + \frac{1}{2} \right), \quad \mathcal{H}_1 = \hbar\omega_4 (d + d^\dagger)^4, \quad (\text{C.8})$$

with²

$$\hbar\omega_4 = C_4 \cdot \left(\frac{\hbar}{2\omega m} \right)^2. \quad (\text{C.9})$$

The actions of d^\dagger and d are, as usual,

$$d^\dagger |k^0\rangle = \sqrt{k} |(k-1)^0\rangle, \quad d |k^0\rangle = \sqrt{k+1} |(k+1)^0\rangle, \quad d^\dagger d |k^0\rangle \equiv \hat{k} |k^0\rangle = k |k^0\rangle, \quad (\text{C.10})$$

where $|k^0\rangle$ denotes the eigenfunctions of the pure oscillator Hamiltonian, \mathcal{H}_0 , and k the occupation number ($\hat{k} = d^\dagger d$ being the occupation number operator). We now assume the nonlinearity part \mathcal{H}_1 to be small compared with \mathcal{H}_0 ($\omega_4 \ll \omega$). Therefore, we can apply a first-order Rayleigh–Schrödinger perturbation theory [16]. The non-perturbed eigenvalues of \mathcal{H}_0 are

$$E_k^0 = \hbar\omega k, \quad k = 0, 1, 2, \dots, \quad (\text{C.11})$$

¹ m does not have to be an actual mass, but can also represent an energy.

²For the cubic nonlinearity: $\hbar\omega_3 = C_3 \cdot \left(\frac{\hbar}{2\omega m} \right)^{3/2}$.

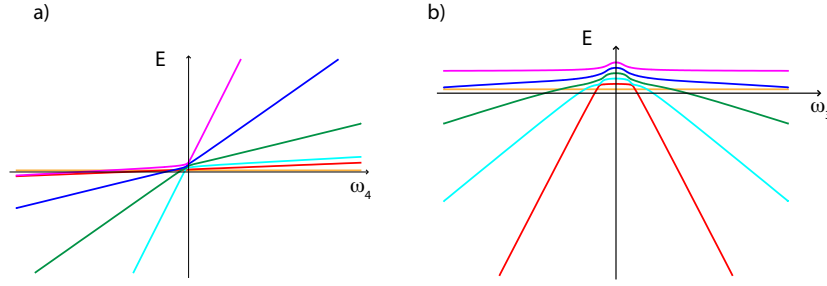


Figure C.1: Energy landscape of the nonlinear resonator with a nonlinearity **(a)** $\hbar\omega_4(d + d^\dagger)^4$ and **(b)** $\hbar\omega_3(d + d^\dagger)^3$. Both nonlinearities result in an anharmonic level spacing. The spectrum was calculated by diagonalizing a part of the Hamiltonian with the program Mathematica.

with corresponding oscillator eigenfunctions $|k^0\rangle$. We have neglected the zero point energy $\hbar\omega/2$ in Eq. (C.11). The first-order corrections to these eigenvalues are

$$E_k^1 = \langle k^0 | \mathcal{H}_1 | k^0 \rangle. \quad (\text{C.12})$$

Expanding the term $(d + d^\dagger)^4$ in Eq. (C.8) we get

$$(d + d^\dagger)^4 = \underbrace{(6\hat{k}^2 + 6\hat{k} + 3)}_{\text{diagonal}} + d^4 + (d^\dagger)^4 + (4\hat{k} + 6)d^2 + (4\hat{k} - 2)(d^\dagger)^2. \quad (\text{C.13})$$

We observe that $(d + d^\dagger)^4$ contains parts that are diagonal in the $|k^0\rangle$ eigenbasis. Therewith, we obtain

$$E_k^1 = \hbar\omega_4 (6k^2 + 6k + 3). \quad (\text{C.14})$$

The nonlinearity of the x^4 -term in the original Hamiltonian (C.6a) yields a anharmonicity in the energy levels. The full energy levels in first-order perturbation theory are $E_k = E_k^0 + E_k^1$; therewith, we obtain the level spacing between two levels:

$$\Delta E = E_{k+1} - E_k = \hbar\omega + \hbar\omega_4 \cdot 12(k+1) \propto k. \quad (\text{C.15})$$

The level spacing is no longer homogeneous due to the energy corrections; it depends on the quantum number k .

In general, a term $\propto x^4$ (or $\propto x^3$) in the Hamiltonian results in an anharmonic level spacing. Fig. C.1(a) shows the energy spectrum of a nonlinear oscillator with a quartic nonlinearity $\hbar\omega_4(d + d^\dagger)^4$. For $\omega_4 > 0$, the level spacing increases with increasing quantum number. For $\omega_4 < 0$ the level spacing decreases with increasing quantum number. For comparison, Fig. C.1(b) shows the energy spectrum of a nonlinear oscillator with a cubic nonlinearity $\hbar\omega_3(d + d^\dagger)^3$. For all values of $\omega_3 \neq 0$, the level spacing decreases with increasing quantum number. A nonlinearity with both quartic and cubic terms has a more complex structure. However, a sufficiently large anharmonicity is still available.

C.3 Minima of the PCQ Potential

In this part of the appendix we show the detailed calculation of the minima and maxima of the PCQ potential. We start with the potential of the PCQ in the φ_\pm representation,

$$U(\varphi_+, \varphi_-) = -E_J [2 \cos \varphi_+ \cos \varphi_- + \alpha(2\pi f + \cos 2\varphi_-)], \quad (\text{C.16})$$

with $0 < \alpha < 1$ and $\varphi_{1,2} = (\varphi_+ \pm \varphi_-)/2$. We set the value of the external flux to $\Phi_0/2$ and thus $f = 1/2$; defining $u = U/E_J$ we get

$$u = -2 \cos \varphi_+ \cos \varphi_- + \alpha \cos 2\varphi_-. \quad (\text{C.17})$$

For the following discussion we restrict the values of the phase differences to $\varphi_{1,2} \in \{-\pi, \pi\}$ since the critical values should be mod π , see also Fig. 2.9(a).

To find the critical points of this potential we firstly have to calculate the gradient and then set it to zero,

$$\frac{\partial u}{\partial \varphi_+} = 2 \sin \varphi_+ \cos \varphi_- \stackrel{!}{=} 0, \quad (\text{C.18a})$$

$$\frac{\partial u}{\partial \varphi_-} = 2 [\cos \varphi_+ \sin \varphi_- - 2\alpha \sin \varphi_- \cos \varphi_-] \stackrel{!}{=} 0. \quad (\text{C.18b})$$

where we have used the identity $\sin(2x) = 2 \sin x \cos x$ in Eq. (C.18b). Therewith, we find several possible critical points in one $\pi \times \pi$ cell,

$$(\varphi_+, \varphi_-)^{(1)} = (0 \bmod \pi, 0 \bmod \pi), \quad (\text{C.19a})$$

$$(\varphi_+, \varphi_-)^{(2)} = (0, \pm \varphi^*), \quad (\text{C.19b})$$

$$(\varphi_+, \varphi_-)^{(3)} = \left(\pm \frac{\pi}{2}, \pm \frac{\pi}{2} \right), \quad (\text{C.19c})$$

where mod π also includes the negative values (e.g. $0 \bmod \pi = -\pi, 0, \pi$) and $\varphi^* = \arccos \frac{1}{2\alpha}$. These pairs now have to be analyzed with the Hessian matrix to decide if they mark a minimum, maximum, or a saddlepoint [119].

The Hessian matrix of the potential u is³

$$H = \begin{pmatrix} \frac{\partial^2 u}{\partial \varphi_+^2} & \frac{\partial^2 u}{\partial \varphi_+ \partial \varphi_-} \\ \frac{\partial^2 u}{\partial \varphi_-^2} & \frac{\partial^2 u}{\partial \varphi_- \partial \varphi_+} \end{pmatrix} = \begin{pmatrix} 2 \cos \varphi_+ \cos \varphi_- & -2 \sin \varphi_+ \sin \varphi_- \\ -2 \sin \varphi_+ \sin \varphi_- & 2 \cos \varphi_+ \cos \varphi_- - 4\alpha (\cos^2 \varphi_- - 1) \end{pmatrix}. \quad (\text{C.20})$$

We now have to determine if the matrices are positive or negative definite which are the criteria for minima or maxima, respectively. A matrix is positive (negative) definite if all eigenvalues are positive (negative). If some eigenvalues are positive and others negative, the matrix is infinite; if the Hessian matrix is infinite for a certain point, this point is a saddlepoint; for more information see [119].

We now analyze the different pairs in Eq. (C.19) separately. For the first points $(\varphi_+, \varphi_-)^{(1)}$ we obtain two cases,

$$(\varphi_+, \varphi_-)^{(1a)} = (0, 0) : \quad H^{(1a)} = \begin{pmatrix} 2 & 0 \\ 0 & 2 - 4\alpha \end{pmatrix}, \quad (\text{C.21a})$$

$$\varphi_+^{(1b)} = \varphi_-^{(1b)} \pm \pi : \quad H^{(1b)} = \begin{pmatrix} -2 & 0 \\ 0 & -2 - 4\alpha \end{pmatrix}. \quad (\text{C.21b})$$

For $\alpha < 1/2$, $H^{(1a)}$ is positive definite and therewith the point $(0, 0)$ is a minimum. For $\alpha > 1/2$, $H^{(1a)}$ is semi-definite; the corresponding points then are saddlepoints. $H^{(1b)}$ is negative definite for all values of α^4 and the points define maxima.

³We have used the identity $\cos(2x) = 2 \cos^2 x - 1$; note, that this is only valid for $x < \pi$.

⁴Remember that $0 < \alpha < 1$.

For the second pair $(\varphi_+, \varphi_-)^{(2)}$ we get

$$(\varphi_+, \varphi_-)^{(2)} = (0, \pm \varphi^*) : \quad H^{(2)} = \begin{pmatrix} 1/\alpha & 0 \\ 0 & -1/\alpha + 4\alpha \end{pmatrix}. \quad (\text{C.22a})$$

For $\alpha > 1/2$, $H^{(2)}$ is positive definite and therewith the points $(0, \pm \varphi^*)$ are minima. $\pm \varphi^*$ is not defined for $\alpha < 1/2$.

For the last pair $(\varphi_+, \varphi_-)^{(3)}$, we obtain

$$(\varphi_+, \varphi_-)^{(3)} = \left(\pm \frac{\pi}{2}, \pm \frac{\pi}{2} \right) : \quad H^{(3)} = \begin{pmatrix} 0 & \pm 2 \\ \pm 2 & 4\alpha \end{pmatrix}, \quad (\text{C.23})$$

$H^{(3)}$ is indefinite for all values of α ; the points $(\varphi_+, \varphi_-)^{(3)}$ are saddlepoints.

For all values of α , the points $(0, \pm \pi)$ and $(\pm \pi, 0)$, corresponding to $(\varphi_1, \varphi_2) = (\pm \pi, \pm \pi)$, are maxima, as shown in Eq. (C.22a). They correspond to the peaks in the potential landscape shown in Fig. 2.9(a). The saddlepoints between these maxima are the points $(\varphi_+, \varphi_-)^{(3)} = (\pm \frac{\pi}{2}, \pm \frac{\pi}{2})$ (see Eq. (C.23)); they correspond to $(\varphi_1, \varphi_2) = (\pm \pi, 0), (0, \pm \pi)$.

For $\alpha < 1/2$, one minimum exists at point $(0,0)$, according to Eq. (C.21a). This minimum bifurcates into the two minima $(0, \pm \varphi^*)$ for $\alpha > 1/2$ (see Eq. (C.22a)). At $\alpha = 1/2$ the points $(\varphi_+, \varphi_-)^{(1a)}$ and $(\varphi_+, \varphi_-)^{(2a)}$ are the same, $(\varphi_+, \varphi_-)^{(1)} = (\varphi_+, \varphi_-)^{(2)} = (0,0)$. In this case, the Hessian matrix $H^{(1a)} = H^{(2a)}$ is positive semidefinite; since the determinant of the matrix is zero, the point $(\varphi_1, \varphi_2) = (0,0)$ is a degenerate critical point (minimum) at $\alpha = 1/2$. Since we want to use the states in the two minima as a qubit, we set $\alpha > 1/2$. The minima are thus located at $(\varphi_1, \varphi_2) = (\varphi^*, -\varphi^*)$ and $(\varphi_1, \varphi_2) = (-\varphi^*, +\varphi^*)$.

Thus, we have four maxima, two minima and five saddlepoints that define the qubit environment. The saddlepoints $(0,0)$ separates minima of the same or neighbouring unit cells; a double well potential as for the rf SQUID is formed between these minima (see Fig. 2.9(c)). The height of the potential at the saddlepoints defines the height of the tunnel barrier; it depends on α .

C.4 Quantization of the 1D Transmission Line Resonator

To calculate the interaction of a qubit with a TLR we firstly have to find a quantum-mechanical expression of the voltage (charge qubit) or the flux (flux qubit) of the transmission line at the position of the qubit. Thus, we have to quantize the field generated by the TLR which we do in this section of the appendix. A transmission line of length l , can be approximated by a 1D model if the height and thickness of the line are much less then the wavelength of the transmitted signal. It can be described by an infinite series of inductors with each node capacitively connected to the ground, as shown in Fig. 2.12; a quantization of the TLR using this approach is given in [22]. We quantize the TLR with a different method, by solving the one-dimensional Maxwell equations for the electric field $\mathcal{E}_y(x,t)$ that is polarized in y -direction and propagates in x -direction and correspondingly the magnetic field $\mathcal{B}_z(x,t)$ that is polarized in z -direction. The x - and y -directions are the in-plane directions in Fig. 2.12, where the TLR defines the x -direction; the z -axis is the out-of-plane axis. We will mainly follow the general quantization arguments of [102] and some specific steps of [22].

The one-dimensional Maxwell equations are

$$\frac{\partial \mathcal{E}_y}{\partial x} = \frac{\partial \mathcal{B}_z}{\partial t}, \quad \frac{\partial \mathcal{E}_y}{\partial t} = \frac{1}{\mu\epsilon} \frac{\partial \mathcal{B}_z}{\partial x}, \quad (\text{C.24})$$

where $\mu = \mu_0\mu_r$ is the permeability and $\epsilon = \epsilon_0\epsilon_r$ the permittivity of the transmission line (ϵ_0 and μ_0 being the vacuum values). The Maxwell equations result in a wave equation

$$\left(\frac{\partial}{\partial x^2} - \frac{1}{v^2} \frac{\partial}{\partial t^2}\right) \mathcal{E}_y = 0, \quad (\text{C.25})$$

with the propagation velocity $c = \frac{1}{\mu\epsilon}$. Eq. (C.25) can be solved by performing a mode expansion of \mathcal{E}_y ,

$$\mathcal{E}_y(x,t) = \sum_k \left(\mathcal{E}_k^-(t) u_k(x) + \mathcal{E}_k^+(t) u_k^*(x) \right). \quad (\text{C.26})$$

Here, $\mathcal{E}_k^\pm(t)$ are the time-dependent expansion coefficients,

$$\mathcal{E}_k^-(t) = \left(\mathcal{E}_k^+(t)\right)^\dagger = \mathcal{N}_k a_k = \mathcal{N}_k a_k(0) e^{-i\omega_k t}, \quad (\text{C.27})$$

where $\omega_k = c \cdot k$ is the frequency of the mode k and a_k (a_k^\dagger) is the bosonic annihilation (creation) operator of the k^{th} resonator mode with the usual commutation relations

$$[a_k, a_{k'}^\dagger] = \delta_{k,k'}, \quad [a_k, a_{k'}] = [a_k^\dagger, a_{k'}^\dagger] = 0. \quad (\text{C.28})$$

\mathcal{N} is a normalization constant that will be chosen such that

$$\mathcal{H}_{\text{TLR}} = \int_0^l dx \left(\frac{\epsilon}{2} \mathcal{E}_y^2(x,t) + \frac{1}{2\mu} \mathcal{B}_z^2(x,t) \right) = \hbar \sum_k \omega_k \left(a_k^\dagger a_k + \frac{1}{2} \right). \quad (\text{C.29})$$

The $u_k(x)$ in Eq.(C.25) are plane waves with

$$u_k(x) = \tilde{\mathcal{N}} e^{ikx} = \tilde{\mathcal{N}} [\cos(kx) + i \sin(kx)], \quad (\text{C.30})$$

where $\tilde{\mathcal{N}}$, again, is a normalization constant such that $\int_0^l dx |u_k|^2 = 1$.

The boundary conditions due to charge neutrality are $\mathcal{E}_y(0,t) = \mathcal{E}_y(l,t) = 0$. Thus, only the sine-part of $u_k(x)$ is a valid solution for $\mathcal{E}_y(x,t)$. Applying the normalization condition for $u_k(x)$, we get ($k = \nu\pi/l$)

$$\mathcal{E}_y(x,t) = i\sqrt{\frac{2}{l}} \sum_{\nu=1}^{\nu_{\text{cutoff}}} \left(\mathcal{N}_\nu a_\nu - \mathcal{N}_\nu^* a_\nu^\dagger \right) \sin\left(\frac{\nu\pi x}{l}\right), \quad (\text{C.31})$$

where ν_{cutoff} takes into account the fact that the TLR is not exactly one-dimensional.

From Eq. (C.24) follows

$$\mathcal{B}_z(x,t) = -i\frac{1}{c}\sqrt{\frac{2}{l}} \sum_{\nu=1}^{\nu_{\text{cutoff}}} \left(\mathcal{N}_\nu a_\nu + \mathcal{N}_\nu^* a_\nu^\dagger \right) \cos\left(\frac{\nu\pi x}{l}\right). \quad (\text{C.32})$$

A convenient choice for \mathcal{N}_ν is

$$\mathcal{N}_\nu = i\sqrt{\frac{\hbar\omega_\nu}{2\epsilon}}. \quad (\text{C.33})$$

with $\omega_\nu = \frac{\nu\pi c}{l}$.

C.4.1 Capacitive Coupling

A charge or a phase qubit couples to the voltage of the resonator via the gate capacitance C_g . The voltage drop over the resonator circuit, V_{rc} , induces an ac part of the dimensionless gate charge in the qubit circuit, N_g^{ac} , which is related to the voltage in the resonator circuit via the gate capacitance C_g as

$$N_g^{\text{ac}} = \frac{C_g}{2e} V_{\text{rc}} = \frac{C_g}{2e} \int dx \mathcal{E}_y(t) = \frac{C_g}{2e} \sum_{\nu=1}^{\nu_{\text{cutoff}}} \sqrt{\frac{\hbar\omega_\nu l}{\nu^2 \pi^2 \epsilon}} (a_\nu + a_\nu^\dagger) \cos\left(\frac{\nu\pi x}{l}\right). \quad (\text{C.34})$$

As shown in Fig. 2.12, the charge qubit is fabricated at the centre ($x = l/2$) of the resonator. Since the mode $\nu = 1$ is minimal at this point, the qubit is coupled to the mode $\nu = 2$ of the resonator at low temperatures. The dimensionless rms charge between the centre conductor and the ground plane then is $N_{\text{rms}}^{(2)} = \frac{C_g}{4\pi\epsilon} \sqrt{\hbar\omega_r l/2\epsilon}$ ($1/\sqrt{2}$ due to the sinusoidal oscillations), with $\omega_r = \omega_2 = 2\pi c/l$. The dimensionless gate charge felt by the qubit then is

$$N_g^{\text{ac}} = N_{\text{rms}}^{(2)} (a + a^\dagger). \quad (\text{C.35})$$

For the phase qubit, that is fabricated at the end of the TLR (Fig. 2.15), the $\nu = 1$ mode ($\lambda/2$ -mode) couples to the qubit. Therefore, the rms value of the dimensionless gate charge for the coupling to a phase qubit is $N_{\text{rms}}^{(1)} = N_{\text{rms}}^{(2)}/\sqrt{2}$, since the resonance frequency now is $\omega_r/\sqrt{2} = \omega_1$.

We now consider the TLR as an infinite series of inductors (total inductance L_r) with each node capacitively (total capacitance C_r) connected to the ground. At the moment where the energy is purely that of the electric field, we have $C_r V_{\text{rc,max}} = \hbar\omega_r/2$. Thus, we can rewrite $N_{\text{rms}}^{(2)}$ and ω_r in terms of C_r and L_r ,

$$N_{\text{rms}}^{(2)} = \frac{C_g V_{\text{max}}}{2e \sqrt{2}} = \frac{C_g}{2e} \sqrt{\frac{\hbar\omega_r}{2C_r}}, \quad \text{with} \quad \omega_r = \frac{1}{\sqrt{L_r C_r}}. \quad (\text{C.36})$$

C.4.2 Inductive Coupling

A flux qubit couples to the flux of the TLR via the mutual inductance M . To calculate this interaction, we firstly remove the complex parts of \mathcal{B}_z via unitary transformations and obtain

$$\mathcal{B}_z(x,t) = \sum_{\nu=1}^{\nu_{\text{cutoff}}} \sqrt{\frac{\hbar\omega_\nu \mu}{l}} (a_\nu + a_\nu^\dagger) \cos\left(\frac{\nu\pi x}{l}\right). \quad (\text{C.37})$$

The flux in the qubit circuit, Φ_x^{ac} , is related to the flux in the TLR circuit, Φ_{rc} , via the mutual inductance M and the TLR inductance L_r ,

$$\Phi_x^{\text{ac}} = \frac{M}{L_r} \Phi_{\text{rc}} = \frac{M}{L_r} \int_A dA \mathcal{B}_z(x,t) = \frac{MA}{L_r} \sum_{\nu=1}^{\nu_{\text{cutoff}}} \sqrt{\frac{\hbar\omega_\nu \mu}{l}} (a_\nu + a_\nu^\dagger) \cos\left(\frac{\nu\pi x}{l}\right), \quad (\text{C.38})$$

with A being the face of the qubit. At low temperatures, the qubit, again, couples to the $\nu = 2$ mode. The rms flux between the centre conductor and the ground plane then is $\Phi_{\text{rms}}^{(2)} = MA\sqrt{\hbar\omega_r \mu/2l}/L_r$, with, again, $\omega_r = \omega_2 = 2\pi c/l$. The flux felt by the qubit is

$$\Phi_x^{\text{ac}} = \Phi_{\text{rms}}^{(2)} (a + a^\dagger). \quad (\text{C.39})$$

Again, we want to rewrite $\Phi_{\text{rms}}^{(2)}$ and ω_r in terms of the inductance and capacitance of the TLR. Using $\Phi_{\text{rc,max}}^2/2L_r = \hbar\omega_r/2$, with Φ_{max} being the maximal flux in the TLR circuit, we get

$$\Phi_{\text{rms}}^{(2)} = M\sqrt{\frac{\hbar\omega_r}{2L_r}}, \quad \text{with} \quad \omega_r = \frac{1}{\sqrt{L_r C_r}}. \quad (\text{C.40})$$

The mutual inductance M for the $\nu = 2$ mode can be estimated via a semi-classical approach (cp. [75]). M is given by

$$M = \frac{\Phi_{\text{rc,rms}}^2}{I_{\text{qc,rms}}^2}, \quad (\text{C.41})$$

with I_{qc} being the current induced in the qubit circuit. I_{qc} can be estimated with the Biot-Sawart law for an infinite 1D conductor,

$$I_{\text{qc,rms}}^2 \approx \frac{2\pi r}{\mu_0} \mathcal{B}_{z,\text{rms}}^2, \quad (\text{C.42})$$

with r is half the width of the gap between the centre conductor and the ground plane (we assume the qubit is placed at the centre of the gap). The mutual inductance then is

$$M \approx \frac{\mu_0 A \mathcal{B}_{z,\text{rms}}^2}{2\pi r \mathcal{B}_{z,\text{rms}}^2} = \frac{\mu_0 A}{2\pi r}. \quad (\text{C.43})$$

C.5 Dispersive Regime of the Generalized JC Model

The following calculation can be reduced to the normal JC model by constraining k to $k = 0, 1$. The Hamiltonian of the generalized JC model is (cp. (2.50))

$$\mathcal{H}_{\text{gJC}} = \hbar \sum_k \omega_k |k\rangle\langle k| + \hbar\omega_r a^\dagger a + \hbar \sum_k g_{k,k+1} \left[|k\rangle\langle k+1| a^\dagger + |k+1\rangle\langle k| a \right]. \quad (\text{C.44})$$

The transition between the two levels $|k\rangle$ and $|k+1\rangle$ is coupled via $g_{k,k+1} = g_{k+1,k}$ and detuned from the resonator by $\Delta_{k,k+1} = \omega_{k+1} - \omega_k - \omega_r$, whereas the different transitions all are off-resonant ($|\Delta_{k,k+1}| \gg \sqrt{n+1} g_{k,k+1}$). To calculate the effective Hamiltonian (cp. Sec. A.5), we choose the unitary transformation as [25]

$$U = \exp \left[\sum_k \underbrace{\frac{g_{k,k+1}}{\Delta_k} \left(|k+1\rangle\langle k| a - |k\rangle\langle k+1| a^\dagger \right)}_{\equiv S_k} \right], \quad (\text{C.45})$$

Again, we expand the transformation up to the order $g_{k,k+1} g_{k',k'+1} / \Delta_{k,k+1}$; for this, we have to calculate the following commutators,

$$\left[\sum_l S_l, \hbar \sum_k \omega_k |k\rangle\langle k| + \hbar\omega_r a^\dagger a \right] = -\hbar \sum_k g_{k,k+1} \left[|k\rangle\langle k+1| a^\dagger + |k+1\rangle\langle k| a \right], \quad (\text{C.46})$$

and

$$\begin{aligned}
& \left[\sum_l S_l, \hbar \sum_k \left[|k\rangle\langle k+1| a^\dagger + |k+1\rangle\langle k| a \right] \right] \\
&= \hbar \sum_k \left\{ \frac{g_{k,k+1}^2}{\Delta_{k,k+1}} \left[2a^\dagger a (|k+1\rangle\langle k+1| - |k\rangle\langle k|) + 2|k+1\rangle\langle k+1| \right] \right. \\
& \quad + \frac{g_{k,k+1}g_{k-1,k}}{\Delta_{k,k+1}} \left[a^2 |k+1\rangle\langle k-1| + (a^\dagger)^2 |k-1\rangle\langle k+1| \right] \\
& \quad \left. + \frac{g_{k,k+1}g_{k+1,k+2}}{\Delta_{k,k+1}} \left[a^2 |k+2\rangle\langle k| + (a^\dagger)^2 |k-2\rangle\langle k| \right] \right\}. \tag{C.47}
\end{aligned}$$

Using Eq. (A.42), we obtain the effective Hamiltonian

$$\begin{aligned}
\mathcal{H}_{\text{gJC}}^{\text{eff}} &= \hbar \sum_k \omega_k |k\rangle\langle k| + \hbar\omega_r a^\dagger a \\
& \quad + \hbar \sum_k \frac{g_{k,k+1}^2}{\Delta_{k,k+1}} \left(a^\dagger a (|k+1\rangle\langle k+1| - |k\rangle\langle k|) + |k+1\rangle\langle k+1| \right) \\
& \quad + \hbar \sum_k \frac{g_{k,k+1}g_{k+1,k+2}}{2\Delta_{k,k+1}} \left(a^2 |k+2\rangle\langle k| + (a^\dagger)^2 |k\rangle\langle k+2| \right) \\
& \quad + \hbar \sum_k \frac{g_{k,k+1}g_{k-1,k}}{2\Delta_{k,k+1}} \left(a^2 |k+1\rangle\langle k-1| + (a^\dagger)^2 |k-1\rangle\langle k+1| \right). \tag{C.48}
\end{aligned}$$

Changing the index of the last sum in Eq. (C.48) and combining the other terms we obtain the effective Hamiltonian of the generalized JC model

$$\begin{aligned}
\mathcal{H}_{\text{gJC}}^{\text{eff}} &= \hbar \sum_k \omega_k |k\rangle\langle k| + \hbar\omega_r a^\dagger a + \hbar \sum_k \chi_{k,k+1} |k+1\rangle\langle k+1| \\
& \quad - \hbar\chi_{0,1} a^\dagger a |0\rangle\langle 0| + \hbar \sum_{k=1}^{\infty} (\chi_{k-1,k} - \chi_{k,k+1}) a^\dagger a |k\rangle\langle k| \\
& \quad + \hbar \sum_k \eta_k \left(a^2 |k+2\rangle\langle k| + (a^\dagger)^2 |k\rangle\langle k+2| \right),
\end{aligned}$$

with

$$\chi_{k,k+1} = \frac{g_{k,k+1}^2}{\Delta_{k,k+1}} \quad \text{and} \quad \eta_k = g_{k,k+1}g_{k+1,k+2} \left(\frac{1}{\Delta_{k+1,k+2}} - \frac{1}{\Delta_{k,k-1}} \right). \tag{C.49}$$

The terms in the last line of Eq. (C.49) describe two-photon transitions and are negligible as compared to the remaining terms due to the smallness of the parameter η_k .

Therefore, the level $|k\rangle$ is shifted by $\hbar\chi_{k,k+1}$; again, an ac Stark shift (a state-dependent shift of the cavity frequency) occurs.

C.6 Time-Dependent “Constant” Term

In this section, we show that a time-dependent term in the Hamiltonian that does not couple to the rest of the system via an operator (we denote this with “constant”) can be neglected

when calculating the time evolution of the wavefunction. We consider a Hamiltonian of the form

$$\mathcal{H}(t) = \mathcal{H}'(t) + C(t), \quad (\text{C.50})$$

with $C(t)$ being a time-dependent, “constant” term, $[\mathcal{H}'(t), C(t)] = 0$. The final time-evolution operator (A.4), not taking into account the time ordering operator, thus reads

$$U(t, t_0) = e^{-\frac{i}{\hbar} \int_0^t H_0(t') dt'} e^{-\frac{i}{\hbar} \int_0^t C(t') dt'}. \quad (\text{C.51})$$

The time-dependent, constant term $C(t)$ is just a function of t , e.g. $C(t) \propto \cos(\omega t)$. Therefore, this term simply yields a global phase in the time-evolution operator. Due to this, time-dependent, “constant” terms in the Hamiltonian can be neglected.

Appendix D

Additional Information on the Mesoscopic Shelving Readout

In this part of the appendix we discuss some properties of coherent states and quantum-optical characteristic functions, where we mainly follow the arguments and explanations given in [99; 120]. After this, we give details on calculations of the MSR.

D.1 Coherent States

A coherent state is a specific kind of eigenstate of the harmonic oscillator whose dynamics most closely represents the behaviour of a classical field. In contrast to Fock states, the photon number of a coherent state is indefinite and the phase is well-defined; therefore, the coherent state is an eigenstate of the annihilation operator a . Coherent states are used to describe fields with a minimal uncertainty such as a laser; these fields are then most closely to classical fields. A single-mode coherent state $|\alpha\rangle$ is generated by the action of the *displacement operator* $\mathcal{D}(\alpha)$ on the vacuum state $|0\rangle$,

$$|\alpha\rangle = \mathcal{D}(\alpha)|0\rangle \equiv e^{\alpha a^\dagger - \alpha^* a}|0\rangle, \quad (\text{D.1})$$

where $\alpha = |\alpha|e^{i\phi}$ is a complex number. The displacement operator is a unitary operator,

$$\mathcal{D}^\dagger(\xi) = \mathcal{D}(-\xi) \equiv \mathcal{D}^{-1}(\xi). \quad (\text{D.2})$$

Using the Baker-Campbell-Hausdorff relation, we get

$$\mathcal{D}(\alpha) = e^{\alpha a^\dagger} e^{-\alpha^* a} e^{-\frac{|\alpha|^2}{2}}. \quad (\text{D.3})$$

It then follows from Eq. (D.1) and $e^{-\delta^* a}|0\rangle = |0\rangle$ that the coherent state can be expressed as

$$|\alpha\rangle = e^{-\frac{|\alpha|^2}{2}} \sum_{n=0}^{\infty} \frac{\alpha^n}{\sqrt{n!}} |n\rangle, \quad (\text{D.4})$$

and analogue

$$\langle\alpha| = e^{\frac{|\alpha|^2}{2}} \sum_{n=0}^{\infty} \frac{(\alpha^*)^n}{\sqrt{n!}} \langle n|. \quad (\text{D.5})$$

We now calculate the action of the annihilation operator a on $|\alpha\rangle$,

$$\begin{aligned} a|\alpha\rangle &= e^{-\frac{|\alpha|^2}{2}} \sum_{n=0}^{\infty} \frac{\alpha^n}{\sqrt{n!}} \sqrt{n} |n-1\rangle = e^{-\frac{|\alpha|^2}{2}} \sum_{n=0}^{\infty} \frac{\alpha^n}{\sqrt{n!}} \sqrt{n} |n-1\rangle \\ &= \alpha e^{-\frac{|\alpha|^2}{2}} \sum_{(n-1)=0}^{\infty} \frac{\alpha^{n-1}}{\sqrt{(n-1)!}} |n-1\rangle = \alpha |\alpha\rangle. \end{aligned} \quad (\text{D.6})$$

The coherent state is an eigenstate of the annihilation operator which means that its photon number is indefinite. Vice versa, we have $\langle\alpha|a^\dagger = \alpha^* \langle\alpha|$. The mean photon number of the coherent state is given by

$$\langle\hat{n}\rangle = \langle\alpha|a^\dagger a|\alpha\rangle = \alpha\alpha^* \langle\alpha|\alpha\rangle = |\alpha|^2. \quad (\text{D.7})$$

The photon number probability distribution $P(n)$ for the coherent state $|\alpha\rangle$ in Eq. (D.5) then is

$$P(n) = |\langle n|\alpha\rangle|^2 = e^{-|\alpha|^2} \frac{|\alpha|^{2n}}{n!} = e^{-\langle\hat{n}\rangle} \frac{\langle\hat{n}\rangle^n}{n!}. \quad (\text{D.8})$$

The coherent state $|\alpha\rangle$ is normalized, since $\langle\alpha|\alpha\rangle = \langle 0|\mathcal{D}^\dagger(\alpha)\mathcal{D}(\alpha)|0\rangle = 1$, but different coherent states are not orthogonal. Let us suppose two coherent states $|\alpha\rangle$ and $|\beta\rangle$; the scalar product of these two states is given by

$$\langle\alpha|\beta\rangle = e^{-|\alpha|^2/2} e^{-|\beta|^2/2} e^{\delta^*\beta} \neq \delta(\alpha - \beta). \quad (\text{D.9})$$

Thus, the coherent states form an over-complete set of eigenstates in which the identity can be resolved in terms of the coherent states via the two-dimensional Fourier integral

$$\frac{1}{\pi} \int d^2\alpha |\alpha\rangle\langle\alpha| = \sum_{n=0}^{\infty} |n\rangle\langle n| = \mathbf{1}, \quad (\text{D.10})$$

where $\int d^2\alpha = \int_{-\infty}^{\infty} d\alpha_r d\alpha_i$ denotes a double integral over the whole complex α -plane (α_r and α_i being the real and imaginary part of α , respectively). Therewith, the trace of an operator \hat{O} evaluated in the coherent state basis is

$$\text{Tr}(\hat{O}) = \frac{1}{\pi} \int d^2\alpha \langle\alpha|\hat{O}|\alpha\rangle. \quad (\text{D.11})$$

D.2 Characteristic Functions and Quasi-Probability Distributions

The quantum description of the properties of the electromagnetic field is necessarily a probabilistic one in that we can only find the probability that a given property of the field has a particular value. Consequently, it might be suitable to use the methods of (classical) statistical physics and to obtain the probability distribution of the possible value of a given property of the field. A characteristic function or a quasi-probability distribution contains all the information necessary to reconstruct the density matrix for the state, including the photon number statistics. In this sense, they are alternative complete descriptions of the state of the field. Both rely on the properties of the coherent states and the displacement operator.

The p -ordered characteristic function is defined via the expectation value of the displacement operator by

$$\chi(\xi, p) = \text{Tr} \left[\rho \mathcal{D}(\xi) \right] e^{p|\xi|^2/2}, \quad (\text{D.12})$$

where ξ is a complex-valued variable with real and imaginary part x and y , respectively. Each value of the parameter p corresponds to a specific ordering of the creation and annihilation operators in this expression; specifically, $p = 1$ represents the normal ordering (P-representation), $p = -1$ the antinormal ordering (Q-representation), and $p = 0$ the symmetric ordering (Wigner-representation) of the operators a^\dagger and a (the specific expressions for these orderings are given below in Eq. (D.14)). If the characteristic function is known, the expectation value of any p -ordered combination of a^\dagger and a can be calculated by differentiation with

$$\langle a^{\dagger m} a^n \rangle_p = \left(\frac{\partial}{\partial \xi} \right)^m \left(-\frac{\partial}{\partial \xi} \right)^n \chi(\xi, p) \Big|_{\xi=0} \quad (\text{D.13})$$

where

$$\langle a^{\dagger m} a^n \rangle_p = \begin{cases} a^{\dagger m} a^n, & p = 1, \\ a^n a^{\dagger m}, & p = -1, \\ \frac{1}{2} [a^{\dagger m} a^n + a^n a^{\dagger m}], & p = 0. \end{cases} \quad (\text{D.14})$$

An alternative to the characteristic function is the quasi-probability distribution $P(\alpha, p)$ that is defined as

$$P(\alpha, p) = \frac{1}{\pi^2} \int d^2 \xi \chi(\xi, p) e^{\alpha \xi^* - \alpha^* \xi}. \quad (\text{D.15})$$

This is a two-dimensional Fourier transform of $\chi(\xi, p)$, where $\int d^2 \xi = \int_{-\infty}^{\infty} dx dy$ is an integral over the complex ξ -plane. Since the quasi-probability distribution $P(\alpha, p)$ is not always positive, a consequent interpretation as a probability distribution is not always possible.

For $p = 1$ we get the Glauber-Sudarshan P-representation of the quasi-probability distribution, $P(\alpha) = P(\alpha, 1)$. The density matrix then can be expressed directly with

$$\rho = \int d^2 \alpha P(\alpha) |\alpha\rangle \langle \alpha|, \quad (\text{D.16})$$

where $|\alpha\rangle$ is a coherent state. The $p = 0$ -ordered quasi-probability distribution is called Wigner (quasi-probability) distribution or function. It can be expressed by

$$W(\alpha) = \frac{2}{\pi^2} \int d^2 \beta \langle \alpha + \beta | \rho | \alpha - \beta \rangle \exp(\alpha^* \beta - \alpha \beta^*). \quad (\text{D.17})$$

For $p = -1$, we get the Q-function, $Q(\alpha) = P(\alpha, -1)$. The representation for $Q(\alpha)$ is simple,

$$Q(\alpha) = \frac{1}{\pi} \langle \alpha | \rho | \alpha \rangle. \quad (\text{D.18})$$

Thus, the Q-function will have zeros for all pure states other than the coherent state (and a squeezed state, see [99]). Unlike $P(\alpha)$ and $W(\alpha)$, $Q(\alpha)$ has an interpretation as a real probability distribution.

Let us now have a look on the application of the characteristic functions and the quasi-probability distributions. A master equation for the density $\rho(t)$ is an operator equation. It is generally not possible to solve this operator equation directly to find $\rho(t)$ in operator form

since the time-dependence is in general not harmonic. We can only derive equations of motion for the expectation values, and if these form a suitable closed set, solve these equations for time-dependent operator averages. However, we can establish a correspondence between the quantum-mechanical operators and ordinary functions, such that the quantities of interest can be calculated with the characteristic functions or the corresponding quasi-probability distributions. The operator master equation then transforms into an equivalent partial differential equation for either the characteristic function or a quasi-probability distribution which represents ρ . The action of a number operator on ρ is then transformed into that of the corresponding ordering of differential operators on $P(\alpha, p)$.

All of the representations introduced above can be used for this transformation. However, the P-distribution may be a generalized function; the Q- and the Wigner distributions are always well-behaved functions. Therefore, the Q- or Wigner representation is often the choice for studies of nonclassical states of the electromagnetic field; they provide the basis for the quantum-classical correspondence. Since the partial differential equations can be solved easier in the Wigner representation, we choose this representation for the dissipative model of the MSR in Sec. 4.4.2.

D.3 Detailed Calculations on the MSR

D.3.1 Master Equation in Terms of ρ_{iF}

To transform the master equation (4.23) for ρ_{QF} onto a set of equations for ρ_{iF} , we have to calculate the commutator with the effective Hamiltonian (4.14) ($k, l = \{+, -, g\}$),

$$\begin{aligned} & \left[\sigma^x (a^\dagger + a), |k\rangle\langle l| \otimes \rho_{iF} \right] = \sigma^x |k\rangle\langle l| \otimes [a^\dagger + a, \rho_{iF}] + [\sigma^x, |k\rangle\langle l|] \otimes \rho_{iF} (a^\dagger + a) \\ & = (|+\rangle\langle l| \delta_{+,l} - |-\rangle\langle l| \delta_{-,l}) [a^\dagger + a, \rho_{iF}] \\ & \quad + \{(|+\rangle\langle l| \delta_{+,l} - |-\rangle\langle l| \delta_{-,l}) - (|k\rangle\langle +| \delta_{+,k} - |k\rangle\langle -| \delta_{-,k})\} \rho_{iF} (a^\dagger + a). \end{aligned} \quad (\text{D.19})$$

Therewith, we obtain a decoupled set of differential equations (4.29).

D.3.2 Transformation into Characteristic Functions

To map the set of equations for the density operators (4.29) onto a set of partial differential equations for the characteristic functions, we calculate the expectation value

$$\chi_i(\xi, t) = \text{Tr}_F [\rho_{iF}(t) \mathcal{D}(\xi)] \quad (\text{D.20})$$

for the different parts of the equations for the density operators. For simplicity, we will just write ρ instead of ρ_{iF} and Tr instead of Tr_F in the following. We introduce some properties of the displacement operator,

$$\begin{aligned} \mathcal{D}(\xi) &= \exp(\xi a^\dagger - \xi^* a), & \mathcal{D}^\dagger(\xi) \mathcal{D}(\xi) &= 1, & \mathcal{D}^\dagger(\xi) &= \mathcal{D}(-\xi) \equiv \mathcal{D}^{-1}(\xi), \\ \mathcal{D}^\dagger(\xi) a^\dagger \mathcal{D}(\xi) &= a^\dagger + \xi^*, & \mathcal{D}^\dagger(\xi) a \mathcal{D}(\xi) &= a + \xi, \\ a^\dagger \mathcal{D}(\xi) &= \left(\frac{\partial}{\partial \xi} + \frac{1}{2} \xi^* \right) \mathcal{D}(\xi), & \mathcal{D}(\xi) a &= - \left(\frac{\partial}{\partial \xi^*} + \frac{1}{2} \xi \right) \mathcal{D}(\xi), \end{aligned} \quad (\text{D.21})$$

and the cyclic property of the trace

$$\mathrm{Tr} [c_1 c_2 c_3] = \mathrm{Tr} [c_i c_j c_k \epsilon_{ijk}] \quad (\text{D.22})$$

with ϵ_{ijk} being the Levi–Civita symbol.

a) Terms $\propto \mathcal{L}[\sigma^-]\rho$

The Liouvillian term consists of three parts,

$$\mathrm{Tr} [\mathcal{L}[\sigma^-]\rho\mathcal{D}(\xi)] = \mathrm{Tr} \left[-\frac{\kappa}{2} \left(\underbrace{a^\dagger a \rho}_{(1)} - \underbrace{2a \overline{\rho a^\dagger}}_{(2)} + \underbrace{\rho a^\dagger a}_{(3)} \right) \mathcal{D}(\xi) \right]. \quad (\text{D.23})$$

The transformations of these parts are given by

$$\begin{aligned} (1) &= \mathrm{Tr} [a^\dagger a \rho \mathcal{D}(\xi)] = \mathrm{Tr} [\rho \mathcal{D}(\xi) a^\dagger a] = \mathrm{Tr} [\rho \mathcal{D}(\xi) a^\dagger \mathcal{D}^\dagger(\xi) \mathcal{D}(\xi) a] \\ &= \mathrm{Tr} [\rho \mathcal{D}^\dagger(-\xi) a^\dagger \mathcal{D}(-\xi) \mathcal{D}(\xi) a] = \mathrm{Tr} [\rho (a^\dagger - \xi^*) \mathcal{D}(\xi) a] \\ &= - \left(\frac{\partial}{\partial \xi} - \frac{1}{2} \xi^* \right) \left(\frac{\partial}{\partial \xi^*} + \frac{1}{2} \xi \right) \chi(\xi, t), \end{aligned} \quad (\text{D.24})$$

$$(2) = -2 \mathrm{Tr} [a \rho a^\dagger \mathcal{D}(\xi)] = -2 \mathrm{Tr} [\rho a^\dagger \mathcal{D}(\xi) a] = 2 \left(\frac{\partial}{\partial \xi} + \frac{1}{2} \xi^* \right) \left(\frac{\partial}{\partial \xi^*} + \frac{1}{2} \xi \right) \chi(\xi, t), \quad (\text{D.25})$$

and

$$\begin{aligned} (3) &= \mathrm{Tr} [\rho a^\dagger a \mathcal{D}(\xi)] = \mathrm{Tr} [\rho a^\dagger \mathcal{D}(\xi) \mathcal{D}^\dagger(\xi) a \mathcal{D}(\xi)] \\ &= \mathrm{Tr} [\rho a^\dagger \mathcal{D}(\xi) (a^\dagger + \xi)] = - \left(\frac{\partial}{\partial \xi} + \frac{1}{2} \xi^* \right) \left(\frac{\partial}{\partial \xi^*} - \frac{1}{2} \xi \right) \chi(\xi, t). \end{aligned} \quad (\text{D.26})$$

Thus, we obtain

$$\mathcal{L}[\sigma^-]\rho \rightarrow -\frac{\kappa}{2} [(1) + (2) + (3)] = -\frac{\kappa}{2} \left(\xi^* \frac{\partial}{\partial \xi^*} + \xi \frac{\partial}{\partial \xi} \right) \chi(\xi, t) - \frac{\kappa}{2} |\xi|^2 \chi(\xi, t). \quad (\text{D.27})$$

b) Terms $\propto (\mathbf{a}^\dagger + \mathbf{a})$

We have to consider two terms to transform the commutators and anticommutators in Eq. (4.23); they are

$$\begin{aligned} (1) &= \mathrm{Tr} [(a^\dagger + a) \rho \mathcal{D}(\xi)] = \mathrm{Tr} [\rho \mathcal{D}(\xi) a^\dagger] + \mathrm{Tr} [\rho \mathcal{D}(\xi) a] \\ &= \mathrm{Tr} [\rho \mathcal{D}^\dagger(-\xi) a^\dagger \mathcal{D}(-\xi) \mathcal{D}^\dagger(-\xi)] - \left(\frac{\partial}{\partial \xi^*} + \frac{1}{2} \xi \right) \chi(\xi, t) \\ &= \mathrm{Tr} [\rho (a^\dagger - \xi^*) \mathcal{D}(\xi)] - \left(\frac{\partial}{\partial \xi^*} + \frac{1}{2} \xi \right) \chi(\xi, t) \\ &= \left(\frac{\partial}{\partial \xi} - \frac{\partial}{\partial \xi^*} \right) \chi(\xi, t) - \frac{1}{2} (\xi + \xi^*) \chi(\xi, t), \end{aligned} \quad (\text{D.28})$$

and

$$\begin{aligned}
(2) &= \text{Tr} \left[\rho \left(a^\dagger + a \right) \mathcal{D}(\xi) \right] = \text{Tr} \left[\rho a^\dagger \mathcal{D}(\xi) \right] + \text{Tr} \left[\rho \mathcal{D}(\xi) \mathcal{D}^\dagger(\xi) a \mathcal{D}(\xi) \right] \\
&= \left(\frac{\partial}{\partial \xi} + \frac{1}{2} \xi^* \right) \chi(\xi, t) + \text{Tr} \left[\rho \mathcal{D}(\xi) (a + \xi) \right] \\
&= \left(\frac{\partial}{\partial \xi} - \frac{\partial}{\partial \xi^*} \right) \chi(\xi, t) + \frac{1}{2} (\xi + \xi^*) \chi(\xi, t).
\end{aligned} \tag{D.29}$$

Therewith, we obtain the commutator and anticommutator, respectively,

$$[a^\dagger + a, \rho] \rightarrow (1) - (2) = -(\xi + \xi^*) \chi(\xi, t), \tag{D.30a}$$

$$\{a^\dagger + a, \rho\} \rightarrow (1) + (2) = 2 \left(\frac{\partial}{\partial \xi} - \frac{\partial}{\partial \xi^*} \right) \chi(\xi, t). \tag{D.30b}$$

D.3.3 Fourier Transform

The characteristic functions $\chi_i(\xi, t)$ ($i = 1, \dots, 9$) have the general form

$$\chi_i(\xi, t) = A_i \exp \left(-\frac{|\xi|^2}{2} + \xi \lambda_{1,i}^* - \xi^* \lambda_{2,i} \right), \tag{D.31}$$

with the prefactors

$$A_i = \begin{cases} \frac{|\beta|^2}{2}, & i = 1, 2, \\ \frac{|\beta|^2}{2} f_1(t), & i = 3, 4, \\ \frac{\beta^* \alpha}{\sqrt{2}} f_2(t), & i = 5, 6, \\ \frac{\beta \delta^*}{\sqrt{2}} f_2(t), & i = 7, 8, \\ |\alpha|^2, & i = 9, \end{cases} \tag{D.32}$$

and the time-dependent functions

$$\lambda_{1,i} = \begin{cases} \eta(t) + \nu(t), & i = 1, 4, 5, \\ -\eta(t) + \nu(t), & i = 2, 3, 6, \\ \nu(t), & i = 7, 8, 9, \end{cases} \quad \text{and} \quad \lambda_{2,i} = \begin{cases} \eta(t) + \nu(t), & i = 1, 3, 7, \\ -\eta(t) + \nu(t), & i = 2, 4, 8, \\ \nu(t), & i = 5, 6, 9. \end{cases} \tag{D.33}$$

As already discussed in Sec. D.2, the field density operators can be calculated with their corresponding Wigner function that is defined by the Fourier transform of the characteristic function,

$$W_i(\delta) = \frac{1}{\pi^2} \int d^2 \xi \chi_i(\xi, t) \exp(\delta \xi^* - \delta^* \xi). \tag{D.34}$$

where δ is a complex variable; the relation between the density operators and the Wigner functions is given by [99]

$$W_i(\delta) = \frac{2}{\pi^2} \int d^2 \gamma \langle \delta + \gamma | \rho_{iF} | \delta - \gamma \rangle \exp(\delta^* \gamma - \delta \gamma^*), \tag{D.35}$$

where γ again denotes a complex variable that defines a coherent state.

We expect that the density operator has the general form

$$\rho_{iF}(t) = B_i |\alpha_{1,i}\rangle \langle \alpha_{2,i}|, \quad (\text{D.36})$$

where the prefactor B_i and the amplitudes $\alpha_{1,i}$ and $\alpha_{2,i}$ ($|\alpha_{1,i}\rangle$ and $|\alpha_{2,i}\rangle$ are coherent states) have to be determined from the Fourier transform.

To calculate the density operator, we now firstly calculate the two equations (D.34) and (D.35) independently; we then compare the two sides to determine the values B_i , $\alpha_{1,i}$, and $\alpha_{2,i}$. The Fourier integral in Eq. (D.34) reads

$$W_i(\delta) = A_i \pi^{-1} \int d^2\xi \exp[-|\xi|^2/2 + \xi(\lambda_{1,i}^* - \delta^*) - \xi^*(\lambda_{2,i} - \delta)] \quad (\text{D.37})$$

Rewriting ξ in its real and imaginary part, $\xi = x + iy$, the integral changes to

$$\begin{aligned} W_i(\delta) &= A_i \frac{1}{\pi^2} \int_{-\infty}^{+\infty} dx dy \exp\left[-\frac{x^2}{2} - \frac{y^2}{2} + (x + iy)(\lambda_{1,i}^* - \delta^*) - (x - iy)(\lambda_{2,i} - \delta)\right] \\ &= \frac{A_i}{\pi^2} \int_{-\infty}^{\infty} dx dy \exp\left[-\frac{1}{2}(x - [\lambda_{1,i}^* - \delta^* - \lambda_{2,i} + \delta])^2 \right. \\ &\quad \left. - \frac{1}{2}(y - i[\lambda_{1,i}^* - \delta^* + \lambda_{2,i} - \delta])^2 - 2(|\delta|^2 + \lambda_{1,i}^* \lambda_{2,i} - \delta^* \lambda_{2,i} - \delta \lambda_{1,i}^*)\right] \\ &= \frac{2A}{\pi} \exp[-2(|\delta|^2 + \lambda_{1,i}^* \lambda_{2,i} - \delta^* \lambda_{2,i} - \delta \lambda_{1,i}^*)], \end{aligned} \quad (\text{D.38})$$

where we have used the Gaussian integral

$$\int_{-\infty}^{\infty} dx e^{-(x-a)^2/b^2} = \sqrt{\pi}b. \quad (\text{D.39})$$

The Fourier integral in Eq. (D.35) contains the expectation value of the density operator,

$$\begin{aligned} \langle \delta + \gamma | \rho_{iF} | \delta - \gamma \rangle &= B_i \langle \delta + \gamma | \alpha_{1,i} \rangle \langle \alpha_{2,i} | \delta - \gamma \rangle \\ &= B_i \exp\left[-\frac{1}{2}(|\delta + \gamma|^2 + |\alpha_{1,i}|^2) + (\delta + \gamma)^* \alpha_{1,i} - \frac{1}{2}(|\delta - \gamma|^2 + |\alpha_{2,i}|^2) + (\delta - \gamma) \alpha_{2,i}^*\right] \\ &= B_i \exp\left[-|\delta|^2 - |\gamma|^2 - \frac{1}{2}(|\alpha_{1,i}|^2 + |\alpha_{2,i}|^2) + (\delta + \gamma)^* \alpha_{1,i} + (\delta - \gamma) \alpha_{2,i}^*\right] \\ &= B_i C(\alpha, \delta) \exp[-|\gamma|^2 - \gamma \alpha_{2,i}^* + \gamma^* \alpha_{1,i}], \end{aligned} \quad (\text{D.40})$$

with

$$C(\alpha, \delta) = \exp\left[-|\delta|^2 - \frac{1}{2}(|\alpha_{1,i}|^2 + |\alpha_{2,i}|^2) + \delta^* \alpha_{1,i} + \delta \alpha_{2,i}^*\right]. \quad (\text{D.41})$$

The Fourier integral can then be calculated as in Eq. (D.38), but now we have to integrate

over the real and imaginary parts γ_r and γ_i , respectively, of $\gamma = \gamma_r + i\gamma_i$,

$$\begin{aligned}
W_i(\delta) &= \frac{2B}{\pi^2} C(\alpha, \delta) d\gamma_r \int_{-\infty}^{\infty} d\gamma_i \exp[-|\gamma|^2 + \gamma(\delta^* - \alpha_{2,i}^*) - \gamma^*(\delta - \alpha_{1,i})] \\
&= \frac{2B}{\pi} C(\alpha, \delta) \exp[-|\delta|^2 + \alpha_{2,i}^* \delta + \alpha_{1,i} \delta^* - \alpha_{2,i}^* \alpha_{1,i}] \\
&= \frac{2B}{\pi} \exp\left[-2(|\delta|^2 - \delta^* \alpha_{1,i} - \delta \alpha_{2,i}^*) - \frac{1}{2}(|\alpha_{1,i}|^2 + |\alpha_{2,i}|^2) - \alpha_{2,i}^* \alpha_{1,i}\right]
\end{aligned} \tag{D.42}$$

Since the two Wigner probability distributions that are given in Eq. (D.38) and (D.42) have to be equal for equal i , B_i , $\alpha_{1,i}$, and $\alpha_{2,i}$ have to fulfill the equality

$$\begin{aligned}
B_i \exp\left[2(\delta^* \alpha_{1,i} + \delta \alpha_{2,i}^*) - \frac{1}{2}(|\alpha_{1,i}|^2 + |\alpha_{2,i}|^2) - \alpha_{2,i}^* \alpha_{1,i}\right] \\
= A_i \exp\left[2(\delta^* \lambda_{2,i} + \delta \lambda_{1,i}^* - \lambda_{1,i}^* \lambda_{2,i})\right].
\end{aligned} \tag{D.43}$$

From this we immediately see that

$$\alpha_{1,i} = \lambda_{2,i}, \quad \text{and} \quad \alpha_{2,i} = \lambda_{1,i}. \tag{D.44}$$

B_i has to be chosen such that

$$B_i = A_i \exp\left[-\lambda_{1,i}^* \lambda_{2,i} + \frac{1}{2}(|\lambda_{1,i}|^2 + |\lambda_{2,i}|^2)\right]. \tag{D.45}$$

With this, we can easily calculate the field operators $\rho_{iF}(t) = B_i |\alpha_{1,i}\rangle \langle \alpha_{2,i}|$ in Eq. (4.54) by using Eqs. (D.32) and (D.33).

The result above can also be obtained by considering the Q-representation,

$$\langle \delta | \rho_{iF}(t) | \delta \rangle = \pi Q_i(\alpha) = \frac{1}{\pi} \int d^2 \xi \chi_i(\xi, t) e^{-|\xi|^2/2} \exp(\delta \xi^* - \delta^* \xi). \tag{D.46}$$

Appendix E

Measurement Techniques

In this part of the appendix we consider the measurement of a quantum-mechanical field state. For this, we firstly introduce the quadrature operators \hat{x} and \hat{p} . Then, we describe the theoretical principles of a homodyne detection scheme. Lastly, we present the theoretical description of a linear amplifier.

E.1 Quadratures

The electric field strength \mathcal{E} of the light field is given by

$$\mathcal{E}_\phi = u^*(x,t)ae^{-i\phi} + u(x,t)a^\dagger e^{i\phi}, \quad \text{with} \quad u(x,t) = u_0 e^{i(kx-\omega t)}. \quad (\text{E.1})$$

where ϕ is a phase shift that is usually picked up by the quantum amplitude a . We have put the time-dependency of the operators a and a^\dagger in the function $u(x,t)$.

We introduce a pair of operators, \hat{x} and \hat{p} that are called the quadratures (quadrature phase and moment, respectively). They correspond to the “real” and “imaginary” part of the “complex” amplitude a ,

$$\hat{x}_\phi = \frac{1}{\sqrt{2}} (a^\dagger e^{i\phi} + ae^{-i\phi}), \quad \hat{p}_\phi = \frac{i}{\sqrt{2}} (a^\dagger e^{i\phi} - ae^{-i\phi}), \quad (\text{E.2})$$

so that

$$ae^{-i\phi} = \frac{1}{\sqrt{2}} (\hat{x}_\phi + i\hat{p}_\phi). \quad (\text{E.3})$$

In optics \hat{x}_ϕ and \hat{p}_ϕ correspond to the in-phase and, respectively, the out-of-phase component of the electric field amplitude of the spatial-temporal mode (with respect to a reference phase)¹. The quadratures can be regarded as the position and the momentum of the electromagnetic oscillator in phase space².

For a coherent state $|\alpha\rangle$, with real and imaginary part α_r and α_i , respectively, the quadratures are

$$\hat{x}_\phi = \frac{1}{\sqrt{2}} (\alpha^* e^{i\phi} + \alpha e^{-i\phi}) = \sqrt{2}\alpha_r, \quad \hat{p}_\phi = \frac{i}{\sqrt{2}} (\alpha^* e^{i\phi} - \alpha e^{-i\phi}) = -\sqrt{2}\alpha_i \quad (\text{E.4})$$

¹For the magnetic field, \hat{p}_ϕ corresponds to the in-phase component of the electric field and \hat{x}_ϕ , vice versa, to the out-of-phase component.

²Note that they have nothing to do with the position and the momentum of a photon

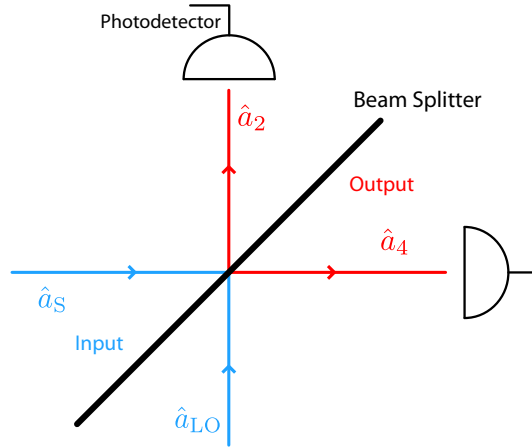


Figure E.1: Sketch of a homodyne detection scheme. Two input signals (with the annihilation operators a_S and a_{LO}) interfere optically to produce two output signals (with a_2 and a_4). These can be measured with photodetectors.

Thus, we can identify the amplitude of the coherent state by measuring both quadratures. We can only measure \hat{x}_ϕ or \hat{p}_ϕ in an experiment due to Heisenberg's uncertainty principle,

$$[\hat{x}_\phi, \hat{p}_\phi] = i. \quad (\text{E.5})$$

However, with the determination of higher quadratures (i.e. $\hat{x}_\phi^2, \hat{x}_\phi^3, \dots$) we get a full state tomography of the signal; see [121] for more information. For the measurement of the intensity of the electric field, we only have to measure \hat{x}_ϕ^2 (\hat{p}_ϕ^2).

E.2 Homodyne and Heterodyne Detection

For the determination of the quadrature of a signal, we use a homodyne measurement scheme. Fig. E.1 shows the measurement scheme of the homodyne detection. The measurable signal, with the annihilation operator a_S , interferes with a coherent laser beam, with the annihilation operator a_{LO} , at a 50:50 beam splitter. The laser-light field is called the *local oscillator*; it provides the phase reference ϕ for the quadrature measurement. The local oscillator should be intense with respect to the signal for providing a precise phase reference. After the optical mixing of the signal with the local oscillator, each emerging beam (a_2 and a_4) is directed to a photodetector, where either the intensities (photocurrents) or the quadratures of the beams are measured, as discussed below.

The interference of the two input signals is given by a linear transformation

$$\begin{pmatrix} a_2 \\ a_4 \end{pmatrix} = \mathcal{B} \begin{pmatrix} a_S \\ a_{LO} \end{pmatrix}, \quad (\text{E.6})$$

described by the matrix

$$\mathcal{B} = \begin{pmatrix} \mathcal{B}_{11} & \mathcal{B}_{12} \\ \mathcal{B}_{21} & \mathcal{B}_{22} \end{pmatrix}. \quad (\text{E.7})$$

The incoming and the outgoing beams are both independent bosonic modes, so their annihilation and creation operators must satisfy ($k, l = S, LO, 2, 4$)

$$[a_k, a_l^\dagger] = \delta_{kl}, \quad \text{and} \quad [a_k, a_l] = [a_k^\dagger, a_l^\dagger] = 0. \quad (\text{E.8})$$

Consequently, \mathcal{B} has to be unitary, $\mathcal{B}^{-1} = \mathcal{B}^\dagger$, because

$$|\mathcal{B}_{11}|^2 + |\mathcal{B}_{12}|^2 = |\mathcal{B}_{21}|^2 + |\mathcal{B}_{22}|^2 = 1, \quad \mathcal{B}_{11}\mathcal{B}_{21}^* + \mathcal{B}_{12}\mathcal{B}_{22}^* = 0. \quad (\text{E.9})$$

We assume a lossless four-port with a real transition matrix \mathcal{B} that is represented in terms of the transmissivity τ and the reflectivity ρ ,

$$\mathcal{B} = \begin{pmatrix} \tau & -\rho \\ \rho & \tau \end{pmatrix}, \quad (\text{E.10})$$

where, due to energy conservation, $\rho^2 + \tau^2 = 1$. Our four-port is a 50 : 50 beam splitter and therewith $\tau = \rho = 1/\sqrt{2}$.

For the field detection, the photocurrent of the photodetectors is measured; this photocurrent I_i ($i = 2, 4$) is a linear function of the photon number, $I_i = a_i^\dagger a_i$. The outgoing field is described by the annihilation operators

$$a_2 = \frac{1}{\sqrt{2}}(a_S - a_{\text{LO}}), \quad a_4 = \frac{1}{\sqrt{2}}(a_S + a_{\text{LO}}). \quad (\text{E.11})$$

The difference of the photocurrents, $I_2 - I_4$ is the quantity of interest because it contains the interference term of the local oscillator and the signal,

$$I_2 - I_4 = a_2^\dagger a_2 - a_4^\dagger a_4 = a_S a_{\text{LO}} + a_{\text{LO}}^\dagger a_S \quad (\text{E.12})$$

We will assume that the local oscillator is powerful enough to be treated classically; therewith, the annihilation and creation operator of the reference field change as (remember that we only consider the time-independent part of the operators)

$$\begin{aligned} a_{\text{LO}} &\rightarrow \alpha_{\text{LO}} = |\alpha_{\text{LO}}| e^{i\phi}, \\ a_{\text{LO}}^\dagger &\rightarrow \alpha_{\text{LO}}^* = |\alpha_{\text{LO}}| e^{-i\phi}. \end{aligned} \quad (\text{E.13})$$

With this, we immediately see that we measure the quadrature phase of the signal by measuring the difference of the intensities of the outgoing beams,

$$I_2 - I_4 = |\alpha_{\text{LO}}| \hat{x}_{\phi, S} \quad (\text{E.14})$$

Therefore, a homodyne detector measures the quadrature component $\hat{x}_{\phi, S}$ of the signal, whereas the reference phase ϕ is provided by the local oscillator. An experimental method for finding the scaling $|\alpha_{\text{LO}}|^2$ in the difference current is to keep a record of the sum current,

$$I_2 + I_4 = a_{\text{LO}}^\dagger a_{\text{LO}} + a_S^\dagger a_S = |\alpha_{\text{LO}}|^2 + a_S^\dagger a_S, \quad (\text{E.15})$$

because it is proportional to $|\alpha_{\text{LO}}|^2$ in leading order.

E.3 Linear Amplifier

In the MSR, the coherent field that leaks out the cavity is amplified with a linear amplifier. Therefore, we discuss some properties of this devices in this part of the appendix. A linear amplifier amplifies the voltage (corresponding to the mean value of the quadrature, $\langle \hat{x} \rangle$) or the power ($\langle \hat{x}^2 \rangle$) of a signal.

E.3.1 Floor Noise

A linear amplifier is a electric device with a certain resistance. Due to this resistance, the linear amplifier has a certain floor noise (Nyquist noise). This thermal noise can be expressed in terms of a mean photon number n_{amp} that is given by the ratio of the thermal energy of the amplifier noise ($T_{\text{N}} \approx 10$ K) and the zero-point energy of the field with frequency $\omega_r/2\pi \approx 10$ GHz which we want to measure,

$$n_{\text{amp}} = \frac{k_{\text{B}}T_{\text{N}}}{\hbar\omega_r} \approx 20. \quad (\text{E.16})$$

This noise is added to the signal at the input of the linear amplifier. The entire input signal is then amplified; the output thus has an additional thermal noise part from the linear amplifier.

However, n_{amp} is only a mean number of photons that is achieved after several measurement. In a single shot, n_{amp} can differ significantly from this value. The probability of measuring y noise photons is given by a Gaussian probability distribution since thermal noise is just white noise,

$$P(y, n_{\text{amp}}) = \sqrt{2\pi n_{\text{amp}}}^{-1} \exp\left[-\frac{(y - n_{\text{amp}})^2}{2n_{\text{amp}}}\right]. \quad (\text{E.17})$$

The standard derivation of this distribution is $\sigma_{\text{N}} = \sqrt{n_{\text{amp}}}$. This means that we can also have a floor noise of e.g. 100 photons with a certain probability.

Therefore, we can calculate the probability of having a floor noise below a certain cutoff photon number n_c by integration,

$$P(y < n_c, n_{\text{amp}}) = \int_{-\infty}^{n_c} dy P(y, n_{\text{amp}}) = \frac{1}{2} + \text{erf}\left(\frac{n_c - n_{\text{amp}}}{\sqrt{2n_{\text{amp}}}}\right), \quad (\text{E.18})$$

with $\text{erf}(x)$ denoting the error function,

$$\text{erf}(x) = \frac{2}{\sqrt{\pi}} \int_0^x dy e^{-y^2}. \quad (\text{E.19})$$

With this we can easily calculate the probability for having a floor noise below n_c photons in a single shot. For $n_c = 40$, this number already approaches unity (99.9996%).

E.3.2 Theoretical Description

For the theoretical description of the linear amplifier we mainly follow the derivations in [122]. In general, a linear amplifier takes the input signal, expressed by the bosonic creation and annihilation operators a_{in} and a_{in}^\dagger (where we only take into account one bosonic mode), and produces an output signal, also expressed by bosonic creation and annihilation operators b_{out} and b_{out}^\dagger . This output signal can be written as linear functions of the input operators:

$$\begin{aligned} b_{\text{out}} &= M a_{\text{in}} + L a_{\text{in}}^\dagger + b_{\text{amp}}, \\ b_{\text{out}}^\dagger &= M^* a_{\text{in}}^\dagger + L^* a_{\text{in}} + b_{\text{amp}}^\dagger, \end{aligned} \quad (\text{E.20})$$

where the operators b_{amp} and b_{amp}^\dagger are responsible for the additive noise of the linear amplifier, $Gn_{\text{amp}} = \langle b_{\text{amp}}^\dagger b_{\text{amp}} \rangle$ (the value G is defined below). Since the input and output operators obey the bosonic commutation relations, we obtain the unitary condition

$$|M|^2 - |L|^2 + [b_{\text{amp}}, b_{\text{amp}}^\dagger] = 1. \quad (\text{E.21})$$

We can split the operators in their Hermitian real and imaginary parts:

$$\begin{aligned} \hat{x}_{\text{in}} &= \frac{1}{\sqrt{2}}(a_{\text{in}}^\dagger + a_{\text{in}}), & \hat{p}_{\text{in}} &= \frac{i}{\sqrt{2}}(a_{\text{in}}^\dagger - a_{\text{in}}), \\ \hat{x}_{\text{out}} &= \frac{1}{\sqrt{2}}(b_{\text{out}}^\dagger + b_{\text{out}}), & \hat{p}_{\text{out}} &= \frac{i}{\sqrt{2}}(b_{\text{out}}^\dagger - b_{\text{out}}), \\ \hat{x}_{\text{amp}} &= \frac{1}{\sqrt{2}}(b_{\text{amp}}^\dagger + b_{\text{amp}}), & \hat{p}_{\text{amp}} &= \frac{i}{\sqrt{2}}(b_{\text{amp}}^\dagger - b_{\text{amp}}), \end{aligned} \quad (\text{E.22})$$

where \hat{x}_i (\hat{p}_i), ($i = \text{in, out, amp}$) are the (phase-independent) quadrature phases (moments) of the input and output signal, and the amplifier noise, respectively. It has to be noted that the averaged quadrature phase of the linear amplifier is zero, $\langle \hat{x}_{\text{amp}} \rangle = 0$, and the averaged quadrat of \hat{x}_{amp} corresponds to the photon number, $\langle \hat{x}_{\text{amp}}^2 \rangle = Gn_{\text{amp}}$.

We can differentiate between two types of linear amplifiers. The most common type is the phase-insensitive linear amplifier, that produces the same ($L = 0$) or the opposite ($M = 0$) phase-shift of the input, in contrast to a phase-sensitive linear amplifiers, whose response depends on the phase of the input. If the input signal of a phase-insensitive linear amplifier has phase-insensitive noise, the output signal will also have phase-insensitive noise. The linear amplifier is prepared in an operating state for which it is phase-insensitive. We can always find a phase transformation of the input and output phase, for which M and L are real and positive. Therewith, we can express Eq. (E.20) in equations for \hat{x}_i and \hat{p}_i , ($i = \text{in, out, amp}$),

$$\begin{aligned} \hat{x}_{\text{out}} &= (M + L)\hat{x}_{\text{in}} + \hat{x}_{\text{amp}}, \\ \hat{p}_{\text{out}} &= (M - L)\hat{p}_{\text{in}} + \hat{p}_{\text{amp}}. \end{aligned} \quad (\text{E.23})$$

We now define the gains $G_1 = (M + L)^2$ and $G_2 = (M - L)^2$ for the quadratures and a mean gain $G = \frac{1}{2}(G_1 + G_2) = M^2 + L^2$. The gain of a phase-insensitive amplifier does not depend on the phase and thus ($G = G_1 = G_2$). A phase-sensitive linear amplifier has phase-dependent gains, but a reduction of the noise added to one quadrature phase requires an increase of the noise added to the other phase. Without loss of generality we can choose a phase-preserving linear amplifier with $L = 0$ and therefore $G = M^2$.

We now consider the measurement of the coherent field calculated in chapter 4. Our input signal is the coherent field state $|\eta(t)\rangle$ (the input operators are $a_{\text{in}} \equiv a$ and $a_{\text{in}}^\dagger \equiv a^\dagger$); with this, we can now calculate the expectation values of \hat{x}_{out} and \hat{x}_{out}^2 that correspond to the voltage and the power of the outcoming signal, respectively,

$$\begin{aligned} \langle \hat{x}_{\text{out}} \rangle &= \langle M\eta(t) | \hat{x}_{\text{in}} + \hat{x}_{\text{amp}} | \eta(t) \rangle = \sqrt{\frac{G}{2}} [\eta(t) + \eta^*(t)], \\ \langle \hat{x}_{\text{out}}^2 \rangle &= G \langle \eta(t) | (\hat{x}_{\text{in}} + \hat{x}_{\text{amp}})^2 | \eta(t) \rangle \\ &= \left[\langle \eta(t) | (Ga_{\text{in}}^\dagger a_{\text{in}} + b_{\text{amp}}^\dagger b_{\text{amp}}) | \eta(t) \rangle + G \langle \eta(t) | a_{\text{in}}^\dagger a_{\text{in}}^\dagger + a_{\text{in}} a_{\text{in}} | \eta(t) \rangle \right] \\ &= G \left[|\eta(t)|^2 + n_{\text{amp}} + 1 + (\eta^*(t))^2 + (\eta(t))^2 \right] \\ &= G \left[|\eta(t)|^2 + n_{\text{amp}} + 1 - (\Im[\eta(t)])^2 \right] = G \left[N^e(t) + n_{\text{amp}} + 1 \right]. \end{aligned} \quad (\text{E.24})$$

In the last step, we have used $N^e(t) = |\eta(t)|^2$ and the fact that $\eta(t) = -ig/\kappa [1 - e^{-\kappa t/2}]$ is purely imaginary and therewith $(\Im[\eta(t)])^2 = |\eta(t)|^2$. We have neglected constant shifts that only originate from the vacuum energies of the input and the noise field.

Therefore, by measuring $\langle \hat{x}_{\text{out}}^2 \rangle$ we can amplify and measure the mean photon number $N^e(t)$ with an additional noise $Gn_{\text{amp}} = \langle b_{\text{amp}}^\dagger b_{\text{amp}} \rangle$. The calculations in Eq. (E.24) also hold for the mean photon number of the ground state, $N^g(t)$, and for a non-negligible crosstalk, where the input signal is the field $(|\eta(t) + \nu(t)\rangle + |-\eta(t) + \nu(t)\rangle)/\sqrt{2}$.

Bibliography

- [1] R. FEYNMAN, Simulating physics with computers, *Int. J. Theor. Phys.* **21**, 467 (1982).
- [2] D. DEUTSCH, Quantum Theory, the Church-Turing Principle and the Universal Quantum Computer, *Proc. Roy. Soc. London A* **400**, 97 (1985).
- [3] Y. MAKHLIN, G. SCHÖN, and A. SHNIRMAN, Quantum-state engineering with Josephson-junction devices, *Rev. Mod. Phys.* **73**, 357 (2001).
- [4] G. WENDIN and V. S. SHUMEIKO, Superconducting Quantum Circuits, Qubits and Computing, arXiv:cond-mat/0508729 (2005).
- [5] G. WENDIN and V. S. SHUMEIKO, Quantum bits with Josephson junctions (Review Article), *Low Temp. Phys.* **33**, 724 (2007).
- [6] M. H. DEVORET, A. WALLRAFF, and J. M. MARTINIS, Superconducting Qubits: A Short Review, arXiv:cond-mat/0411174 (2004).
- [7] Y. NAKAMURA, Y. A. PASHKIN, and J. S. TSAI, Coherent control of macroscopic quantum states in a single-Cooper-pair box, *Nature* **398**, 786 (1999).
- [8] M. STEFFEN, M. ANSMANN, R. C. BIALCZAK, N. KATZ, E. LUCERO, R. McDERMOTT, M. NEELEY, E. M. WEIG, A. N. CLELAND, and J. M. MARTINIS, Measurement of the Entanglement of Two Superconducting Qubits via State Tomography, *Science* **313**, 1423 (2006).
- [9] M. A. NIELSEN and I. L. CHUANG, *Quantum Computation and Quantum Information* (University Press, Cambridge, 2001).
- [10] O. ASTAFIEV, Y. A. PASHKIN, T. YAMAMOTO, Y. NAKAMURA, and J. S. TSAI, Single-Shot measurement of the Josephson charge qubit, *Phys. Rev. B* **69**, 180507 (2004).
- [11] A. WALLRAFF, D. I. SCHUSTER, A. BLAIS, L. FRUNZIO, J. MAJER, M. H. DEVORET, S. M. GIRVIN, and R. J. SCHOELKOPF, Approaching Unit Visibility for Control of a Superconducting Qubit with Dispersive Readout, *Phys. Rev. Lett.* **95**, 060501 (2005).
- [12] I. SIDDIQI, R. VIJAY, F. PIERRE, C. M. WILSON, M. METCALFE, C. RIGETTI, L. FRUNZIO, and M. H. DEVORET, RF-Driven Josephson Bifurcation Amplifier for Quantum Measurement, *Phys. Rev. Lett.* **93**, 207002 (2004).
- [13] A. LUPAȘCU, C. J. M. VERWIJS, R. N. SCHOUTEN, C. J. P. M. HARMANS, and J. E. MOOIJ, Nondestructive Readout for a Superconducting Flux Qubit, *Phys. Rev. Lett.* **93**, 177006 (2004).

- [14] K. B. COOPER, M. STEFFEN, R. McDERMOTT, R. W. SIMMONDS, S. OH, D. A. HITE, D. P. PAPPAS, and J. M. MARTINIS, Observation of Quantum Oscillations between a Josephson Phase Qubit and a Microscopic Resonator Using Fast Readout, *Phys. Rev. Lett.* **93**, 180401 (2004).
- [15] D. P. DIVINCENZO, The Physical Implementation of Quantum Computation, *Fortschr. Phys.* **48**, 771 (2000).
- [16] E. FICK, *Einführung in die Grundlagen der Quantentheorie* (Akademische Verlagsgesellschaft, Frankfurt am Main, 1968).
- [17] A. H. MYERSON, D. J. SZWER, S. C. WEBSTER, D. T. C. ALLCOCK, M. J. CURTIS, G. IMREH, J. A. SHERMAN, D. N. STACEY, A. M. STEANE, and D. M. LUCAS, High-Fidelity Readout of Trapped-Ion Qubits, *Phys. Rev. Lett.* **100**, 200502 (2008).
- [18] L. F. W. YU-XI LIU and F. NORI, Quantum tomography for solid-state qubits, *Europhys. Lett.* **67**, 874 (2004).
- [19] K. HORNBERGER, Introduction to decoherence theory, arXiv:quant-ph/0612118 (2006).
- [20] D. F. WALLS and G. J. MILBURN, *Quantum Optics* (Springer, Berlin, 2008).
- [21] E. T. JAYNES and F. W. CUMMINGS, Comparison of the quantum and semiclassical radiation theories with application to the beam maser, *Proc. IEEE* **51**, 89 (1963).
- [22] A. BLAIS, R.-S. HUANG, A. WALLRAFF, S. M. GIRVIN, and R. J. SCHOELKOPF, Cavity quantum electrodynamics for superconducting electrical circuits: An architecture for quantum computation, *Phys. Rev. A* **69**, 062320 (2004).
- [23] C. F. WILDFEUER, *Erzeugung verschränkter Zustände im Zwei-Moden-Jaynes-Cummings-Modell*, Ph.D. thesis, Universität Siegen (2003).
- [24] A. B. KLIMOV, L. L. SÁNCHEZ-SOTO, A. NAVARRO, and E. C. YUSTAS, Effective Hamiltonians in quantum optics: a systematic approach, *J. Mod. Opt.* **49**, 2211 (2002).
- [25] J. KOCH, T. M. YU, J. GAMBETTA, A. A. HOUCK, D. I. SCHUSTER, J. MAJER, A. BLAIS, M. H. DEVORET, S. M. GIRVIN, and R. J. SCHOELKOPF, Charge-insensitive qubit design derived from the Cooper pair box, *Phys. Rev. A* **76**, 042319 (2007).
- [26] A. WALLRAFF, D. I. SCHUSTER, A. BLAIS, J. M. GAMBETTA, J. SCHREIER, L. FRUNZIO, M. H. DEVORET, S. M. GIRVIN, and R. J. SCHOELKOPF, Sideband Transitions and Two-Tone Spectroscopy of a Superconducting Qubit Strongly Coupled to an On-Chip Cavity, *Phys. Rev. Lett.* **99**, 050501 (2007).
- [27] D. I. SCHUSTER, *Circuit Quantum Electrodynamics*, Ph.D. thesis, Yale University (2007).
- [28] J. I. CIRAC and P. ZOLLER, Quantum Computations with Cold Trapped Ions, *Phys. Rev. Lett.* **74**, 4091 (1995).
- [29] M. G. RAIZEN, J. M. GILLIGAN, J. C. BERGQUIST, W. M. ITANO, and D. J. WINELAND, Ionic crystals in a linear Paul trap, *Phys. Rev. A* **45**, 6493 (1992).

- [30] R. BLATT and A. STEANE, Quantum information processing with trapped ions, in: T. VAN DER PYL, A. KARLSON, and M. BELINA-PODGATSKY, (Eds.), *Quantum Information Processing and Communication in Europe* (European Communities, 2005).
- [31] H. HÄFFNER, W. HÄNSEL, C. F. ROOS, J. BENHELM, D. CHEK-AL KAR, M. CHWALLA, T. KÖRBER, U. D. RAPOL, M. RIEBE, P. O. SCHMIDT, C. BECHER, O. GÜHNE, W. DÜR, and R. BLATT, Scalable multiparticle entanglement of trapped ions, *Nature* **438**, 643 (2005).
- [32] B. E. KANE, A silicon-based nuclear spin quantum computer, *Nature* **393**, 133 (1998).
- [33] Q. ZHANG, A. GOEBEL, C. WAGENKNECHT, Y.-A. CHEN, B. ZHAO, T. YANG, A. MAIR, J. SCHMIEDMAYER, and J.-W. PAN, Experimental quantum teleportation of a two-qubit composite system, *Nat. Phys.* **2**, 678 (2006).
- [34] J. P. REITHMAIER, G. SEK, A. LOFFLER, C. HOFMANN, S. KUHN, S. REITZENSTEIN, L. V. KELDYSH, V. D. KULAKOVSKII, T. L. REINECKE, and A. FORCHEL, Strong coupling in a single quantum dot-semiconductor microcavity system, *Nature* **432**, 197 (2004).
- [35] R. J. SCHOELKOPF and S. M. GIRVIN, Wiring up quantum systems, *Nature* **451**, 664 (2008).
- [36] D. VION, A. AASSIME, A. COTTET, P. JOYEZ, H. POTHIER, C. URBINA, D. ESTEVE, and M. H. DEVORET, Manipulating the Quantum State of an Electrical Circuit, *Science* **296**, 886 (2002).
- [37] A. LUPAȘCU, S. SAITO, T. PICOT, P. C. DE GROOT, C. J. P. M. HARMANS, and J. E. MOOIJ, Quantum non-demolition measurement of a superconducting two-level system, *Nat. Phys.* **3**, 119 (2007).
- [38] R. SIMMONDS, NIST Homepage.
- [39] J. SIEWERT, R. FAZIO, G. M. PALMA, and E. SCIACCA, Aspects of Qubit Dynamics in the Presence of Leakage, *J. Low Temp. Phys.* **118**, 795 (2000).
- [40] M. BÜTTIKER, Zero-current persistent potential drop across small-capacitance Josephson junctions, *Phys. Rev. B* **36**, 3548 (1987).
- [41] P. LAFARGE, P. JOYEZ, D. ESTEVE, C. URBINA, and M. H. DEVORET, Two-electron quantization of the charge on a superconductor, *Nature* **365**, 422 (1993).
- [42] V. BOUCHIAT, D. VION, P. JOYEZ, D. ESTEVE, and M. H. DEVORET, Quantum coherence with a single Cooper pair, *Physica Scripta* **T76**, 165 (1998).
- [43] Y. NAKAMURA, Y. A. PASHKIN, and J. S. TSAI, Rabi Oscillations in a Josephson-Junction Charge Two-Level System, *Phys. Rev. Lett.* **87**, 246601 (2001).
- [44] Y. NAKAMURA, Y. A. PASHKIN, T. YAMAMOTO, and J. S. TSAI, Charge Echo in a Cooper-Pair Box, *Phys. Rev. Lett.* **88**, 047901 (2002).

- [45] T. YAMAMOTO, Y. A. PASHKIN, O. ASTAFIEV, Y. NAKAMURA, and J. S. TSAI, Demonstration of conditional gate operation using superconducting charge qubits, *Nature* **425**, 941 (2003).
- [46] Y. MAKHLIN, G. SCHOEN, and A. SHNIRMAN, Josephson-junction qubits with controlled couplings, *Nature* **398**, 305 (1999).
- [47] A. A. HOUCK, J. A. SCHREIER, B. R. JOHNSON, J. M. CHOW, J. KOCH, J. M. GAMBETTA, D. I. SCHUSTER, L. FRUNZIO, M. H. DEVORET, S. M. GIRVIN, and R. J. SCHOELKOPF, Controlling the Spontaneous Emission of a Superconducting Transmon Qubit, *Phys. Rev. Lett.* **101**, 080502 (2008).
- [48] A. COTTET, *Implementation of a quantum bit in a superconducting qubit*, Ph.D. thesis, Université Paris VI (UPMC) (2002).
- [49] A. COTTET, D. VION, A. AASSIME, P. JOYEZ, D. ESTEVE, and M. H. DEVORET, Implementation of a combined charge-phase quantum bit in a superconducting circuit, *Physica C* **367**, 197 (2002).
- [50] E. COLLIN, G. ITHIER, A. AASSIME, P. JOYEZ, D. VION, and D. ESTEVE, NMR-like Control of a Quantum Bit Superconducting Circuit, *Phys. Rev. Lett.* **93**, 157005 (2004).
- [51] A. O. CALDEIRA and A. J. LEGGETT, Quantum tunnelling in a dissipative system, *Ann. Phys. (N.Y.)* **149**, 374 (1983).
- [52] R. ROUSE, S. HAN, and J. E. LUKENS, Observation of Resonant Tunneling between Macroscopically Distinct Quantum Levels, *Phys. Rev. Lett.* **75**, 1614 (1995).
- [53] J. R. FRIEDMAN, V. PATEL, W. CHEN, S. K. TOLPYGO, and J. E. LUKENS, Quantum superposition of distinct macroscopic states, *Nature* **406**, 43 (2000).
- [54] R. GROSS and A. MARX, *Applied Superconductivity: Josephson Effect and Superconducting Electronics* (Lecture Notes,, 2005).
- [55] M. MARIANTONI, H. CHRIST, and M. J. STORCZ, Private Communication (Matlab Program).
- [56] J. E. MOOIJ, T. P. ORLANDO, L. LEVITOV, L. TIAN, C. H. VAN DER WAL, and S. LLOYD, Josephson Persistent-Current Qubit, *Science* **285**, 1036 (1999).
- [57] C. H. VAN DER WAL, A. C. J. TER HAAR, F. K. WILHELM, R. N. SCHOUTEN, C. J. P. M. HARMANS, T. P. ORLANDO, S. LLOYD, and J. E. MOOIJ, Quantum Superposition of Macroscopic Persistent-Current States, *Science* **290**, 773 (2000).
- [58] T. P. ORLANDO, J. E. MOOIJ, L. TIAN, C. H. VAN DER WAL, L. S. LEVITOV, S. LLOYD, and J. J. MAZO, Superconducting persistent-current qubit, *Phys. Rev. B* **60**, 15398 (1999).
- [59] Y. NAKAMURA, F. YOSHIHARA, K. HARRABI, A. NISKANEN, and J. TSAI, Coherence and decoherence in Josephson junction qubits, (PowerPoint Presentation).
- [60] R. F. VOSS and R. A. WEBB, Macroscopic Quantum Tunneling in $1\ \mu\text{m}$ Nb Josephson Junctions, *Phys. Rev. Lett.* **47**, 265 (1981).

-
- [61] J. M. MARTINIS, M. H. DEVORET, and J. CLARKE, Energy-Level Quantization in the Zero-Voltage State of a Current-Biased Josephson Junction, *Phys. Rev. Lett.* **55**, 1543 (1985).
- [62] J. M. MARTINIS, M. H. DEVORET, and J. CLARKE, Experimental tests for the quantum behavior of a macroscopic degree of freedom: The phase difference across a Josephson junction, *Phys. Rev. B* **35**, 4682 (1987).
- [63] J. M. MARTINIS, S. NAM, J. AUMENTADO, and C. URBINA, Rabi Oscillations in a Large Josephson-Junction Qubit, *Phys. Rev. Lett.* **89**, 117901 (2002).
- [64] E. LUCERO, M. HOFHEINZ, M. ANSMANN, R. C. BIALCZAK, N. KATZ, M. NEELEY, A. D. O'CONNELL, H. WANG, A. N. CLELAND, and J. M. MARTINIS, High-Fidelity Gates in a Single Josephson Qubit, *Physical Review Letters* **100**, 247001 (2008).
- [65] M. STEFFEN, J. M. MARTINIS, and I. L. CHUANG, Accurate control of Josephson phase qubits, *Phys. Rev. B* **68**, 224518 (2003).
- [66] R. W. SIMMONDS, K. M. LANG, D. A. HITE, S. NAM, D. P. PAPPAS, and J. M. MARTINIS, Decoherence in Josephson Phase Qubits from Junction Resonators, *Phys. Rev. Lett.* **93**, 077003 (2004).
- [67] A. D. ARMOUR, M. P. BLENCOWE, and K. C. SCHWAB, Entanglement and Decoherence of a Micromechanical Resonator via Coupling to a Cooper-Pair Box, *Phys. Rev. Lett.* **88**, 148301 (2002).
- [68] E. K. IRISH and K. SCHWAB, Quantum measurement of a coupled nanomechanical resonator-Cooper-pair box system, *Phys. Rev. B* **68**, 155311 (2003).
- [69] A. A. HOUCK, D. I. SCHUSTER, J. M. GAMBETTA, J. A. SCHREIER, B. R. JOHNSON, J. M. CHOW, L. FRUNZIO, J. MAJER, M. H. DEVORET, S. M. GIRVIN, and R. J. SCHOELKOPF, Generating single microwave photons in a circuit, *Nature* **449**, 328 (2007).
- [70] M. HOFHEINZ, E. M. WEIG, M. ANSMANN, R. C. BIALCZAK, E. LUCERO, M. NEELEY, A. D. O'CONNELL, H. WANG, J. M. MARTINIS, and A. N. CLELAND, Generation of Fock states in a superconducting quantum circuit, *Nature* **454**, 310 (2008).
- [71] F. DEPPE, M. MARIANTONI, E. P. MENZEL, A. MARX, S. SAITO, K. KAKUYANAGI, H. TANAKA, T. MENO, K. SEMBA, H. TAKAYANAGI, E. SOLANO, and R. GROSS, Two-photon probe of the Jaynes-Cummings model and symmetry breaking in circuit QED, *Nature Physics* **4**, 686 (2008).
- [72] A. WALLRAFF, D. I. SCHUSTER, A. BLAIS, L. FRUNZIO, R.-S. HUANG, J. MAJER, S. KUMAR, S. M. GIRVIN, and R. J. SCHOELKOPF, Strong coupling of a Single Photon to a Superconducting Qubit Using Circuit Quantum Electrodynamics, *Nature* **431**, 162 (2004).
- [73] I. CHIORESCU, P. BERTET, K. SEMBA, Y. NAKAMURA, C. J. P. M. HARMANS, and J. E. MOOIJ, Coherent dynamics of a flux qubit coupled to a harmonic oscillator, *Nature* **431**, 159 (2004).

- [74] J. JOHANSSON, S. SAITO, T. MENO, H. NAKANO, M. UEDA, K. SEMBA, and H. TAKAYANAGI, Vacuum Rabi Oscillations in a Macroscopic Superconducting Qubit LC Oscillator System, *Phys. Rev. Lett.* **96**, 127006 (2006).
- [75] T. LINDSTRÖM, C. H. WEBSTER, J. E. HEALEY, M. S. COLCLOUGH, C. M. MUIRHEAD, and A. Y. TZALENCHUK, Circuit QED with a flux qubit strongly coupled to a coplanar transmission line resonator, *Superconductor Science and Technology* **20**, 814 (2007).
- [76] M. A. SILLANPÄÄ, J. I. PARK, and R. W. SIMMONDS, Coherent quantum state storage and transfer between two phase qubits via a resonant cavity, *Nature* **449**, 438 (2007).
- [77] M. NEELEY, M. ANSMANN, R. C. BIALCZAK, M. HOFHEINZ, N. KATZ, E. LUCERO, A. O'CONNELL, H. WANG, A. N. CLELAND, and J. M. MARTINIS, Process tomography of quantum memory in a Josephson-phase qubit coupled to a two-level state, *Nat. Phys.* **4**, 523 (2008).
- [78] M. MARIANTONI, Private Communication.
- [79] A. WALLRAFF, Private Communication.
- [80] M. BOISSONNEAULT, J. GAMBETTA, and A. BLAIS, Non-linear dispersive regime of circuit QED: The dressed dephasing model (2008).
- [81] I. SIDDIQI, R. VIJAY, M. METCALFE, E. BOAKNIN, L. FRUNZIO, R. J. SCHOELKOPF, and M. H. DEVORET, Dispersive measurements of superconducting qubit coherence with a fast, latching readout (2005).
- [82] A. LUPAȘCU, C. J. P. M. HARMANS, and J. E. MOOIJ, Quantum state detection of a superconducting flux qubit using a dc-SQUID in the inductive mode, *Phys. Rev. B* **71**, 184506 (2005).
- [83] P. BERTET, I. CHIORESCU, K. SEMBA, C. J. P. M. HARMANS, and J. E. MOOIJ, Detection of a persistent-current qubit by resonant activation, *Phys. Rev. B* **70**, 100501 (2004).
- [84] A. LUPAȘCU, E. F. C. DRIESSEN, L. ROSCHIER, C. J. P. M. HARMANS, and J. E. MOOIJ, High-Contrast Dispersive Readout of a Superconducting Flux Qubit Using a Nonlinear Resonator, *Phys. Rev. Lett.* **96**, 127003 (2006).
- [85] T. PICOT, A. LUPAȘCU, S. SAITO, C. J. P. M. HARMANS, and J. E. MOOIJ, Role of relaxation in the quantum measurement of a superconducting qubit using a nonlinear oscillator, arXiv:0808.0464 (2008).
- [86] M. I. DYKMAN and M. A. KRIVOGLAZ, Fluctuations in nonlinear systems near bifurcations corresponding to the appearance of new stable states, *Physica A* **104**, 480 (1980).
- [87] M. STEFFEN, M. ANSMANN, R. MCDERMOTT, N. KATZ, R. C. BIALCZAK, E. LUCERO, M. NEELEY, E. M. WEIG, A. N. CLELAND, and J. M. MARTINIS, State Tomography of Capacitively Shunted Phase Qubits with High Fidelity, *Phys. Rev. Lett.* **97**, 050502 (2006).

- [88] R. McDERMOTT, R. W. SIMMONDS, M. STEFFEN, K. B. COOPER, K. CİCAK, K. D. OSBORN, S. OH, D. P. PAPPAS, and J. M. MARTINIS, Simultaneous State Measurement of Coupled Josephson Phase Qubits, *Science* **307**, 1299 (2005).
- [89] Q. ZHANG, A. G. KOFMAN, J. M. MARTINIS, and A. N. KOROTKOV, Analysis of measurement errors for a superconducting phase qubit, *Phys. Rev. B* **74**, 214518 (2006).
- [90] B. ENGLERT, G. MANGANO, M. MARIANTONI, R. GROSS, J. SIEWERT, and E. SOLANO, Mesoscopic Shelving Readout of Superconducting Qubits, preprint.
- [91] H. DEHMELT, Radiofrequency Spectroscopy of Stored Ions, *Adv. At. Mol. Phys.* **3** (5), 53 (109) (1967 (1969)).
- [92] H. DEHMELT, Proposed $10^{14} \Delta\nu < \nu$ Laser Fluorescence Spectroscopy on Tl^+ Mono-Ion Oscillator II (spontaneous quantum jumps), *Bull. Am. Phys. Soc.* **20**, 60 (1975).
- [93] W. NAGOURNEY, J. SANDBERG, and H. DEHMELT, Shelved optical electron amplifier: Observation of quantum jumps, *Phys. Rev. Lett.* **56**, 2797 (1986).
- [94] D. J. WINELAND, C. MONROE, W. M. ITANO, D. LEIBFRIED, B. E. KING, and D. M. MEEKHOF, Experimental Issues in Coherent Quantum-State Manipulation of Trapped Atomic Ions, *J. Res. Natl. Inst. Stand. Technol.* **103**, 259 (1998).
- [95] Y. XI LIU, J. Q. YOU, L. F. WEI, C. P. SUN, and F. NORI, Optical Selection Rules and Phase-Dependent Adiabatic State Control in a Superconducting Quantum Circuit, *Phys. Rev. Lett.* **95**, 087001 (2005).
- [96] E. M. PURCELL, Spontaneous Emission Probabilities at Radio Frequencies, *Phys. Rev.* **69**, 681 (1946).
- [97] M. MARIANTONI, F. DEPPE, A. MARX, R. GROSS, F. K. WILHELM, and E. SOLANO, Two-resonator circuit quantum electrodynamics: A superconducting quantum switch, *Phys. Rev. B* **78**, 104508 (2008).
- [98] E. SOLANO, G. S. AGARWAL, and H. WALTHER, Strong-Driving-Assisted Multipartite Entanglement in Cavity QED, *Phys. Rev. Lett.* **90**, 027903 (2003).
- [99] S. M. BARNETT and P. M. RADMORE, *Methods in Theoretical Quantum Optics* (Oxford University Press, New York,, 1997).
- [100] P. LOUGOVSKI, F. CASAGRANDE, A. LULLI, and E. SOLANO, Strongly driven one-atom laser and decoherence monitoring, *Phys. Rev. A* **76**, 033802 (2007).
- [101] J. GAMBETTA, W. A. BRAFF, A. WALLRAFF, S. M. GIRVIN, and R. J. SCHOELKOPF, Protocols for optimal readout of qubits using a continuous quantum nondemolition measurement, *Phys. Rev. A* **76**, 012325 (2007).
- [102] COHEN-TANNOUJJI, *Atoms and Fields* (WILEY-VCH Verlag, Weinheim, 2004).
- [103] J. R. SCHRIEFFER and P. A. WOLFF, Relation Between the Anderson and Kondo Hamiltonians, *Phys. Rev.* **149**, 491 (1966).

-
- [104] W. BUCKEL and R. KLEINER, *Supraleitung* (WILEY-VCH Verlag, Weinheim, 2004).
- [105] M. TINKHAM, *Introduction to Superconductivity* (Dover Publications, Mineola, NY,, 2004).
- [106] A. J. LEGGETT, *Quantum Liquids* (Oxford University Press, New York,, 2006).
- [107] W. MEISSNER and R. OCHSENFELD, Ein neuer Effekt bei Eintritt der Supraleitfähigkeit, *Naturwissenschaften* **21**, 787 (1933).
- [108] B. D. JOSEPHSON, Possible new effects in superconductive tunnelling, *Phys. Lett.* **1**, 251 (1962).
- [109] J. BARDEEN, L. N. COOPER, and J. R. SCHRIEFFER, Theory of Superconductivity, *Phys. Rev.* **108**, 1175 (1957).
- [110] E. MADELUNG, Quantentheorie in hydrodynamischer Form, *Z. Phys.* **40**, 322 (1927).
- [111] D. BOHM, A Suggested Interpretation of the Quantum Theory in Terms of “Hidden” Variables, *Phys. Rev.* **85**, 166 (1952).
- [112] L. D. LANDAU, E. M. LIFSCHITZ, and L. P. PITAJEWSKI, *Lehrbuch der Theoretischen Physik*, vol. 9 (Akademie-Verlag, Berlin,, 1992).
- [113] W. C. STEWART, Current-Voltage Characteristics of Josephson Junctions, *Appl. Phys. Lett.* **12**, 277 (1968).
- [114] D. E. MCCUMBER, Effect of ac Impedance on dc Voltage-Current Characteristics of Superconductor Weak-Link Junctions, *J. Appl. Phys.* **39**, 3113 (1968).
- [115] K. K. LIKHAREV, Single-Electron Devices and Their Applications, *Proc. IEEE* **87**, 606 (1999).
- [116] G. MANGANO, Private Communication.
- [117] J. CLARKE and A. I. BRAGINSKI, *The SQUID Handbook* (WILEY-VCH Verlag, Weinheim, 2004).
- [118] D. T. PEGG and S. M. BARNETT, Phase properties of the quantized single-mode electromagnetic field, *Phys. Rev. A* **39**, 1665 (1989).
- [119] I. N. BRONSTEIN, K. A. SEMENDJAJEW, G. MUSIOL, and H. MÜHLIG, *Taschenbuch der Mathematik* (Verlag Harri Deutsch, Frankfurt am Main, 2001).
- [120] H. J. CARMICHAEL, *Statistical Methods in Quantum Optics I* (Springer, Berlin, 1999).
- [121] U. LEONHARDT, *Measuring the Quantum State of Light* (Cambridge University Press, 2003).
- [122] C. M. CAVES, Quantum limits on noise in linear amplifiers, *Phys. Rev. D* **26**, 1817 (1982).
- [123] D. ADAMS, So long, and thanks for all the fish, in: *The Ultimate Hitchhiker’s Guide* (Wings Books, New York, 1996).

Acknowledgements

At the end of this thesis, I would like to thank all people, who were (directly and indirectly) involved in this thesis.

Prof. Dr. Rudolf Gross for offering me the chance to do my diploma thesis under his supervision. I would also like to thank for several advices during this year, for motivating discussions, for the detailed proof-reading, and many helpful suggestions on the thesis.

Prof. Dr. Jan von Delft for the great opportunity to join his group, for supporting my work and my further scientific education, for his feedback, and also for proof-reading my thesis.

Prof. Dr. Enrique Solano for attracting me to this interesting field of research in the first place, for suggesting me this project, and for supervising it. I would also like to thank him for his scientific and moral support during my diploma thesis, for his time and patience, and for always being there for my questions. I have learned a lot from him and he has helped me to grow scientifically and personally.

Matteo Mariantoni for many helpful discussions about the research and my thesis and for often helping me out with experimental issues. I appreciate his helpfulness and enjoyed working together.

Dr. Jens Siewert and **Giuseppe Mangano**, also for many helpful discussions and for the interesting and fruitful collaboration.

Wolfgang Münder and **Alexander Buchner** for being my roommates over several months. Thanks a lot for the great physical and non-physical discussions and for cheering up my days. **Peter Fritsch** for having patience with me and my Mac so many times and also for many interesting discussions. **Cheng Guo** for the helpful input concerning layout issues and for many nice conversations.

I would like to extend my gratitude to **all members** of the Chair for Theoretical Solid State Physics at the LMU. All of you have created a great climate in a very friendly group and made this past year a memorable experience.

My family for all the backup they gave me through five years of studies. My **mother** for the recreative weekends, the supporting talks, for encouraging me, and for always being proud of

me. My little sister **Katharina** for not driving me totally crazy (I know that you will find your way!). And my sister **Michaela** (where I also include **Oliver**) for always being there for me, for cheering me up, and, of course, for supplying me with coffee and chocolate.

Last but not least I want to thank a special person, **Christian Seidel**, not only for helping me with so many physical and technical problems concerning my thesis and for proof-reading it, but also for always being there for me, for supporting me, for motivating me, for believing in me, and for brightening up my life.

So long, and thanks for all the fish . . . [123].